Application of MODIS-ASTER (Master) Simulator Data to Geological Mapping of Young Volcanic Regions in Baja California, Mexico

Thesis by

Jane Ellen Dmochowski

In Partial Fulfillment of the
Requirements for the Degree of Doctor
of Philosophy

California Institute of Technology
Pasadena, California

2005
(Submitted July, 2004)

I dedicate this thesis to Dennis and Jacqueline Heinemann.

“Nothing in life is to be feared, it is only to be understood.” Marie Curie (1867- 1934)

“The scientist does not study nature because it is useful; he studies it because he delights in it, and he delights in it because it is beautiful. If nature were not beautiful, it would not be worth knowing, and if nature were not worth knowing, life would not be worth living.”

Jules Henri Poincaré (1854-1912)

Acknowledgements

As with all scientific endeavors, my research has greatly benefited from those who have gone before me. This thesis would not have been possible without the work of scientists such as Eugene Schmidt, Alexander Goetz, Michael Sawlan, Alain Demant, Joann Stock, Brian Hausback, Francisco Paz, and others referenced in this thesis.

I would like to especially thank my advisors and collaborators: Joann Stock, who supported me through two very different projects and a few comings and goings; Rob Clayton, who never ceased to be supportive and genuine; Francisco Paz, whose energy and climbing prowess is second to none; Joao Rosa, for his hospitality and enthusiasm; Arturo Martin-Barajas, whose relaxed manner and knowledge of Mexican geology is an inspiration to all; Julie Parra and Chloe Winant, whose enthusiasm to learn made my return to Caltech a pleasure; Brian Hausback, without whom I would never have contemplated how guano might be used for geologic dating; Chris Farrar, whose humor was vital to our field excursions; Dave Pieri, whose kindness is infectious; and Simon Hook, for his clarity in teaching me the nuances of MASTER data as well as important life lessons.

A bit reluctant to enter Caltech those many years ago, I dreaded there would *only* be scientists. Besides, it was far from an exotic locale, situated just 40 miles from my hometown. Little did I know, however, that I would travel the world, in more ways than one, during my years at Caltech and in doing so, make the best friends of my life.

Through the adventurous spirit of my advisor, Joann Stock, I was able to explore the many beauties of Baja California and mainland Mexico; see the geothermal fields and glaciers of New Zealand; go skiing in Chile; spend six months dancing, I mean researching, in Brazil; peer up at the looming Mount Erebus on the Antarctic continent; even face down icebergs while floating on 50 foot waves in the South Pacific. For those places my research did not send me, Caltech sent them to me, in the form of irreplaceable friends. Through the international diversity at Caltech, I was able to gain friendships with people from: Italy, Iceland, Russia, Israel, Guyana, Germany, Turkey, Argentina, Spain, Canada, Ireland, China, Romania, Columbia, Lebanon, India, South Africa, Brazil, Mexico, and England; to name just a few.

I would never have had the courage to undertake graduate study if not for the superb mentoring of my undergraduate professors at UCSB: Tanya Atwater, Art Sylvester, and Ralph Archuleta. And, I would never have come to Caltech had it not been for two graduate students, Tim Melbourne and Sharon Kedar, who somehow convinced me that they were fairly "normal" and quite enjoyed Caltech. I am also thankful to Julie Nazareth, Dave Evans, Emily Brodsky, Debbie Smith, and Sarah Stewart-Mukhopadhyay for their supportive friendships in my early years at Caltech. I give a special thanks to Magali Billen, who is a warm friend, a trusted shipmate, and an expert flower arranger, not to mention a bright scientist.

After my leave of absence from Caltech and subsequent return, I faced a hurdle in assimilating back into the culture. I was only able to do so with the friendships of

Patricia Persaud, Rowena Lohman, Anupama Venkataraman, and my fellow chocolate, tea, and (salty!) licorice lover, Vala Hjorleifsdottir. The long lunches and gripe sessions were vital to my survival. Special thanks also go to Joe Akins whose unfeigned character is always a breath of fresh air. I would like to give recognition to Patricia Persaud and Mike Oskin for their insightful conversations during our "Mexican Geology Club" meetings.

I owe tremendous thanks to the GPS staff. Donna Sackett was an invaluable source of support to me in my first years at Caltech—she is greatly missed. Special recognition also goes to JoAnne Giberson, Shaun Healy, Viola Carter, Jean Grinols, Elisa Loeffen**,** Rosemary Miller, Evelina Cui**,** Michelle Medley and Sue Yamada.

Also important to my success were the friendships I made outside of GPS. Thank you to those who befriended me, despite my geophysics affiliation: Moira Regelson, Derek Debe, Jim Kempf, Chantal Morgan-D'Apuzzo, Adrian Ponce, Akif Tezcan, Jasmin Faraone-Manella, Xenia Amashukeli, Alex Bäcker, Eva Peral, Claudine Chen, Elizabeth Krider, Will Wehbi, Freda Caldwell, Cindy Quezada, the TACIT crew, and my fellow soccer buddies on "Kicking Buck." I also owe special gratitude to Harry and Shirley Gray who have shown incredible generosity to Ivan and me.

This last year and a half of work in Philadelphia was made tolerable by the hospitality of the University of Pennsylvania Chemistry Department. Thank you for giving me a place to work, not insisting I leave my door open, and welcoming me. I also owe gratitude to

my Philadelphia friends and yoga teachers. I especially acknowledge the tremendous support of the women of the Philadelphia RBB—may all our dreams come true.

Finally, I am greatly indebted to my family and friends who have supported me unconditionally, even well before I had any aspiration of undertaking a Ph.D. My parents gave me the gift of unconditional love and instilled in me a strong desire for knowledge. They were neither pushy when I contemplated what to do with my life, nor critical when I took wrong turns. I would like to give special thanks to my mother, whose insistence that we visit places off the beaten path, like Pisgah Crater, most certainly influenced my love of Earth Science. And here is an ode to my father who woke me at 5:00AM each morning of my senior year of high school to finish my Physics homework before he headed off to work. I would like to pay tribute as well to my wonderful siblings and their equally special spouses: Christa, Andrew, Shelley, Charlie, Melissa, and Thornton. I could not ask for a more loving family. To my grandfather, Jack, who is always a source of entertainment when I feel like procrastinating: Thank you for amusing me with stories of Downer's Grove and the latest in Reality TV. And to Kamaryn: I thank you for your honesty and love. I am grateful to the entire Dmochowski family. You have been so welcoming and have greatly eased my transition to the East Coast. Lastly, I would like to thank my husband, Ivan Dmochowski. You are my confidant, my cheerleader, and my best friend. Your unyielding support and love is second to none. Thank you for your patience and understanding. More importantly, thank you for purchasing our doggie, Leite, with our last five hundred dollars. May we continue to make such smart investments.

Abstract

Visible, near infrared, short-wave infrared, and thermal infrared multi-channel remote sensing data, MODIS-ASTER (MASTER), are used to extract geologic information from two volcanic regions in Baja California, Mexico: Tres Vírgenes-La Reforma Volcanic Region and the volcanic island of Isla San Luis. The visible and near infrared and short-wave infrared data were atmospherically corrected and classified. The resulting classification roughly delineates surfaces that vary in their secondary minerals. Attempts to identify these minerals using ENVI's Spectral Analyst^{TM} were moderately successful.

The analysis of the thermal infrared data utilizes the shift to longer wavelengths in the Reststrahlen band as the mineralogy changes from felsic to mafic to translate the data into values of weight percent SiO_2. The results indicate that the general approach tends to underestimate the weight percent SiO_2 in the image. This discrepancy is removed with a "site calibration," which provides good results in the calculated weight percent SiO_2, with errors of a few percent. However, errors become larger with rugged topography or low solar angle at the time of image acquisition.

Analysis of bathymetric data around Isla San Luis, and consideration of the island's alignment with the Ballenas transform fault zone to the south and volcanic seamounts nearby, suggest Isla San Luis is potentially volcanically active and could be the product of a "leaky" transform fault. The results from the image analysis in the Tres Vírgenes-La Reforma Volcanic Region show the La Reforma and El Aguajito volcanic centers to be bimodal in composition and verify the most recent volcanism in the Tres Vírgenes region

to be basaltic-andesite. The results of fieldwork and image analysis indicate that the volcanic products of the central dome of La Reforma are likely a sequence of welded ash flow tuffs and lavas of varied composition, evidence of its origin as a caldera.

Chapter 1: Introduction

Abstract

Visible, near infrared, short-wave infrared, and thermal infrared multi-channel remote sensing data, MODIS-ASTER (MASTER), are used to extract geologic information from two volcanic regions in Baja California, Mexico: Tres Vírgenes-La Reforma Volcanic Region and the volcanic island of Isla San Luis. The visible, near infrared and short-wave infrared data were atmospherically corrected and classified. The resulting classification roughly delineates surfaces that vary in their secondary minerals. Attempts to identify these minerals using ENVI's Spectral Analyst™ were moderately successful.

The analysis of the thermal infrared data utilizes the shift to longer wavelengths in the Reststrahlen band as the mineralogy changes from felsic to mafic to translate the data into values of weight percent SiO_2. The results indicate that the general approach tends to underestimate the weight percent SiO_2 in the image. This discrepancy is removed with a "site calibration," which provides good results in the calculated weight percent SiO_2, with errors of a few percent. However, errors become larger with high topographic relief or low solar angle at the time of image acquisition.

Analysis of bathymetric data around Isla San Luis, and consideration of the island's alignment with the Ballenas transform fault zone to the south and volcanic seamounts nearby, suggest that Isla San Luis is potentially volcanically active and could be the product of a "leaky" transform fault. The results from the image analysis in the Tres

Vírgenes-La Reforma Volcanic Region show the La Reforma and El Aguajito volcanic centers to be bimodal in composition and verify the most recent volcanism in the Tres Vírgenes region to be basaltic-andesite. The results of fieldwork and image analysis indicate that the volcanic products of the central dome of La Reforma are likely a sequence of welded ash flow tuffs and lavas of varied composition, evidence of its origin as a caldera.

1.1 Introduction

This thesis involves the use of multi-channel remote sensing data, MODIS-ASTER (MASTER) (Fig. 1), to extract geologic information from two volcanic regions in Baja California, Mexico: Tres Vírgenes-La Reforma Volcanic Region (TVLRVR) and the volcanic island of Isla San Luis (ISL) in the Puertecitos Volcanic Province (PVP) (Fig. 2), in order to gain a better understanding of these recent volcanic centers. Additionally, this thesis describes the capabilities of the MASTER instrument in lithologic mapping.

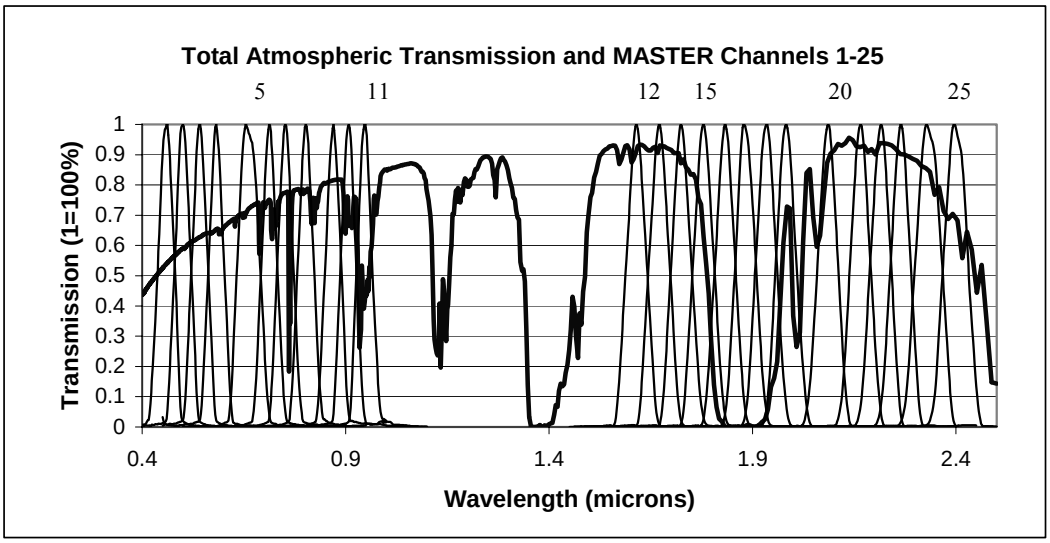

Figure 1. Plot of atmospheric transmission overlain by the system response functions of MASTER bands 1 - 25.

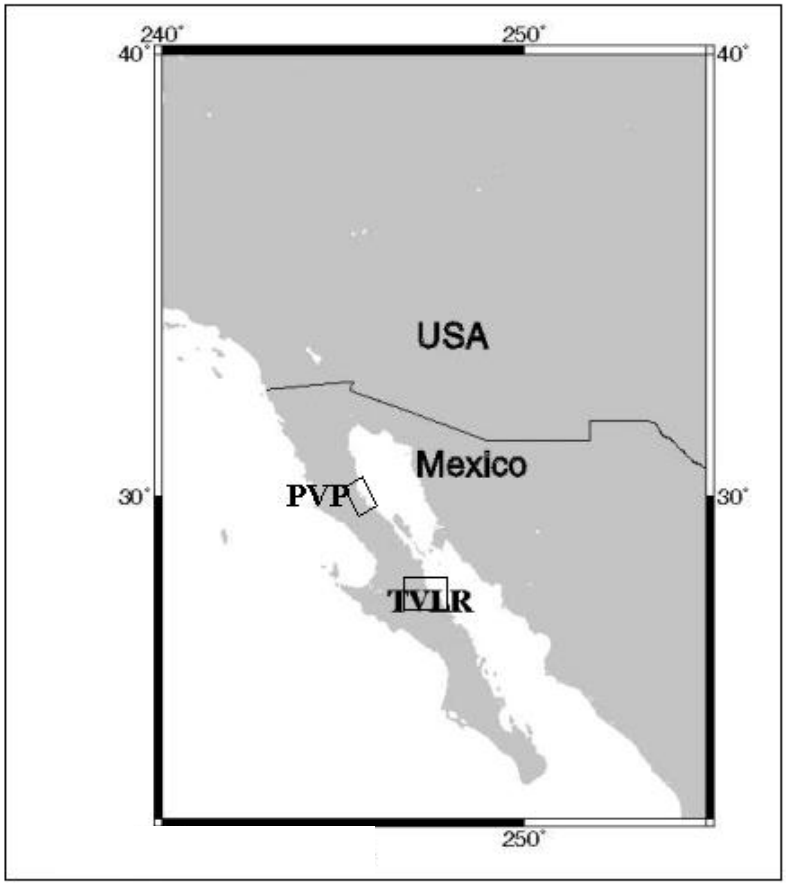

Figure 2. Map of Baja California and the Southwestern United States showing the location of the Tres Vírgenes -La Reforma Volcanic Region (labeled TVLR) and the Puertecitos Volcanic Province (labeled PVP).

1.2 Geologic Background

The peninsula of Baja California, Mexico, has undergone tremendous transformation in the last 25 million years. In this time it has transitioned from a region of arc volcanism, related to the subduction of the Guadalupe microplate to a transtensional region on the western edge of the transform plate boundary between the Pacific and North American plates [*Gastil*, 1979; *Sawlan*, 1991]. Between 25 Ma and 12 Ma, the triple junction between the Pacific, Guadalupe, and North American plates propagated southward down

the margin of western Baja California, shutting off the arc-related volcanism in the peninsula [*Mammerickx and Klitgord*, 1982]. In northern Baja California, it appears that arc-related volcanism ceased at 17-15 Ma [*Martín et al.*, 2000]. Farther south it continued until approximately 12 Ma [*Sawlan and Smith*, 1984b], when the Guadalupe-Pacific rise ceased to spread [*Mammerickx and Klitgord*, 1982] and subduction presumably stopped. During the time of subduction, Baja California was still part of mainland Mexico. It was not until approximately 6 Ma that the extension became localized to the region now known as the Gulf of California [*Oskin et al.*, 2001]. The complete transfer of Baja California to the Pacific plate is known to have occurred prior to 3.5 Ma, as evidenced by the formation of magnetically lineated oceanic crust at the Alarcon Rise in the southern portion of the Gulf of California [*Lonsdale*, 1989]. As early as 30 Ma, the broad area of the Gulf Extensional Province north through Arizona and New Mexico has undergone extension [Henry and Aranda-Gomez, 1992].

The North American-Pacific plate boundary is now a series of rift basins and transform faults [*Zanchi*, 1994; *Stock and Hodges*, 1990; *Persaud et al.* [2003]; *Lewis and Stock*, 1998; and others]. Around 3.3 Ma, the plate boundary made a westward jump from the Tiburon basin to the Upper Delphin basin, and after 2 Ma the southern Tiburon basin jumped to the Lower Delphin basin [*Lonsdale*, 1989; *Stock*, 2000].

The oblique rifting that is now occurring in the Gulf of California began 6 Ma [*Oskin et al.*, 2001]; however, evidence of seafloor spreading is only found in the Alarcon basin and southward [*Klitgord and Mammerickx*, 1982]. In the northern Gulf of California,

recent studies indicate there is active distributed deformation characterized by segmented basins, and both intrusive and extrusive magmatism [*Persaud et al.*, 2003]. *Persaud et al.* [2003] suggest that seafloor spreading is not present in the northern Gulf of California, due to the lack of strain-partitioned and focused deformation. The broad shear zone beneath the thick sediment cover from the Colorado River delta causes this distributed strain pattern [*Persaud et al.*, 2003].

Volcanism during this phase of rifting has occurred in several locations on the Baja California Peninsula. The TVLRVR, on the east coast of Baja California (27.5°N), includes three volcanic systems—La Reforma caldera to the east, El Aguajito volcanic complex to the north, and the Tres Vírgenes volcanoes to the southwest. The PVP extends N-S from latitude 30°30' N to 29°55' N. Its east-west extent spans from central Baja California to the Gulf of California and includes Isla San Luis, as well as other islands near the coast. The PVP includes rhyolitic-dacitic welded tuffs, rhyolite dome fields, intermediate composition volcanoes, and small-volume local mafic lavas.

Both PVP and TVLRVR described above are extremely remote; many of the interiors of the volcanic centers have no fresh water, few roads, and in some cases are only accessible by foot, pack animal, or boat along the coastline. In the case of Isla San Luis, a boat is necessary to reach the island and entrance to the island is restricted due to its status as a bird sanctuary in the Islas del Golfo nature preserve. To reach the central block of the La Reforma Caldera requires a multi-day backpacking trip, as well as government approval since it is within a biosphere reserve. Because of the difficulties with access, previous

geological studies of these sites had very limited field observations and primarily relied on conventional air photo interpretation. However, many of the volcanic units are difficult to differentiate on the air photos. By using remote sensing as a tool in lithological classification of the rocks in this region, the few available geological ground observations can be extended much more reliably than was previously possible.

1.2.1 Tres Vírgenes – La Reforma Region

The TVLRVR is on the western edge of the Gulf of California, which formed as a result of the continental rifting and the transfer of crust from the North America plate to the Pacific plate. As a result of extensional stress, NW-SE faults were generated and the Santa Rosalia basin was formed [*Hernández*, 1998]. This began the deposition of marine sediments in this region. The volcanism of the TVLRVR is mostly calc-alkaline with some tholeiitic and peralkaline affinities [*Sawlan*, 1986; *Schmidt*, 1975; and *Demant*, 1984]. The volcanism is related to the extensional deformation accompanying the formation of the Gulf of California [*Sawlan*, 1981; *Sawlan and Smith*, 1984a; *Colletta and Angelier*, 1981]. Subduction in this region, responsible for forming the Comondú Volcanics to the south and west of this region, shut off approximately 12.5 - 11 Ma [*Mammerickx and Klitgord*, 1982].

The TVLRVR is seismically active [*Guerrero-Guadarrama*, 1998; *Wong et al.*, 2001; *Garduño-Monroy et al.*, 1993] and has active fumaroles [*Hernández*, 1998]. Previous geologic mapping in the region was conducted by *Demant* [1984], *Garduño-Monroy et*

al. [1993], *Hernández* [1998], *Romero-Rojas et al.* [1997], *Schmidt* [1975], *Vargas-Ledezma and Garduño-Monroy* [1988], and *Wong et al.* [2001].

La Reforma is thought to be the oldest volcanic edifice in the TVLRVR. The La Reforma volcanic complex has been dated ca. 1.09 Ma [*Schmidt*, 1975]. However, the geologic history of the complex has received differing explanations [*Demant*, 1984; *Schmidt*, 1975; *Walker et al.*, 1992]. *Demant* [1984] and *Demant and Ortlieb* [1981] interpreted the central dome of La Reforma to be a block of Miocene Comondú Formation uplifted by piston-like movement. This contrasts with the interpretation by *Schmidt* [1975], who described the feature not as a caldera, but as a system of tectonic blocks, and *Walker et al.* [1992], who described the complex as an updomed structure that has been circularly eroded.

The El Aguajito volcanic complex was determined to be a caldera based on its arcuately aligned rhyolite domes that appear to have developed over a pre-existing ring fracture [*Garduño-Monroy et al.*, 1993]. The resurgence of the central dome was determined by the dips of the ignimbrite sheets in the region that appear to radiate outward from the center of the volcanic edifice [*Garduño-Monroy et al.*, 1993]. By inferring that the 0.8 Ma silicic domes conceal the ring fracture of the caldera, *Garduño-Monroy et al.* [1993] determined the caldera to be 10 km in diameter.

Garduño-Monroy et al. [1993] noted that El Aguajito's eruptive products overlie those of the La Reforma caldera. The observation and interpretation of *Garduño-Monroy et al.*

[1993] and *Sawlan* [1981] imply that the volcanic vents in the TVLRVR have erupted in a counterclockwise fashion from La Reforma to Volcán La Virgen over the last few million years.

As volcanic activity moved from the volcanic complexes of La Reforma and El Aguajito to the Tres Vírgenes volcanic centers, the stress regime changed to a trans-tensional system, and old normal faults were reactivated as lateral faults [*Hernández*, 1998; *Umhoefer and Teyssier*, 1991]. The Tres Vírgenes volcanic centers were formed in this zone of weakness. The three volcanoes of Tres Vírgenes are aligned in a NE-SW direction and get progressively younger to the southwest. This NE-SW alignment of volcanic vents in the region was attributed by *Umhoefer and Teyssier* [1991] to a N-S extensional zone.

From NE to SW the volcanic centers of Tres Vírgenes are named El Viejo, El Azufre[1], and La Virgen. El Viejo and El Azufre are composed primarily of dacitic lava domes and lavas and are the two oldest edifices of the Tres Vírgenes volcanoes [*Capra et al.*, 1998; *Demant*, 1984; *Sawlan*, 1981; *Garduño-Monroy et al.*, 1993]. La Virgen is a calc-alkaline stratovolcano [*Capra et al.*, 1998; *Demant*, 1984; *Sawlan*, 1981].

There are few isotopic dates available on the volcanic deposits from Tres Vírgenes volcanoes. *Hernández* [1998] reports K/Ar dates that show a north to south migration of volcanism: 0.44 Ma (El Viejo volcanic products) and 0.28 Ma (El Azufre volcanic products). A visiting missionary, Rev. Fernando Consag, is thought to have witnessed an

[1] El Azufre volcano is also referred to as La Soufre by *Sawlan* [1981].

eruption from Volcán La Virgen in 1746 [*Ives*, 1962]. Unfortunately, more definitive evidence of historical volcanic eruptions in the TVLRVR is not available. A ^{14}C analysis of carbonized wood within a middle unit yielded a date of 6515± 75 y.b.p. [*Capra et al.*, 1998], which signifies that the upper unit must be younger and eruptions have taken place at La Virgen less than 6,515 years ago.

1.2.2 Isla San Luis

The Puertecitos Volcanic Province is located on the western edge of the Gulf Extensional Province at latitude 30°N. The PVP is an important region in understanding the evolution of the Gulf of California due to the compositions and ages of its volcanic products (which range from Miocene to Holocene). ISL is approximately 3.5 by 2.5 km^2 in size and is located approximately 5 km from the Baja California coast, offshore of the Puertecitos Volcanic Province, west of the Upper Delphin Basin, in the Gulf of California. Volcanism is highly differentiated and the compositional variation has been regular, from early basaltic andesite to the recent rhyolitic domes [*Paz-Moreno and Demant*, 1999].

Isla San Luis' morphology indicates that it has erupted recently. A K-Ar date of 11.7 Ma was obtained on the intermediate lavas exposed along the western shore [*Rossetter*, 1973], but is now thought to be suspect [*Hausback et al.*, 2003]. More recent analyses show that volcanism on Isla San Luis began at least 4725 years before present and continued until perhaps 1225 years ago [*Hausback et al.*, 2003].

1.3 Overview of this Thesis

The MASTER data set has an instantaneous field of view of 2.5 milliradians and a total field of view of 85.92 degrees [*Hook et al.*, 2001]. For the data used in this thesis, the average acquisition height is 2.3 km, which yields images with a 5.75 meter pixel size and a swath width of approximately 4 km. The data have 50 spectral channels: 11 in the visible and near infrared range, 14 in the short-wave infrared range, 15 in the mid-infrared range, and 10 in the thermal infrared range. These provide capability for mapping of lithologies; however, this work shows that mineral mapping with this instrument is very limited. This thesis divides the MASTER data set into two subsets for data processing. The VNIR-SWIR data are used for lithologic classifications, and the TIR data are used for mapping the weight percent silica of the surfaces.

Chapter 2 describes the preliminary work needed to create the classifications. The calibrated VNIR-SWIR data must be first georeferenced. The data are then atmospherically corrected using ACORN, an ENVI plug-in module, and the ENVI empirical line calibration (ELC) feature. Following the atmospheric correction, the data are in apparent reflectance. The 28 separate atmospherically corrected images are then mosaicked together, and the Pixel Purity Indices (PPI^{TM}) are computed. Once the most spectrally pure pixels are identified, the endmembers are chosen using ENVI's N-dimensional Visualizer^{TM}. This tool allows the user to view an n-dimensional Euclidean space.

Chapter 2 discusses how the classification was produced using the Spectral Angle Mapper algorithm within ENVI. ENVI's Spectral Analyst^{TM} compares the endmembers to known spectra. MASTER is a multispectral instrument, not hyperspectral, due to the limited number of bands covering the electromagnetic spectrum. However, this processing technique is still useful in determining the purest endmembers, classifying the data, and determining the most likely lithology of the endmembers. The resulting classification for the TVLRVR is shown in Plate 1.

TIR data are atmospherically corrected using a radiative transfer algorithm (MODTRAN 3.5) within the WINVICAR software, driven with the National Center for Environmental Prediction (NCEP) atmospheric profiles. The TIR can be processed (with the TES algorithm within WINVICAR) to emissivity and compared to lab spectral data for samples from the area. Emissivity images allow mapping of the regional variation in wt. % SiO_2. This quantitative estimation is an important factor in distinguishing among the igneous rocks in the region, which vary greatly from mafic to silicic in composition.

In **Chapter 2**, the atmospheric correction and classification of 28 images of VNIR-SWIR MASTER data in the Tres Vírgenes-La Reforma Volcanic Region are discussed. The VNIR-SWIR MASTER data can be atmospherically corrected to a reasonable accuracy with both the ACORN software and the Empirical Line Calibration (ELC) mode in ENVI. It is shown that a reliable correction is difficult to obtain for those bands in the water absorption region (MASTER bands 11, 15 - 19, and 25). Atmospherically corrected MASTER data, resized to exclude the bands highly affected by water

absorption, are classified. **Chapter 2** discusses how MASTER data can be atmospherically corrected to a reasonable accuracy with both the ACORN software and the ELC mode in ENVI. If known spectra are available within one line for both a dark and light spectrum, the ELC appears to be a more accurate method for the MASTER data. However, with either technique, a reliable correction is difficult to obtain for those bands in the water absorption region (MASTER bands 11, 15 - 19, and 25), even if atmospheric parameters are known.

This analysis described in **Chapter 2** yields a classification map that roughly delineates surfaces that vary in their secondary minerals, produced by weathering and alteration, namely ferric oxides, hydrates, hydroxyls, and carbonates (Plate 1). ENVI's Spectral Analyst™ is only moderately successful at identifying these minerals. It is necessary to have auxiliary information about the lithology of the underlying rock and secondary minerals within the surface represented by each endmember for precise lithologic identification.

Chapter 3 illustrates the shift to longer wavelengths of the main spectral feature in the thermal infrared wavelength region (Reststrahlen band) as the mineralogy changes from felsic to mafic. This correlation is utilized to map weight percent silica, using the MASTER data. The size of this shift is translated into weight percent SiO_2 of the surface using a reference curve, derived from laboratory data. The results indicate that the

general approach tends to underestimate the weight percent SiO_2 in the image[2]. This discrepancy can be removed by performing a site calibration with measurements from field samples. These site calibrated, georectified, masked and mosaicked data, with each pixel assigned a weight percent silica value, are shown in Plate 2.

This thesis addresses two primary questions. First, the author details the extent to which geologic information can be extracted from MASTER data. The MASTER dataset from Baja California collected in April of 1999 was the first scientific dataset acquired with the MASTER instrument. Although its neoteric nature has its share of drawbacks, these data also present a unique opportunity to contribute to future work with this instrument. Since the MASTER instrument was developed for the Advanced Spaceborne Thermal Emission Reflection Radiometer (ASTER) satellite as well as the Moderate Resolution Imaging Spectroradiometer (MODIS) projects, these studies contribute to a general understanding of these instruments as well. Secondly, using the analyzed MASTER images, digital elevation models, ASTER satellite imagery and bathymetric data, this thesis explores the eruptive history of La Reforma, El Aguajito and Tres Vírgenes, and Isla San Luis and how their eruptive evolution is related to the Gulf of California.

In **Chapter 3**, a test portion of the TIR image 9900302U is analyzed for weight percent silica. An approach is described for determining the shift in the Reststrahlen band using a Gaussian curve. The size of this shift is translated into weight percent SiO_2 of the surface

[2] In the Hiller Mountains test region, discussed by *Hook et al.* [2005], results indicate the general approach slightly overestimates the weight percent SiO_2 of low silica rocks (e.g. basalt) and underestimates the weight percent SiO_2 of high silica rocks (e.g. granite).

using a reference curve, derived from laboratory data. The approach has applicability to other study areas and can also be fine-tuned to give greater accuracy in a particular study area, if field samples are available.

This approach is further assessed using remotely acquired airborne multispectral thermal infrared images from the La Reforma Caldera, Baja California Sur, Mexico. The results indicate that the general approach tends to underestimate the weight percent SiO_2 in the image[3]. This discrepancy is removed by fine-tuning the general approach with measurements from field samples; these data agree with the calculated weight percent SiO_2, with errors of a few percent.

In **Chapter 4**, several images are constructed in order to summarize and revise previous geologic mapping done in the TVLRVR. These images include a classification of atmospherically corrected MASTER multi-channel VNIR-SWIR data, a weight percent silica map, a mosaicked ASTER image, and a Thematic Mapper image draped over a digital elevation model. These images help to better delineate previously mapped units and revise erroneously mapped regions. A major revision is the composition of La Reforma's resurgent dome, which was believed to be composed of Miocene Comondú Volcanics, but is now designated as younger welded ash-flow tuffs and lavas. This new understanding of the central region of La Reforma is more conclusive evidence of its identification as a caldera. The La Reforma caldera and the El Aguajito volcanic

[3] In the Hiller Mountains test region, also discussed by *Hook et al.* [2005], results indicate the general approach slightly overestimates the weight percent SiO_2 of low silica rocks (e.g. basalt) and underestimates the weight percent SiO_2 of high silica rocks (e.g. granite).

complex appear to be bi-modal volcanic centers, and the Tres Vírgenes volcanoes are calc-alkaline, well differentiated volcanoes.

The weight percent silica technique works well overall, but errors in separating the temperature and the emissivity in the thermal infrared data in regions of high topographic relief and low solar angle diminish the ability of the Gaussian fitting technique to accurately estimate the weight percent silica. This effect appears as a flattening of the TIR spectrum, changing the weight percent silica value. Pixels that are in the shadows have elevated weight percent silica. The temperature emissivity technique, and therefore the weight percent silica technique, work best on flat terrain, or with images collected at exactly solar noon. This problem is discussed further in **Chapters 4 and 5**.

Chapter 4 also summarizes the evolution of the TVLRVR in the last few million years from bimodal caldera structures, within a largely extensional regime, to stratovolcanoes within a transtensional regime and confirms that La Reforma is likely a caldera, due to its composition and morphology, as well as the existence of both ignimbrite outflow sheets and a megabreccia unit indicating a mass-wasting event associated with collapse. **Chapter 4** also discusses the classification of El Aguajito as a caldera. While it is possible that the rhyolitic domes surrounding the central dome could conceal a ring fracture, the lack of a megabreccia unit within the central portion of the volcanic complex and no recognizable collapse features prohibits a definitive identification of the El Aguajito volcanic complex as a caldera. The possibility that the magmatic piping of La

Reforma and El Aguajito are connected and collapse took place only at the La Reforma caldera is proposed in **Chapter 4**.

In **Chapter 5**, I use the same type of remote sensing (MASTER) data to map the extent of volcanic deposits on a Holocene volcanic island, Isla San Luis. It is shown that the weight percent silica map and the classification moderately delineate the geologic units. The lack of easily identifiable alteration minerals on ISL and the high percentage of surface area covered in seafowl excrement diminish the effectiveness of the MASTER image analysis for this island. Also, the high topographic relief of ISL and the low solar angle during image acquisition cause the weight percent silica map to be heavily affected by the incomplete separation of temperature emissivity using the TES algorithm.

Also included in **Chapter 5** is an analysis of the bathymetric data collected near Isla San Luis. These data, in conjunction with the geological constraints and other evidence of recent volcanism in the region, suggest a tectonic origin of ISL along a leaky transform fault within the transtensional regime of the Gulf of California. This interpretation is supported by many recent volcanic observations, including the presence of fumarolic gas emissions that continue today from the northern rhyolite dome. Some of the offshore vents can be seen as local maxima in the bathymetric data. Isotopic dates on mollusk shells from beach deposits interbedded with the volcanic layers on ISL yield ages from 4725 to 2888 y.b.p. The latest eruptions are younger but undated. Based on these dates and the present elevations of the beach deposits, **Chapter 5** discusses the estimation that ISL has been uplifted at approximately a rate of ~0.7 cm/yr for the last ~3000 years.

Other evidence of recent volcanism that suggests ISL remains potentially active is further discussed in **Chapter 5**.

References

Capra, L., J.L. Macias, J.M. Espindola, and C. Siebe, Holocene plinian eruption of La Virgen volcano, Baja California, Mexico, *Journal of Volcanology and Geothermal Research*, *80* (3-4), 239-266, 1998.

Colletta, B., and J. Angelier, Faulting evolution of the Santa Rosalia Basin, Baja California, Mexico, in *Geology of Northwestern Mexico and Southern Arizona*, edited by L. Ortlieb, and J. Roldan-Quintana, pp. 265-274, Estacion Regional del Noroeste, Instituto de Geologia, U.N.A.M., Hermosillo, Sonora, Mexico, 1981.

Demant, A., The Reforma Caldera, Santa Rosalia Area, Baja California, A volcanological, petrographical and mineralogical study, in *Neotectonics and sea level variations in the Gulf of California area, a Symposium*, edited by V. Malpica-Cruz, S. Celis-Gutiérrez, J. Guerrero-Garcia, and L. Ortlieb, pp. 77-96, Univ. Nal. Auton, México, Inst. Geologia, México, D. F., 1984.

Demant, A., and L. Ortlieb, Plio-Pleistocene Volcano-Tectonic Evolution of La Reforma Caldera, Baja California, Mexico, *Tectonophysics*, *71* (1-4), 194-194, 1981.

Garduño-Monroy, V.H., H. Vargas-Ledezma, and J.O. Campos-Enriquez, Preliminary geologic studies of Sierra El Aguajito (Baja California, Mexico): a resurgent-type caldera, *Journal of Volcanology and Geothermal Research*, *59*, 47-58, 1993.

Gastil, G.R., The record of Cenozoic volcanism around the Gulf of California, *Geological Society of America Bulletin*, *90* (839-857), 1979.

Guerrero-Guadarrama, J.L., Actividad Sísmica del Campo Geotérmico de Las Tres Vírgenes, *Geotermia*, *14*,, 87-100, 1998.

Hausback, B.P., A. Cook, C.D. Farrar, A. Martin, F. Paz-Moreno, J.M. Stock, and J.E. Dmochowski, Isla San Luis volcano, Baja California, Mexico - late Holocene eruptions, in *Geological Society of America, Cordilleran Section*, Puerto Vallarta, Jalisco, Mexico, 2003.

Henry, C. D. and J. J. Aranda-Gomez, The real southern Basin and Range: Mid- to late Cenozoic extension in Mexico, *Geology,* 20, 701-704, 1992.

Hernández, A.L., Geological Synthesis of Las Tres Vírgenes Geothermal Area, B. C. S., Mexico, *Geotermia, Revista Mexicana de Geoenergia*, *14* (1), 3-14, 1998.

Hernández, A.L., Geological Synthesis of Las Tres Vírgenes Geothermal Area, B. C. S., Mexico, *Geotermia, Revista Mexicana de Geoenergía*, *14* (1), 3-14, 1998.

Hook, S.J., J.E. Dmochowski, K.A. Howard, L.C. Rowan, K.E. Karlstrom, and J.M. Stock, Mapping variations in weight percent silica measured from multispectral thermal infrared imagery—Examples from the Hiller Mountains, Nevada, USA and Tres Vírgenes-La Reforma, Baja California, Baja California Sur, Mexico, *Remote Sensing of Environment*, *95*, 273-289, 2005.

Hook, S.J., J.J. Myers, K.J. Thome, M. Fitzgerald, and A.B. Kahle, The MODIS/ASTER airborne simulator (MASTER)—a new instrument for earth science studies, *Remote Sensing of Environment*, *76*, 93-102, 2001.

Ives, R.L., Dating of the 1746 eruption of Tres Vírgenes Volcano, Baja California del Sur, Mexico, *Geological Society of America Bulletin*, *73*, 647-648, 1962.

Klitgord, K.D., and J. Mammerickx, Northern East Pacific Rise - Magnetic Anomaly and Bathymetric Framework, *Journal of Geophysical Research*, *87* (NB8), 6725-&, 1982.

Lewis, C.J., and J.M. Stock, Late Miocene to recent transtensional tectonics in the Sierra San Fermín, northeastern Baja California, Mexico, *Journal of Structural Geology*, *20* (8), 1043-1063, 1998.

Lonsdale, P., Geology and tectonic history of the Gulf of California, in *The Eastern Pacific Ocean and Hawaii*, edited by D.M. Hussong, E.L. Winterer, and R.W. Decker, pp. 499-521, Geological Society of America, Boulder, Colorado, 1989.

Mammerickx, J., and K.D. Klitgord, Northern East Pacific Rise - Evolution from 25 My Bp to the Present, *Journal of Geophysical Research*, *87* (NB8), 6751-6759, 1982.

Martín, A., J.M. Fletcher, M. López-Martínez, and R. Mendoza-Borunda, Waning Miocene subduction and arc volcanism in Baja California: the San Luis Gonzaga volcanic field, *Tectonophysics*, *318* (1-4), 27-51, 2000.

Oskin, M.E., J.M. Stock, and A. Martin-Barajas, Rapid localization of Pacific-North America plate motion in the Gulf of California, *Geology*, *29* (5), 459-462, 2001.

Paz-Moreno, F.A., and A. Demant, The Recent Isla San Luis volcanic centre: petrology of a rift-related volcanic suite in the northern Gulf of California, Mexico, *Journal of Volcanology and Geothermal Research*, *93* (1-2), 31-52, 1999.

Persaud, P., J.M. Stock, M.S. Steckler, A. Martín-Barajas, J.B. Diebold, A. González-Fernández, and G.S. Mountain, Active deformation and shallow structure of the Wagner, Consag, and Delfín Basins, northern Gulf of California, Mexico, *J. Geophys. Res.*, *108*, 2355, 2003.

Romero-Rojas, S.A., D.A. Maraver-Romero, A.A. Avalos-Zermeno, and E. Aparicio-Cordero, Carta Geologico-Minera Santa Rosalia G12-1, in *Consejo de Recursos Minerales*, Secretaria de Comercio y Fomento Industrial, 1997.

Rossetter, R.J., Geology of the San Luis and San Lorenzo Island Groups, Gulf of California, Masters of Science thesis, California State University, San Diego, San Diego, 1973.

Sawlan, M.G., Late Cenozoic Volcanism in the Tres Vírgenes Area, in *GSA Cordilleran Section*, edited by L. Ortlieb, and J. Roldan-Quintana, pp. 309-319, U.N.A.M. Institue Geol., Estacion Regional del Noroeste, Hermosillo, Mexico, 1981.

Sawlan, M.G., Petrogenesis of Late Cenozoic Volcanic Rocks from Baja California Sur, Mexico, Ph.D. thesis, University of California, Santa Cruz, Santa Cruz, 1986.

Sawlan, M.G., Magmatic evolution of the Gulf of California rift, in *The Gulf and Peninsular Province of the Californias: American Association of Petroleum Geologists Memoir*, edited by J.P. Dauphin, and B.R. Simoneit, pp. 301-369, 1991.

Sawlan, M.G., and J.G. Smith, Late Cenozoic volcanic suites in Northern Baja California Sur, Mexico: Their relation to subduction and rifting along the Baja California

Peninsula, *Geological Society of America, Abstracts with Programs*, *16* (6), 645, 1984a.

Sawlan, M.G., and J.G. Smith, Late Cenozoic volcanic suites in northern Baja California Sur, Mexico; their relations to subduction and rifting along the Baja California peninsula, *Geological Society of America Abstracts with Programs*, *16*, 645, 1984b.

Schmidt, E.K., Plate tectonics, volcanic petrology, and ore formation in the Santa Rosalia Area, Baja California, Mexico, Master of Science thesis, The University of Arizona, pp. 194, 1975.

Stock, J.M., and K.V. Hodges, Miocene to Recent Structural Development of an Extensional Accommodation Zone, Northeastern Baja-California, Mexico, *Journal of Structural Geology*, *12* (3), 315-328, 1990.

Stock, J. M., Relation of the Puertecitos Volcanic Province, Baja California, Mexico, to development of the plate boundary in the Gulf of California, in Delgado-Granados, H., Aguirre-Diaz, G., and Stock, J. M., eds., Cenozoic Tectonics and Volcanism of Mexico: Boulder, Colorado, *Geological Society of America Special Paper,* 334, 143-156, 2000.

Umhoefer, P.J., and C. Teyssier, A preliminary structural geology study of the El Azufre Canyon area, north of Tres Vírgenes Volcano, Northern Baja California Sur, in *Primera Reunion Internacional Sobre Geologia de La Peninsula de Baja California*, Universidad Autonoma de Baja Califonia Sur, La Paz, Baja California Sur, Mexico, 1991.

Vargas-Ledezma, H., and V.H. Garduño-Monroy, Estudio Geologico-Geotermico de La Caldera El Aguajito, B.C.S., pp. 41, Comision Federal de Electricidad, 1988.

Walker, G.P., Z. Jurado, S. Rowland, and A. Carrillo, La Reforma cryptodome: an alternative mechanism to caldera subsidence and resurgent doming, in *29th International Geological Congress Meeting*, pp. 481, Kyoto, Japan, 1992.

Wong, V., C.J. Rebollar, and L. Munguia, Attenuation of coda waves at the Tres Vírgenes Volcanic Area, Baja California Sur, Mexico, *Bulletin of the Seismological Society of America*, *91* (4), 683-693, 2001.

Zanchi, I., The Opening of the Gulf of California near Loreto, Baja- California, Mexico - from Basin and Range Extension to Transtensional Tectonics, *Journal of Structural Geology*, *16* (12), 1619-1639, 1994.

Chapter 2: Processing of the VNIR-SWIR MASTER Data

Abstract

The 28 images of visible and near-infrared to short-wave infrared MASTER data in the Tres Vírgenes-La Reforma Volcanic Region were atmospherically corrected and classified. The VNIR-SWIR MASTER data can be atmospherically corrected to a reasonable accuracy with both the ACORN software and the Empirical Line Calibration (ELC) mode in ENVI. The ELC appears to be a more accurate method for the MASTER data. However, with both techniques, a reliable correction is difficult to obtain for those bands in the water absorption region (MASTER bands 11, 15 - 19, and 25). Classifying the atmospherically corrected MASTER data, resized to exclude the bands highly affected by water absorption, was done successfully by choosing endmembers with the highest Pixel Purity Indices (PPI^{TM}) values. Endmembers from a select number of field spectra and one image-derived region were added to the list of endmembers to expand the classification. This yielded a classification map that roughly delineated surfaces that vary in their secondary minerals, produced by weathering and alteration, namely ferric oxides, hydrates, hydroxyls, and carbonates. Attempts to identify these minerals using ENVI's Spectral Analyst^{TM} were only moderately successful. It is necessary to have auxiliary information about the lithology of the underlying rock and secondary minerals within the surface represented by each endmember for precise lithologic identification.

2.1 Introduction

The low rainfall, sparse vegetation cover, and a wide range of rock compositions of the Tres Vírgenes La Reforma Volcanic Region (TVLRVR) make it ideal for testing the MASTER sensor's ability to discriminate lithologic units. The remoteness and ruggedness of the area make application of aerial photographs and other remotely sensed imagery, such as MASTER, particularly useful in geologic mapping. The interior of the La Reforma Caldera has no fresh water or passable roads, and is accessible only by foot or pack animal. Previous geological studies of the region had very limited field observations and primarily relied on conventional air photo interpretation. However, many of the volcanic units are difficult to differentiate on the air photos. By using MASTER data as a tool in lithological classification of the rocks in this region, the few available geological ground observations can be extended much more reliably than was previously possible.

This chapter outlines the approach used for classifying Visible and Near-infrared to Short-wave Infrared (VNIR-SWIR) MASTER data (MASTER channels 1 - 25). The motivation for this work was first to gain more information about the surfaces within the TVLRVR and secondly to determine how well VNIR-SWIR MASTER data can be atmospherically corrected with commercial software and to what extent these atmospherically corrected data are useful in lithologic determination.

The VNIR portion of the spectrum is a source of information about absorption in transition metals, particularly iron, useful in mapping surfaces with a high concentration

of hematite and goethite [*Hunt et al.*, 1972, *Rowan et al.*, 1986]. It is also useful for detecting chlorophyll absorption by photosynthesizing plants [*Knipling*, 1970]. The SWIR portion of the spectrum is useful in detecting carbonates, hydrates, and hydroxides [*Boardman and Kruse*, 1994; *Clark et al.*, 1991; *Crowley*, 1993; *Kruse*, 1988; *Rowan et al.*, 1995; *Rowan et al.*, 1996]. The VNIR and SWIR portions of the electromagnetic spectrum are not useful in detecting the main constituents of igneous rocks, quartz and feldspars, due to their lack of absorption features in the VNIR and SWIR wavelengths. Therefore, the goal of atmospherically correcting, classifying and identifying endmembers within the (VNIR-SWIR) MASTER data is to yield additional information about the surfaces, namely the presence of vegetation, iron oxides, carbonates, hydrates, and hydroxides, to complement that obtained by the weight percent silica technique, which will be discussed in chapter 3.

First, the steps used in geo-rectifying the images will be presented. Then, I discuss the theoretical framework and method of determining the best atmospheric correction for this data set, in order to produce reflectance values that can be compared to field and library spectral data. Lastly, the method of classification and identification of the endmembers will be described, as well as the likely lithology represented by each endmember.

2.2 Geological Background

The TVLRVR is made up of Quaternary and Tertiary volcanic rocks including basaltic-andesite lavas; intracaldera rhyolite ash flow tuffs and andesitic, dacitic, and rhyolite lavas; Mesozoic granitic basement rocks; an intrusive body of diorite porphyry; and

detritus derived from the rocks listed above. In addition, there are Pliocene marine and terrestrial sedimentary rocks. In many cases, these surfaces are highly weathered and altered.

2.3 Theoretical Framework

The MASTER sensor is a passive remote sensing instrument [*Hook et al.*, 2001]. Therefore, the radiance collected at the aircraft originated from sunlight, traversed the atmosphere, was reflected off the surface of the earth, and traversed the atmosphere a second time as it made its way to the aircraft (Fig. 1). The measured radiance at the sensor, therefore, is controlled by the transmission of light through the atmosphere, as shown in Equation 1, simplified from *Chandrasekhar* [1960].

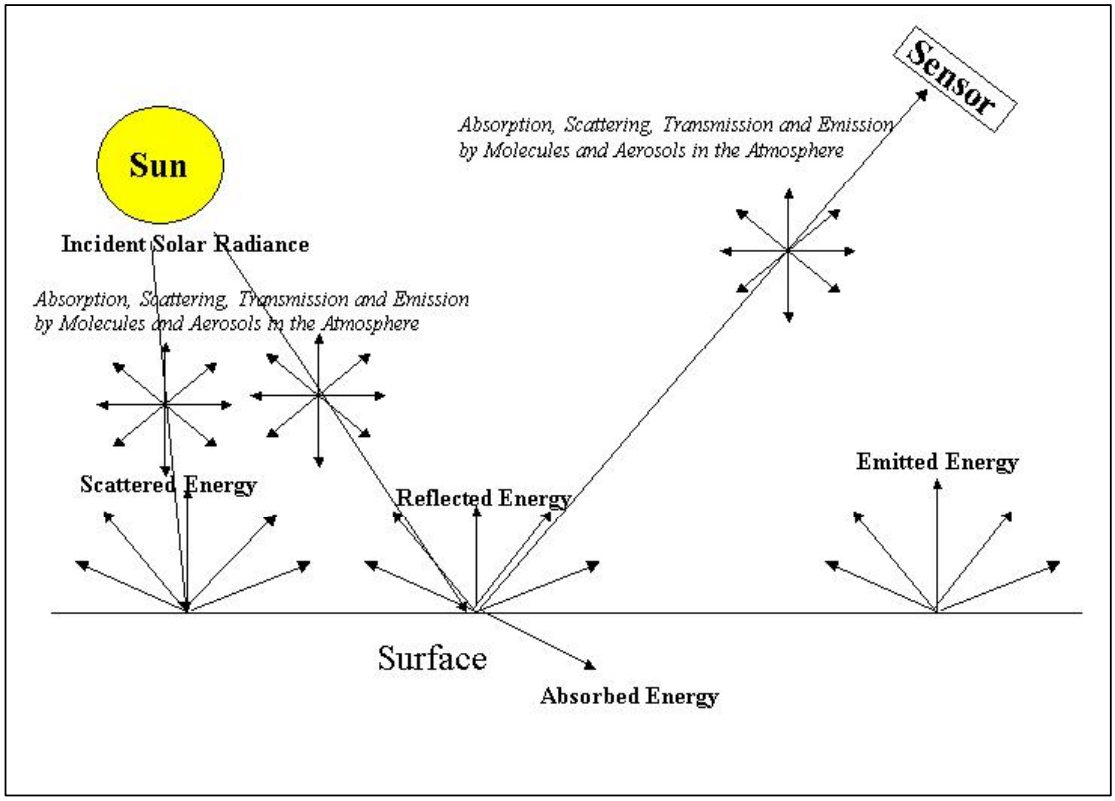

Figure 1. Schematic of the path of light from the sun to the sensor. Note that the energy arriving at the sensor is a combination of reflected, scattered and emitted energy.

Equation 1:

$L_t = F_0/\pi\{R_a + T_d R T_u/(1-S_r)\}$

Where:

L_t=total radiance arriving at the sensor (Wm^{-2} sr^{-1})

F_0=top of the atmospheric solar irradiance (Wm^{-2})

R_a=reflectance (ratio of reflected to incident irradiance) of the atmosphere (dimensionless)

T_d=downward transmittance (ratio of transmitted to incident irradiance) of the atmosphere (dimensionless)

R=spectral reflectance of the surface (dimensionless)

T_u=upward transmittance of the atmosphere (dimensionless)

S_r=downward reflectance of the atmosphere (dimensionless)

The spectrum of each surface is a combination of the spectral signatures of the materials that compose the surface. Different surfaces reflect different proportions of the incoming solar radiation in each part of the electromagnetic spectrum. For example, water absorbs, to varying degrees from the visible through the thermal infrared, with large absorption from 0.9 to 1.1 μm; vegetation has a peak of reflection in the green, strong reflection in the near-infrared, and absorption in the blue and the red wavelengths. These differences in the amount of radiance reflected from a surface, at different wavelengths, give the spectrum of a surface its spectral signature, made up of peaks and troughs, which are often referred to as spectral features. The amplitude ("depth") of an individual feature within the spectral signature is grain-size dependent, and absorption features shape the spectra.

There are two processes that cause absorption features. The first process is electronic. The interactions between electrons include crystal field effects, charge transfer, semiconduction, and color centers [Clark, 1999]. The second process affecting absorption is vibrational. Molecular vibrations (fundamental, overtone, or a combination of molecular vibrations) will cause absorption. The fundamental vibration modes are the

strongest. These typically occur beyond 2.5 microns for solid materials. The fundamental vibration of the Si-O bond is used for the weight percent silica technique and will be discussed in chapter 3.

The VNIR part of the electromagnetic spectrum (MASTER bands 1 - 11) is influenced by electronic transitions that occur in the transition elements, such as iron. Fe^{3+} absorbs electromagnetic energy in the 0.85 to 0.92 micron range, which promotes an electron to an excited state. This Fe^{3+} absorption feature between 0.85 and 0.92 microns is readily apparent in all iron-containing minerals. This feature is important in lithologic identification, because the most common minerals produced by the weathering of olivine, pyroxene, amphibole, and biotite (four of the primary minerals in mafic igneous rocks) are the iron oxides, which include limonite, hematite, and goethite. Vegetation can be identified due to its peak reflectance near 0.7 μm and absorption at shorter wavelengths [*Goetz*, 1981]. The VNIR is also affected by the wings of charge-transfer bands in the ultraviolet of the electromagnetic spectrum [*Goetz*, 1981] (Fig. 2). The library spectra convolved to the MASTER bands 1 - 10 with their continua[4] removed are shown in Figure 3.

[4] The continuum is the extrapolation of the baseline of the general curve, which fits a smooth curve, extending across the base of the absorption bands [*Clark and Roush*, 1984]. This baseline is removed to highlight absorption features in spectra, and the resulting spectra are considered to have their continuum removed [*Clark and Roush*, 1984]. The reduction to a spectrum with its continuum removed is determined by the following subtraction: The depth of an absorption band, D, is equal to $1- R_b/R_c$, where R_b is the reflectance at the center of the trough of an absorption feature and R_c is the continuum base.

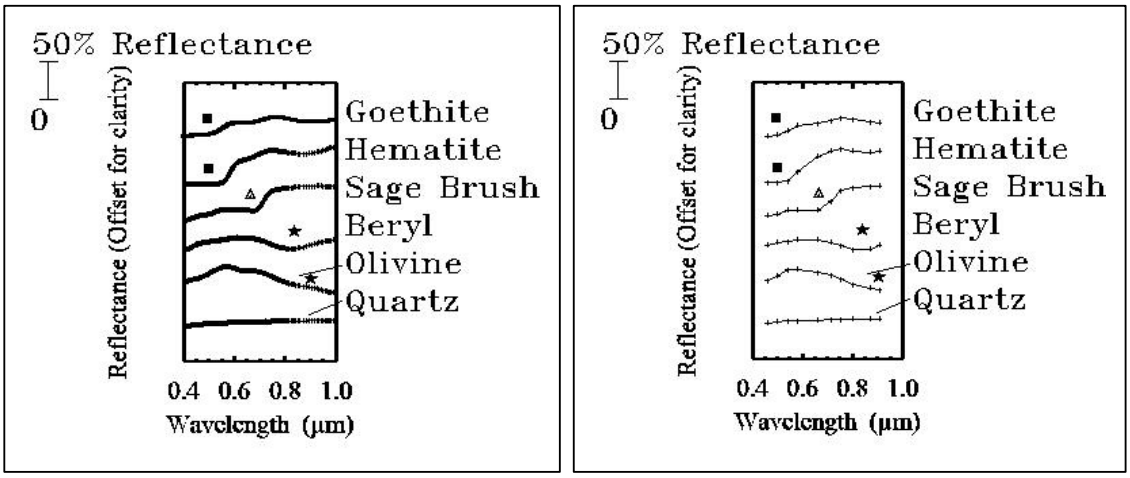

Figure 2. On the left are selected library spectra of minerals with crystal field and charge-transfer features in the VNIR part of the electromagnetic spectrum. Quartz and the vegetation spectrum for sage brush are shown for comparison. On the right are the identical spectra convolved to MASTER bands 1 - 10. The square denotes the absorption features caused by the wings of charge transfer bands in the ultraviolet (Fe-O). The triangle denotes the absorption features of vegetation in the blue and red wavelengths. The star denotes the absorption features between 0.85 and 0.92 microns associated with the crystal field effects of Fe.

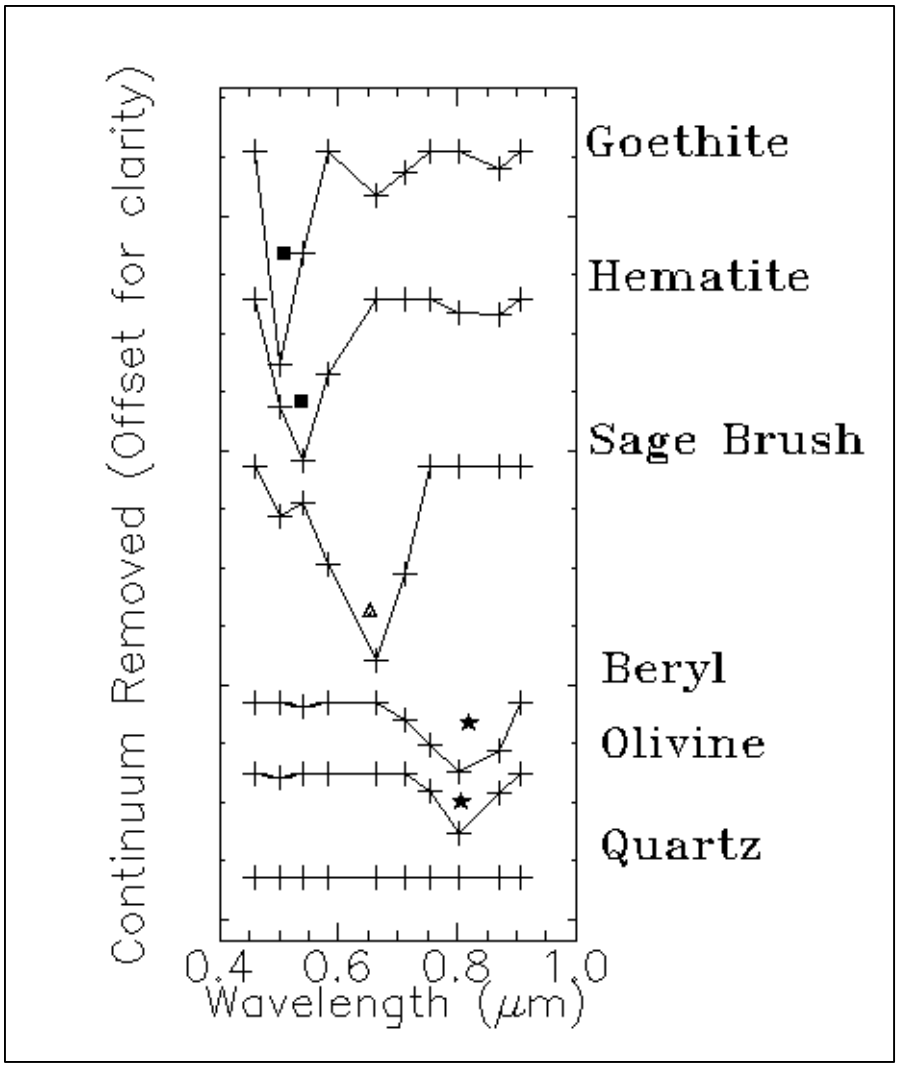

Figure 3. Reflectance library spectra of minerals with crystal field and charge-transfer features in the VNIR part of the electromagnetic spectrum. Quartz and the vegetation spectrum for sage brush are shown for comparison. The spectra have been convolved to MASTER bands 1 - 10 and their continua have been removed. The square denotes the absorption features caused by the wings of charge transfer bands in the ultraviolet (Fe-O). The triangle denotes the absorption features of vegetation in the blue and red wavelengths. The star denotes the absorption features between 0.85 and 0.92 microns associated with the crystal field effects of Fe.

In the SWIR wavelength bands (MASTER bands 20 - 25), there are diagnostic spectral absorption features due to overtone bending and stretching vibrations for layered silicates and carbonates. Some examples of these, as well as their spectra when convolved to

MASTER bands 20 - 24, are shown in Figure 4. The library spectra convolved to the MASTER bands 20 - 24 with their continua removed are shown in Figure 5. The spectral signatures described above are summarized in Figure 6, taken from *Hunt* [1977].

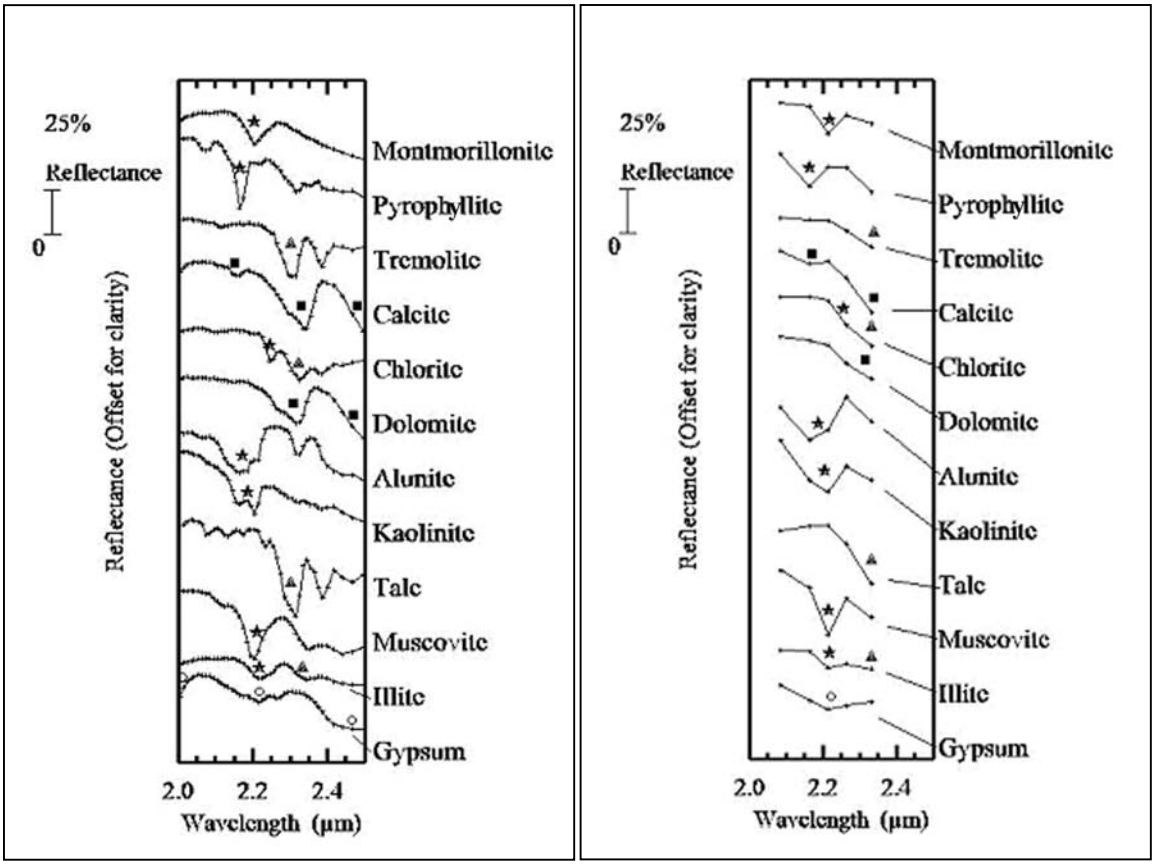

Figure 4. On the left are library spectra of minerals containing overtone vibrational absorption features for Al-OH, Mg-OH, H20 and CO3. On the right are the same spectra convolved to MASTER bands 20, 21, 22, 23, and 24. The star denotes absorption features caused by Al-OH. The triangle denotes absorption features caused by Mg-OH. The square denotes absorption features caused by CO_3. The circle denotes absorption features caused by H20.

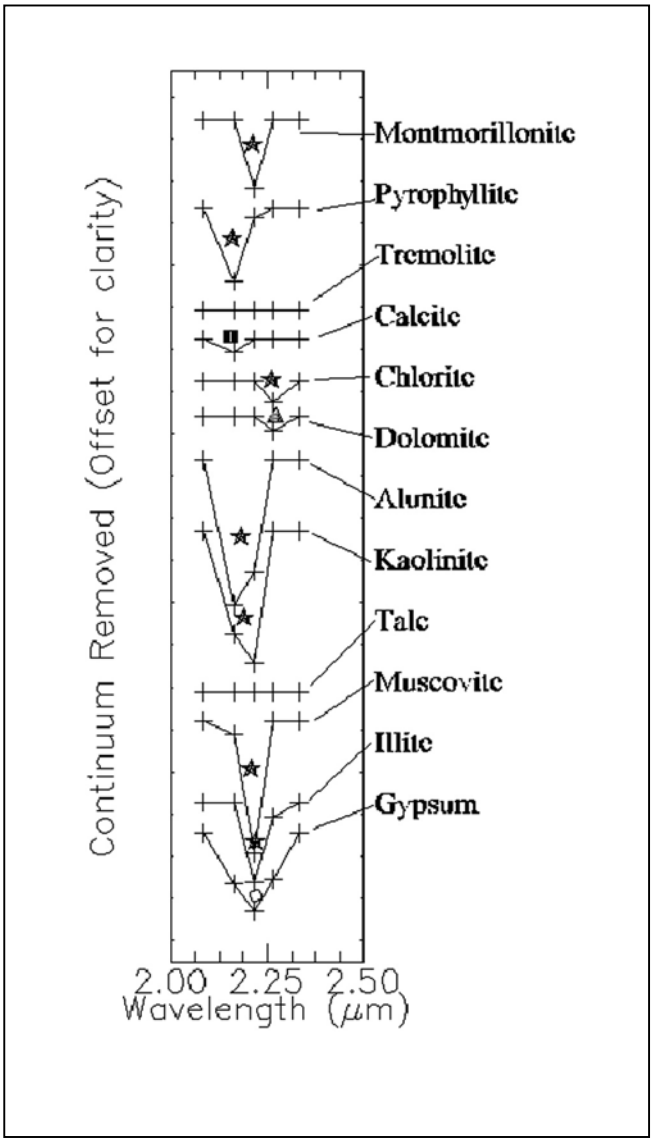

Figure 5. Reflectance library spectra of minerals containing overtone vibrational absorption features for Al-OH, Mg-OH, H20 and CO3. These spectra have been convolved to MASTER bands 20, 21, 22, 23, and 24, and their continua have been removed. The star denotes absorption features caused by Al-OH. The triangle denotes absorption features caused by Mg-OH. The square denotes absorption features caused by CO3. The circle denotes absorption features caused by H20.

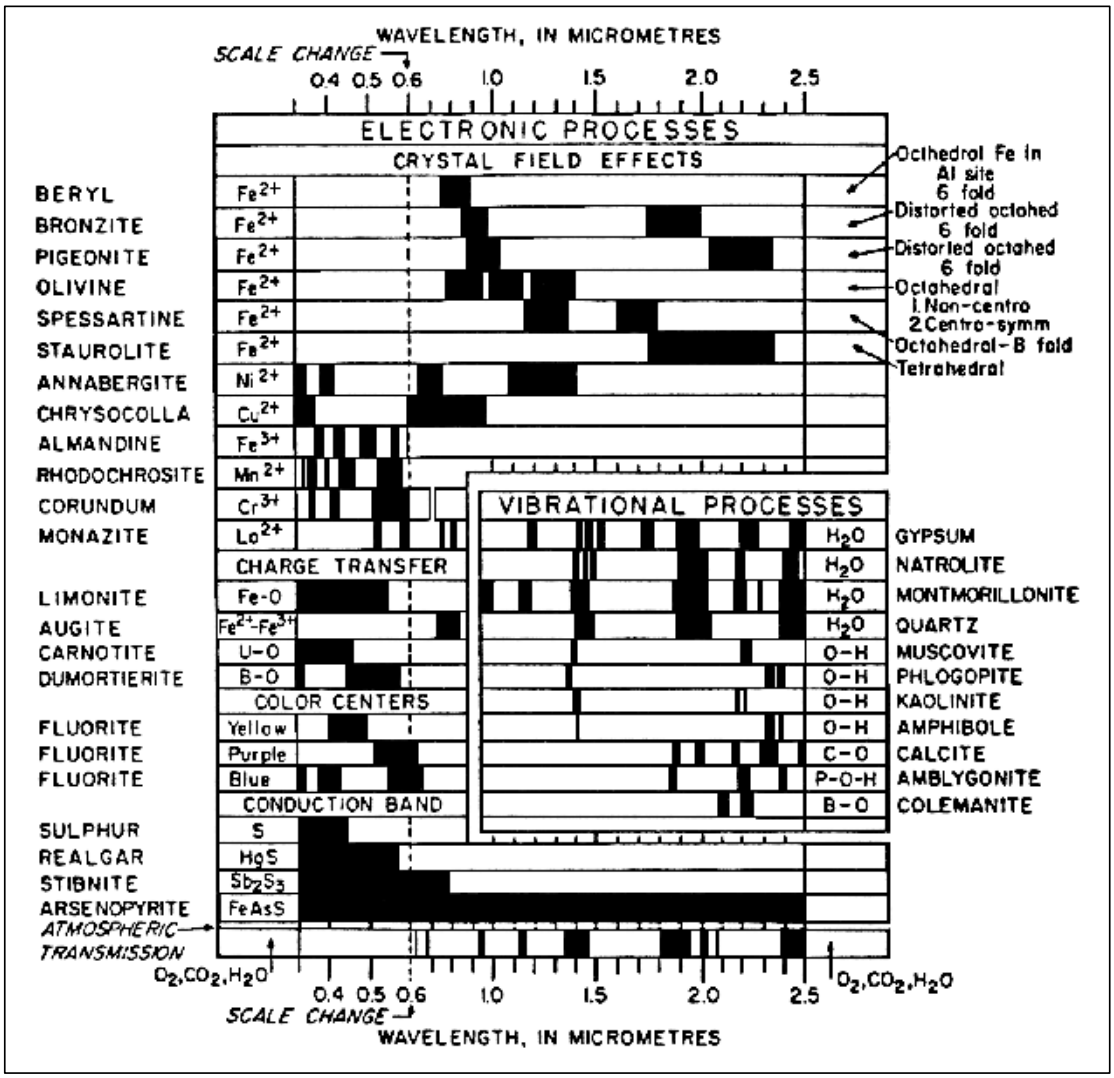

Figure 6. Spectral signature diagram from Hunt [1977]. The widths of the black bars indicate the relative widths of absorption bands.

The total atmospheric transmittance, T(λ), in the 0.4 - 2.5 micron region of the spectrum (detected with MASTER bands 1 - 25) is influenced by absorption and scattering in the atmosphere. There are two types of scattering, Rayleigh scattering and Mie scattering. Scattering of light by air molecules is caused by Rayleigh scattering. By definition,

Rayleigh scattering involves the scattering of incident light of frequency ν in all directions. Mie scattering, the scattering of light due to its interactions with particulates larger than the wavelength of light (e.g., from smoke, haze and fumes) is less of a factor in the atmospheric correction of the MASTER data in Baja California, due to the high visibility. Absorption in the atmosphere can primarily be attributed to seven gases. These include water vapor, H_2O; ozone, O_3; carbon monoxide, CO; oxygen, O_2; carbon dioxide, CO_2; nitrous oxide N_2O; and methane, CH_4. The primary absorbers in the VIS-SWIR part of the spectrum are oxygen, carbon dioxide, ozone, and water. Water vapor generally decreases with increasing altitude, but also varies spatially and temporally. Carbon dioxide, nitrous oxide, methane, and oxygen mix uniformly in the troposphere. Ninety percent of the ozone is located near 25 km above the surface of the earth, which is above the flight height of the MASTER sensor for the TVLRVR data set; the remainder varies with latitude and season. Carbon dioxide varies on a daily and seasonal basis. Through spectral analysis, it is evident that water most heavily influences the data collected in MASTER bands 1 - 25. At an average collection height of 2.3 km, the calibrated radiance at sensor is also affected by ozone, oxygen and carbon dioxide.

In order to determine the most likely lithology of the picture elements (pixels) of the MASTER data they need to be compared to field and spectral library data. This involves transforming the radiance detected at the sensor, $L_0(\lambda)$, to the surface reflectance, $R(\lambda)$, taking into consideration the effects of the atmosphere. However, the spectra recorded at the sensor are highly affected by the atmosphere, as shown in Equation 1. In order to atmospherically correct the MASTER data both an Empirical Line Calibration (ELC)

[*Farrand et al.*, 1994] and a radiative transfer model, Atmospheric Correction Now (ACORN) [*Miller*, 2002 and *Goetz*, 2002], were utilized. A Single Spectrum Enhancement (SSE) was also used in conjunction with the ACORN results.

After atmospheric correction, the data are still influenced by the shade effect. From this effect, some pixels appear darker than they normally would be due to the shadow cast on them by nearby topography. The topographic shade factor acts like a black endmember, mixing with the pixel's intrinsic spectrum. Therefore, the reflectance produced from the atmospheric correction of radiometrically and spectrally calibrated data is referred to as apparent reflectance. In order to correct for the shade effect, a digital elevation model (DEM) with much higher resolution than the multispectral data is necessary. At this time, such a DEM is not available for the TVLRVR.

2.4 Data Analysis

2.4.1 Introduction

MASTER data are available spectrally and radiometrically calibrated. In order to create the classifications, the calibrated data are first georeferenced. The georeferencing was done in ENVI, using an ASTER image as the registration base. The data were then atmospherically corrected using ACORN, an ENVI plug-in module, and the ENVI empirical line calibration (ELC) feature. Following the atmospheric correction, the data are in apparent reflectance. The 28 separate atmospherically corrected images were then mosaicked together and an MNF transform was performed to determine if the dimensionality could be reduced. Next, the Pixel Purity Indices (PPI^{TM}) were computed.

The PPI™ feature in ENVI finds the most extreme, or outlying, pixels when viewed in multidimensions. These pixels are referred to as pure as they should represent pixels with the most homogeneous surface in the image. The PPI™ is a measure of the relative degree of local convexity, in any dimension. It is computed by using repeated projections of n-dimensional scatterplots onto a lower dimensional subspace and marking the extreme pixels in each projection. The digital number (DN) of each pixel in the PPI™ image corresponds to the number of times that pixel was recorded as extreme (higher PPI™ indicates a higher purity).

Once the most spectrally pure pixels are identified, the endmembers are chosen using ENVI's N-dimensional Visualizer™. This tool allows the user to view an n-dimensional Euclidean space, where n is the number of bands, each band is associated with an axis, and all axes are orthogonal. The value of a spectrum in a single band determines its coordinates along the associated axis in spectral space.

The classification was produced using the Spectral Angle Mapper algorithm within ENVI, and ENVI's Spectral Analyst™ was run on the endmembers to determine their similarity to known spectra. The above processing technique, shown in Figure 7, is typically performed on hyperspectral data. Hyperspectral data are defined as an over determined data set, having more than enough bands to delineate the absorption features of the surfaces imaged. MASTER is not hyperspectral, but rather multispectral, due to the limited number of bands covering the electromagnetic spectrum. However, this

processing technique is still useful in determining the purest endmembers, classifying the

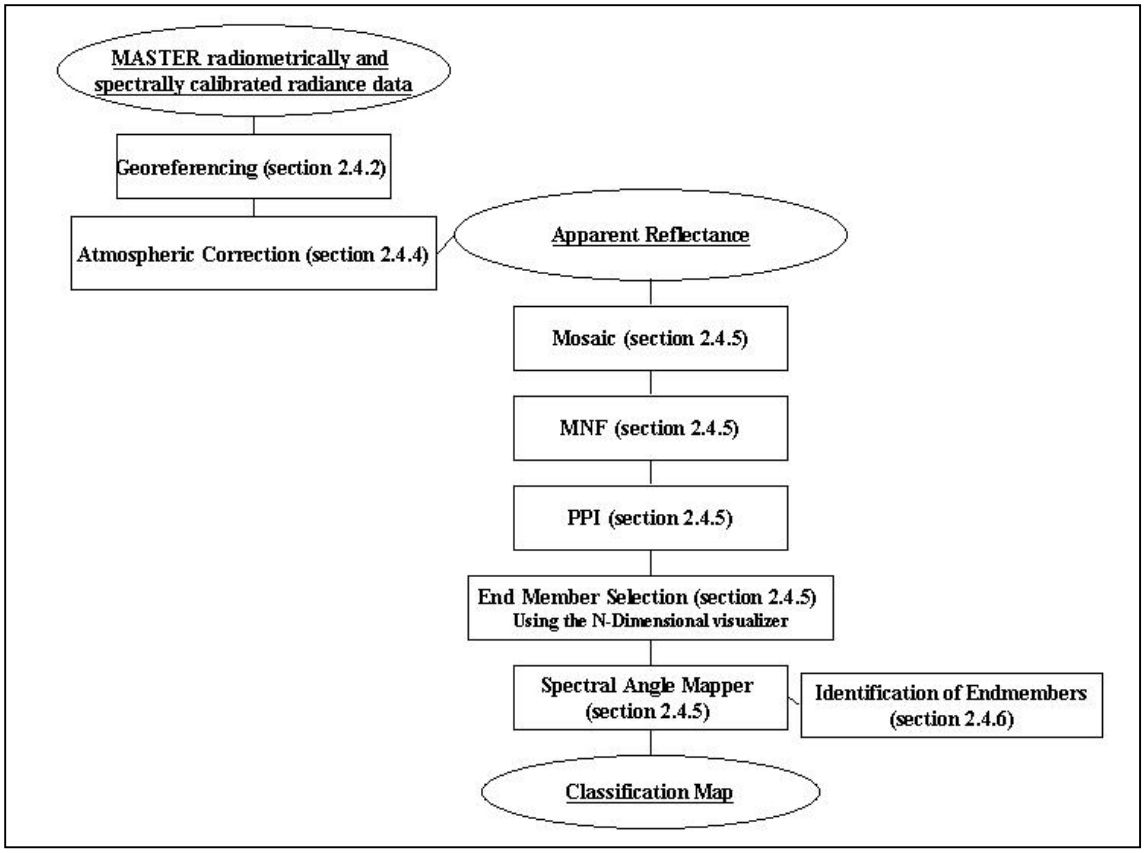

data, and determining the most likely lithology of the endmembers.

Figure 7. Flow diagram of steps required for processing radiance to generate classification maps. The section numbers refer to sections in the text where the processing step is discussed.

2.4.2 Georeferencing

In order to create the classifications, the spectrally and radiometrically calibrated data are first georeferenced. The georeferencing was done in ENVI, using an ASTER image as the registration base. Two ASTER level 1B images were mosaicked to produce this base image. Because ASTER 1B images are available georeferenced based on spacecraft

information, the images were both converted to map orientation using the Mexico NAD27 datum prior to mosaicking the images.

With an average flight height of 2.2 km, the MASTER images in the TVLRVR have an average pixel size of 5.5 m by 5.5 m. The average density of ground control points chosen for each MASTER image was approximately 5.6 ground control points per 100,000 pixels. The average number of pixels per image is 4,664,742. With this density of ground control points, the average RMS error in the location calculated for a warping using a 2^{nd} degree polynomial was 20 meters, as calculated by ENVI's prediction model. However, the actual misfit in location after warping varied by image. Images with large topographic variations had spatial mismatches in location up to 150 m, and mismatches also varied within images. For some lines a 3rd degree polynomial was used, because the higher degree polynomial decreased the RMS error. However, using a 4th or higher degree polynomial did not decrease the RMS error. The RMS error decreased significantly up to the average density of ground control points noted above. However, adding more ground control points did not decrease the RMS error for the MASTER data collected in Baja California in April and May of 1999, due to their severe warping. The data were warped with 2nd and 3rd degree polynomials (using that which yielded the smallest RMS error) and were resampled with cubic convolution. The spatial resolution of the data was reduced to a 15-meter pixel size after georectification to decrease the noise in the data and minimize computation time of further processing. The images were also cut to minimize the inclusion of water from the Gulf of California.

2.4.3 Field Reflectance Measurements

In order to compute an empirical line calibration, reflectance spectra acquired *in situ* (field spectra) with a field spectrometer must be available for the region. Therefore, the reflectance spectra of 17 distinct surfaces were measured *in situ* with the Analytical Spectral Devices Field Spectrometer (ASD). Collection sites, however, were primarily chosen to sample a variety of surfaces within the region. Only two regions were sufficiently homogeneous and well located to be used for atmospheric correction input and validation (regions for "Basalt" and "Pavement," in Fig. 8).

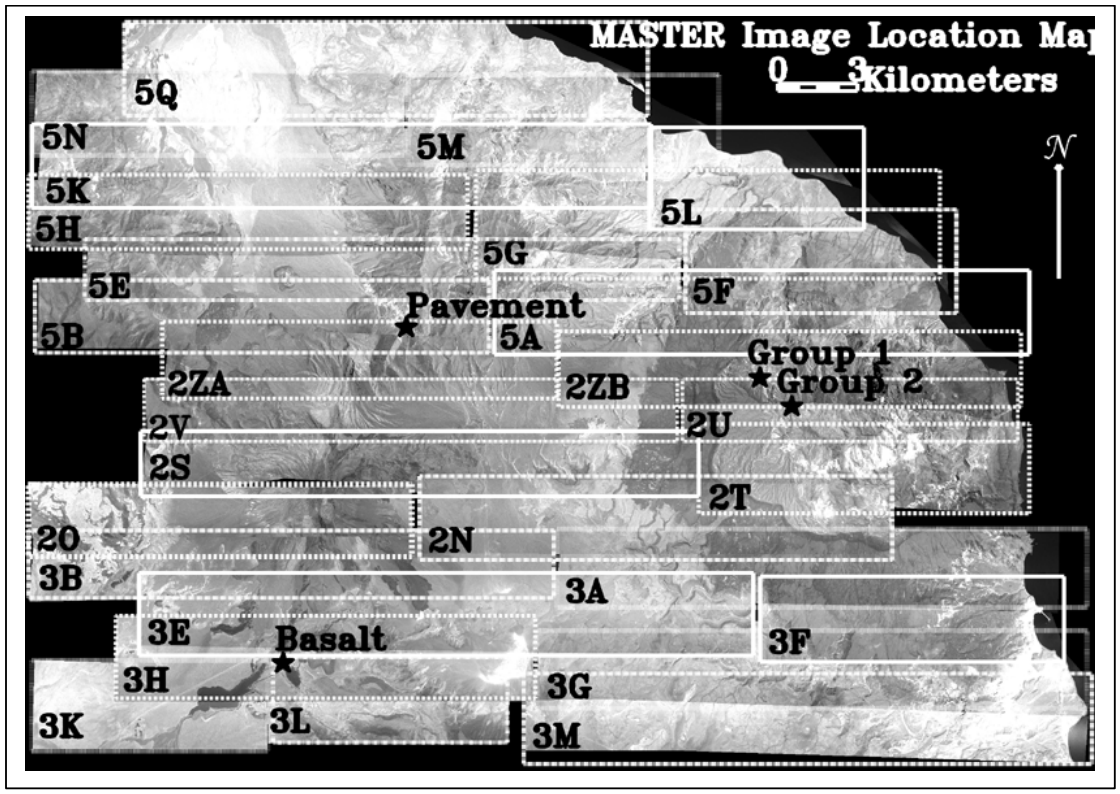

Figure 8. Boxes representing the location of the MASTER images overlain on the mosaic of the 28 MASTER images. The name of each image has been abbreviated to its last two characters (i.e., image 9900303H is shown as 3H). The name of each image is located in the lower left hand corner of its representative box. The borders of the lines vary for easier distinction between overlapping lines. Sample locations for field reflectance spectra are shown as black stars.

The ASD instrument used for field collection contains a fiber optic cable with a full view angle of 25°. This cable is divided into three fiber-optic bundles, each of which delivers the collected light to the entrance slit of one of three spectrometers covering the spectral range 0.35 - 2.5 μm. The 0.35 - 1.0 μm bundle has a sampling interval of 1.4 nm and a spectral resolution of approximately 3 nm. The 0.9 μm to 1.8 μm bundle has a spectral sampling of 2 nm and spectral resolution is 10 - 11 nm. The 1.7 μm to 2.5 μm bundle has a spectral sampling of 2 nm with spectral resolution of 10 - 11 nm. A white spectrum from a "monolithic Spectralon" sample was acquired at the time of each surface reflectance measurements, and the surface reflectance measurement were later divided by the appropriate white spectrum to minimize atmospheric and shade effects within the field spectra.

2.4.4 Atmospheric Correction

The following three sections describe the methods attempted to atmospherically correct the VNIR-SWIR MASTER data.

2.4.4.1 ACORN

The ACORN module relies on user input of date and time of image capture, mean elevation within image, atmospheric visibility, precipitable water vapor (PWV), and the altitude of image acquisition (in order to determine atmospheric pressure) [*Goetz*, 2002; *Miller*, 2002]. PWV is the total atmospheric water vapor contained in a vertical column of unit cross-sectional area extending from the surface to the top of the atmosphere. PWV is

reported in terms of the height, in ENVI as millimeters, to which the water vapor contained in a vertical column of unit cross-sectional area would stand if completely condensed and contained in a container of the same unit cross section. Visibility, defined as the greatest distance that prominent objects can be seen and identified by unaided, normal eyes, is between 80 km and 100 km on a clear day.

ACORN is an atmospheric-model-based conversion of radiance to apparent surface reflectance, using radiative transfer, which requires no known spectra as input. ACORN uses look-up tables, which are calculated with MODTRAN4, to determine the quantity of water vapor on a pixel-by-pixel basis. MODTRAN4 models atmospheric gas absorption and scattering. Using the look-up tables generated by MODTRAN4, the calibrated radiances are converted to apparent surface reflectance. As with similar radiative transfer codes, the calibrated data are atmospherically corrected using both the calibrated radiance at sensor data and the atmospheric parameters in order to derive and model the scattering and absorption processes of the atmosphere. The radiative transfer code then calculates the transmittance of the various paths and the different components of the sky irradiance and path radiance.

With input parameters from the multi-channel mode, ACORN determines the water vapor using MODTRAN4 radiative transfer calculations. In order to estimate the water vapor measurement, ACORN assigns pixels with a high concentration of vegetation a high Dense, Dark Vegetation index (DDV), and then matches these spectra to known spectral profiles of vegetation. In cases where a good match is not found, ACORN uses the fixed

visibility and PWV input by the user. ACORN uses the MODTRAN4 model atmosphere selected, based on the input parameters of date, time, location, and latitude. In this way, ACORN estimates the concentration of well-mixed gases CO_2, O_3, N_2O, CO, CH_4, and O_2. The visibility is estimated using the 0.4 - 1.0 μm portion of the electromagnetic spectrum. The code searches for negative radiances and adjusts visibility to minimize them. After ACORN produces its initial atmospheric correction, known spectra may be input to correct output reflectance using a calculated gain. This is referred to in the ACORN module as the Single Spectrum Enhancement (SSE), which is similar to an empirical line calibration. The SSE can only be computed for images that contain field spectra.

For the MASTER data set in the TVLRVR, unfortunately, no atmospheric data were collected at the time of image acquisition. Additionally, very few of the field spectra correspond to large, homogeneous regions, which are most ideal for testing the validity of an atmospheric correction. Thus, a test of the ACORN module was done on a similar dataset (over the Ivanpah Playa, California) where the MASTER data were collected simultaneously with atmospheric data and field spectra from an ASD spectrometer.

The goal of atmospherically correcting the Ivanpah dataset was to determine the ability of ACORN to atmospherically correct well-controlled datasets. The site of ground spectra collection in Ivanpah Playa is shown with a star in Figure 9. The atmospheric data include the aerosol optical depth for 0.3805, 0.4001, 0.4374, 0.5188, 0.6091, 0.6702, 0.7787, 0.8670, and 1.0301 microns and the derived PWV, Junge parameter, ozone

density, and 550 nm optical depth. (The Junge parameter [*Cachorro et al.*, 1993], based on the Junge particle size distribution [*Junge*, 1963], is a representation of the aerosol size, with 3 being a fairly average number, and 4 indicating abnormally large aerosol size.) The average values for these parameters from data acquisition on June 10, 2002 over a six-and-a-half hour time period are shown in Table 1.

Wavelength (μm)	Aerosol Optical Depth (dimensionless)
0.3805	0.069805
0.4001	0.066877
0.4374	0.063147
0.5188	0.073105
0.6091	0.074445
0.6702	0.054394
0.7787	0.050557
0.867	0.040857
1.0301	0.038487
Derived PWV (cm)	0.630054
Junge parameter (dimensionless)	2.591405
Ozone Density (billion of molecules/cm^3	0.174802
550 nm optical depth (dimensionless)	0.05608

Table 1. Atmospheric data collected at Ivanpah on the date of MASTER overflight, June 10, 2002.

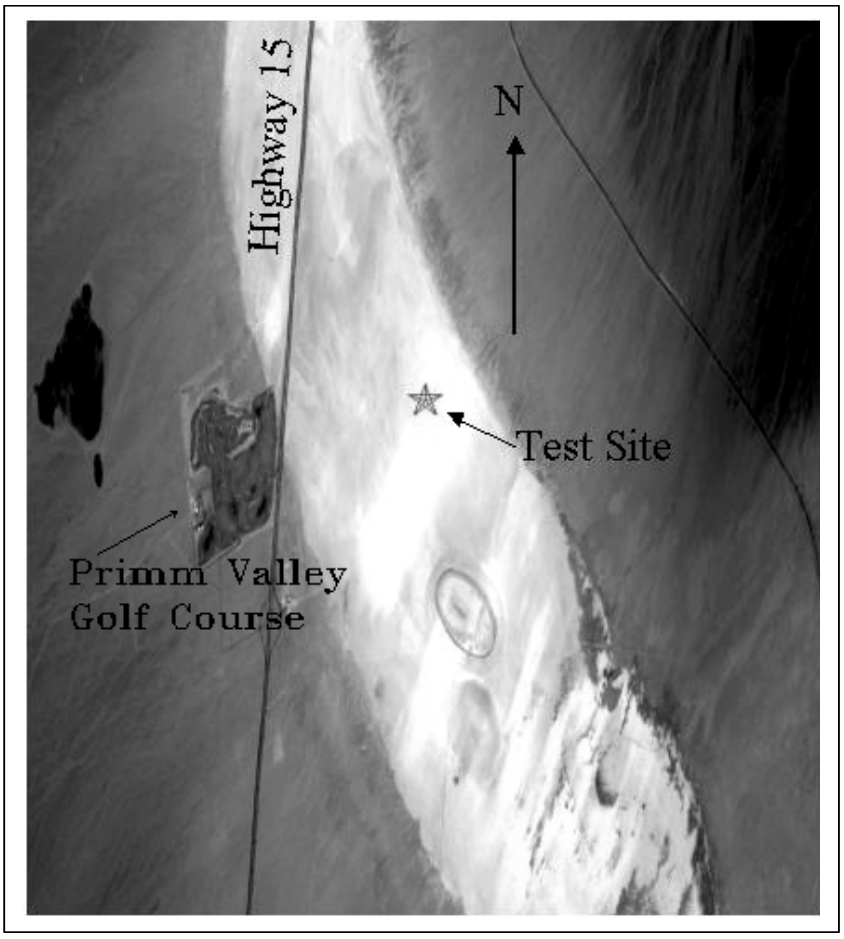

Figure 9. MASTER image of the Ivanpah site, with the target region denoted by a star. Note that the image has not been georectified.

Using these data, 50 atmospheric corrections were run on the Ivanpah Playa image, varying only the independent variables, PWV and visibility. The mean of the spectra within the target site was calculated for each run, and these mean spectra were compared to the mean of the field spectra. The only variables changed from run to run were the PWV and visibility, which are independent of one another. The mean of the field spectra was convolved to MASTER bands 1 - 25 for comparison to the computed MASTER reflectance values. The comparison of spectra for selected PWV values is shown in Figure 10, and for selected visibility values in Figure 11.

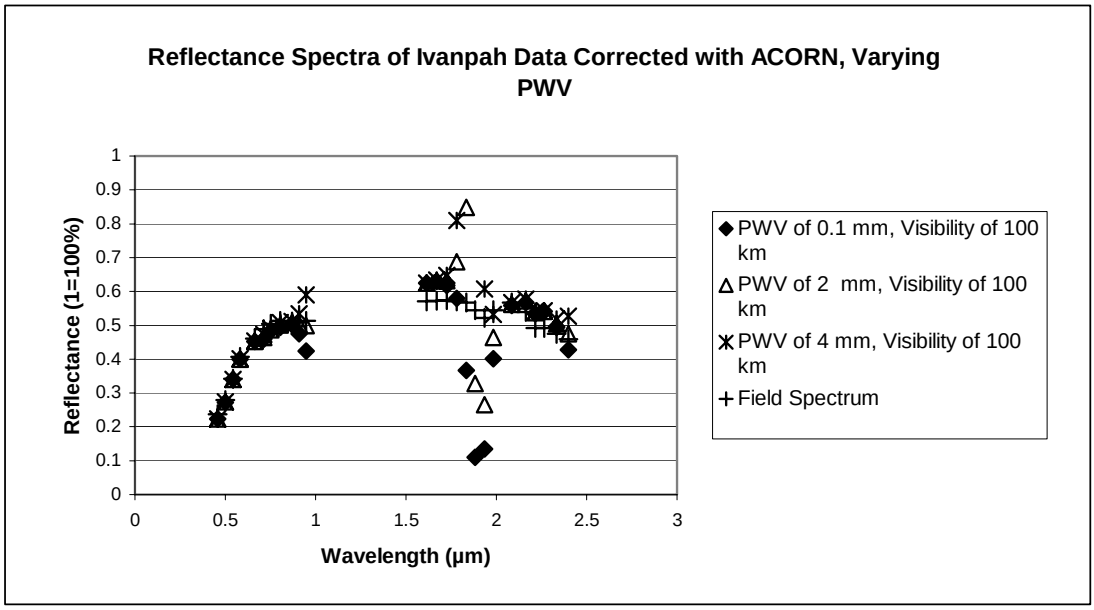

Figure 10. Reflectance of the target site within the Ivanpah MASTER dataset, showing the target field mean spectrum and the corrected mean spectra. Data are atmospherically corrected using ACORN with a fixed visibility of 100 km and varying the PWV.

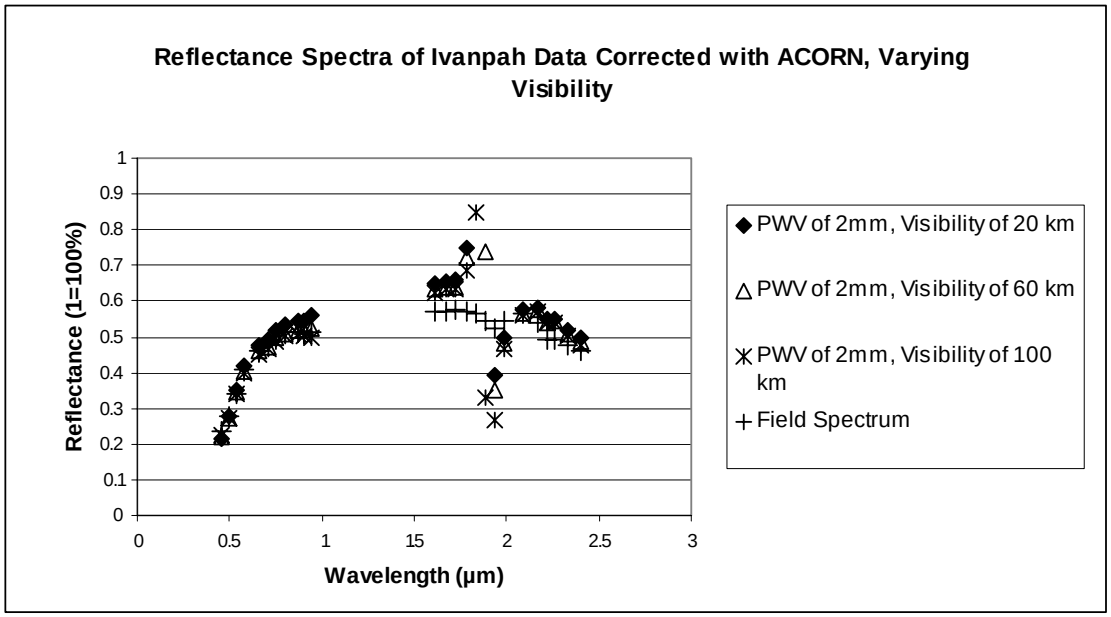

Figure 11. Reflectance of the target site within the Ivanpah MASTER dataset, showing the target field mean spectrum and the corrected mean spectra. Data are atmospherically corrected using ACORN with a fixed PWV of 2 mm and varying the visibility.

Despite the known atmospheric conditions during the image acquisition, where PWV is measured and the derived 550 nm optical depth can be used to assess the atmospheric visibility, the correction is poor. In fact, the best fit to the mean of the field spectra is that for an atmospheric correction based on an atmospheric visibility of 100 km, and PWV of 1.8 mm (Fig. 12). The 100 km atmospheric visibility, the maximum visibility allowed in ACORN, is consistent with a 550 nm aerosol optical depth[5] of 0.05608. However, the mean PWV on the day of image acquisition was 6.30054 mm. The PWV value determined by the best fitting spectrum generated by ACORN is 72% lower than this value. While it is reasonable to assume the PWV could vary by 20 - 30%, a 72% difference is considerably outside the expected error range. Within six-and-an-half hours of atmospheric measurements on the day of image acquisition, the PWV value varied from 4.23 mm to 8.15 mm. The largest errors are within bands 16, 17, and 18 and to a lesser degree, bands 11, 15, and 19. These bands had very low signal-to-noise ratios in both the Ivanpah and TVLRVR datasets, because these bands fall within large absorption regions (Fig. 13). Omitting bands 16 - 18 yields a better fit (Fig. 14, for varying PWV values; and Fig. 15, for varying Visibility values).

[5] Aerosol optical depth, usually reported for various VNIR wavelengths, is a measure of how much light is prevented from passing through a column of atmosphere due to airborne particles. Aerosols absorb and reflect incoming sunlight, thus reducing visibility and increasing optical depth. An aerosol optical depth at 550 nm of less than 0.1 indicates a clear sky with maximum visibility.

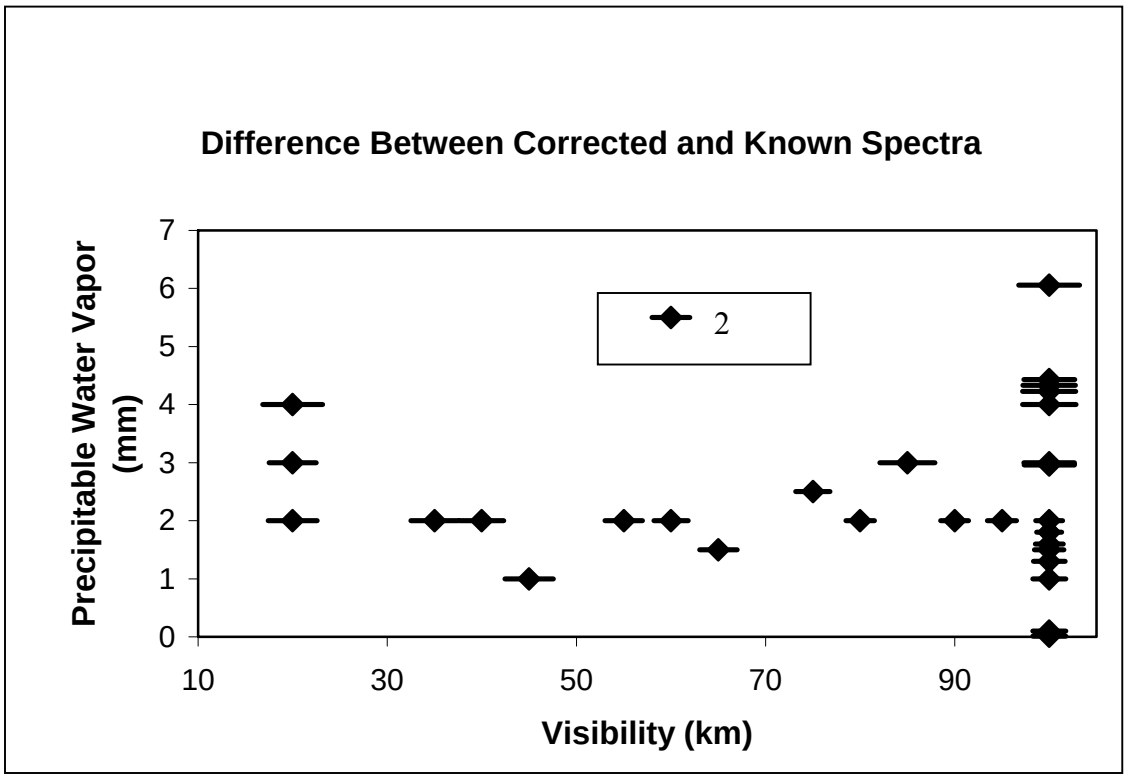

Figure 12. Plot of the difference in reflectance values between the field spectrum and the atmospherically corrected image spectrum for each trial of ACORN. A diamond is shown for each trial, located at the corresponding visibility and precipitable water vapor values. The horizontal bar represents how much the atmospherically corrected spectrum varied from the known field spectrum of the target. The difference was calculated as a sum of the absolute values of the differences between the image and the field spectrum for each of MASTER's first 25 channels. A width corresponding to a total difference of 2 is shown in the central, top portion of the figure. It should be noted that the difference between the corrected image and the field spectrum gets smaller for values near a precipitable water vapor of 1.8 mm and a visibility of 100km; therefore, these values were chosen as the best fit.

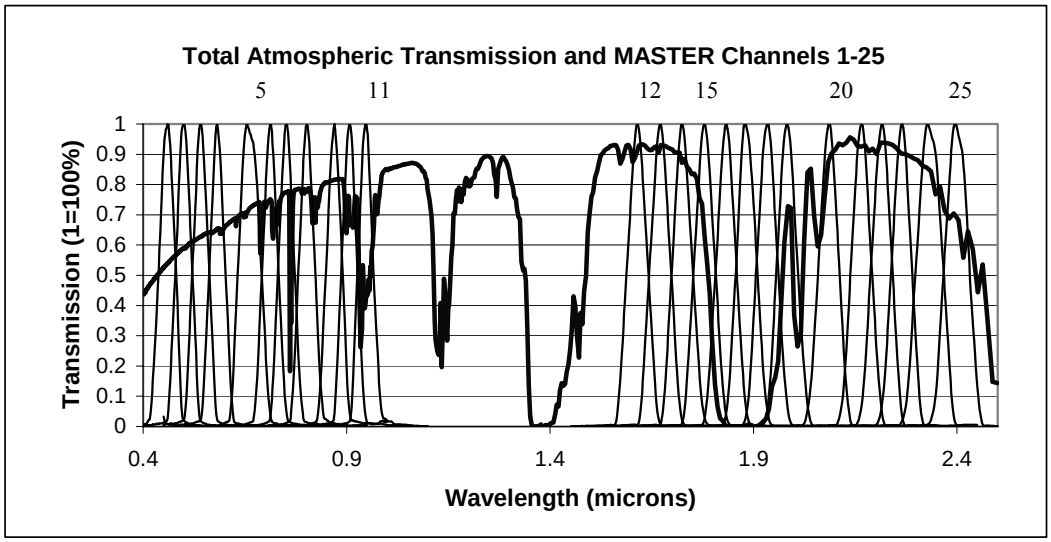

Figure 13. Plot of atmospheric transmission overlain by the system response functions of MASTER bands 1 - 25.

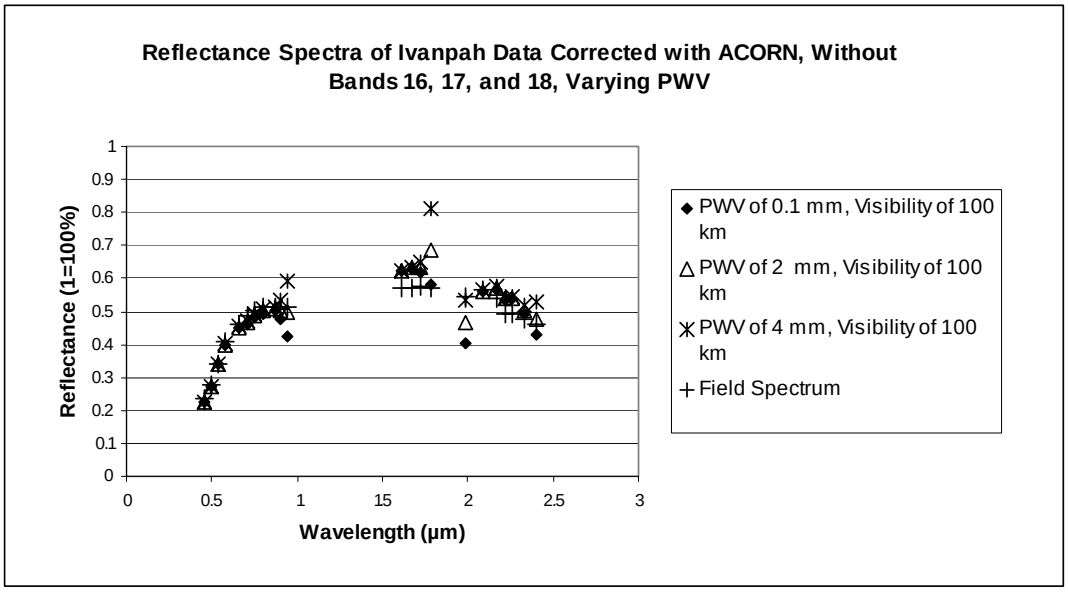

Figure 14. Reflectance of the target site within the Ivanpah MASTER dataset, omitting bands 16 - 18, showing the target field mean spectrum and the corrected mean spectra. Data are atmospherically corrected using ACORN with a fixed visibility of 100 km and varying the PWV.

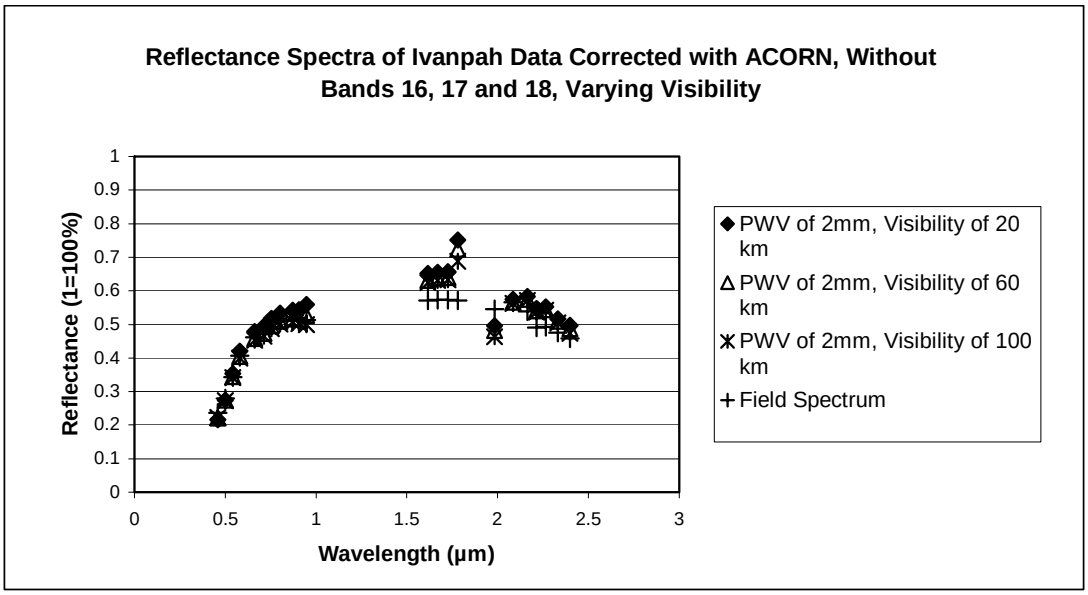

Figure 15. Reflectance of the target site within the Ivanpah MASTER dataset, omitting bands 16 - 18, showing the target field mean spectrum and the corrected mean spectra. Data are atmospherically corrected using ACORN with a fixed PWV of 2 mm and varying the visibility.

The experiment with the Ivanpah Playa data shows ACORN can moderately correct bands outside the water absorption regions without the input of field spectra. However, even though the atmospheric parameters were directly measured, it is difficult to correct MASTER bands 16, 17, and 18, which lie within water absorption regions. It is also difficult to approximate the atmospheric parameters that are best used as ACORN input.

With the insight gained from the Ivanpah data, attempts were made to atmospherically correct the images from the TVLRVR with ACORN. There are 28 images within the TVLRVR (Fig. 8). Seven of the images contain one or more field spectra; however, in six out of seven of these images, the spectra are not in homogeneous, well-located regions and the images do not contain both dark and light field spectra. For the images that do contain one or more field spectra, the procedure described for the Ivanpah Playa

data was repeated with several variations of PWV and visibility. Figures similar to those for the Ivanpah playa were generated and the best fitting spectra were determined (Fig. 16, for image 9900303L; and Fig. 17, for image 9900305B).

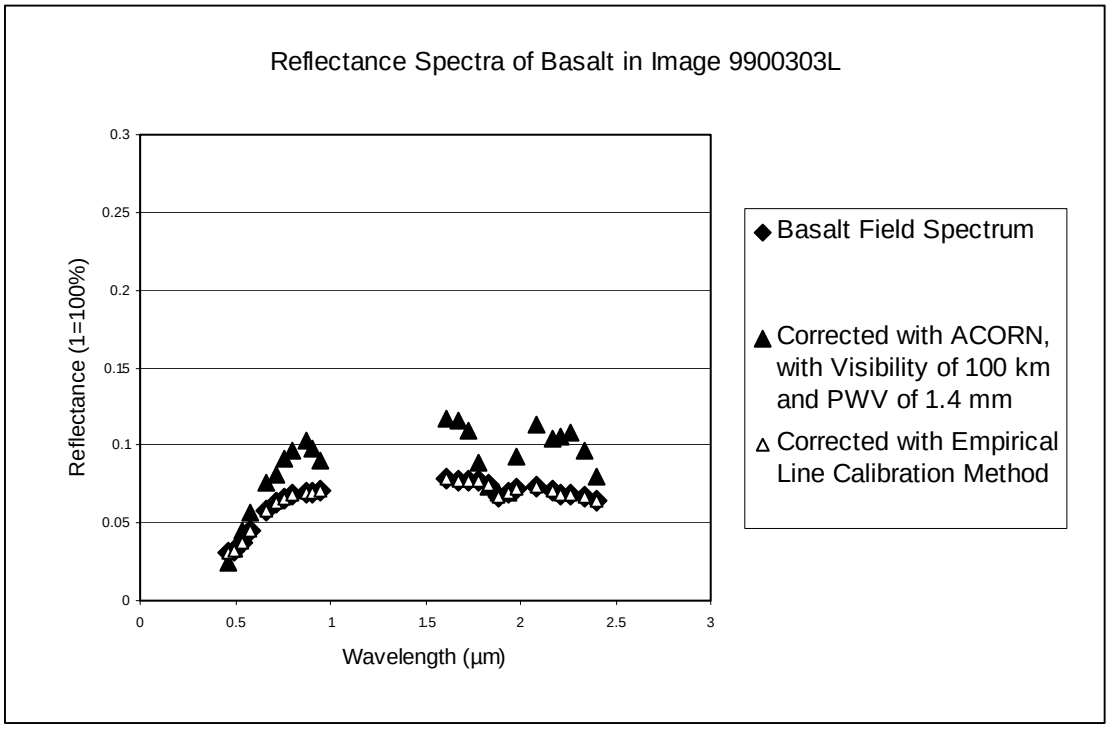

Figure 16. Shown are the reflectance spectra of the "Basalt" region in image 9900303L for the mean field reflectance spectrum, the mean for the data corrected with ACORN, and the mean for the data corrected with Empirical Line Calibration.

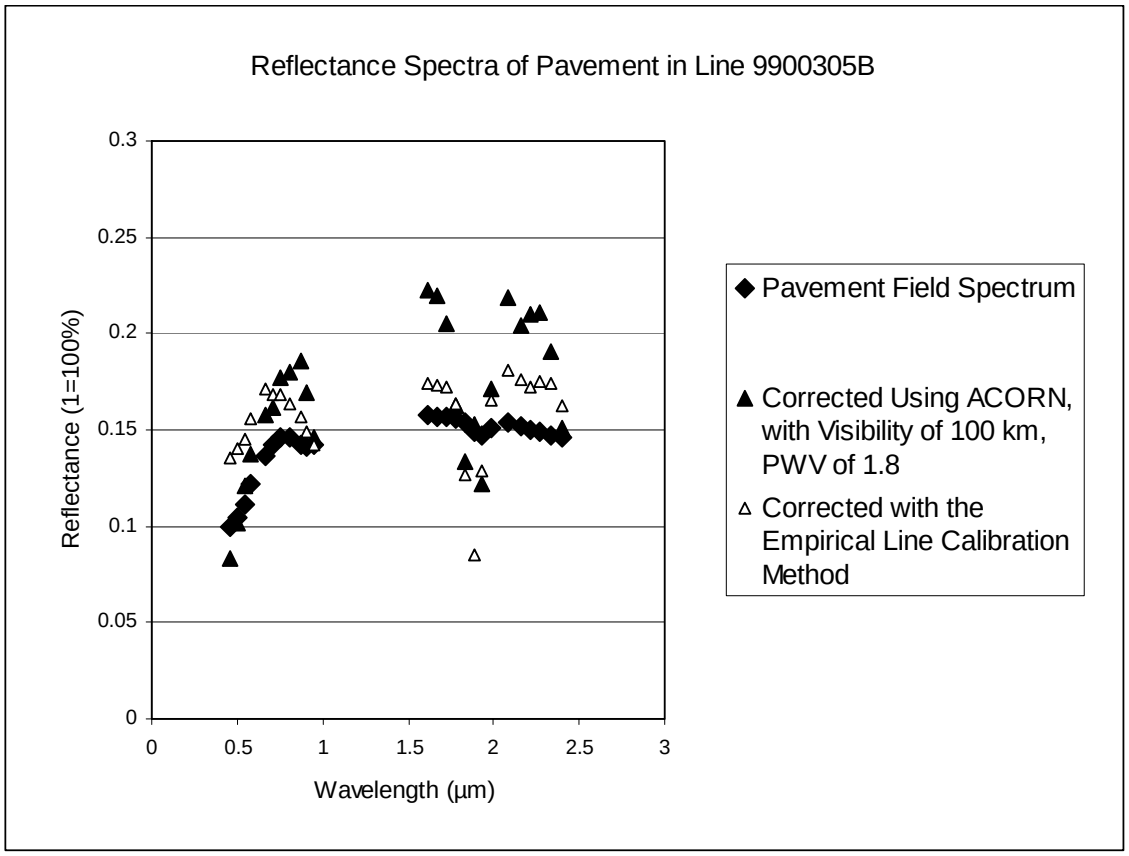

Figure 17. Shown are the reflectance spectra of the "Pavement" region in image 9900305B for the mean field reflectance spectrum, the mean for the data corrected with ACORN, and the mean for the data corrected with Empirical Line Calibration.

Using reflectance data output from ACORN for the TVLRVR, the Single Spectrum Enhancement (SSE) was used to force the image spectra to fit the known field spectra. This method works well to atmospherically correct the spectra similar to the target spectrum; however, in some cases the SSE over-corrects or under-corrects other pixels within the image. Without known spectra for these regions, it is difficult to correct for these errors.

In order to calculate an SSE on the 27 other images in the TVLRVR that do not contain both dark and light field spectra (Fig. 8), a technique was developed to find matching dark and light spectra on adjacent images. In this way, one can continue from one atmospherically corrected image to the next using known spectra from the previously corrected image. This technique, described in Appendix A, did not atmospherically correct adjacent images well due to the variability between the matching regions.

2.4.4.2 Empirical Line Calibration

The Empirical Line Calibration method (ELC) is an alternative technique that can be used to atmospherically correct the data. This method involves locating two spectrally uniform targets in the image, one spectrally dark with relatively low reflectance values, and one spectrally light with relatively high reflectance values. Using measured field spectra to characterize the reflectance spectra of the two targets, the correlating spectra are then extracted from the images for the target areas. A mean radiance spectrum for each target area is then calculated using ENVI's empirical line calibration mode. ENVI produces a linear regression between the field and lab spectra and a linear transform is determined for the radiance to reflectance for each band. The gains and offsets computed are then applied to each pixel. The transform is shown in Equation 2.

Equation 2.

Reflectance = gain x radiance + offset (errors)

In order to test this method, an empirical line calibration was computed for image 9900303H, using the field spectra "Basalt" and "Pavement." Using regions that matched the location of the mean field spectrum, "Basalt," and a region within image 9900303H that contained a similar surface to the mean field spectrum for "Pavement" (located in image 9900305B), matching pairs were chosen of image and field spectra data. The resulting calibration coefficients were used to calibrate the other 27 images in the TVLRVR. When these calibration coefficients were used to correct image 9900305B, the matching region for the field spectrum "Pavement" correlated moderately well (Fig. 17). Lines 9900305B and 9900302ZA overlap, as do 9900302ZA and 9900302V (Fig. 8); therefore, pixels representing the same surfaces can be compared to see how well the atmospherically corrected images compare to one another (Fig. 18).

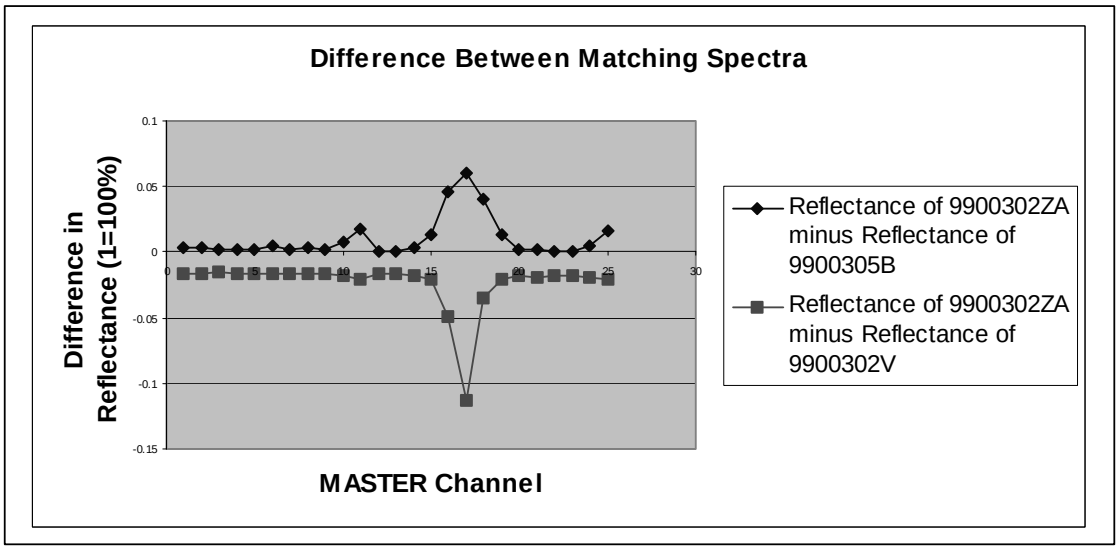

Figure 18. Plot of the difference between the reflectance spectra of matching regions for images 9900302ZA and 9900302V and for images 9900302ZA and 9900305B.

Attempts were made to improve the gains and offsets (computed with image 9900303H) using the "Pavement" spectrum, within image 9900305B. However, because there were not both dark and light spectra available, the corrections improved the match for the pixels identified as "Pavement," but they did not improve the fit between identical regions on line 9900305B and 9900302ZA.

Image 9900303L is an adjacent image to 9900303H and also contains the rock unit from which the field spectra "Basalt" were obtained. Using the same method described above, image 9900303L was atmospherically corrected. This yields a very good match to the "Basalt" spectrum (Fig. 16).

2.4.4.3 Determination of the Best Atmospheric Correction

Based on the data analysis performed on the TVLRVR (using the "Basalt" and "Pavement" field spectra and their corresponding regions in image 9900303H), it appears that the best atmospheric correction for the TVLRVR is obtained with the ELC. The calibration coefficients derived from the ELC technique appear to atmospherically correct other images within lines 9900302 (collected April 29, 1999) and 9900303 (collected April 30, 1999); however, they work less well for images within line 9900305 (collected May 3, 1999). The system response functions for the MASTER sensor may have shifted at some time between April 30, 1999 and May 3, 1999, causing the ELC coefficients computed for 9900303H not to apply to image 9900305B. The system response functions are only available pre-flight for April, 1999. However, a 0.003 micron shift is observed in pre- and post-flight calibration readings of the system response functions for

port 1 (channels 1 - 11) obtained for MASTER in August of 1998. These data are publicly available at http://masterweb.jpl.nasa.gov/.

Alternatively, the coefficients for line 9900302 may not be accurate for line 9900305 due to a difference in atmospheric conditions. Certainly, within scenes with high topographic relief, there are large differences in atmospheric path distance because of the very low flight elevation. This can adversely affect methods, such as the empirical line method, that use the surface as a reference [*Farrand et al.*, 1994]. Because the TVLRVR is a coastal region, it is very likely that the atmospheric conditions, even within one image, vary greatly with distance from the coast. Unfortunately, the ACORN radiative transfer code and the ELC method do not account for this variation, and it is source of error that needs to be addressed.

Comparison of the mean spectra (corrected using the ELC method) of identical regions visible in two images (9900302ZA and 9900302V or 9900302ZA and 9900305B) reveals that although the ELC works well, the results are superior for images within lines acquired on April 29, 1999 and April 30, 1999 (lines 9900302 and 9900303, respectively) (Fig. 18). The images within line 9900305 show more error, particularly for bands 11, 15 - 19, and 25, all of which fall within water absorption regions (Fig. 13). Image 9900303L, however, which was acquired on the same day and within 20 minutes of image 9900303H, appears to be atmospherically corrected fairly well (Fig. 16).

In order to determine if the system response functions shifted between the flight days of April 30, 1999 and May 3, 1999, the data in images 9900305B (collected May 3, 1999) and 9900302ZA (collected April 29, 1999) were compared. Approximately 30% of image 9900305B overlaps with 9900302ZA (Fig. 8). Two regions that were imaged on both 9900305B and 99002ZA, one spectrally dark and one spectrally light, were chosen within these images. The mean and standard deviation were computed for regions of interest within these matching regions, composed of 5 pixels each. An increase in noise[6], which would cause an increase in the standard deviation within a homogeneous region, could indicate that the system response function may have shifted. Inspection of Figure 19, for a spectrally dark region and Figure 20, for a spectrally light region, shows no increase in noise in image 9900305B. Therefore, the errors seen in the atmospheric correction on image 9900305B using the calibration factors from image 9900303H are most likely due to changes in the atmospheric conditions, and not a shift in the system response functions.

[6] If the system response function shifts, it can move into absorption wavelengths, regions of low transmittance, and therefore yield a lower signal to noise ratio after the shift.

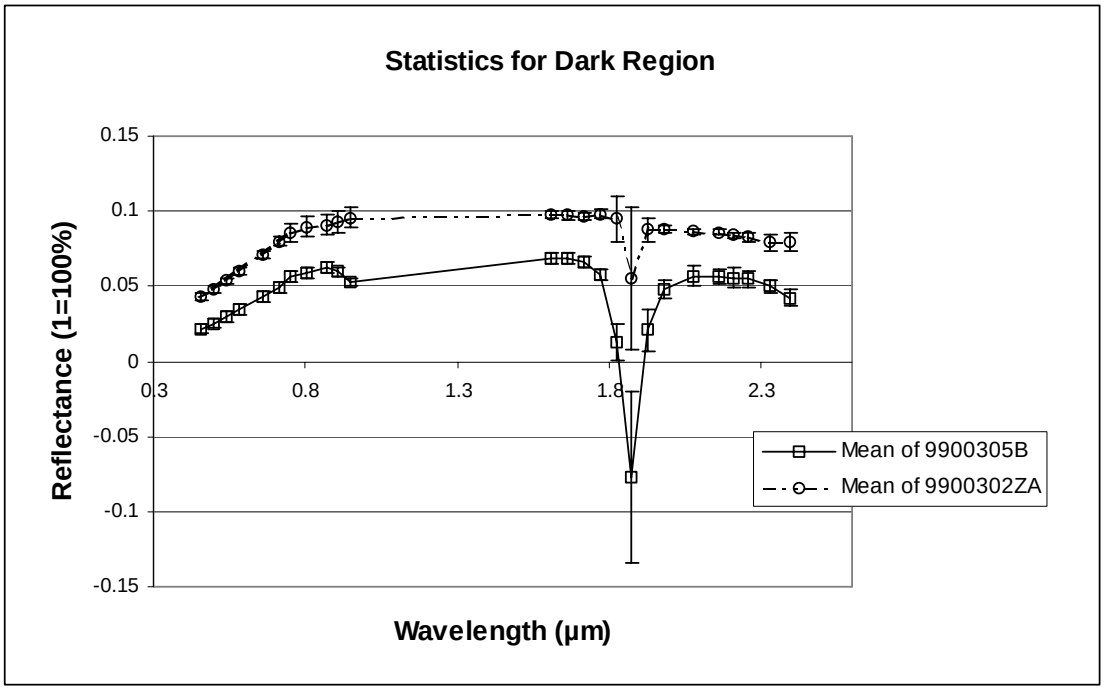

Figure 19. Plots of the mean and standard deviations for a matching spectrally dark region within images 9900302ZA and 9900305B. The error bars represent one standard deviation from the mean.

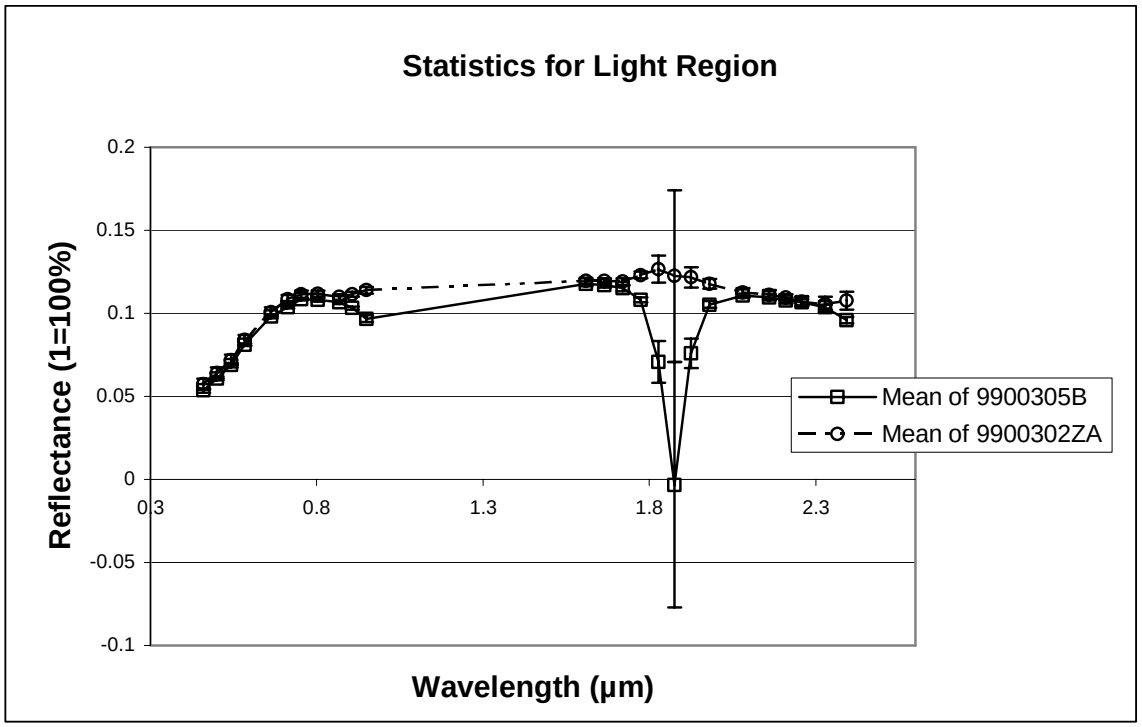

Figure 20. Plots of the mean and standard deviations for a matching spectrally light region within images 9900302ZA and 9900305B. The error bars represent one standard deviation from the mean.

Based on the example of field and atmospherically corrected spectra in Figures 16 and 17, the ELC method appears to atmospherically correct the MASTER data most accurately. However, very few well-located matches of field spectra are available to do a rigorous test of both the ACORN and Empirical Line Calibration method. If no field data are available, atmospheric correction with ACORN can also be obtained. ACORN with SSE yields results similar to ELC, except that ELC the calibration coefficients cannot be easily transferred to nearby images. Other radiative transfer models, such as HATCH [*Qu et al.*, 2003] cannot be employed in this case because their algorithms rely on channels in the absorption portions of the spectrum near 1.4 and 2 microns. MASTER does not contain data in these regions because it was designed to avoid these absorption features.

Due to the large errors and high noise in bands 11, 15 - 19, and 25, further processing was done on the 18 well-corrected bands. Using the 18 bands that appear to be well corrected (bands 1 - 10, 12 - 14, and 20 - 24) for all images within the TVLRVR does not forfeit a large amount of spectral information. Figures 2 and 4 show library spectra of minerals containing overtone vibrational and electronic absorption features. What can be seen is that although only 10 bands in the VNIR and 5 bands in the SWIR were used to determine the shape of the spectra, it is still possible to differentiate between many of the minerals' absorption features. In Figures 3 and 5 the absorption features detected with the MASTER data are highlighted, because the library spectra shown in these figures have been convolved to the MASTER wavelengths available, and the continua of the

spectra are removed. The following absorption features are clearly visible and distinguishable: those caused by the wings of charge transfer bands in the ultraviolet (Fe-O), centered on MASTER bands 2 and 3 (0.4589 μm and 0.5414 μm); those of vegetation, centered on MASTER band 5 (0.6624 μm); and those between 0.85 and 0.92 microns associated with the crystal field effects of Fe, centered on MASTER band 8 (0.803 μm). Less distinguishable are the absorption features caused by Al-OH, centered on MASTER bands 21 and 22 (2.1648 μm and 2.2146 μm); the absorption features caused by Mg-OH, centered on MASTER band 23 (2.2638 μm); the absorption features caused by CO_3, centered on MASTER band 22 (2.2146 μm); and the absorption features caused by H_20, centered on MASTER band 23 (2.2638 μm). The absorption features for Al-OH and CO_3 can appear very similar, as can absorption features for Mg-OH and H_20. Unfortunately, some of the absorption features are located either within band 24 or at longer wavelengths. When the absorption feature occurs at longer wavelengths, such as that for the CO_3 feature within calcite, the spectrum may slope toward the longer wavelength, but with the continuum removed, the feature is not highlighted.

Most surface materials have diagnostic absorption features that are 20 to 40 nm wide at Full Width Half Maximum (FWHM) [*Hunt*, 1977]. MASTER is not able to discriminate such narrow spectral features. It has an approximate FWHM of 50 nm in bands 1 - 25. (Note the width of the spectral response functions in Figure 13.) Because the bands are not contiguous, the MASTER instrument will not allow for specific mineral identification without previous knowledge of the geology of the region. However, it does appear that enough information is available with the reduced data set of 18 bands to detect the

presence of features in the 0.4 to 1 micron portion of the spectrum, such as the electronic features of Fe^{3+} (Fig. 2), and overtone vibrational features in the 2.5 micron region of the spectrum, such as Al-O (2.16 to 2.22 μm), Mg-OH (2.3 to 2.35 μm), and CO_3 (2.3 to 2.35 μm) (Fig. 4).

2.4.5 Producing Classification

Following the atmospheric correction, the data are in apparent reflectance. The 28 separate, atmospherically corrected MASTER images for the TVLRVR were then mosaicked together. Before the georeferenced images were mosaicked, the edges of each image (the most warped section of the image) were cut. The final mosaic was completed using nearest neighbor resampling.

After all 28 images were atmospherically corrected and mosaicked, a Minimum Noise Fraction (MNF) transform was performed to determine if the dimensionality of the data could be reduced. Ideally, an MNF produces a spectral subset of the data without the noise. An MNF transform is produced by two principal component analysis rotations and a noise-whitening step [*Green et al.*, 1988]. The first rotation uses the principal components of the noise covariance matrix. The second rotation uses the principal components derived from the original image after it has been noise whitened by the first rotation and rescaled by the noise standard deviation. The MASTER sensor, however, is an underdetermined system so all 18 bands were used in further processing.

After the MNF transform, the Pixel Purity Indices (PPI^{TM}) were computed. The PPI^{TM} feature in ENVI finds the most extreme, or outlying, "pure" pixels when viewed in multidimensions. The PPI^{TM} function in ENVI creates randomly oriented test vectors and projects the n-dimensional (18 dimensions, in this study) spectral points onto these vectors. The pixels within a minimum and maximum of threshold values are flagged as extreme. This was done for 5000 iterations in this study. The digital number (DN) of each pixel in the PPI^{TM} image corresponds to the number of times that pixel was recorded as extreme, where high PPI^{TM} indicates purity.

Once the most spectrally pure pixels were identified, the endmembers were chosen using ENVI's N-dimensional Visualizer^{TM}. The N-dimensional Visualizer^{TM} is a tool that allows the user to view an n-dimensional Euclidean space, where n is the number of bands, each band is associated with an axis, and all axes are orthogonal. The value of a spectrum in a single band determines its coordinates along the associated axis in spectral space. Within the ENVI's N-dimensional Visualizer^{TM} the pixels with a high PPI^{TM} were flagged, and out of these, 17 endmembers were chosen. Of these endmembers, 5 were pixels in the turbulent, reflective water in the Gulf of California. The remaining 12 endmembers; field spectra of "Basalt," "Wttfgp[7]," and "Faroash;" and one endmember derived from the atmospherically corrected image, "LV-Veg" were used in further processing. The VNIR reflectance spectra of these endmembers and their spectra with

[7] The field spectra of "Basalt," "Wttfgp," and "Faroash" were chosen for the classification because they had high separability (low matches in the Spectral Analyst^{TM} to one another and the endmembers derived from the N-dimensional Visualizer^{TM}). "Wttfgp" was collected from a tuff unit within the Las Minitas region. "Faroash" was collected from as ash unit in the Puertecitos Volcanic Province in Northern Baja California.

the continua removed are shown in Figure 21. The SWIR reflectance spectra are shown in Figure 22.

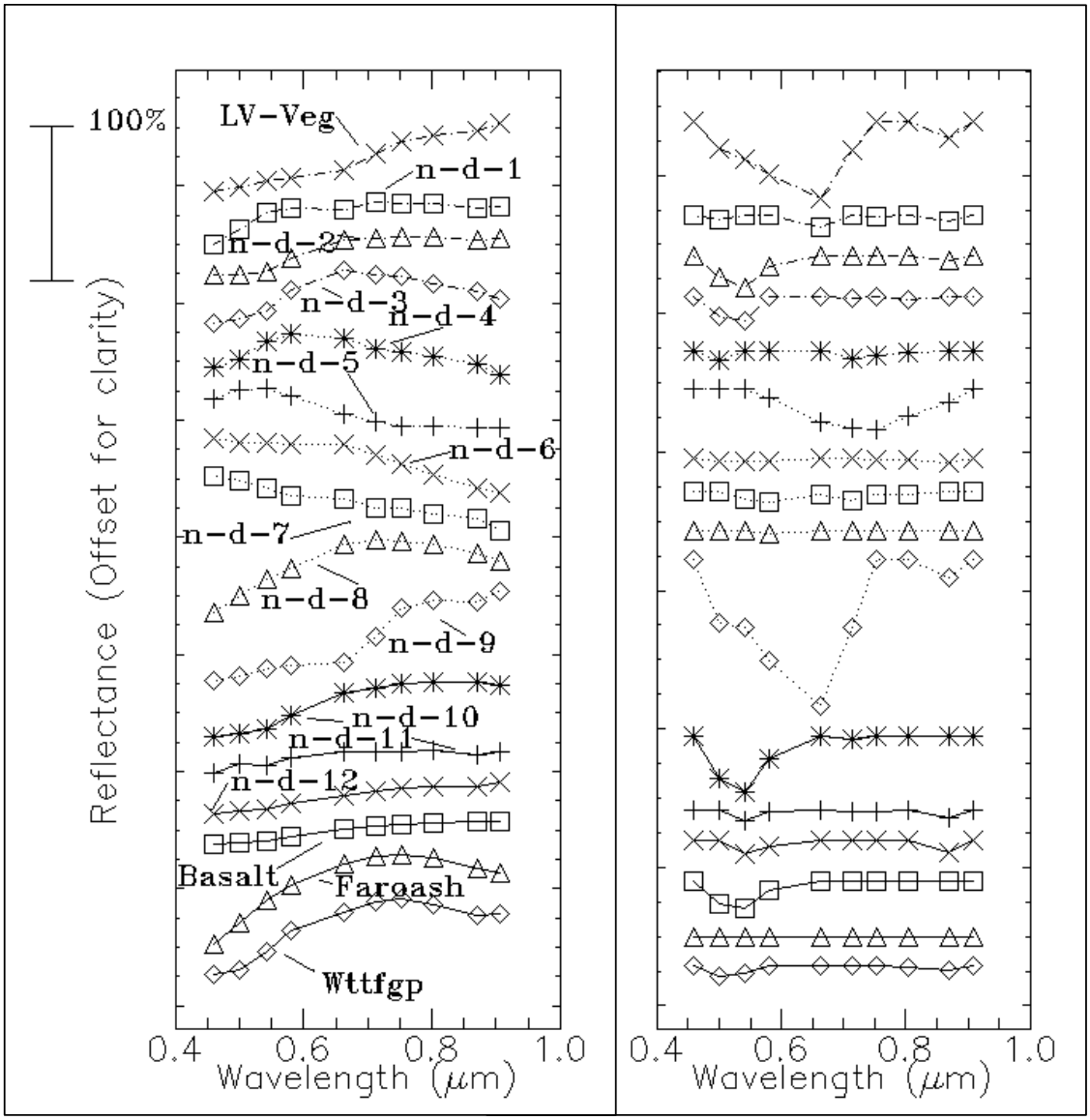

Figure 21. Shown on the left are the reflectance spectra of the endmembers for the VNIR wavelength bands. Shown on the right are the spectra with their continua removed. The spectra are offset for clarity, and the bar in the upper left hand corner represents the scale on the y-axis.

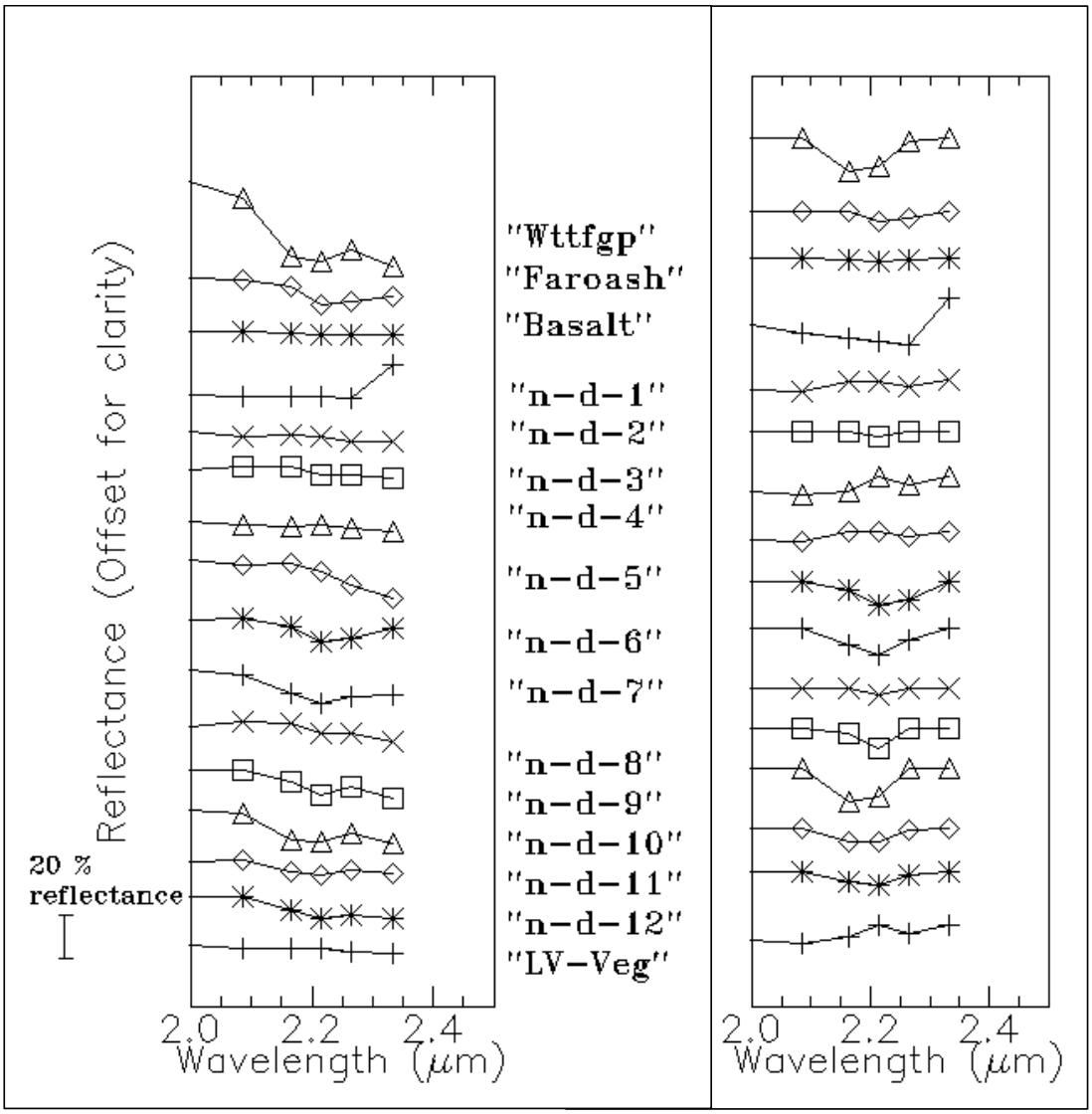

Figure 22. Shown on the left are the reflectance spectra of the endmembers for the SWIR wavelength bands. Shown on the right are the spectra with their continua removed. The spectra are offset for clarity, and the bar in the upper left hand corner represents the scale on the y-axis.

The classification was produced using Spectral Angle Mapper (SAM) [*Kruse et al.*, 1993]. A value of zero radians defines a perfect fit. This technique, when used on calibrated reflectance data, is relatively insensitive to illumination and albedo effects because it uses an n-dimensional angle to match pixels to reference spectra. The algorithm treats the pixels as n-dimensional vectors, with the dimensionality equal to the

number of bands, and determines the spectral similarity between two spectra by calculating the angle in radians between the spectra [*Kruse et al.*, 1993].

Supervised classifications were produced for the MASTER images as well. A supervised classification has the advantage that the image does not need to be atmospherically corrected before classification. These classifications were made with classes of selected pixels within regions of known lithology. The classification of the remaining pixels was based on these classes. The results outlined surfaces that likely had similar geochemistry, but because they are based on an average of pre-selected pixels, they did not yield as much information about the surfaces as the classification scheme outlined above.

2.4.6 Determining the Likely Lithology of the Endmembers

Because the data were atmospherically corrected, theoretically the endmembers could be identified from spectral libraries and field spectra. The 12 endmembers derived from the N-dimensional Visualizer™, one endmember chosen from the image, "LV-Veg," along with the field spectra "Basalt," "Wttfgp," and "Faroash" were analyzed with the Spectral Analyst™. The comparison was run against the USGS mineral and vegetation library spectra using the endmembers' bands 1 - 10 (0.45890 μm - 0.907 μm) and separately against the USGS mineral and vegetation library spectra using the endmembers' bands 20 - 24 (2.08450 μm - 2.33250 μm). A complete report of the USGS spectral libraries is given by *Clark et al.* [2003]. The best fits to VNIR wavelength bands (MASTER bands 1 - 10) of each endmember are summarized in Table 2, and the best fits to the SWIR wavelength bands (20 - 25) of each endmember are summarized in Table 3. The five

most likely matches for the VNIR and the SWIR wavelengths are listed in Appendix B. The best fit is determined with a combination of the Spectral Angle Mapper algorithm and the Spectral Feature Fitting™ (SFF™). SFF™ is an absorption-feature-based methodology, where the unknown spectrum is scaled to match each library spectrum after continuum removal from both spectra. The output from the Spectral Analyst™ is a number from zero to 2, with two being a perfect match with both the SAM and SFF™ spectral matching algorithms, with each contributing one point. When assessing the degree of fitting from these algorithms, several things are important. For example, a good fit is relative. If an endmember matches a particular mineral with a very high score, it is only meaningful if that score is significantly higher than a score between that mineral and very different minerals. A "significant" difference is difficult to ascertain, however. A flat spectrum, one devoid of absorption features, will fit other flat spectra very well, but this is not an indication of a good match. Whereas, a spectrum with very large features may not have a perfect fit to another spectrum with a large feature, but the common feature, varying just slightly, may indicate the endmember shares a similar chemical make-up to that of the known mineral. Additionally, some of the minerals in the USGS spectral library are known to have impurities, such that the spectrum of the rock may not be entirely attributed to the mineral family to which the sample is assigned [*Clark et al.*, 2003]. Careful consideration has been given to all of these factors when determining the likely lithology of the endmembers.

Compared to the USGS Mineral and Vegetation Spectral Libraries, using bands 1-10 (.4589-.91 microns)		
n-d #1	Montmorillonite; Phyllosilicate; $(Na,Ca)0.33(Al,Mg)_2Si_4O10(OH)_2•nH_20$	1.883
n-d #2	Microcline (Feldspar group); Tectosilicate; $KAlSi_3O_8$	1.844
n-d #3	Microcline (Feldspar group); Tectosilicate; $KAlSi_3O_8$	1.851
n-d #4	Gypsum (Selenite); Sulfosalt; $CaSO_4•2H_20$	1.851
n-d #5	Augite (Pyroxene group); Inosilicate; $(Ca,Mg,Fe^{2+},Fe^{3+},Ti,Al)_2(Si,Al)_2O_6$	1.784
n-d #6	Magnetite (Spinel group); Oxide; $Fe^{+2}Fe^{+3}{}_2O_4$	1.874
n-d #7	Galena; Sulfide; PbS	1.833
n-d #8	Andradite (Garnet group); Nesosilicate; $Ca_3(Fe^{+3})_2(SiO_4)_3$	1.911
n-d #9	Juniper; Shrub	1.613
n-d #10	Hematite; Oxide; alpha-Fe_2O_3	1.814
n-d #11	Dickite (Kaolinite-Serpentine group); Phyllosilicate; $Al_2Si_2O_5(OH)_4$	1.957
n-d #12	Kaolinite/Smectite (50% Kaol.)(Kaolinite-Serpentine group); Nesosilicate; Al_2SiO_5	1.821
Basalt	Staurolite HS188; Nesosilicate; $Fe_2{}^{+2}Al_9O_6(SiO_4)_4(O,OH)_2$	1.837
Faroash	Montmorillonite; Phyllosilicate; $(Na,Ca)_{0.33}(Al,Mg)_2Si_4O_{10}(OH)_2•nH_20$	1.969
Wttfgp	Grossular; Nesosilicate; $Ca_3Al_2(SiO_4)_3$	1.916
LV-veg	Rubber Rabbitbrush; Shrub	1.502

Table 2. Best matches to the USGS mineral and vegetation spectral libraries for the VNIR wavelengths to the endmembers determined from the MASTER image and selected field spectra.

Compared to the USGS Mineral and Vegetation Spectral Libraries, using bands 20-24 (2.0-2.33250 microns)		
	Mineral Name/Plant Name; Mineral Type/Plant Type; Formula	Score
n-d #1	Pinnoite; Hydrous Borate; $MgB_2O_4•3H_2O$	1.886
n-d #2	Beryl; Cyclosilicate; $MgB_2O_4•3H_2O$	1.876
n-d #3	Alunite; Sulfate; $KAl_3(SO_4)_2(OH)_6$	1.888
n-d #4	Kaolinite/Smectite; Phyllosilicate; $Al_2Si_2O_5(OH)_4$ + $(Na,Ca)0.33(Al,Mg)_2Si_4O_{10}(OH)_2•r$	1.929
n-d #5	Diaspore; Hydroxide; AlO(OH)	1.993
n-d #6	Gypsum; Sulfosalt; $CaSO_4•2H_2O$	1.921
n-d #7	Hematite; Oxide; alpha-Fe_2O_3	1.926
n-d #8	Chlorite Mg-rich; Phyllosilicate; $(Mg,Fe)_3(Si,Al)_4O_{10}(OH)_2$-$(Mg,Fe)_3(OH)_6$	1.98
n-d #9	Dry Long Grass; Grass	1.95
n-d #10	Oligoclase (Plagioclase); Tectosilicate; $(Na,Ca)Al(Al,Si)Si_2O_8$	1.973
n-d #11	Labradorite HS105 Plagioclase; Tectosilicate; $(NaAlSi,CaAl_2)Si_2O_8$	1.986
n-d #12	Manganite; Hydroxide; MnO(OH)	1.827
Basalt	Augite (Pyroxene group); Inosilicate; $(Ca,Na)(Mg,Fe,Al,Ti)(Si,Al)_2O_6$	1.966
Faroash	Spessartine; Nesosilicate; $Mn_3Al_2(SiO_4)_3$	1.96
Wttfgp	Alunite; Sulfate; $(Na,K)Al_3(SO_4)_2(OH)_6$ (Na_{82})	1.802
LV-Veg	Dry Long Grass	1.941

Table 3. Best matches to the USGS mineral and vegetation spectral libraries for the SWIR wavelengths to the endmembers determined from the MASTER image and selected field spectra.

As examples, Figures 23 and 24 show a range in quality of matches to the spectral library data. A poor match between endmember “n-d-10” and the mineral malachite is shown in Figure 23, with the continuum removed to highlight the spectral features. The match between “n-d-10” and malachite yields a score of 0.338 in the Spectral Analyst™, with a combination of the SAM and SFF™ algorithms. A good match between endmember “n-d-10” and the mineral Hematite is shown in Figure 24, with the continuum removed to highlight the spectral features. This match yields a score of 1.814 in the Spectral Analyst™ for comparison of the VNIR wavelengths.

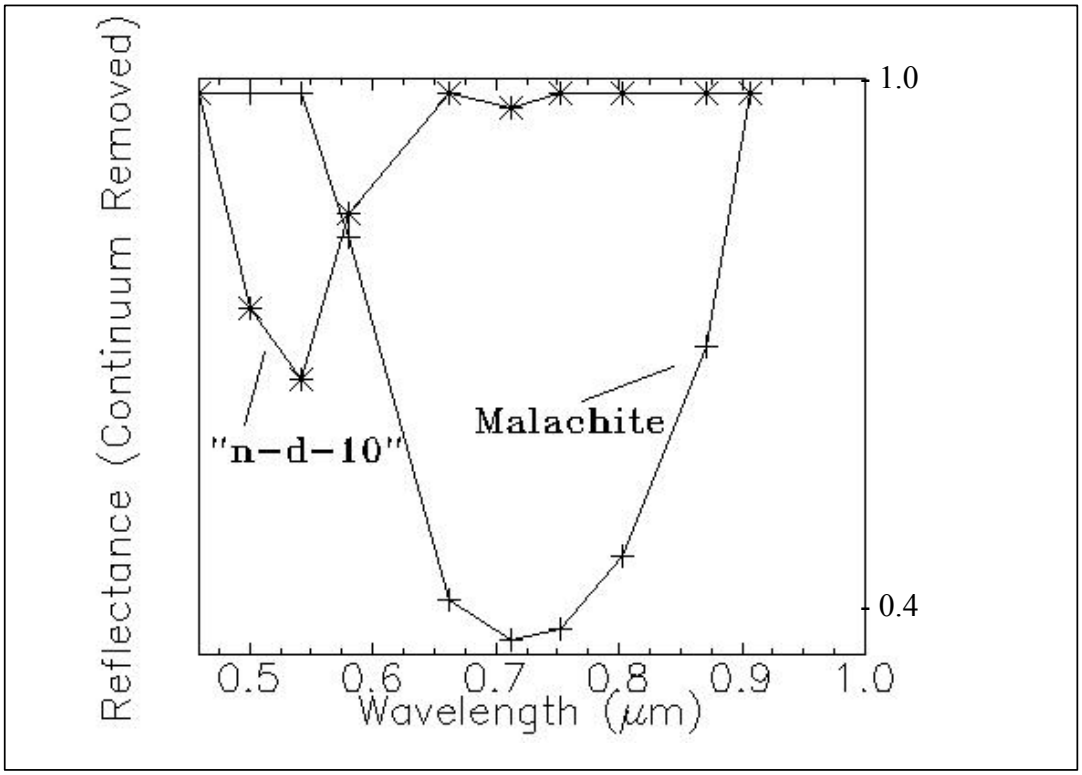

Figure 23. Reflectance spectrum of the endmember "n-d-10" and the mineral malachite. The continuum has been removed to highlight the spectral features.

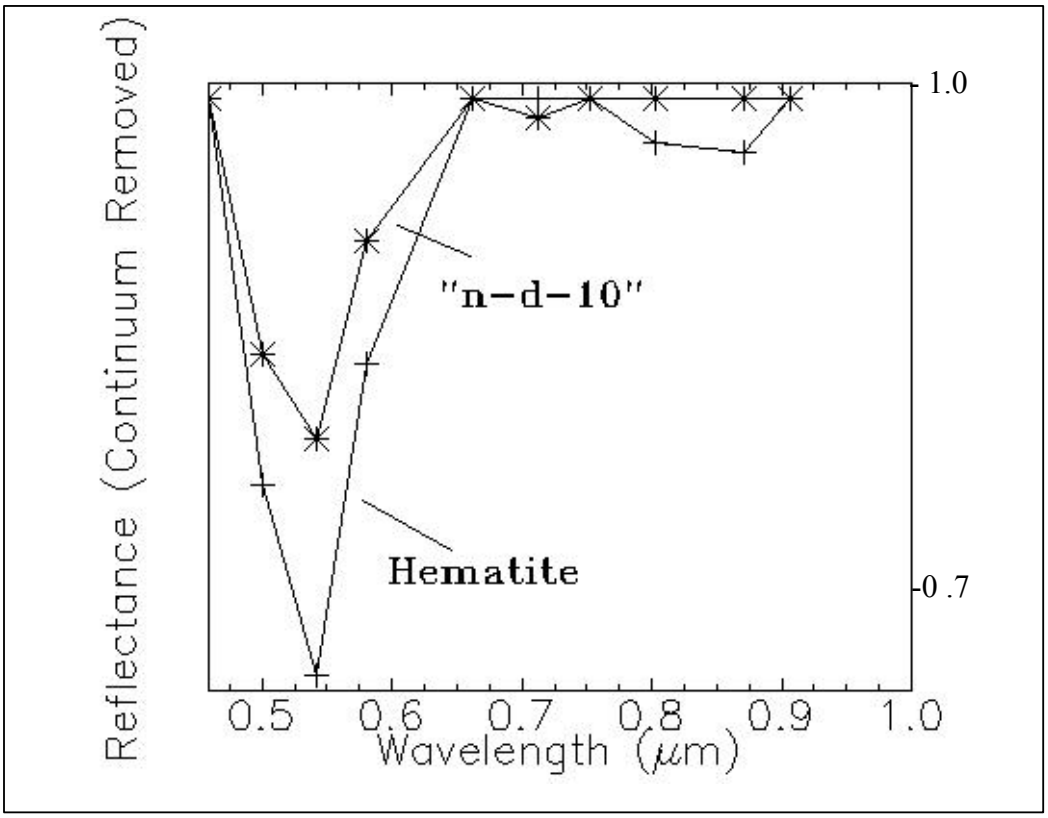

Figure 24. Reflectance spectrum of the endmember "n-d-10" and the mineral hematite. The continuum has been removed to highlight the spectral features.

The Spectral Analyst^{TM} yields higher matches for spectra when compared for the SWIR wavelengths, since there are only 5 available MASTER bands for this comparison. In this study, a score of 1.8 for the VNIR spectrum and a score of 1.9 for the SWIR wavelengths are considered good matches. However, careful consideration must be given to the factors influencing apparent matches mentioned above. For vegetation spectra in the VNIR wavelengths, a very good match is one above 1.5. This lower score is due to the mixing of the VNIR features from the underlying rock surface with the vegetation spectrum and the vast differences among vegetation spectra in the VNIR. While the spectral signature for chlorophyll present in photosynthesizing plants is very distinctive, the reflection from vegetation in the near infrared and in the visual ranges of

the spectrum varies considerably with how much chlorophyll is in the plant [*Labovitz and Masuoka*, 1984].

2.5 Discussion of Spectral Analyst™ Results for Individual Endmembers

The following section discusses the Spectral Analyst™ results for each endmember individually. The matches to the VNIR and SWIR are computed separately, due to the fact that different minerals produce absorption features in these separate sections of the electromagnetic spectrum. Including the bands outside the region of the absorption feature decreases the reliability of the match. The reality is that within the approximately 15-meter[8] pixel size of the MASTER image there will be a mixture of several minerals and in some cases vegetation. Because the MASTER sensor is not a hyperspectral instrument, the identifications are not intended to produce absolute mineral matches; however, the Spectral Analyst™ was used to determine if a mineral identification could aid in determining the lithology of the surface represented by each endmember. The top five matches in the VNIR and SWIR wavelength regions are shown in Appendix B.

In most cases the underlying rock is of igneous origin. However, the primary minerals of igneous rocks, quartz and feldspar, are devoid of absorption features in the VNIR and SWIR. Therefore, the spectral signatures of these surfaces will primarily be shaped by secondary minerals caused by weathering and alteration of the original rock, or in the case of the sedimentary rocks, primary carbonates, hydrates, or hydroxides.

[8] Original images were resized from an original average pixel size of 5 meters to 15 meters to increase signal to noise ratio and decrease computation time.

Locations referred to in the following sections can be found in Plate 1.

LV-Veg: This endmember was made directly from the atmospherically corrected MASTER data mosaic from an average of 15 pixels that covered a significant portion of vegetation near the summit of La Virgen. Pixels classified as this endmember make up 0.7782% of the classified pixels.

In the VNIR and SWIR wavelengths, "LV-Veg" most closely matched the library spectra of various vegetation, rather than mineral spectra, due to its strong reflection in the near infrared wavelengths and relatively flat SWIR spectrum. The most closely matching spectrum within the USGS library is Rubber Rabbit brush in the VNIR wavelengths (score of 1.5, Table 2), and dry, long grass in the SWIR wavelengths (score of 1.9, Table 3). MASTER data are not of high enough spectral resolution to distinguish one type of vegetation from another very clearly; however, the highest scoring match, 1.408, within the VNIR wavelengths (the most diagnostic region for vegetation) to the mineral spectral library is with kerogen. This waxy substance is composed of chemical compounds formed by the low-grade metamorphism of organic molecules derived from decaying plant and animal matter. The second most closely matched mineral was Hydroxylapatite, yielding a score of 1.403. These matches are of very low likelihood, and therefore this endmember seems to clearly represent vegetation.

"n-d-1": This endmember was derived from the N-dimensional Visualizer™. It makes up 6.6088% of the classified pixels. Pixels classified as "n-d-1" are most commonly found in the La Reforma caldera in the region to the south of the resurgent dome, mapped as the intra-caldera non-welded tuffs by *Demant* [1984]. It is also found in the canyons to the southwest of the La Reforma caldera, within the arroyos of the region mapped as ignimbritic out-flow sheets by *Demant* [1984].

As shown in Table 2, using bands 1 - 10 the endmember "n-d-1" most closely matches the spectrum of a montmorillonite sample, with a score of 1.883. A total of eight mineral samples have a matching score above 1.85 (between 1.853 and 1.883) for the VNIR wavelengths, including two samples of montmorillonite, three samples of alunite, two samples of saponite and one smectite sample. However, there is considerable ambiguity due to the relatively small spectral features in VNIR wavelengths for this endmember. The small features in the VNIR part of the spectrum of these library spectra are known to be due to small amounts of hematite and jarosite [*Hunt et al.*, 1973]. It is possible the very small feature seen in MASTER band 5 (Fig. 21) could be due to a small amount of vegetation in this endmember.

Using bands 20 - 24, "n-d-1" most closely matches a sample of pinnoite, with a score of 1.886 (Table 3). It also has fairly high score for matches with samples of sillimanite, beryl, gypsum, and dumorite. *Hunt et al.* [1973] point out that the sillimanite sample in the USGS library is slightly altered to montmorillonite, which accounts for the strong hydroxyl (2.2μm) band. By observation, it is likely that the major feature in the "n-d-1"

spectrum at the SWIR wavelengths, centered around MASTER band 22, results from an H_20 or an Al-OH absorption feature. The endmember "n-d-1" matches montmorillonite with a score of 1.712. Additionally, montmorillonite is a common alteration mineral of volcanic ash [*Klein and Hurlbut*, 1985], and many pixels within known regions of volcanic ash are classified as "n-d-1." Therefore, it is possible that endmember "n-d-1" represents altered volcanic ash, most likely with a high abundance of montmorillonite and a small amount of vegetation. It is possible this endmember has secondary gypsum as well, due to the broad shape of the feature in the SWIR wavelengths (Fig. 22).

"n-d-2": This endmember was derived from the N-dimensional Visualizer^{TM}. Pixels classified as "n-d-2" make up 31.6745% of the classified pixels. This endmember encompasses much of what is mapped as the andesite lavas of the La Reforma Caldera (outside the collapse circle). Also, many of the recent basaltic-andesitic lavas are classified as this endmember, including the three recent basaltic to andesitic lavas to the east and southeast of the La Reforma resurgent dome.

As shown in Table 2, the endmember "n-d-2" most closely matches the spectrum of a microcline sample, with a score of 1.844, using bands 1 - 10. Using the VNIR wavelengths, nine other mineral samples yield a spectral match with "n-d-2," with scores between 1.802 and 1.843. These mineral samples include other tectosilicates, nesosilicates, phyllosilicates and halites. Small features in the VNIR part of the spectrum of these library spectra are known to be due to small amounts of hematite and jarosite [*Hunt et al.*, 1973]. It is difficult to determine if any one or a combination of

these minerals make up a large portion of the lithology which "n-d-2" represents, due to the fairly small spectral features of the "n-d-2" spectrum; however, it is clear that this endmember represents a surface with some ferric oxides, due to the small feature centered near MASTER band 3 (Fig. 21).

Using bands 20 - 24, a sample of beryl is best matched to "n-d-2," with a score of 1.876. The beryl sample is known to have trace amounts of other elements [*Clark et al.*, 1993], likely giving it the absorption feature in the SWIR, which is matching "n-d-2." Eleven other mineral samples match "n-d-2" in the SWIR wavelengths with scores from 1.800 to 1.861. These mineral samples include sulfates, phyllosilicates, a nesosilicate, a sulfide, an inosilicate, a tectosilicate, and a hydrous borate. However, given the small number of bands in the SWIR wavelengths, these matches are not particularly significant. By observation of the subtle feature centered on MASTER band 22 in the SWIR spectrum, it seems likely that "n-d-2" contains some Al-OH or hydrate mineral. The location of the pixels identified as this endmember in regions known to be surfaces of basalt and andesite rocks, the similarity of the "n-d-2" spectrum to the field spectrum "Basalt," with more pronounced absorption features in the SWIR wavelengths, and the likely presence of iron oxides within the surface make it likely that this endmember represents a weathered surface of basaltic and andesitic rocks.

"n-d-3": This endmember was derived from the N-dimensional Visualizer^{TM}. It makes up only 0.0729% of the classified pixels. The largest portion of pixels classified as "n-d-3" are in a small region, 3 km inland from Punta El Bajito (Plate 1), in a unit mapped as

Quaternary alluvium by *Demant* [1984]. These appear to be the detritus of the rocks classified with the endmembers "Wttfgp" and "n-d-6."

As shown in Table 2, the endmember "n-d-3" most closely matches the spectrum of a microcline sample, with a score of 1.851, using bands 1 - 10. There are 10 other mineral specimens with spectra that match "n-d-3" in the VNIR wavelengths with scores larger than 1.8, including two other samples of microcline, two halides, three phyllosilicates, one hydrous sulfate, and two nesosilicates. As with "n-d-2," it is likely that "n-d-3" represents a surface with some ferric oxides due to its Fe-O absorption features.

Using bands 20 - 24, "n-d-3" matches a sample of alunite with a score of 1.888 (Table 3), and this is the only mineral with a matching score of above 1.800. The second highest score of 1.776 is for another alunite sample. Given the fairly high match with alunite and the lack of other closely matched spectra, it is likely "n-d-3" represents a surface including alunite in its composition. Alunite forms from the action of sulfuric acids (often from hydrothermal solutions) upon potassium rich feldspars [*Klein and Hurlbut*, 1985]. Pixels classified as this endmember are located in a region that is known to have been altered by sulfuric acids within hydrothermal solutions, rich in ore metals [*Wilson*, 1948]. Therefore, this endmember likely represents a surface within the area mapped by *Demant* [1984] as a Quaternary marine unit that contained some amount of potassium feldspar that has been at least partially hydrothermally altered to alunite.

"n-d-4": This endmember was derived from the N-dimensional Visualizer^{TM}. Pixels classified as "n-d-4" make up 0.5304% of the classified pixels. The largest portion of

pixels identified as "n-d-4" are in arroyos and adjacent to the roads just west of Punta El Bajito (Plate 1).

As shown in Table 2 the endmember "n-d-4" most closely matches the spectrum of a gypsum sample in the VNIR wavelengths (score of 1.851); however the VNIR wavelengths are not diagnostic of the presence of gypsum. It is difficult to determine the lithology of "n-d-4" with MASTER bands 1 - 10, due to the flat nature of the "n-d-4" spectrum in the VNIR.

Within the SWIR wavelengths, five mineral specimens yield matching scores of over 1.900 with "n-d-4." Kaolinite/smectite is the closest match (score of 1.929, Table 3), and the four others include another smectite sample, one tectosilicate and two phyllosilicates. In all cases, the common feature being matched is centered at MASTER band 22[9], the position of the Al-OH and water features. The strong matches with this feature in the SWIR are a good indication that this endmember represents a lithology with a significant percentage of secondary minerals containing Al-OH, such as kaolinite. This surface likely represents weathered detritus.

"n-d-5": This endmember was derived from the N-dimensional Visualizer™. Pixels classified as this endmember make up only 0.0049% of the classified pixels. Pixels identified as this endmember are present in a small region adjacent to the resurgent dome of the La Reforma caldera, mapped as intra-caldera non-welded tuffs by *Demant* [1984]

[9] The water feature in gypsum minerals appears have a feature centered on band 22 as well, but this feature is broader (Fig. 4).

but mapped as a small outcrop of the Comondú Formation within tuffaceous deposits assigned to the Boleo Formation by *Schmidt* [1975].

As shown in Table 2, the endmember "n-d-5" most closely matches the spectrum of an augite sample, using bands 1 - 10, with a score of 1.784. This endmember also has high scores (1.783 and 1.767, respectively) for matches with samples of acmite and jadeite (other pyroxenes), as well as glauconite (score of 1.741). However, after glauconite, the scores drop to 1.660. The library spectrum of augite is dominated by both Fe^{2+} and Fe^{3+} absorptions, which produce a broad band centered near 1.0 μm. It is likely that endmember "n-d-5" contains some Fe^{2+} and Fe^{3+} bearing mineral, such as pyroxene, which is giving it the broad absorption feature toward 1.0 μm, but it is impossible to determine which mineral this is, or what percent of the surface represented by "n-d-5" is made up of this mineral.

Using bands 20 - 24 gives the highest score for a match with a sample of diaspore (score of 1.993, Table 3); however, endmember "n-d-5" has a score of over 1.9 for more than 20 different minerals within the USGS spectral library when matching just bands 20 - 24. This ambiguity is due to the lack of obvious absorption features in the SWIR wavelengths. In conclusion, the lithology of the surface represented by endmember "n-d-5" is difficult to determine with the matching of the MASTER bands. On Plate 1, pixels classified as endmember "n-d-5" are surrounded by pixels classified as "n-d-1," likely representing tuffaceous deposits. Endmember "n-d-5" likely represents a flow deposit within this tuffaceous unit, a lava flow that was mapped as part of the Comondú

Formation by *Schmidt* [1975]. The small feature present in the SWIR wavelengths of "n-d-5", centered at MASTER band 22, makes it likely this endmember contains some Al-OH or CO_3 containing mineral, but it is impossible to determine the identity of this mineral.

"n-d-6": This endmember was derived from the N-dimensional Visualizer™. It makes up 0.0524% of the classified pixels. Pixels identified as this endmember are located only within the southern portion of Punta Santa Maria (Plate 1) and two isolated regions, mapped as Pre-Reforma, Quaternary alluvium and Pliocene sediments by *Demant* [1984] just off the roads leading south from Punta Santa Maria (Plate 1), within a gypsum mine owned by CAOPAS mining company.

As shown in Table 2, the endmember "n-d-6" most closely matches the spectrum of a sample of magnetite, with a score of 1.874, using bands 1 - 10. This particular magnetite spectrum from the USGS library is from a sample heavily contaminated by quartz [*Hunt et al.*, 1971a]. Magnetite is frequently associated with the heavy fraction of beach and river sands because of its resistance to weathering, and could be present in large amounts in the deposits in the Boleo Formation, within which pixels classified as this endmember are located. Also, endmember "n-d-6" matches a sample of galena, due to the peak near 0.4 μm and absorption in the longer wavelengths. In the galena sample in the USGS library, there is an intense absorption in the conduction band, which extends into the infrared [*Hunt et al.*, 1971b], which can be attributed to the sulphur conduction band (Fig. 6). While it is unlikely that the surface within one pixel has sufficient amounts of galena

to cause the spectral signature to diagnose this mineral, it is possible that there is sulphur on the surface, from hydrothermal vents known to be present in the region, that causes the same conduction band feature as that seen in the galena sample. However, the VNIR MASTER bands for this endmember are not particularly diagnostic of lithology.

Using bands 20 - 24, "n-d-6" most closely matches a sample of gypsum, with a score of 1.921 (Table 3). Only two other mineral samples, dumortierite[10] and another gypsum specimen, yield a match to "n-d-6" with a score over 1.900. The fourth highest match is to a sample of pectolite[11]. The much higher matches for the gypsum and dumortierite samples make it likely "n-d-6" represents a surface rich in one or both of these minerals. However, dumortierite occurs most commonly in coarse-grained acid igneous rocks or pegmatites rich in aluminum, especially when altered by contact metamorphism. Additionally, this region is known to be part of the CAOPAS gypsum mine, and Punta Santa Maria (Plate 1) is their operating port. Therefore, it is reasonable to assume "n-d-6" represents a surface rich in gypsum. It is likely that endmember "n-d-6" represents the gypsum member of the Boleo Formation, described by *Ochoa-Landin et al.* [2000], and the transported gypsum from mining operations. This endmember might also contain sulfur, or magnetite from river and sand deposits within the Santa Rosalia Formation.

"n-d-7": This endmember was derived from the N-dimensional Visualizer™. Pixels identified as this endmember make up 0.2949% of the classified pixels. Pixels identified as this endmember are located along the beaches and within isolated regions within many

[10] Dumortierite is a boro-silicate mineral that is commonly found in pegmatites and metamorphic rocks.
[11] Pectolite is a silicate mineral that is commonly found as a secondary mineral in basaltic rocks.

of the arroyos. A large concentration of pixels identified as this endmember are also present within the CAOPAS gypsum mine region, near Punta Bajito (Plate 1).

As shown in Table 2, the endmember "n-d-7" most closely matches the spectrum of a sample of galena, with a score of 1.833, using bands 1 - 10. Three of the four top matches with scores over 1.800 are to the mineral galena, with the other being to a mineral sample of topaz. For similar reasons to that explained for "n-d-6," "n-d-7" likely contains sulfur deposits.

Using bands 20 - 24, "n-d-7" most closely matches a sample of hematite, with a score of 1.926. This is the only match with a score above 1.900, and the next highest score is for a sample of olivine with a score of 1.898. However, these scores are misleading, since the spectra of hematite and olivine in the SWIR are relatively flat, thus not lending themselves to reliable spectral matching. There is a feature in the SWIR bands of "n-d-7" roughly in line with the water feature in gypsum, expressed in the MASTER bands as a broad feature centered at band 22 (Fig. 4). In fact, "n-d-7" does have a weak match with a sample of gypsum (scoring 7th of the spectra in the USGS mineral library) with a score of 1.792. It is not straightforward to determine the representative lithology of endmember "n-d-7" using spectral matching techniques, but it is likely some portion of the surface represented by "n-d-7" is composed of gypsum and sulphur. Due to the classification of pixels as endmember "n-d-7" along the shoreline, just north of the port of the CAOPAS mine and adjacent to other regions classified as "n-d-6," it can be assumed this

endmember represents a surface of deposits composed of a variety of materials including gypsum and perhaps sulfur, very similar to endmember "n-d-6".

"n-d-8": This endmember was derived from the N-dimensional Visualizer™. It makes up 0.2969% of the classified pixels. The highest abundance of the pixels identified as "n-d-8" are located within the region mapped as Pliocene submarine volcanic rocks by *Demant* [1984], located in the southeast portion of La Reforma Caldera, southeast of Arroyo de Punta Arenas (Plate 1) and within the region of tuffaceous deposits [*Demant*, 1984; *Schmidt*, 1975], directly southeast of the resurgent dome. Pixels identified as "n-d-8" are also present in a small region between El Viejo and Volcan El Azufre, just northwest of Cañon El Azufre, near the geothermal power plant. The surface in this region is mapped as marine sand and pyroclastic flow deposits from El Aguajito by *Garduño-Monroy et al.* [1993].

As shown in Table 2, the endmember "n-d-8" most closely matches the spectrum of a sample of andradite, using bands 1 - 10; however, it also matches several other mineral spectra, including goethite, with a score of 1.891 and muscovite with a score of 1.884.

Using bands 20 - 24, "n-d-8" most closely matches a sample of chlorite (1.98, Table 3); however, a wide range of minerals with hydroxyl and carbonate features near 2.2 - 2.3 μm fit endmember "n-d-8" very well. The second most likely match is with a sample of dolomite, with a score of 1.976. Although it is not significantly higher than some of the other minerals that match endmember "n-d-8," the very good match with a carbonate

mineral could indicate that endmember "n-d-8" represents a surface of the limestone member of the Boleo Formation, described by *Ochoa-Landin et al.* [2000]. This member contains marine limestone (some of which is fossiliferous and in some places tuffaceous).

By inspection, the SWIR spectrum of endmember "n-d-8" is very similar to the spectra of calcite, chlorite, and dolomite (Table 3 and Fig. 4), which are all carbonate containing minerals, but because the primary CO_3 feature is not well delineated by the five MASTER bands available in the SWIR region of the spectrum, this match is difficult to determine. It is highly possible, however, that endmember "n-d-8" represents a surface with a high fraction of carbonate rocks, perhaps the limestone member of the Boleo Formation.

"n-d-9": This endmember was derived from the N-dimensional Visualizer™. It makes up just 0.0109% of the classified pixels. Pixels identified as this endmember are located only near the summit of La Virgen, and other regions where there is a known high density of vegetation.

As shown in Table 2, the endmember "n-d-9" most closely matches the spectra of grasses and shrubs within the USGS vegetation spectral library (highest score of 1.95 for dry long grass, Table 2). Similarly to LV-Veg, the highest scoring match within the VNIR wavelengths (the most diagnostic region for vegetation) to the mineral spectral library was with kerogen (matching score of 0.884). The second most closely matched mineral was hydroxylapatite, yielding a score of 0.850. These matches indicate a very low

probability. Therefore, as with LV-Veg, this endmember clearly represents vegetation. "LV-Veg" and "n-d-9" are mapped together as "Vegetation" in the final classification.

"n-d-10": This endmember was derived from the N-dimensional Visualizer™. It makes up 0.1335% of the classified pixels. Pixels identified as this endmember are located near the summits of the recent basaltic volcanic edifices surrounding La Reforma. Additionally, pixels identified as endmember "n-d-10" are located on the summit of a volcanic edifice within the region to the north of the La Reforma caldera, mapped as andesitic lavas by *Demant* [1984].

As shown in Table 2, the endmember "n-d-10" most closely matches the spectrum of hematite (score of 1.814), using bands 1 - 10. Although there are other close matches, hematite is a very reasonable match, given the location of pixels identified as this endmember near vents of mafic lavas. The very obvious Fe-O absorption feature centered at MASTER band 3 is an indication of a surface containing ferric oxides.

Using bands 20 - 24, endmember "n-d-10" most closely matches oligoclase (score of 1.973, Table 3). However, there are many good matches in the SWIR wavelengths, given the fairly flat SWIR spectrum of "n-d-10." Therefore, endmember "n-d-10" most likely represents a lithology with large amounts of oxidized iron commonly found near the vents of the recent basaltic and andesitic lava units and cinder cones.

"n-d-11": This endmember was derived from the N-dimensional Visualizer™. Pixels classified as "n-d-11" make up 12.1656% of the classified pixels. Much of the alluvium surrounding both the La Reforma and El Aguajito calderas, as well as some alluvium located at the base of El Azufre is identified as this endmember. Some isolated regions of alluvium and playa surrounding La Virgen are also identified as "n-d-11".

As shown in Table 2, the endmember "n-d-11" most closely matches the spectrum of dickite, using bands 1 - 10 (score of 1.957). Although dickite is a significantly higher match than the other minerals, dickite does not have particularly diagnostic features in the VNIR, and the VNIR spectrum of "n-d-11" is relatively flat; therefore, the match in the VNIR is unreliable. The very small features present, centered at bands 3 and 9, could represent a small percentage of hematite or other iron-bearing mineral.

Using bands 20 - 24 "n-d-11" most closely matches a sample of olivine (score of 1.986, Table 3); however, "n-d-11" matches over 40 spectra within the USGS spectral library using bands 20 - 24 with a score of 1.9 or higher. The abundance of the high matches is due to the fairly flat spectral shape of "n-d-11." There is a small feature present, centered at MASTER band 23, which could represent the presence of a Mg-OH, hydrate- or carbonate-bearing mineral, but the feature is very small. The relatively flat spectral shape of "n-d-11" is likely indicative of high quartz content, which would be reasonable, given the large percentage of alluvium classified as this endmember. This endmember represents the surface of a wide variety of sand and other detritus located in the arroyos and the beaches within the TVLRVR.

"n-d-12": This endmember was derived from the N-dimensional Visualizer™. It makes up 0.1485% of the classified pixels. Pixels identified as this endmember are located only on the slopes of the El Azufre volcano.

As shown in Table 2, the endmember "n-d-12" most closely matches the spectrum of a kaolinite/smectite sample, using bands 1 - 10 (score of 1.821). However, kaolinite and the other samples with good matches do not have diagnostic features in the VNIR. The small features centered at bands 3 and 8 indicate a high likelihood that endmember "n-d-12" represents a surface containing an iron oxide containing mineral, such as hematite.

Using bands 20 - 24 "n-d-12" most closely matches a sample of manganite (score of 1.827, Table 3). The match to manganite appears to be significant, because the score is 1.827, and the next highest score is 1.695, for pectolite. However, it is very unlikely that the mineral manganite, a manganese ore mineral, is present in a significant abundance at the peak of the El Azufre volcano. Endmember "n-d-12" appears to have a peak near 2.3 μm (band 18) that does not match the spectra well in the USGS spectral library; however, it is difficult to see the full shape of the spectrum due to the limited atmospherically corrected MASTER SWIR bands. Therefore, it is difficult to determine the representative lithology of endmember "n-d-12." The slopes of the El Azufre volcano have been mapped as dacitic lavas [*Capra et al.*, 1998]; therefore, this endmember can be assumed to represent the weathered surface of a dacitic lava.

Basalt: This endmember is derived from the mean of spectra collected in the field with the ASD spectrometer at the site labeled "Basalt" in Figure 8. The surface measured is within one of the most recent basaltic-andesite lavas of the La Virgen volcano. The "Basalt" endmember comprises 24.6598% of the classified pixels. Pixels identified as this endmember make up most of the lavas mapped as recent basaltic emissions from Tres Vírgenes, by *Demant* [1984]. Additionally, much of the resurgent dome of La Reforma and recent basaltic-andesite lavas surrounding it are, in part, classified as "Basalt."

As shown in Table 2, the endmember "Basalt" most closely matches the spectrum of a sample of andalusite, using bands 1 - 10 (score of 1.837); however, it also yields a score of 1.786 for a match with hematite. The hematite is a more likely match, given the known nature of the "Basalt" endmember as that of basaltic andesite lava flow, which easily alters to hematite on exposed surfaces. "Basalt" matches a sample of augite best using bands 20 - 24 (score of 1.966, Table 3); however, there are many good matches to "Basalt" in the SWIR wavelengths due the absence of large absorption features at these wavelengths. This endmember represents basalt to andesite lavas that have undergone some weathering and oxidation on the surface, which has produced a thin hematite coating.

Faroash: This endmember is derived from the mean of spectra collected in the field with the ASD spectrometer. The collection site is located in the Puertecitos Volcanic Province

in Baja California, Mexico, approximately 400 km north of the TVLRVR. It is an outcrop of volcanic ash that crops out just south of the beach camp of Punta Bufeo. The "Faroash" endmember makes up 22.5341% of the classified pixels. Much of the alluvium and regions mapped as rhyolitic tuff by *Romero-Rojas et al.* [1997] are classified as "Faroash."

As shown in Table 2, the endmember "Faroash" most closely matches the spectrum of montmorillonite, using bands 1 - 10 (score of 1.969). However, several samples give good matches to the endmember "Faroash" in the VNIR wavelengths. Using bands 20 - 24, the best match is with a sample of spessartine (score of 1.96, Table 3). As with the VNIR wavelengths, several samples give good matches to the endmember "Faroash" in the SWIR wavelengths, making the determination of the lithology very difficult. However, because this endmember was collected in the field, it is known that the endmember represents a rhyolitic ash deposit.

Wttfgp: This endmember is derived from the mean of spectra collected in the field with the ASD spectrometer. The collection site is located in the Las Minitas region inside the La Reforma caldera, in Group 1 in Figure 8. The outcrop that was measured with the ASD spectrometer was a white altered tuff that was mapped as part of the Boleo Formation by *Schmidt* [1975], and as intra-caldera, non-welded tuffs by *Demant* [1984]. Pixels classified as this endmember make up 0.0610% of the classified pixels. Pixels identified as this endmember are located in very small regions within the La Reforma

caldera, the largest group of which are located in the unit mapped as Quaternary alluvium by *Demant* [1984], located approximately 3 km inland from Punta El Bajito (Plate 1).

As shown in Table 2, the endmember "Wttfgp" most closely matches the spectrum of a grossular sample, using bands 1 - 10 (score of 1.916). This match seems unlikely, as grossular is not common in tuff deposits. Using bands 20 - 24, ""Wttfgp" most closely matches alunite. This match, with a score of 1.802 (Table 3) is significant, especially being 0.054 points above the second match. Additionally, alunite is often formed by the interaction of sulfuric acid with rocks rich in potassium feldspar [*Klein and Hurlbut*, 1985]. There is known alteration by volcanic vents in the Minitas region [*Schmidt*, 1975], where this endmember was collected with the ASD; therefore, this endmember likely represents a surface of a volcanic tuff with some portion of fragments containing potassium feldspar that have been altered to alunite.

2.6 Discussion of Spectral Analyst™ Matches

The Spectral Analyst™ is only moderately helpful in determining the lithology of the surfaces represented by each endmember. In most cases, the identifications are not so absolute that a particular mineral can be assumed to constitute a large portion of the represented surface without auxiliary knowledge of the surface represented by the endmember. However, by careful analysis of the continuum-removed library spectra, convolved to the MASTER channels (Figs. 3 and 5) and the continuum-removed endmember spectra (Figs. 21 and 22) a few observations can be made. Surfaces with iron

oxides have small absorptions features (dips) in the continuum-removed MASTER bands 2, 3 and 8. Surfaces with a large amount of vegetation have small absorption features in the continuum-removed MASTER band 5. Surfaces containing Al-OH minerals typically have small absorption features in the continuum-removed MASTER bands 21 and 22. Surfaces containing Mg-OH minerals typically have small absorption features in the continuum-removed MASTER band 23. Surfaces containing carbonate minerals typically have small absorption features in the continuum-removed MASTER band 22. And hydrate minerals usually show a small absorption feature in continuum-removed MASTER band 23.

Minerals with very similar absorption features, such as hematite and goethite, are very difficult to differentiate using the bands available in this study (Fig. 2). However, many of the matches of the endmembers are compatible with what is known about the surface. This verifies that the atmospheric correction of the data was moderately successful, and limited lithologic identification is possible with atmospherically corrected (VNIR-SWIR) MASTER data. Data incorrectly modified would not match the mineral spectra in a predictable way.

The Spectral Analyst^{TM} is helpful in the determination of the lithology of each endmember, but by inspection of known library spectra convolved to the MASTER bands with their continua removed (Figs. 3 and 5), it is clear that the identification of particular

features within the endmembers is limited. Some features can be determined, however. Absorption features caused by the wings of charge transfer bands in the ultraviolet (Fe-O), the absorption features of vegetation, and the absorption features between 0.85 and 0.92 microns associated with the crystal field effects of Fe are clearly visible and distinguishable. However, the absorption features caused by Al-OH, the absorption features caused by Mg-OH, the absorption features caused by CO_3, and the absorption features caused by H_20 are less distinguishable. The absorption features for Al-OH and CO_3 can appear very similar, as can absorption features for Mg-OH and H_20. Unfortunately, some of the absorption features in the SWIR part of the electromagnetic spectrum are located either within MASTER band 24 or at longer wavelengths. When the absorption feature occurs at longer wavelengths, such as that for the CO_3 feature within calcite, the spectrum may slope toward the longer wavelength, However, with the continuum removed, the feature is not highlighted, and it is difficult to confidently match the MASTER SWIR spectra to carbonate minerals using the Spectral Analyst^{TM}.

2.7 Conclusion

The classification produced with the techniques discussed in this chapter is shown in Plate 1. This classified image will be discussed further in chapter 4, including a discussion of how this classification updates our current knowledge of the TVLRVR.

In conclusion, MASTER data can be atmospherically corrected to a reasonable accuracy with both the ACORN software and the ELC mode in ENVI. If known spectra are available within one line for both a dark and light spectrum, the ELC appears to be a

more accurate method for the MASTER data. However, with either technique, a reliable correction is difficult to obtain for those bands in the water absorption region (MASTER bands 11, 15 - 19, and 25), even if atmospheric parameters are known.

Classifying the atmospherically corrected MASTER data, resized to exclude the bands highly affected by water absorption, was done successfully by choosing endmembers with the highest PPI^{TM} values. Endmembers from a selected number of field spectra and one image-derived region were added to the list of endmembers to expand the classification. This yielded a classification map that roughly delineated surfaces that vary in their secondary minerals, produced by weathering and alteration, namely ferric oxides, hydrates, hydroxyls, and carbonates. Attempts to identify these minerals using ENVI's Spectral Analyst^{TM} were only moderately successful. It is necessary to have auxiliary information about the lithology of the underlying rock and secondary minerals within the surface represented by each endmember for precise lithologic identification.

References

Boardman, J.W., and F.A. Kruse, Automated spectral analysis: A geological example using AVIRIS data, northern Grapevine Mountains, Nevada, in *10th Thematic Conference, Geologic Remote Sensing*, San Antonio, Texas, 1994.

Cachorro, V.E., A.M. Defrutos, and M.J. Gonzalez, Analysis of the Relationships between Junge Size Distribution and Angstrom-Alpha Turbidity Parameters from Spectral Measurements of Atmospheric Aerosol Extinction, *Atmospheric Environment Part A-General Topics*, *27* (10), 1585-1591, 1993.

Capra, L., J.L. Macias, J.M. Espindola, and C. Siebe, Holocene Plinian eruption of La Virgen volcano, Baja California, Mexico, *Journal of Volcanology and Geothermal Research*, *80* (3-4), 239-266, 1998.

Chandrasekhar, S., *Radiative Transfer*, Clarendon Press, Oxford, 1950, reprinted by Dover Publications, New York, 393 pp., 1960.

Clark, R.N., Chapter 1: Spectroscopy of Rocks and Minerals, and Principles of Spectroscopy in Remote Sensing for the Earth Sciences, in *Manual of Remote Sensing*, edited by A.N. Rencz, pp. 3- 58, John Wiley and Sons, New York, 1999.

Clark, R.N., and T.L. Roush, Reflectance spectroscopy: Quantitative analysis techniques for remote sensing applications, *Journal of Geophysical Research*, *89* (B7), 6329-6340, 1984.

Clark, R.N., G.A. Swayze, A.J. Gallagher, T.V.V. King, and W.M. Calvin, The U. S. Geological Survey, Digital Spectral Library: Version 1 (0.2 to 3.0μm), in *U.S. Geological Survey Open File Report 93-592*, U.S. Geological Survey, Denver, CO, 1993.

Clark, R.N., G.A. Swayze, A.J. Gallagher, and F.A. Kruse, Mapping with imaging spectrometer data using the complete band shape least-squares fit to multiple spectral features from multiple materials, in *Third AVIRIS Workshop*, pp. 2-3, JPL, Pasadena, CA, 1991.

Clark, R.N., G.A. Swayze, R. Wise, K.E. Livo, T. M. Hoefen, R. F. Kokaly, and S. J. Sutley, USGS Digital Spectral Library splib05a, in *USGS Open File Report 03-395*, 2003.

Crowley, J.K., Mapping Playa Evaporite Minerals with Aviris Data - a 1st Report from Death-Valley, California, *Remote Sensing of Environment*, *44* (2-3), 337-356, 1993.

Demant, A., The Reforma Caldera, Santa Rosalia Area, Baja California, A volcanological, petrographical and mineralogical study, in *Neotectonics and sea level variations in the Gulf of California area, a Symposium*, edited by V. Malpica-Cruz, S. Celis-Gutiérrez, J. Guerrero-Garcia, and L. Ortlieb, pp. 77-96, Univ. Nal. Auton, México, Inst. Geologia, México, D. F., 1984.

Farrand, W.H., R.B. Singer, and E. Merényi, Retrieval of apparent surface reflectance from AVIRIS data: a comparison of empirical line, radiative transfer, and spectral mixture methods, *Remote Sensing of Environment*, *47*, 311-321, 1994.

Garduño-Monroy, V.H., H. Vargas-Ledezma, and J.O. Campos-Enriquez, Preliminary geologic studies of Sierra El Aguajito (Baja California, Mexico): a resurgent-type caldera, *Journal of Volcanology and Geothermal Research*, *59*, 47-58, 1993.

Goetz, A.F.H., Spectroscopic remote sensing for geological applications, *Proceedings of the Society of Photo-Optical Instrumentation Engineers (SPIE)*, *M*, 77-21, 1981.

Goetz, A.F.H., Relative performance of HATCH and three other techniques for atmospheric correction of Hyperion and AVIRIS data, in *EO-1 Science Validation Meeting*, NASA, Hilo, HI, 2002.

Green, A.A., M. Berman, P. Switzer, and M.D. Craig, A transformation for ordering multispectral data in terms of image quality with implications for noise removal, *IEEE Transactions on Geoscience and Remote Sensing*, *26* (1), 65-74, 1988.

Hook, S.J., J.J. Myers, K.J. Thome, M. Fitzgerald, and A.B. Kahle, The MODIS/ASTER airborne simulator (MASTER)—a new instrument for earth science studies, *Remote Sensing of Environment*, *76*, 93-102, 2001.

Hunt, G.R., Spectral signatures of particulate minerals in the visible and near-infrared, *Geophysics*, *42*, 501-513, 1977.

Hunt, G.R., J.W. Salisbury, and C.J. Lenhoff, Visible and near-infrared spectra of minerals and rocks: III. Oxides and hydroxides, *Modern Geology*, *2*, 195-205, 1971a.

Hunt, G.R., J.W. Salisbury, and C.J. Lenhoff, Visible and near-infrared spectra of minerals and rocks: IV. Sulphides and Sulphates, *Modern Geology*, *3*, 1-14, 1971b.

Hunt, G.R., J.W. Salisbury, and C.J. Lenhoff, Visible and near-infrared spectral of minerals and rocks: V. Halides, phosphates, arsenates, vanadates, and borates, *Modern Geology*, *3*, 121-132, 1972.

Hunt, G.R., J.W. Salisbury, and C.J. Lenhoff, Visible and near-infrared spectra of minerals and rocks: VI. Additional silicates, *Modern Geology*, *4*, 85-106, 1973.

Junge, C., *Air chemistry and radioactivity*, 382 pp., Academic Press, New York, 1963.

Klein, C., and C. Hurlbut, *Manual of Mineralogy*, 596 pp., John Wiley & Sons, New York, 1985.

Knipling, E.B., Physical and physiological basis for the reflectance of visible and near-infrared radiation from vegetation, *Remote Sensing of Environment*, *1*, 155-159, 1970.

Kruse, F.A., Use of Airborne Imaging Spectrometer Data to map minerals associated with hydrothermally altered rocks in the northern Grapevine Mountains, Nevada, and California, *Remote Sensing of Environment*, *24* (1), 31-51, 1988.

Kruse, F.A., A.B. Lefkoff, J.B. Boardman, K.B. Heidebrecht, A.T. Shapiro, P.J. Barloon, and A.F.H. Goetz, The Spectral Image Processing System (SIPS) - interactive visualization and analysis of imaging spectrometer data, *Remote Sensing of Environment*, *44*, 145 - 163, 1993.

Labovitz, M.L., and E.J. Masuoka, Changes in vegetation spectra with leaf deterioration under 2 methods of preservation, *Photogrammetric Engineering and Remote Sensing*, *50* (12), 1737-1745, 1984.

Miller, C.J., Performance assessment of ACORN atmospheric correction algorithm., in *Algorithms and Technologies for Multispectral, Hyperspectral, and Ultraspectral Imagery VIII; Aerosense 2002*, SPIE, Orlando, FL, 2002.

Ochoa-Landin, L., J. Ruiz, T. Calmus, E. Perez-Segura, and F. Escandon, Sedimentology and Stratigraphy of the Upper Miocene Boleo Formation, Santa Rosalia, Baja California, Mexico, *Revista Mexicana de Ciencias Geologicas*, *17* (2), 83-96, 2000.

Qu, Z., B.C. Kindel, and A.F.H. Goetz, The High Accuracy Atmospheric Correction for Hyperspectral Data (HATCH) model, *IEEE Transactions on Geoscience and Remote Sensing*, *41* (6), 1223-1231, 2003.

Romero-Rojas, S.A., D.A. Maraver-Romero, A.A. Avalos-Zermeno, and E. Aparicio-Cordero, Carta Geologico-Minera Santa Rosalia G12-1, *Consejo de Recursos Minerales*, Secretaria de Comercio y Fomento Industrial, 1997.

Rowan, L.C., T.L. Bowers, J.K. Crowley, C. AntonPacheco, P. Gumiel, and M.J. Kingston, Analysis of airborne visible infrared imaging spectrometer (AVIRIS) data of the Iron Hill, Colorado, carbonatite alkalic igneous complex, *Bulletin of the Society of Economic Geologists*, *90* (7), 1966-1982, 1995.

Rowan, L.C., R.N. Clark, and A.A. Green, Mapping minerals in the Mountain Pass, California area using Airborne Visible-Infrared Imaging Spectrometer (AVIRIS)

data, in *11th Conference of Geologic Remote Sensing*, pp. 1177-1178, Ann Arbor, Michigan: Environmental Institute of Michigan (ERIM), 1996.

Rowan, L.C., M.J. Kingston, and J.K. Crowley, Spectral reflectance of carbonatites and related alkalic igneous rocks - Selected Samples from 4 North-American Localities, *Economic Geology*, *81* (4), 857-871, 1986.

Schmidt, E.K., Plate tectonics, volcanic petrology, and ore formation in the Santa Rosalia Area, Baja California, Mexico, Master of Science thesis, The University of Arizona, pp. 194, 1975.

Wilson, I.F., Buried topography, initial structures and sedimentation in Santa Rosalia, Baja California, Mexico, *American Association Petroleum Geologists Bulletin*, *32*, 1762-1807, 1948.

Chapter 3: A Method of Mapping Weight Percent Silica Variation from Remotely Acquired Multispectral Thermal Infrared Data

Abstract

Remotely sensed multispectral thermal infrared (8 - 12 μm) images acquired from aircraft and spacecraft are increasingly being used to aid in mapping variations in surface silicate mineralogy [*Gillespie*, 1986]. These studies utilize the shift to longer wavelengths in the main spectral feature in this wavelength region (Reststrahlen band) as the mineralogy changes from felsic to mafic. This chapter describes an approach for determining the size of this wavelength shift using a Gaussian curve. The size of this shift is translated into weight percent SiO_2 of the surface using a reference curve, derived from laboratory data. The approach has broad applicability to many study areas and can also be fine-tuned to give greater accuracy in a particular study area, if field samples are available.

The approach was assessed using remotely acquired airborne multispectral thermal infrared images from the La Reforma Caldera, Baja California Sur, Mexico. The results indicate that the general approach tended to underestimate the weight percent SiO_2 in the image[12]. This discrepancy was removed by fine-tuning the general approach with measurements from field samples and provided good results in the calculated weight percent SiO_2 with errors of a few percent.

[12] In the Hiller Mountains test region, also discussed by *Hook et al.* [2005], results indicate the general approach slightly overestimates the weight percent SiO_2 of low silica rocks (e.g. basalt) and underestimates the weight percent SiO_2 of high silica rocks (e.g. granite).

The results from the Tres Vírgenes La Reforma Volcanic Region (TVLRVR) dataset verify the most recent volcanism to be basaltic-andesite as previously mapped. They also indicate that the intracaldera products are a sequence of ash flow tuffs and lavas of varied composition.

3.1 Introduction

This chapter describes the method employed to produce weight percent silica maps, based on a relationship derived from library spectral data. A description of the method and its testing on both the La Reforma data and data from Hiller Mountains, Nevada is included in *Hook et al.*, 2005. This chapter elaborates on that work to describe the method and the analysis of the Tres Vírgenes La Reforma Volcanic Region (TVLRVR) MASTER data in more detail. The eastern half of image 9900302U has been chosen to demonstrate this method (Fig. 1).

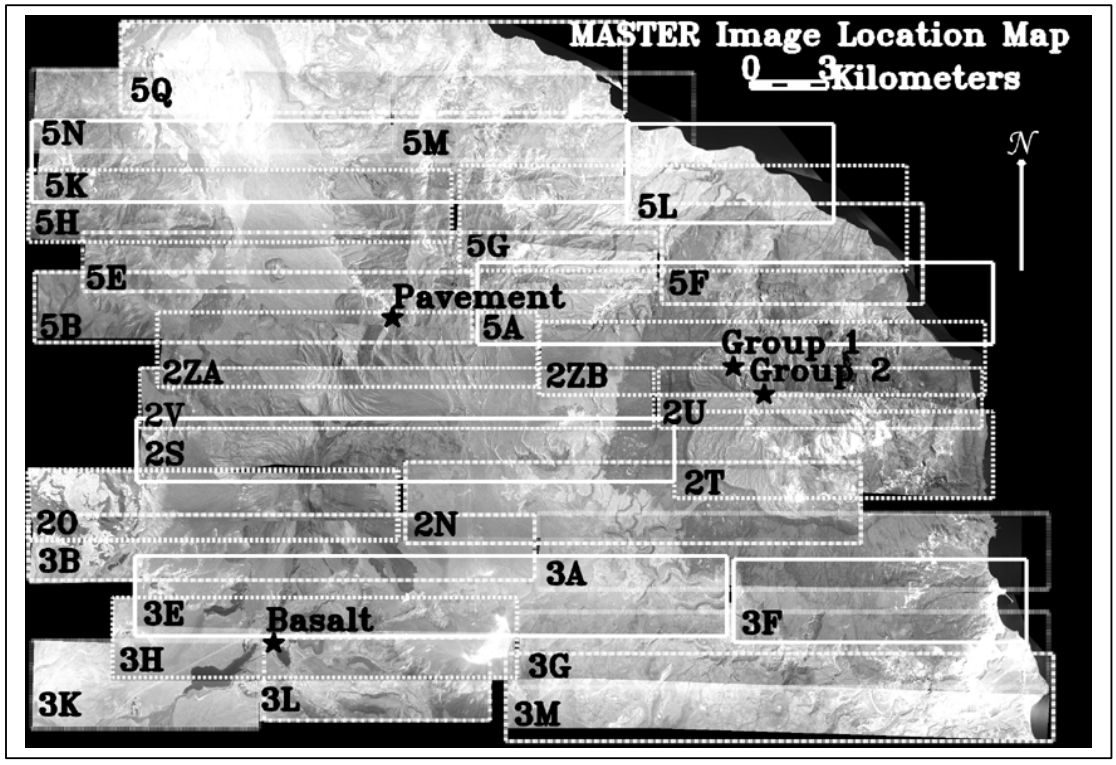

Figure 1. Boxes representing the location of the MASTER images overlain on the mosaic of the 28 MASTER images. The name of each image has been abbreviated to its last two characters (i.e., image 9900303H is shown as 3H). The name of each image is located in the lower left hand corner of its representative box. The borders of the lines vary for easier distinction between overlapping lines. Sample locations for field reflectance spectra discussed in chapter 2 are shown as black stars.

Numerous studies have demonstrated the usefulness of remotely sensed data for geological mapping [*Abrams et al.*, 1991; *Clark*, 1999; *Clark et al.*, 1991; *Crowley*, 1993; *Cudahy et al.*, 1999; *Goetz*, 1981; *Goetz et al.*, 1985]. These studies typically utilize data from the visible through short-wave infrared (0.4 - 2.5 μm) portion of the electromagnetic spectrum [*Gillespie et al.*, 1986; *Sabine et al.*, 1994]. This is largely because high spatial resolution datasets covering this wavelength range are available globally (e.g., ASTER

and Landsat). The spectral features observed in rocks in this wavelength region are primarily due to iron oxide and hydroxyl-bearing minerals. Only a few studies [*Gillespie et al.*, 1986; *Sabine et al.*, 1994] have focused on the use of remotely sensed data covering the thermal infrared (8 - 12 μm) portion of the electromagnetic spectrum where features related to differences in Si-O bonding of silicate minerals can be observed. Differences in Si-O bonding are manifest as shifts in the position of the minimum in the emissivity spectra of rocks in the thermal infrared.

Variations in silicate mineralogy are particularly useful for geological mapping because they are an important criterion in classifying and interpreting igneous rocks as well as sedimentary and metamorphic rocks derived from them. Studies utilizing thermal infrared data have demonstrated that it is possible to distinguish between rock types based on differences in silicate mineralogy [*Abrams et al.*, 1991; *Cudahy et al.*, 1999; *Hook et al.*, 1994; *Lahren et al.*, 1988; *Sabine et al.*, 1994; *Watson et al.*, 1996]. Such qualitative studies are useful but do not provide a quantitative basis for comparing similar lithotypes between regions. More recently, studies have used the shift in the emissivity minimum to estimate the weight percent SiO_2 of igneous rocks [*Gillespie et al.*, 1986 and *Sabine et al.*, 1994]. In these studies the authors customized the technique for their sites and as a result their approach is not readily applicable to other study areas. The work was also limited by calibration problems associated with the available instrumentation. The present study describes a general method for estimating silica content from multispectral thermal infrared data with broad applicability to many study areas that can be fine-tuned for a particular area for greater accuracy if field samples are available. The coefficients

necessary for estimating weight percent SiO_2 are derived for the newer airborne and spaceborne instruments including the Advanced Spaceborne Thermal Emission and Reflectance radiometer (ASTER) and the Moderate Resolution Imaging Spectrometer (MODIS) /ASTER airborne simulator (MASTER).

MASTER is a 50-channel airborne imaging spectrometer [*Hook et al.*, 2001] with 25 channels in the visible to short-wave infrared (0.4 - 2.4 μm), 15 channels in the mid infrared (MIR, 3.1 - 5.3 μm) and 10 channels in the thermal infrared (TIR, 7.8 - 12.9 μm). The MASTER data used in this study were acquired on April 29, 1999 from the B200 aircraft and have a spatial resolution of approximately 5.5 m. Only the thermal infrared channels of MASTER, covering the 7 - 13 μm region, are used in this chapter (Fig. 2).

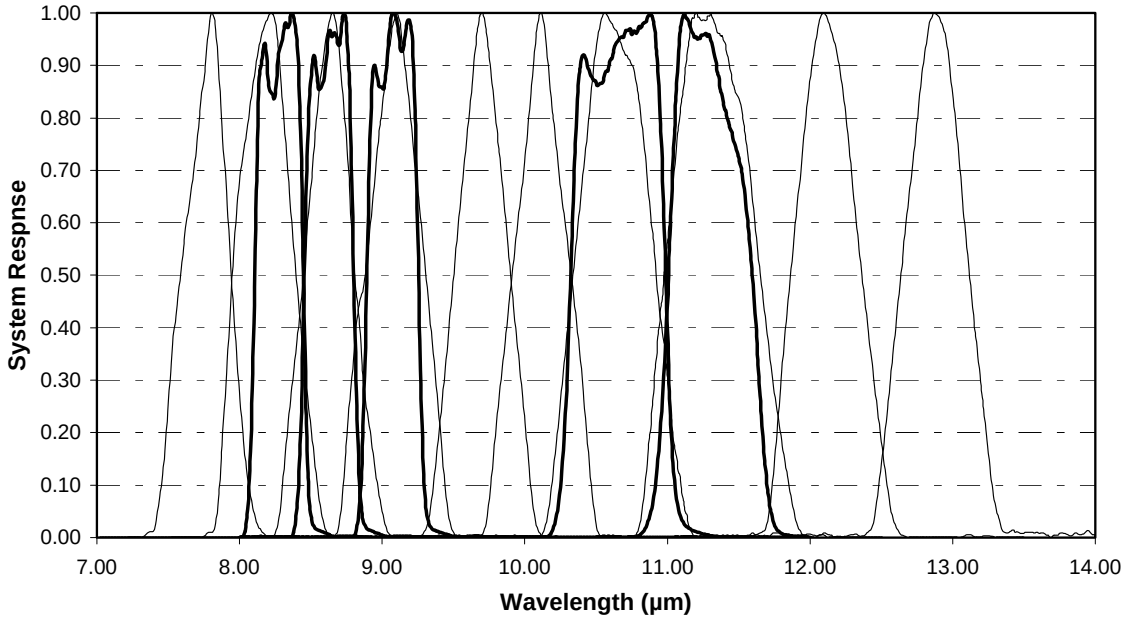

Figure 2. System response functions for the MASTER and ASTER thermal infrared channels. The MASTER system response functions are for April 1999. ASTER system response functions shown in bold.

The technique outlined in this chapter was also used to produce weight percent silica maps for ASTER data. Unfortunately, reliable results could not be obtained from the ASTER images. This is likely due to the fact that ASTER's five TIR bands do not adequately encompass the Reststrahlen band (Fig.2). In particular, the ASTER instrument is lacking bands in the 9.3 μm to 10 μm region. When the ASTER emissivity spectra are fit to a Gaussian curve they either yield erroneously short wavelengths for the Gaussian minimum (leading to incorrectly high weight percent silica values) or erroneously long wavelengths (leading to incorrectly low weight percent silica values).

Chapter three first provides the theoretical framework for remote sensing of silicate rocks in the thermal infrared region. The technique for deriving the weight percent SiO_2 of igneous rocks using thermal infrared data is then explained. This is followed by a description of the geology of the study area and the data processing procedure. The processed data are then interpreted and the algorithm for determining the weight percent SiO_2 assessed. Finally, the approach is summarized and conclusions are drawn.

3.2 Theoretical Framework

3.2.1 The Reststrahlen Band

The reflectance and emissivity spectra of minerals exhibit diagnostic features at various wavelengths that provide a means for their remote discrimination and identification. These features are caused by the interaction of electromagnetic energy with the atoms and molecules that make up the mineral. Light of infrared frequencies can generally promote molecules from a vibrational ground state to vibrational excited states. Different Si-O bonded structures vary in their interaction with thermal infrared light (8 - 12μm). Collectively the Si-O spectral features in the thermal infrared are referred to as the Reststrahlen band. The emissivity minimum for this band occurs at shorter wavelengths (8.5 μm) for framework silicates (e.g., quartz and feldspar) and progressively longer wavelengths for silicates having sheet, chain, and isolated tetrahedral structure [*Hunt*, 1980]. Because framework silicates dominate felsic igneous rocks and chain silicates dominate mafic igneous rocks, the minimum of the Reststrahlen band moves to longer wavelengths as the weight percent SiO_2 decreases (Fig. 3).

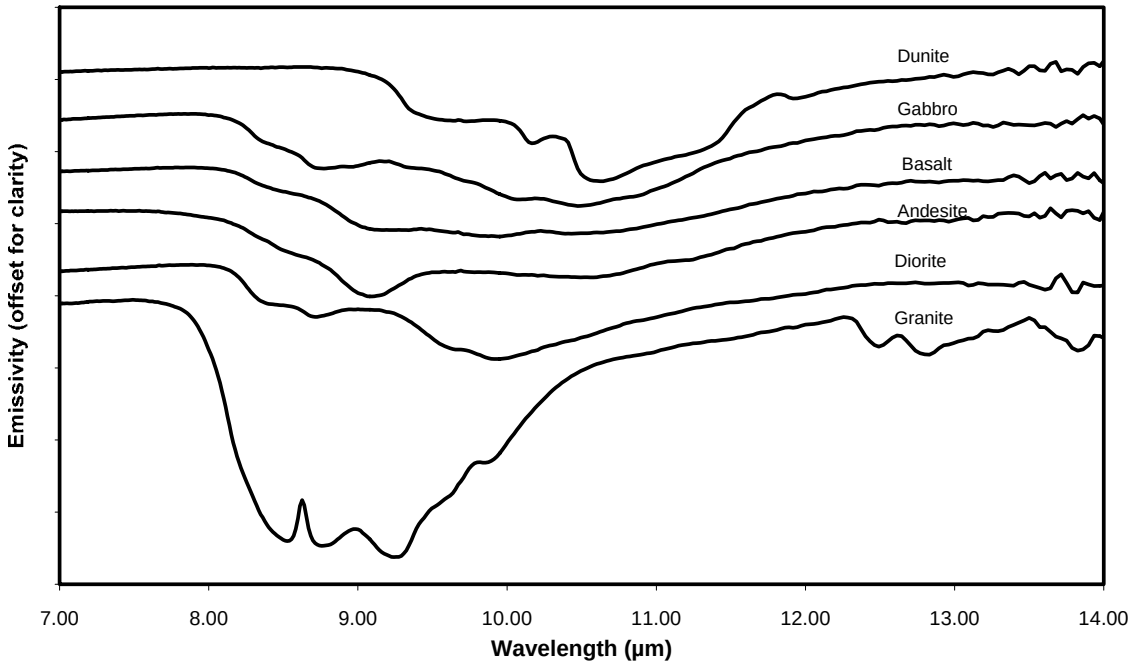

Figure 3. Laboratory hemispherical reflectance spectra of a variety of igneous rocks ranging in composition from ultramafic to felsic. Spectra obtained from the ASTER spectral library.

3.2.2 Determination of Relationship between Wavelength Minimum and Weight Percent Silica

3.2.2.1 Method

In order to take advantage of the systematic shift in the Reststrahlen minimum in igneous rock composition, it is necessary to establish a technique for the determination of the minimum as well as the most suitable chemical parameter. *Gillespie et al.* [1986] determined the minimum using a Gaussian function and *Sabine et al.* [1994] expanded on Gillespie's work by evaluating the relationship between the Gaussian minimum and a variety of chemical and modal parameters. *Sabine et al.* [1994] found the highest

correlation between SiO_2 content and the Gaussian minimum. The Gaussian minimum for the samples used by *Sabine et al.* [1994] was determined from emissivity spectra derived from Thermal Infrared Multispectral Scanner (TIMS) data. The TIMS instrument is a multispectral scanner that acquires 6 channels of data in the thermal infrared (7 - 13 μm) wavelength region. The TIMS instrument was the forerunner to the MASTER instrument, which has 10 channels in the TIR.

The TIMS data used by *Sabine et al.* [1994] were obtained over the Desolation Wilderness area of the northern Sierra Nevada. The rocks exposed there are primarily granitoids and provided a range in weight percent SiO_2 from 50 to 70%. In order to determine the weight percent SiO_2, the emissivity minimum from the TIMS data was regressed against the weight percent SiO_2 obtained from field samples. Because the minimum from the TIMS emissivity spectra was used, any artifacts in the TIMS spectra were incorporated in the relationship between the minimum and SiO_2 content, limiting the general applicability of the technique to other areas or datasets derived from other instruments. In order to determine the applicability of the technique to igneous rock spectra in general, we evaluated the relationship using the spectral data for igneous rocks in the ASTER spectral library (http://speclib.jpl.nasa.gov). The ASTER spectral library includes hemispherical reflectance spectra from 35 igneous rock samples with weight percent SiO_2 contents ranging from 43 to 76 percent.

The emissivity minimum of the laboratory spectra was determined with 3 and 4 term Gaussian functions:

$$f(x) = A_0 e^{\frac{-z^2}{2}} \quad \text{(3 term)}$$

$$f(x) = A_0 e^{\frac{-z^2}{2}} + A_3 \quad \text{(4 term)}$$

where:

$$z = \frac{x - A_1}{A_2} \text{ and x = wavelength } (\mu\text{m})$$

A_0 through A_3 are the fit values for the Gaussian function *f(x)*. The 4 terms of the Gaussian function correspond to the amplitude, position of the minimum value, area enclosed by the function and offset, respectively.

Sabine et al. [1994] determined a linear relationship between the minimum wavelength, which is obtained by fitting a 3 term Gaussian function [*Berk et al.,* 1998] to TIMS data, and the weight percent SiO_2, which is obtained by chemical analysis of samples from locations in the TIMS imagery. *Sabine et al.* [1994] also showed fit values for spectra of the field samples. In this study Gaussian-fit values were calculated for the laboratory spectra and the laboratory spectra were convolved with the system response of two instruments, as well as various MASTER channel combinations producing several datasets of Gaussian-fit values. The position coefficient of the fit (A_1 term) from each sample in each dataset was plotted against its corresponding laboratory weight percent SiO_2 value and a least squares fit performed on each dataset. Figure 4 shows a plot of the minimum obtained using 3- and 4-term Gaussian fits for the full resolution emissivity spectra from the spectral library covering the 8 - 12 μm wavelength region versus the corresponding weight percent SiO_2 values. Table 1 lists the coefficients obtained from performing least squares fits on the various datasets, including the correlation

coefficients. Evaluation of many channel combinations is important because some channels are more strongly affected by the atmosphere and can be difficult to correct. Often it is better to exclude these channels if they cannot be adequately corrected. Otherwise, residual atmospheric correction errors will negatively influence the Gaussian fitting algorithm, which assumes the emissivity data derived from the scanner contain no artifacts. This point is discussed further in the subsequent section on data processing.

	3 Term Gaussian Model				4 Term Gaussian Model			
Sample Set	**N**	**m**	**c**	**R^2**	**N**	**m**	**c**	**R^2**
7-14 um (full resolution)	35	-44.161	513.13	0.6617	35	-41.326	482.81	0.7082
8-12 um (full resolution)	35	-14.952	203.17	0.7925	33	-16.453	218.15	0.8034
MASTER 1-10 channels (7.737-12.888 um)	35	-26.228	322.24	0.8216	35	-25.981	319.47	0.8307
MASTER 1-9 channels (7.737-12.131 um)	35	-28.655	343.6	0.7705	35	-27.806	334.74	0.7867
MASTER 2-10 channels (8.153-12.888 um)	35	-0.3802	57.46	0.4719	35	-0.0017	56.318	0.105
MASTER 2-9 channels (8.153-12.131 um)	35	-7.8321	131.52	0.71	34	-10.9	162.29	0.7755
MASTER 3-8 channels (8.604-11.331 um)	35	-0.8772	62.367	0.4846	35	-0.568	60.982	0.2565
ASTER (8.287-11.289 um)	35	-7.5624	131.19	0.5832	35	-10.548	160.25	0.662
ASTER (8.287-11.289 um) excluding ultramafics	32	-14.27	194.76	0.7581	32	-16.203	213.97	0.7615

Table 1. Results from fitting the ASTER spectral library igneous rocks with a 3-term and 4-term Gaussian model. N = number of samples; m and c = coefficients for linear fit (y = mx +c) of minimum versus Wt % silica; R2 = correlation coefficient. A value of N less than 35 indicates that the Gaussian model failed to adequately fit certain spectra (failed spectra are not included in calculating the overall fit). Wavelength range shown is from centroid value of first channel to centroid value of last channel.

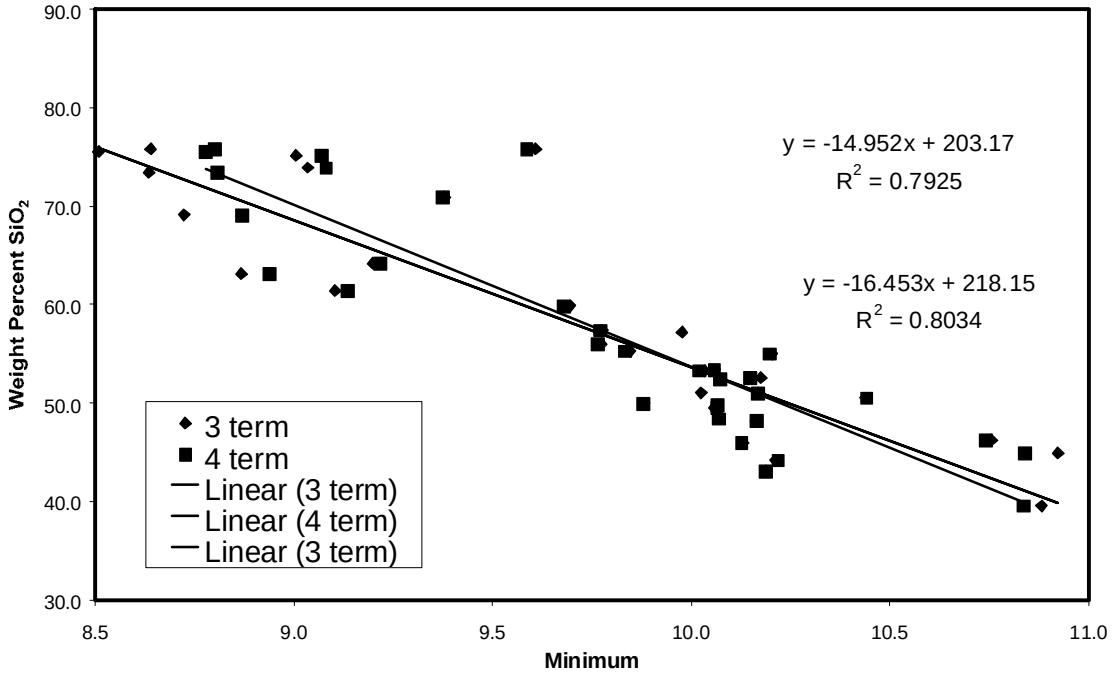

Figure 4. Gaussian-fit minimum values derived from the library spectra plotted against their corresponding weight percent silica values. Minimum values were obtained by fitting 3- and 4-term Gaussian functions to laboratory hemispherical emissivity spectra of igneous rocks. The spectra and weight percent silica values were obtained from the ASTER Spectral Library.

3.2.2.2 Results of the Gaussian Fitting to the Convolved Library Data

The highest correlation coefficient was obtained using the library data convolved to the 10 MASTER channels (41 - 50) and fit with a 4-term Gaussian function (r^2=0.83). The results obtained using the 3-term Gaussian fit were only slightly worse (r^2=0.82) as was the case for the other datasets, except the 42 - 50 and 43 - 48 channel combinations, which are discussed subsequently. This result supports using the 3-term Gaussian fit for most image manipulations where computational speed is important. The 3-term fit to the library data convolved to the 10 MASTER channels was similar to the fit for the full resolution library data for the 8 - 12 μm wavelength region (r^2=0.79). This was better than the 3-term fit to the full resolution library data for the 7 - 14 μm region (r^2=0.66).

This is due to the fact that the Reststrahlen band, fitted by the Gaussian model, is between 8 and 12 μm. By including a wider wavelength range, the values outside the Reststrahlen band diminish the ability of the Gaussian model to correctly fit the band. Further examination of Table 1 indicates that if a similar analysis is performed using MASTER channels 41 - 49 or 42 - 49 the correlation coefficients are similar to using channels 41 - 50. However, if channels 42 - 50 or 43 - 48 are used, the correlation coefficients are much worse (channels 42 - 50, r^2=0.47; channels 43 - 48, r^2=0.48). This can be explained by examining plots in which the Gaussian model is superimposed on the original library spectra Figure 5 (for channels 43 - 48), Figure 6 (for channels 42 - 50), and Figure 7 (for channels 42 - 49). If MASTER channels 42 - 49 are used (Fig. 7), the fit is equally influenced by the values outside the Reststrahlen band. If channels 42 - 50 are used, the fit is more strongly influenced by the longer wavelength channels outside the Reststrahlen band (Fig. 6) leading to erroneous results. If just MASTER channels 43 - 48 are used, the wavelength range does not fully encompass the Reststrahlen band and the ability of the Gaussian function to correctly locate the minimum of the full Reststrahlen band is reduced (Fig. 5).

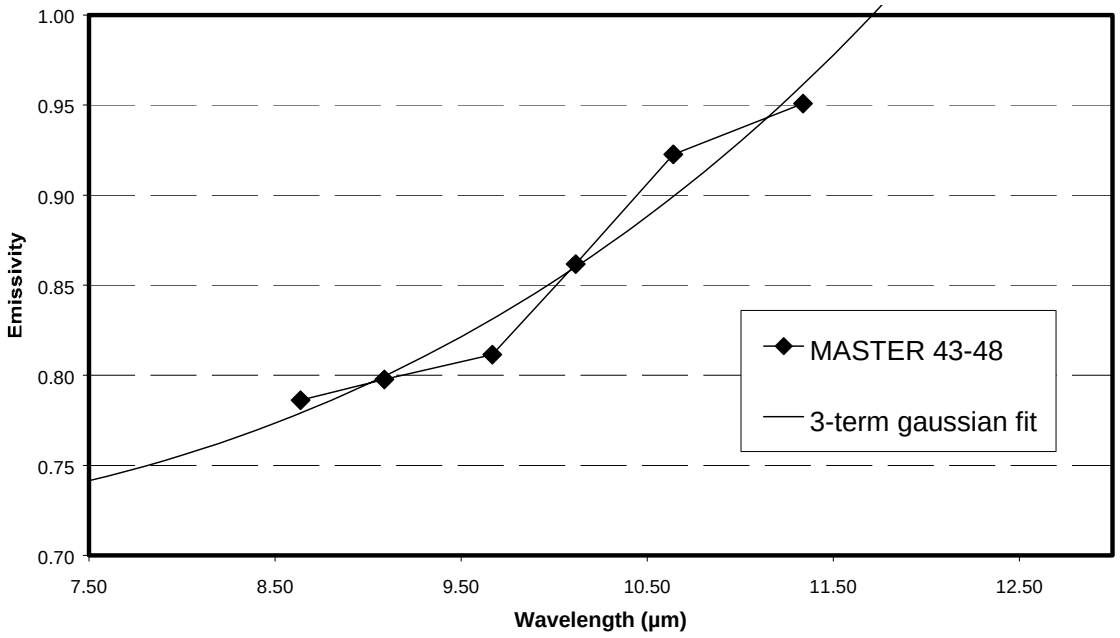

Figure 5. 3-term Gaussian function fitted to a library spectrum of quartz monzonite convolved to MASTER channels 43 - 48, illustrating the effect of not fully encompassing the reststrahlen band on the fit.

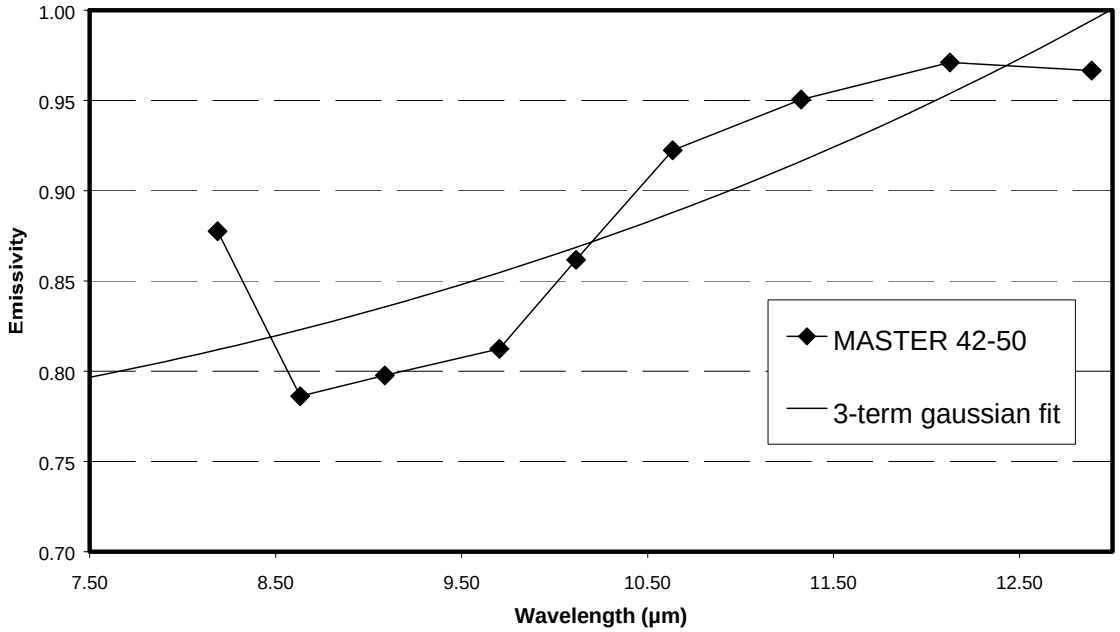

Figure 6. 3-term Gaussian function fitted to a library spectrum of quartz monzonite convolved to MASTER channels 42 - 50, illustrating the influence of the longest wavelength channel (channel 50) on the fit.

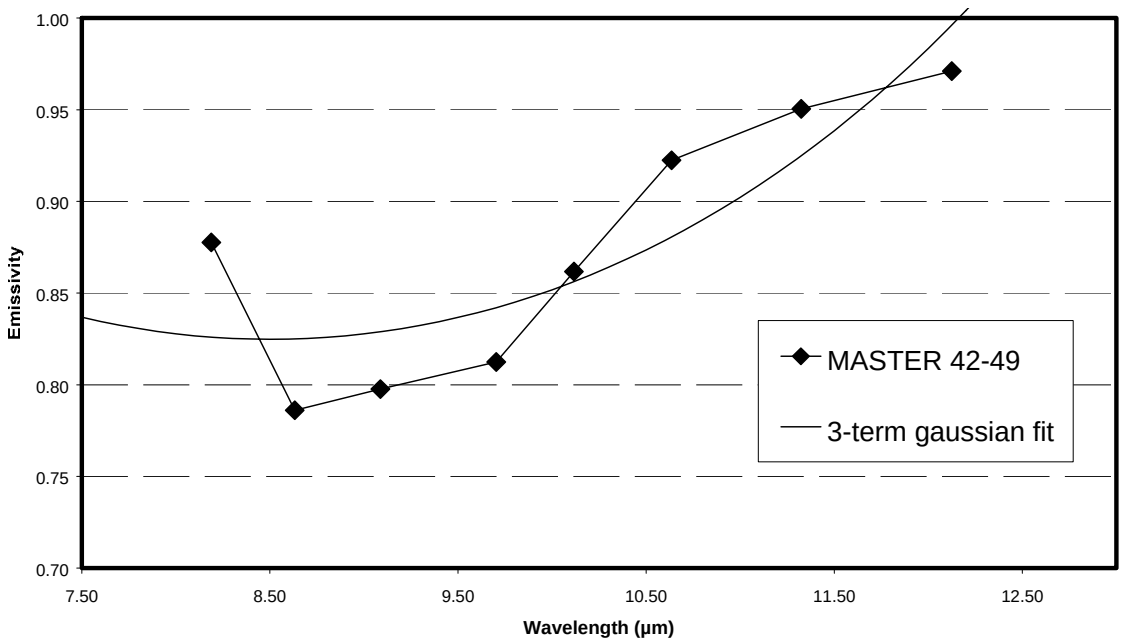

Figure 7. 3-term Gaussian function fitted to a library spectrum of quartz monzonite convolved to MASTER channels 42 - 49, illustrating the effect of excluding the longest wavelength channel on the fit.

Table 1 also provides the coefficients for the library data convolved to the ASTER channels. Since these data are available globally, albeit with low spatial resolution, the ability to map weight percent SiO_2 with ASTER is highly desirable. The correlation coefficient for the library data convolved to the ASTER wavelengths and fit by a 3-term Gaussian function is 0.58 (Table 1). The lower correlation coefficient for ASTER as opposed to the 10-channel MASTER data results from the ASTER channels not fully encompassing the Reststrahlen band. ASTER (with TIR bands 10 - 14 at 8.125 - 8.475 µm, 8.475 - 8.825 µm, 8.925 - 9.275 µm, 10.25 - 10.95 µm, 10.95 - 11.65 µm, respectively) does not contain sufficiently long wavelengths. The igneous rocks most

strongly affected by this limitation are ultramafic rocks. If the results from ultramafic rocks are excluded, the correlation coefficient increases to 0.76 (Table 1).

It should also be noted that the channel positions of some instruments (i.e., MASTER) shift over time and require frequent calibration [*Hook et al.*, 2001]. If the shift is large it may require the regression coefficients to be recalculated. In this work the MASTER system response files were taken to match the MASTER overflight. The MASTER system response files are available at: http://masterweb.jpl.nasa.gov.

3.3 Geological Background

The TVLRVR is ideal for testing weight percent silica classification due to the low rainfall, sparse vegetation cover, and wide range of rock compositions. Some distinctions between rock units are difficult to discern in the visible parts of the spectrum, as discussed in chapter 2. For testing and illustration of the mapping of weight percent silica method, a small region within the La Reforma caldera was chosen, the eastern half of image 9900302U (Fig. 1). The La Reforma caldera exposes a varied series of Quaternary and Tertiary volcanic rocks including basaltic-andesite lavas; intracaldera rhyolite ash flow tuffs and andesitic, dacitic, and rhyolite lavas; an intrusive body of diorite porphyry, and detritus derived from the rocks listed above. In addition, there are Pliocene marine sandstones and mudstones, particularly adjacent to the Gulf of California coast.

Remoteness and ruggedness of parts of the study area make application of aerial photographs and other remotely sensed imagery particularly useful in geologic mapping. The interior has no fresh water or passable roads, and is accessible only by foot or pack animal. To reach the central block of the caldera requires a multi-day backpacking trip. Thus, previous geological studies of the region had very limited field observations and primarily relied on conventional air photo interpretation. However, many of the volcanic units are difficult to differentiate on the air photos. By using remote sensing as a tool in lithological classification of the rocks in this region, the few available geological ground observations can be extended much more reliably than was previously possible.

The La Reforma caldera is on the east coast of Baja California, Mexico, at 27.5° N, just south of the border between Baja California Norte and Baja California Sur. The region, including three Quaternary volcanic systems—La Reforma caldera to the east, El Aguajito caldera to the north, and the Tres Vírgenes volcanoes to the southwest—is seismically active [*Guerrero-Guadarrama*, 1998]. Cretaceous granitic rocks probably form the basement of this region, as evidenced by several outcrops within the volcanic centers [*Sawlan*, 1981]. The volcanism at Tres Vírgenes is compositionally somewhat anomalous, as it has the major and trace element characteristics of typical calcalkaline arc lavas [*Sawlan*, 1986]. The volcanism is related not to an active subduction zone, but rather to the extensional deformation leading to the formation of the Gulf of California [*Sawlan*, 1981; *Sawlan and Smith*, 1984, *Colletta and Angelier*, 1981]. Responsible for forming the Comondú formation (andesitic lavas and debris flows) to the south and west

of this region, subduction shut off approximately 12.5 - 11 Ma [*Mammerickx and Klitgord*, 1982].

The La Reforma volcanic complex has been dated ca. 1.09 Ma [*Schmidt*, 1975]. However, the geologic history of the complex is not well understood. La Reforma has a typical caldera morphology, with a ring escarpment approximately 10 km in diameter and a central block surrounded by associated silicic domes, which stands 700 m above the caldera margins. Pyroclastic and lava outflow sheets flank the rim of the caldera and can be seen in the deep canyon walls. *Demant* [1981] and *Demant* [1984] interpreted the central block of La Reforma as a block of Miocene Comondú formation uplifted by piston-like movement. This contrasts with the interpretation by *Schmidt* [1975] who described the feature not as a caldera, but as a system of tectonic blocks, and *Walker et al.* [1992] who described the complex as an updomed structure that has been circularly eroded. In fact, La Reforma is likely a caldera, due to its composition and morphology. The central dome is not a block of Miocene Comondú formation, but was recently shown to be composed of welded ash-flow tuffs and lavas [*Hausback et al.*, 2000], more typical of a caldera resurgent dome.

3.4 Data Processing

3.4.1 Introduction

MASTER data are provided as calibrated at sensor radiance in hierarchical data format (HDF). The algorithm for mapping weight percent SiO_2 uses the surface emissivity as

input, which requires that the surface emissivity be extracted from the radiance at sensor data. This involved correcting the data for atmospheric effects and performing a temperature and emissivity (T/E) separation. In addition, a decorrelation stretch image was produced from the atmospherically corrected data to aid in interpreting the weight percent SiO_2 map. A decorrelation stretch image is commonly used for interpreting thermal infrared data as it enhances emissivity variations, related to differences in composition. Differences in emissivity are displayed as color differences while the temperature variations, related to differences in topography, are displayed as differences in brightness [*Gillespie et al.*, 1986].

3.4.2 Atmospheric Correction

The atmospheric component to the radiance at sensor was removed using the MODTRAN radiative transfer model [*Berk et al.*, 1989]. MODTRAN derives values for the atmospheric correction based on an input atmospheric profile, which may be obtained directly from default profiles in MODTRAN, or modified or replaced with local atmospheric data. No local atmospheric profiles were available; therefore, numerical forecast profiles from the National Center for Environmental Prediction (NCEP) were used instead. The NCEP produces global model values on a 1-degree by 1-degree grid at 6 hr intervals. Because the site does not lie on a grid node the NCEP values were interpolated in time and space to coincide with the aircraft overpass. In order to assess the atmospheric correction, the kinetic temperature spectrum of an area of water was examined. Water has a known emissivity in the thermal infrared and therefore if the atmospheric correction is performed correctly, the water temperatures derived for each

channel should be constant. Initial examination indicated there was approximately 2 °C of spread in the water temperatures for the central 8 channels. This spread was attributed to an incomplete correction for water vapor and ozone. Therefore the amount of water vapor and ozone in the atmospheric profile was adjusted until there was less than 1 °C of spread in the central 8 channels (Table 2). Even after adjustment, the temperatures for channel 41 are lower than the other channels due to an incomplete atmospheric correction. Atmospheric correction of channel 41, centered on 7.77 μm, is particularly difficult because this wavelength region is strongly influenced by atmospheric water vapor. Clearly, if this channel were used in determining the emissivity minimum for mapping weight percent SiO_2, the result would be influenced by incomplete atmospheric correction. Therefore channels 42 - 49 were used to determine weight percent SiO_2. Note channel 50 was not included in the determination, as it would have adversely affected the fitting procedure as discussed in the previous section.

Channel	Central Wavelength (μm)	Emissivity	Min T (C)	Max T (C)	Mean T (C)	Standard Deviation
41	7.766	0.982	1.350	18.190	10.626	3.007
42	8.188	0.983	15.440	18.290	16.779	0.467
43	8.632	0.984	16.190	17.740	16.927	0.279
44	9.087	0.985	15.670	17.230	16.386	0.232
45	9.703	0.987	15.240	17.320	16.270	0.325
46	10.116	0.989	15.270	16.990	16.175	0.297
47	10.635	0.991	15.430	17.100	16.280	0.295
48	11.325	0.990	15.190	17.410	16.345	0.392
49	12.125	0.984	13.370	19.240	16.012	0.958
50	12.888	0.975	9.610	23.680	16.024	1.986

Table 2. Surface kinetic temperature values derived from the MASTER data for the La Reforma Caldera.

3.4.3 Temperature Emissivity Separation

After atmospheric correction, the emissivity information was extracted from channels 42 - 49 using the TES technique [*Gillespie et al.*, 1998]. In the TES technique, the difference between the maximum and minimum beta residual of a given pixel (MMD) is used to determine the unknown minimum emissivity of the pixel using a calibration curve developed from laboratory spectra. The MMD is dependent on the channel placement for a given instrument and therefore a calibration curve was developed specifically for the 8 central MASTER channels (Fig. 8). The initial curve developed for ASTER by *Gillespie et al.* [1998] used 86 laboratory spectra in the ASTER spectral library. Since that time additional samples have been added to the ASTER library. This enabled the regression for the MASTER equations to be developed using 314 spectra. The names of the sample groups used for the regression from the ASTER spectral library are included in Table 3 together with the regression coefficients for ASTER and MASTER. The emissivity data for each pixel were then fitted with a 3-term Gaussian function and the minimum of the Gaussian function used with the appropriate coefficients from Table 1 to determine the weight percent SiO_2. These data were used to produce weight percent SiO_2 maps of the study area.

			Coefficients			
Instrument	**Count**	**Channels**	**a**	**b**	**c**	**r^2**
MASTER	8.00	42-49	0.990	0.757	0.834	0.960
MASTER	10.00	41-50	1.001	0.761	0.812	0.970
ASTER	5.00	10-14	0.994	0.687	0.737	0.983
Equation: Y = a-b*x^c						

Table 3. Regression coefficients used with the TES technique. The coefficients were calculated for MASTER channels 41 - 50 and 42 - 49. The ASTER spectral library datasets used for the regressions were: JHU lunar, JHU igneous-solid, JHU metamorphic-powders (500 - 1500 µm particle size), JHU sedimentary-powders (500 - 1500 µm particle size), JHU soils, JHU vegetation, JHU water, JPL soils, USGS borates, USGS carbonates, USGS chlorides, USGS sulfides, USGS igneous-solid, USGS metamorphic-solid and USGS sedimentary-solid. Values for ASTER taken from Gillespie et al. [1998].

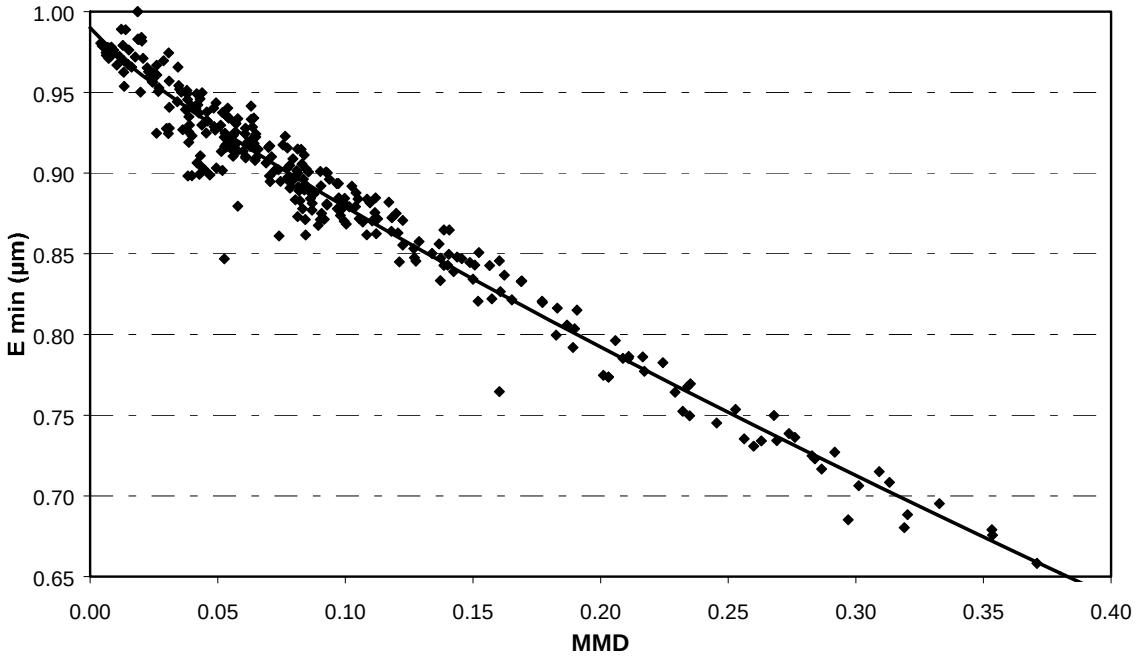

Figure 8. Empirical calibration curve of the difference between the maximum and minimum (MMD) of the beta residuals and the minimum emissivity. The calibration curve was developed using data from the ASTER spectral library.

Images were panoramically corrected after processing and prior to production of the final image. Panoramic correction removes the increasing distortion from the center to the edge of the image associated with the change in pixel size due to increasing scan angle.

3.4.4. Site Calibration

Known weight percent silica values were obtained for 22 surfaces within the MASTER data from the TVLRVR (Fig. 9). Nine of these were derived from samples collected in the field, and the remaining 13 were from published studies from *Demant* [1984] and *Sawlan* [1981]. The average weight percent SiO_2 for a block of pixels ranging from 3X3 to 9X9, centered on each sample site on the image, was then compared to the results from the chemical analysis of the field samples (Table 4). Examination of this table indicates the largest positive difference (field sample minus image) is 18.95 percentage points, and the smallest difference is 2.55 percentage points, with an average error of 9.53 percentage points and a standard deviation of 6.74 percentage points. These fairly large errors can in large part be attributed to the nature of the rocks in the region[13]. Large surface areas within the TVLRVR are covered by ash and ignimbrites. These rock types have flat emissivity spectra, due to their aphyric nature, making the fitting of a Gaussian curve to these spectra difficult. Assigning the surface a weight percent silica, based on these spectra, results in high errors. *Crisp and Bartholomew* [1992] showed that a dusting of 1 - 20 μm palagonite particles and 20 - 250 μm particle clumps, covering just 50% of a

[13] The errors for the other test region (Hiller Mountains, Nevada) discussed by *Hook et al.* [2005] are much smaller. The largest posititive difference is 11 percentage points, and the largest negative difference is 6 percentage points, yielding an average error of 2 percentage points and a standard deviation of 5 percentage points. The Hiller Mountains test region does not contain ash and ignimbritic rocks.

sample of quartzite can reduce its mid-infrared reflectance by 50%. This reduction in reflectance, yielding a flatter emissivity spectrum, seems to be occurring in the rocks in the TVLRVR.

	Weight Percent Silica			
Site	Image	Laboratory/Reported	Std Dev	Difference
dem1079	50.6712	59.69	6.377255	9.0188
dem749	57.87903	72.29	10.19009	14.41097
dem1094	53.95205	65.69	8.299983	11.73795
dem1104	50.79452	55.56	3.369705	4.765482
saw129	50.48733	57.23	4.767789	6.742672
saw131	52.12563	61.5	6.628681	9.374371
saw103	50.11805	52.67	1.804505	2.551955
saw188	55.5849	67.73	8.58788	12.1451
saw186	52.71889	63.98	7.962808	11.26111
saw91	52.69382	64.02	8.008819	11.32618
saw365	52.37133	59.1	4.757887	6.728669
saw88	51.48717	59.51	5.672995	8.022827
saw262	53.91788	66.29	8.748411	12.37212
saw372	53.27332	72.22	13.39733	18.94668
3v9022	50.88296	65.06	10.02468	14.17704
3v9023	50.88996	60.1	6.512483	9.210042
3v9024	50.48733	60.68	7.207307	10.19267
3v9025	50.08474	54.17	2.888716	4.085262
3v9026	51.14858	58.3	5.056817	7.151419
3v9027	55.0775	65.85	7.617311	10.7725
3v9028	49.99357	51.04	0.739936	1.046427
lr030101	52.92376	62.77	6.962343	9.84624
lr030115	57.55043	70.82	9.383003	13.26957

Table 4. Comparison of weight percent silica determined by chemical analysis of field samples and the MASTER data for the La Reforma Caldera. Of the samples only one occurs in the area covered in the images presented (DEM1104). Data from MASTER are averages of 3x3 blocks of pixels centered on the sample location.

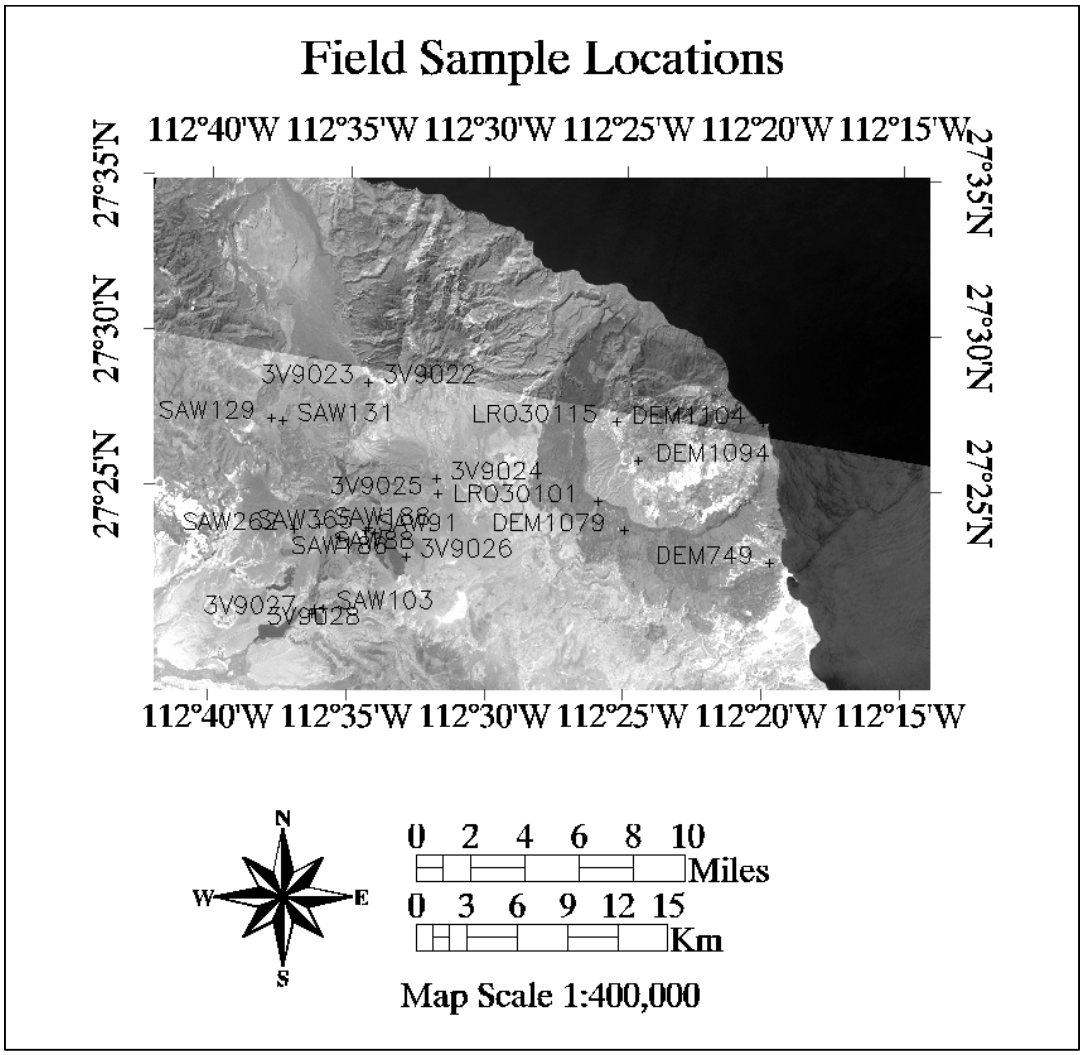

Figure 9. Location map of the field samples collected in this study and that of Sawlan [1981] and Demant [1984].

Figure 10 shows the emissivity spectra[14] of 7 of the 9 samples[15] collected in the TVLRVR (Fig. 9). Figure 11 is shown for comparison. Table 5 shows the weight percent silica values derived from a regression to the image and the laboratory spectra of the samples, and their known weight percent silica values are shown for comparison. From

[14] Laboratory spectra were collected with a Nicolet Fourier Transform Infra-Red (FTIR) interferometer spectrometer at the Jet Propulsion Laboratory.
[15] Two of the field samples were not available for the laboratory spectra collection.

inspection of Table 5, it is clear that the weight percent silica computed directly from the field samples matches the image derived weight percent silica estimates better than the known values. This indicates the under-estimation of the weight percent silica mapping technique is due to the nature of the rocks in this area, not a problem with the MASTER data or the atmospheric correction. The rocks in the TVLRVR do not have the same relationship between weight percent silica and Gaussian minimum as do the rocks in the ASTER library, which were used for determining the weight percent silica-Gaussian minimum relationship. This is likely due to the alteration minerals present in the region as well as the high proportion of ash and ignimbiritic rocks.

Sample	3-term Gaussian Minimum	"A" Known Wt. % Silica	"B" Wt % silica Calculated from regression to laboratory spectrum	"C" Wt % silica Calculated from regression to channels in image	"B" - "A"	"B" - "C"	"A" - "C"
3V9023	9.94813	60.1	53.6280034	50.889958	-6.472	2.7380	9.2100
3V9024a	9.82816	60.68	54.59940712	50.487328	-6.0806	4.1120	10.192
3V9024b	9.85209	60.68	54.40563671	50.487328	-6.2744	3.9183	10.192
3V9025a	9.92437	54.17	53.82037391	50.084738	-0.3496	3.7356	4.0852
3V9025b	10.0059	54.17	53.16062393	50.084738	-1.0094	3.0758	4.0852
3V9026a	9.953	58.3	53.5885547	51.148581	-4.7114	2.4399	7.1514
3V9026b	9.90222	58.3	53.99976326	51.148581	-4.3002	2.8511	7.1514
3V9027a	9.72397	65.85	55.44303279	55.077496	-10.407	0.3655	10.772
3V9027b	9.73588	65.85	55.34667263	55.077496	-10.503	0.2691	10.772
3V9027c	9.7982	65.85	54.84203723	55.077496	-11.008	-0.2355	10.772
3V9028a	9.97561	51.04	53.40551468	49.993573	2.36551	3.4119	1.0464
3V9028b	10.1588	51.04	51.92203889	49.993573	0.88204	1.9284	1.0464
3V9028c	9.97178	51.04	53.43649741	49.993573	2.3965	3.4429	1.0464
LR030101a	9.31086	62.77	58.78806662	52.92376	-3.9819	5.8643	9.8462
LR030101b	9.78419	62.77	54.95544943	52.92376	-7.8146	2.0316	9.8462
				Average =	-4.4846	2.6633	7.1478

Table 5. Comparison of the known weight percent silica for field samples to their weight percent silica calculated from regression to the image and laboratory emissivity spectra.

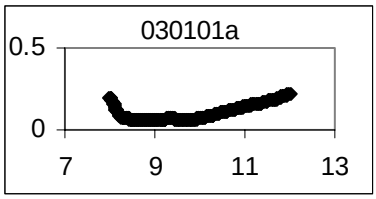
030101a
0.5
0
7
9
11
13

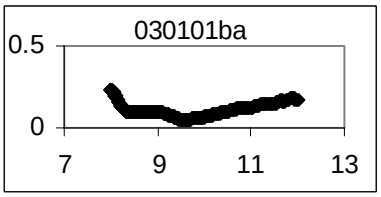
030101ba
0.5
0
7
9
11
13

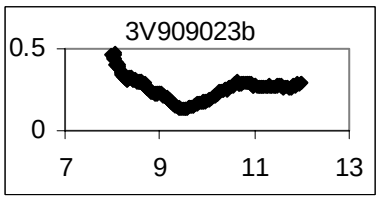
3V909023b
0.5
0
7
9
11
13

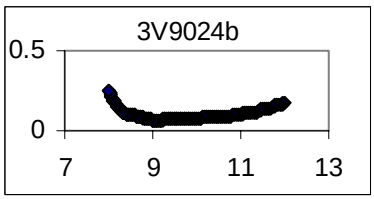
3V9024b
0.5
0
7
9
11
13

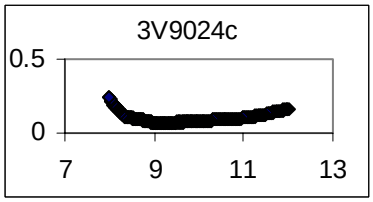
3V9024c
0.5
0
7
9
11
13

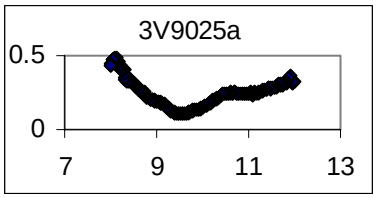
3V9025a
0.5
0
7
9
11
13

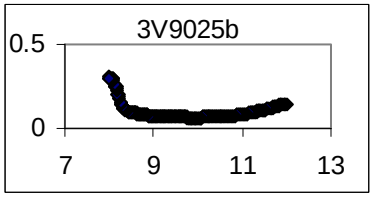
3V9025b
0.5
0
7
9
11
13

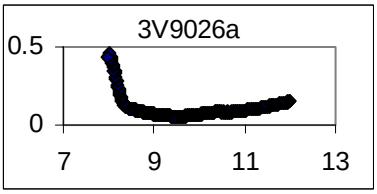
3V9026a
0.5
0
7
9
11
13

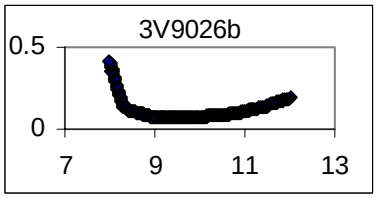
3V9026b
0.5
0
7
9
11
13

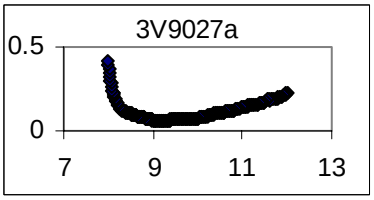
3V9027a
0.5
0
7
9
11
13

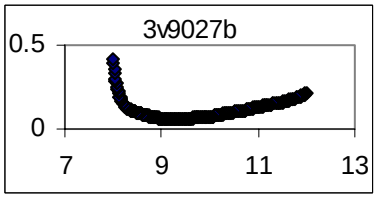
3v9027b
0.5
0
7
9
11
13

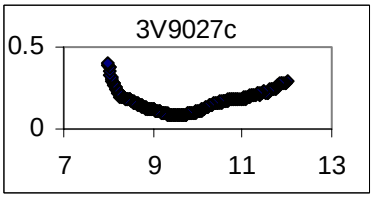
3V9027c
0.5
0
7
9
11
13

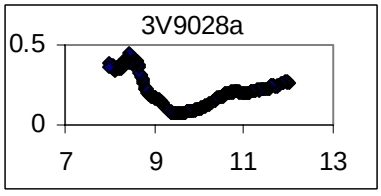
3V9028a
0.5
0
7
9
11
13

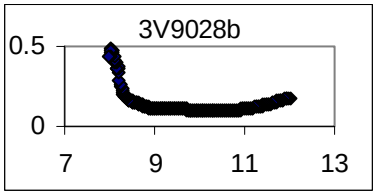
3V9028b
0.5
0
7
9
11
13

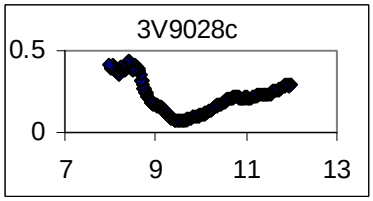
3V9028c
0.5
0
7
9
11
13

Figure 10. (Previous page) Emissivity spectra, from 8 - 12 microns, of 7 field samples. Some of these samples were measured on more than one surface of the sample.

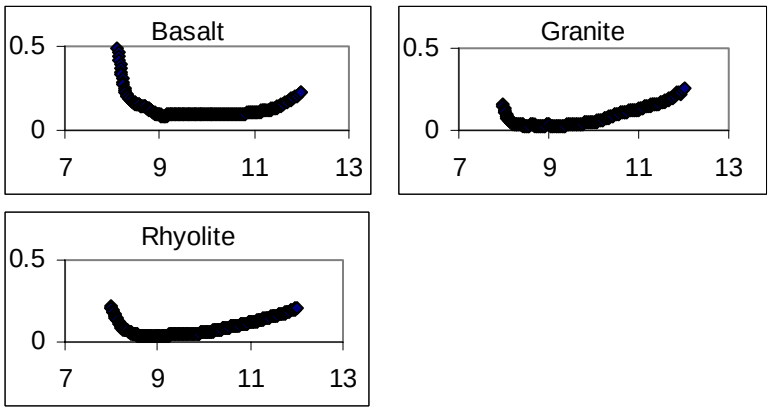

Figure 11. Emissivity spectra, from 8 - 12 microns, of 3 samples from the ASTER spectral library.

In order to correct for the under-determination of weight percent silica for the surfaces in the TVLRVR, a site calibration was employed. Figure 12 shows the regression to the known weight percent silica and the derived weight percent silica for 20 of the 22 field samples available within the TVLRVR map (Fig. 9). A regression was done to the equation $y = mx + b$, where x is the image derived weight percent silica and y is the known weight percent silica. With the coefficients m and b, a site calibration was computed on the data. The effect of the site calibration on the known surfaces is shown in Figure 13. The site calibration is applied to each pixel in the image to better estimate its true weight percent silica. The result for the test region discussed in this chapter is shown in Figure 14.

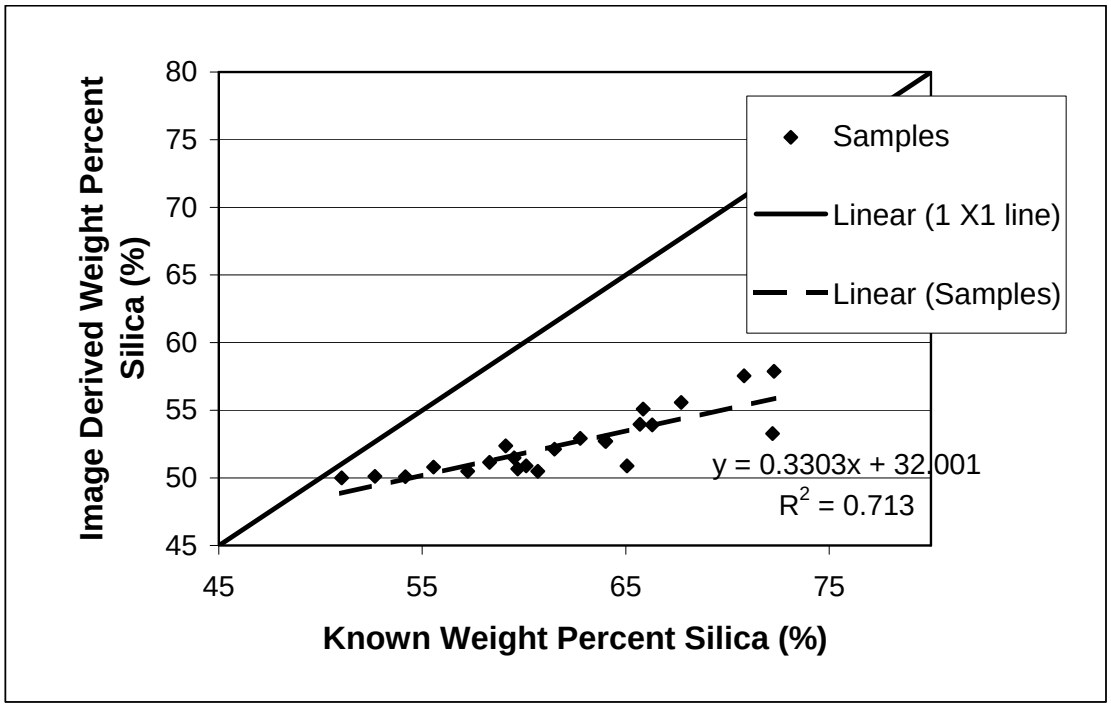

Figure 12. Plot of weight percent silica values derived from the image, before site calibration, versus their known weight percent silica values. The equation on the plot represents the linear regression to the sample points.

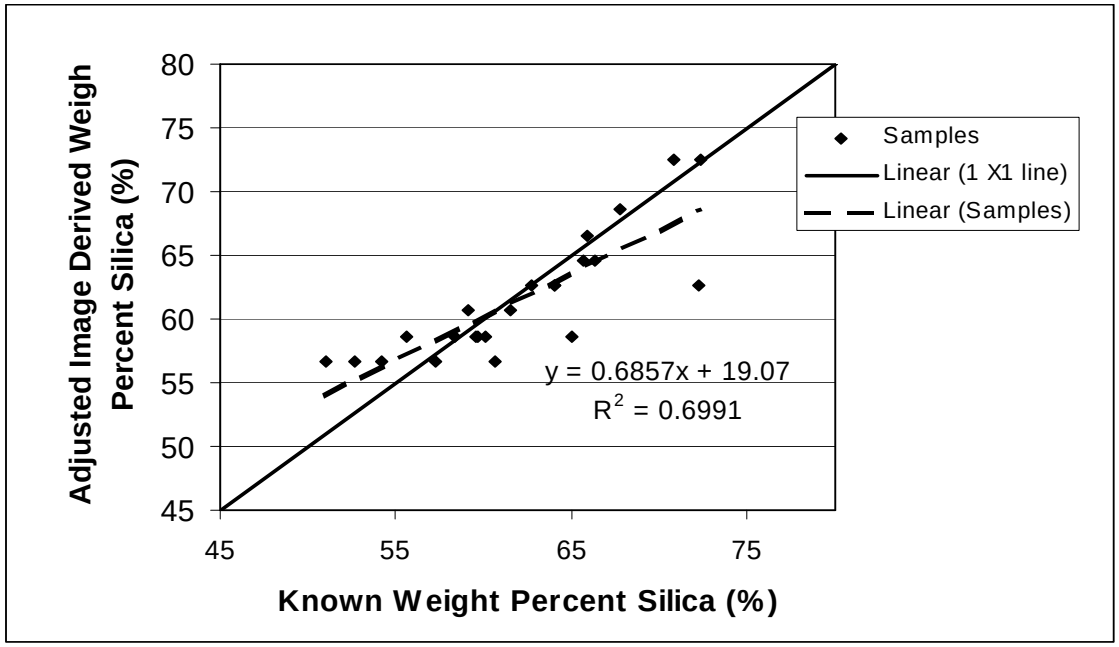

Figure 13. Plot of weight percent silica values derived from the image, after site calibration, versus their known weight percent silica values. The formula for the site calibration is y= mx+c where m = 1.982029 and c = -42.4187. The equation on the plot represents the linear regression to the sample points.

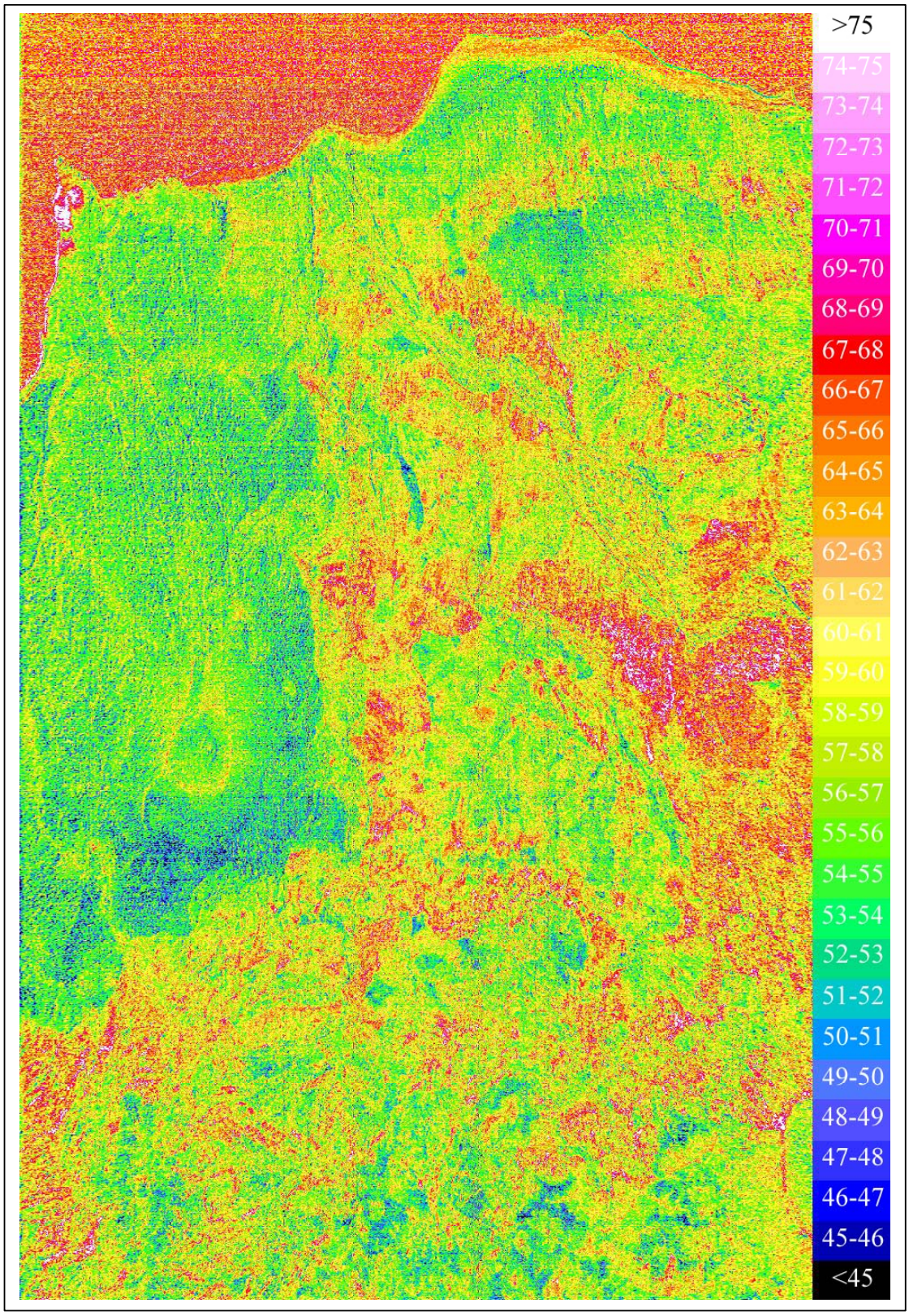

Figure 14. Weight percent silica map of the test region within the eastern half of image 9900302U of the TVLRVR.

3.5 Data Interpretation

Figure 15 shows a decorrelation stretch image of MASTER channels 47, 44 and 43 displayed in red, green and blue respectively. Figure 16 shows a geologic map of the area based on *Schmidt* [1975] and *Demant* [1984], with revisions from field mapping and image analysis. The mapped units can be distinguished in the decorrelation stretch (Fig. 15); however, due to the low altitude acquisition of these data (2 km), tilting and pitching of the aircraft have warped the image considerably. The image shown in Figure 15[16] is an approximately 5km by 3km region (eastern flank) of the La Reforma caldera. Included are a recent scoria cone, a portion of the intracaldera sequence of ash flow tuffs and lavas, and an intrusive diorite porphyry.

[16] The results for the entire Tres Vírgenes-La Reforma region are shown in Plate 2 and discussed in Chapter 4.

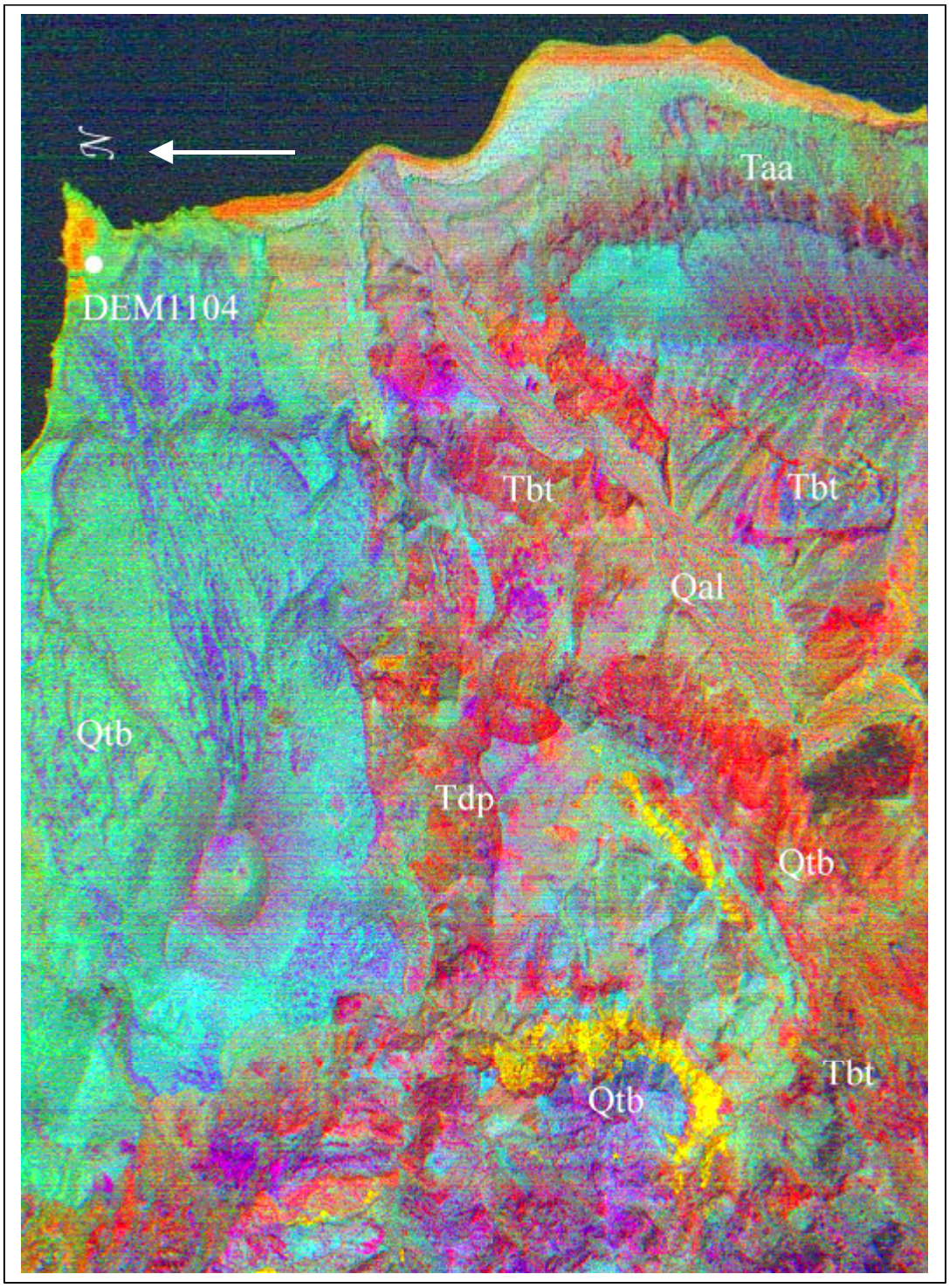

Figure 15. Decorrelation stretch of MASTER channels 47, 44 and 43 displayed in red, green and blue respectively for the La Reforma Caldera study area. Labels are discussed in text.

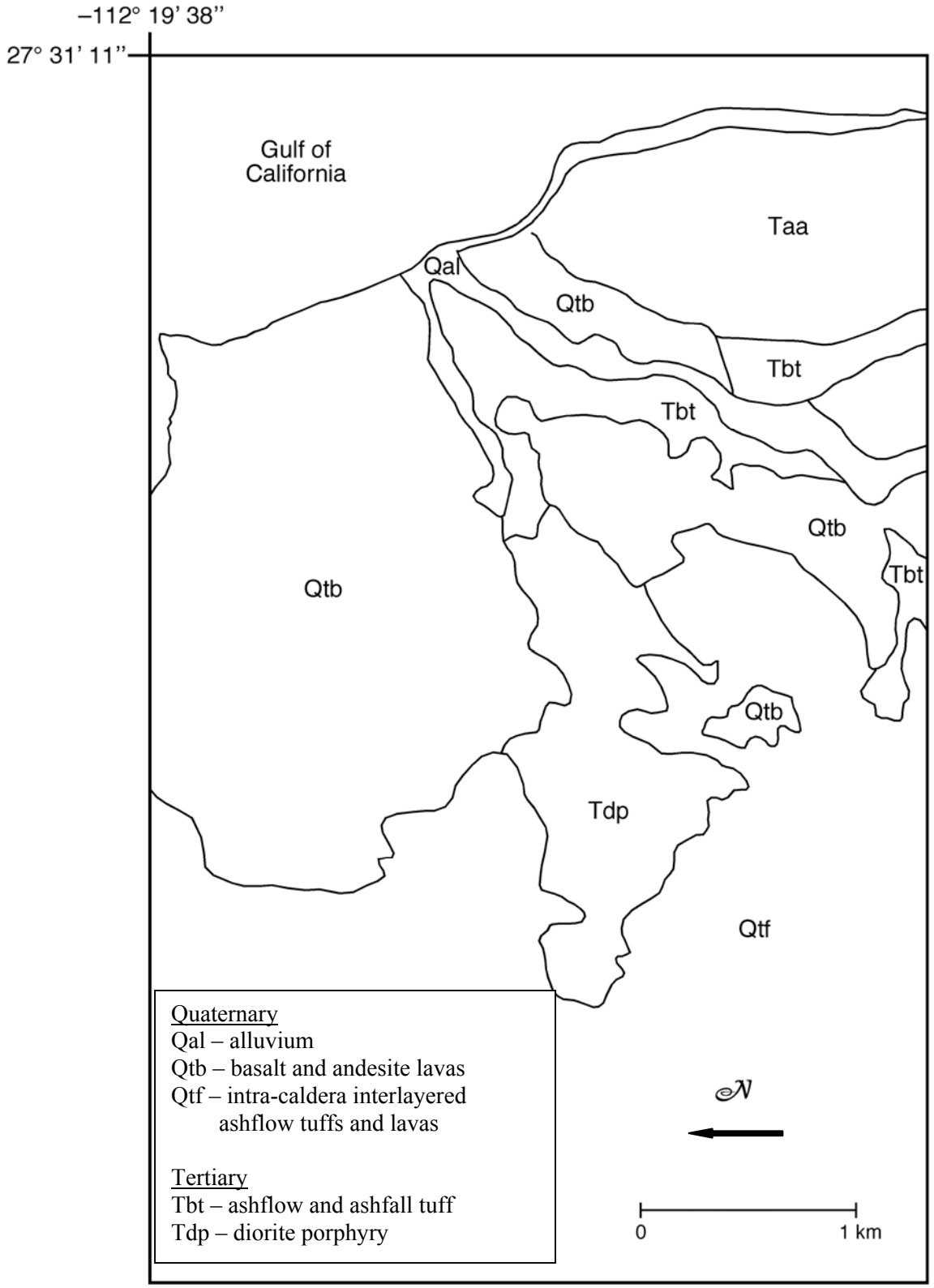

Figure 16. Geological map of the region within the La Reforma caldera, the eastern half of image 9900302U, used for testing of the mapping of weight percent silica technique.

The oldest rocks exposed in Figure 15 are highly weathered diorite porphyritic intrusions of Tertiary age that appear as various colors from orange to purple in the decorrelation stretch image (Tdp, Fig. 15). Due to the high degree of weathering of this unit, the surface composition is fairly diverse, rendering this unit difficult to discriminate in the decorrelation stretch. Also of Tertiary age are the ash flow, ash fall, and pumice fall tuffs associated with the pre-collapse explosive products of the caldera, which appear as orange and green (Tbt, Fig. 15). The intracaldera sequence of interlayered ash flow tuffs and lavas (Qtf) appears pink in the decorrelation stretch. The Quaternary basaltic andesite lavas (Qtb) appear blue and green in Figure 15. However, part of this unit (directly below the Qtb symbol) is bright red in the decorrelation stretch (Fig. 15), and the weight percent silica map (Fig. 14). Previously believed to be of mafic to intermediate composition, this indication of a more silicic composition warrants further investigation and may indicate that additional revisions of the geologic map are necessary. This will be discussed further in Chapter 4. The Quaternary sediments appear reddish-orange along the coastline but are of mixed color within the arroyo, indicating that less weathering and sorting has occurred in this location. The updated geological map is in moderate agreement with the images, but Figure 15 highlights some mineralogical differences.

The map patterns reveal highly variable weathered diorite porphyry, ash flow tuffs and lavas to the west (in the center of the caldera) and more recent basaltic-andesite lavas to the east, on the flank of the caldera. This supports the theory by *Demant* [1984] that the rising mafic magmas, associated with the current tectonics of continental extension in the

area, are blocked from rising in the interior of the caldera due to a molten, shallow reservoir beneath the caldera. Thus, the recent basaltic-andesite lavas only erupt on the caldera's flanks. A similar scoria cone to the one shown in Figure 15 is found on the southeastern flank of the caldera as well.

3.6 Summary and Conclusions

Multispectral Thermal Infrared Images were acquired from Tres Vírgenes-La Reforma, Baja California Sur, Mexico. These data were used to test a new technique for remotely estimating the weight percent SiO_2 of silicate rocks exposed on the surface. The technique uses laboratory emissivity data from widely available spectral libraries to develop a relationship between the known shift in the Reststrahlen band to longer wavelengths and decreasing weight percent SiO_2. This relationship is then applied to the emissivity data extracted from the images. The relationship is shown to depend on how well the emissivity data encompass the Reststrahlen band. Different relationships were developed for various channel combinations as well as instruments. The channel combinations were selected to include the wavelength region that can be readily corrected for atmospheric effects typically encountered with airborne and spaceborne terrestrial thermal infrared data.

The results indicate that, using the relationship developed from the library data, the image derived weight percent SiO_2, on average, agrees with the field samples only to about 7 %. The library relationship tends to underestimate weight percent silica values. This

difference can be attributed to the flattened emissivity spectra from TVLRVR, and it can be corrected based on the availability of a few field samples from the study region. With the site calibration, the image derived weight percent SiO_2, on average, agrees with the field samples to about 3%.

Examination of the weight percent silica map (Fig. 14) suggests the intracaldera products are highly varied products of mafic to silicic eruptions. The more recent volcanic products on the flanks of the caldera are of mafic to intermediate composition. It is likely, however, that a portion of the mapped unit Qtb, Quaternary basaltic-andesite lavas, is more silicic than previously described by *Schmidt* [1975] and *Demant* [1984].

References

Abrams, M.J., E.A. Abbott, and A.B. Kahle, Combined use of visible, reflected infrared and thermal infrared images for mapping Hawaiian lava flows, *Journal of Geophysical Research*, *96*, 475-484, 1991.

Berk, A., L.S. Bernstein, G.P. Anderson, P.K. Acharya, D.C. Robertson, J.H. Chetwynd, and S.M. Adler-Golden, MODTRAN cloud and multiple scattering upgrades with application to AVIRIS, *Remote Sensing of Environment*, *65* (3), 367-375, 1998.

Berk, A., L.S. Bernstein, and D.C. Robertson, MODTRAN: A Moderate Resolution Model for LOWTRAN 7, Air Force Geophysics Laboratory, Bedford, Mass, 1989.

Clark, R.N., *Remote Sensing for the Earth Sciences: Manual of Remote Sensing*, John Wiley & Sons, Inc., 1999.

Clark, R.N., G.A. Swayze, A.J. Gallagher, and F.A. Kruse, Mapping with imaging specrometer data using the complete band shape least-squares fit to multiple spectral features from multiple materials, in *Third AVIRIS Workshop*, pp. 2-3, JPL, Pasadena, CA, 1991.

Colletta, B., and J. Angelier, Faulting evolution of the Santa Rosalia Basin, Baja California, Mexico, in *Geology of Northwestern Mexico and Southern Arizona*, edited by L. Ortlieb, and J. Roldan-Quintana, pp. 265-274, Estacion Regional del Noroeste, Instituto de Geologia, U.N.A.M., Hermosillo, Sonora, Mexico, 1981.

Crisp, J., and M.J. Bartholomew, Mid-Infrared Spectroscopy of Pahala Ash Palagonite and Implications for Remote Sensing, *Journal of Geophysical Research*, *97* (E9), 14,691-14,699, 1992.

Crowley, J.K., Mapping Playa Evaporite Minerals with Aviris Data - a 1st Report from Death-Valley, California, *Remote Sensing of Environment*, *44* (2-3), 337-356, 1993.

Cudahy, T.J., L.B. Whitbourn, P.M. Conner, P. Mason, and R.N. Phillips, Mapping surface mineralogy and scattering behavior using backscattered reflectance from a hyperspectral midinfrared airborne CO_2 laser system (MIRACO(2)LAS), *IEEE Transactions on Geoscience and Remote Sensing*, *37*, 2019-2034, 1999.

Demant, A., Plio-Quaternary volcanism of the Santa Rosalia area, Baja California, Mexico, in *Geology of Northwestern Mexico and Southern Arizona, Field Guides and papers*, edited by L. Ortlieb, and J. Roldan, pp. 295-307, 1981.

Demant, A., The Reforma Caldera, Santa Rosalia Area, Baja California, A volcanological, petrographical and mineralogical study, in *Neotectonics and sea level variations in the Gulf of California area, a Symposium*, edited by V. Malpica-Cruz, S. Celis-Gutiérrez, J. Guerrero-Garcia, and L. Ortlieb, pp. 77-96, Univ. Nal. Auton, México, Inst. Geologia, México, D. F., 1984.

Gillespie, A., Lithologic mapping of silicate rocks using TIMS, *Proceedings of the TIMS Data User's Workshop, JPL Publications*, *86-38*, 29-44, 1986.

Gillespie, A.R., A.B. Kahle, and R. Walker, Color enhancement of highly correlated images: Decorrelation and HSI Contrast Stretches, *Remote Sensing of Environment*, *20*, 209-235, 1986.

Gillespie, A.R., S. Rokugawa, T. Matsunaga, S.J. Cothern, S.J. Hook, and A.B. Kahle, A temperature and emissivity separation algorithm for advanced spaceborne thermal emission and reflection radiometer (ASTER) images, *IEEE Transactions on Geoscience and Remote Sensing*, *36* (4), 1113-1126, 1998.

Goetz, A.F.H., Spectroscopic remote sensing for geological applications, *Proceedings of the Society of Photo-Optical Instrumentation Engineers (SPIE)*, *M*, 77-21, 1981.

Goetz, A.F.H., G. Vane, J.E. Solomon, and B.N. Rock, Imaging Spectrometry for Earth Remote Sensing, *Science*, *228* (4704), 1147-1153, 1985.

Guerrero-Guadarrama, J.L., Actividad Sísmica del Campo Geotérmico de Las Tres Vírgenes, *Geotermia*, *14*,, 87-100, 1998.

Hausback, Brian P, J.M. Stock, J.E. Dmochowski, C.D. Farrar, S.J. Fowler, K. Sutter, P. Verke, and C. Winant, To be or not to be a caldera - La Reforma caldera, Baja California Sur, Mexico, in *Geological Society of America*, pp. A502, 2000.

Hook, S.J., J.E. Dmochowski, K.A. Howard, L.C. Rowan, K.E. Karlstrom, and J.M. Stock, Mapping variations in weight percent silica measured from multispectral thermal infrared imagery—Examples from the Hiller Mountains, Nevada, USA and Tres Vírgenes-La Reforma, Baja California, Baja California Sur, Mexico, *Remote Sensing of Environment*, *95*, 273-289, 2005.

Hook, S.J., K.E. Karlstrom, C.F. Miller, and K.J.W. Mc Caffrey, Mapping the Piute Mountains, CA with Thermal Infrared Multispectral Scanner (TIMS) Data, *Journal of Geophysical Research*, *99*, 15,605-15,622, 1994.

Hook, S.J., J.J. Myers, K.J. Thome, M. Fitzgerald, and A.B. Kahle, The MODIS/ASTER airborne simulator (MASTER) — a new instrument for earth science studies, *Remote Sensing of Environment*, *76*, 93-102, 2001.

Hunt, G.R., Electromagnetic radiation: The communication link in remote sensing, in *Remote Sensing in Geology*, edited by B.S. Siegal, and A.R. Gillespie, pp. 5-45, John Wiley, New York, 1980.

Lahren, M.M., R.A. Schweickert, and J.V. Taranik, Analysis of the northern Sierra accreted terrain, California, with airborne thermal infrared multispectral scanner data, *Geology*, *16*, 525-528, 1988.

Mammerickx, J., and K.D. Klitgord, Northern East Pacific Rise - Evolution from 25 My Bp to the Present, *Journal of Geophysical Research*, *87* (NB8), 6751-6759, 1982.

Sabine, C., V.J. Realmuto, and J.V. Taranik, Quantitative estimation of granitoid composition from thermal infrared multispectral scanner (TIMS) data, Desolation Wilderness, northern Sierra Nevada, California, *Journal of Geophysical Research*, *99*, 4,261-4,271, 1994.

Sawlan, M.G., Late Cenozoic Volcanism in the Tres Vírgenes Area, in *GSA Cordilleran Section*, edited by L. Ortlieb, and J. Roldan-Quintana, pp. 309-319, U.N.A.M. Institue Geol., Estacion Regional del Noroeste, Hermosillo, Mexico, 1981.

Sawlan, M.G., Petrogenesis of Late Cenozoic Volcanic Rocks from Baja California Sur, Mexico, Ph.D. thesis, University of California, Santa Cruz, Santa Cruz, 1986.

Sawlan, M.G., and J.G. Smith, Late Cenozoic volcanic suites in northern Baja California Sur, Mexico; their relations to subduction and rifting along the Baja California peninsula, *Geological Society of America Abstracts with Programs*, *16*, 645, 1984.

Schmidt, E.K., Plate tectonics, volcanic petrology, and ore formation in the Santa Rosalia Area, Baja California, Mexico, Master of Science thesis, The University of Arizona, pp. 194, 1975.

Walker, G.P., Z. Jurado, S. Rowland, and A. Carrillo, La Reforma cryptodome: an alternative mechanism to caldera subsidence and resurgent doming, in *29th International Geological Congress Meeting*, pp. 481, Kyoto, Japan, 1992.

Watson, K., L.C. Rowan, T.L. Bowers, C. Anton-Pacheco, P. Gumiel, and S.H. Hiller, Lithologic analysis from multispectral thermal infrared data of the alkalic rock complex at Iron Hill, Colorado, *Geophysics*, *61* (706-721), 1996.

Chapter 4: Revisions to the Geology of the Tres Vírgenes-La Reforma Region

Abstract

Several images were constructed in order to summarize and revise previous geologic mapping done in the Tres Vírgenes-La Reforma Volcanic Region (TVLRVR). These images included a classification of atmospherically corrected MASTER multi-channel VNIR-SWIR data, a weight percent silica map, a mosaicked ASTER image, and a Thematic Mapper image draped over a digital elevation model. These images help to better delineate previously mapped units and revise erroneously mapped regions. One major revision is the composition of La Reforma's resurgent dome, which was previously interpreted as Miocene Comondú Volcanics, but is now designated as younger welded ash-flow tuffs and lavas. This new understanding of the central region of La Reforma is more conclusive evidence of its origin as a caldera. The La Reforma caldera and the El Aguajito volcanic complex appear to be bi-modal volcanic centers, and the Tres Vírgenes volcanoes are calc-alkaline, well-differentiated, volcanoes.

4.1 Introduction

Chapter 4 will first introduce the main volcanic edifices of the Tres Vírgenes-La Reforma Volcanic Region (TVLRVR): La Reforma caldera, El Aguajito volcanic complex, and the Tres Vírgenes volcanoes. A description of the new work used to update the knowledge of the region will then be discussed. This work includes a classification of atmospherically corrected MASTER data (channels 1 - 25) (Plate 1), to distinguish the secondary minerals of the surfaces within the TVLVR, as discussed in Chapter 2; a

weight percent silica map (Plate 2) based on atmospherically corrected MASTER data (channels 41 - 50), as discussed in Chapter 3; a mosaic of two ASTER images (Tres Vírgenes and El Aguajito complexes, Fig. 1; La Reforma, Fig. 2); and a Thematic Mapper image draped over a digital elevation model (Tres Vírgenes and El Aguajito complexes, Fig. 3; La Reforma, Fig. 4). Findings from fieldwork in the region will also be presented. Lastly, this chapter makes revisions to the current understanding of the geology of the TVLRVR.

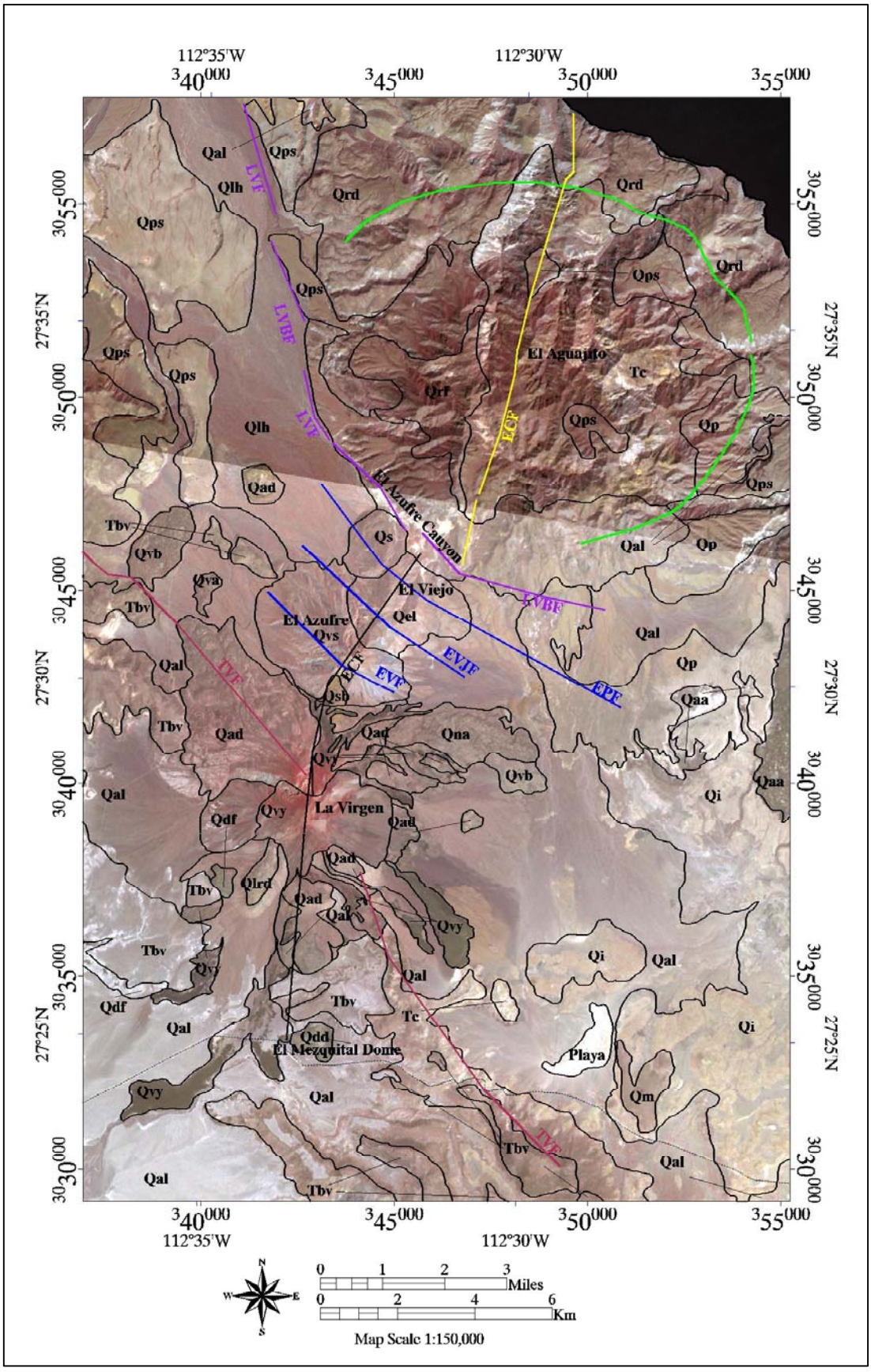
112°35'W
112°30'W
340000
345000
350000
355000
27°35'N
27°30'N
27°25'N
305000
304500
304000
303500
303000
Qal
Qps
Qlh
Qrd
Qad
Qvb
Qva
Qel
Qvs
Qsb
Qna
Qvy
Qdf
Qlrd
Qdd
Qs
Qp
Qaa
Qi
Qm
Tbv
Tc
El Aguajito
El Azufre Canyon
El Viejo
El Azufre
La Virgen
El Mezquital Dome
Playa
LVF
LVBF
ECF
EVF
EVJF
EPF
ITVF
0 1 2 3 Miles
0 2 4 6 Km
Map Scale 1:150,000

Figure 1. (Previous page) Geologic units and faults on top of a mosaic of two ASTER images (Red: band 3, Green: band 2, Blue: band 1). The colored lines represent the following: black, faults of unspecified slip; green, ring fractures; blue, normal faults with the hanging wall to the NE; yellow, normal faults with the hanging wall to the W, with overprinting of dextral motion; purple, normal faults with the hanging wall to the SW, with overprinting of dextral motion; magenta, dextral strike-slip faults. The dotted line is the Transpeninsular Highway. Geologic unit abbreviations are described in Table 1. Map datum and projection: NAD27 Mexico, UTM zone 12.

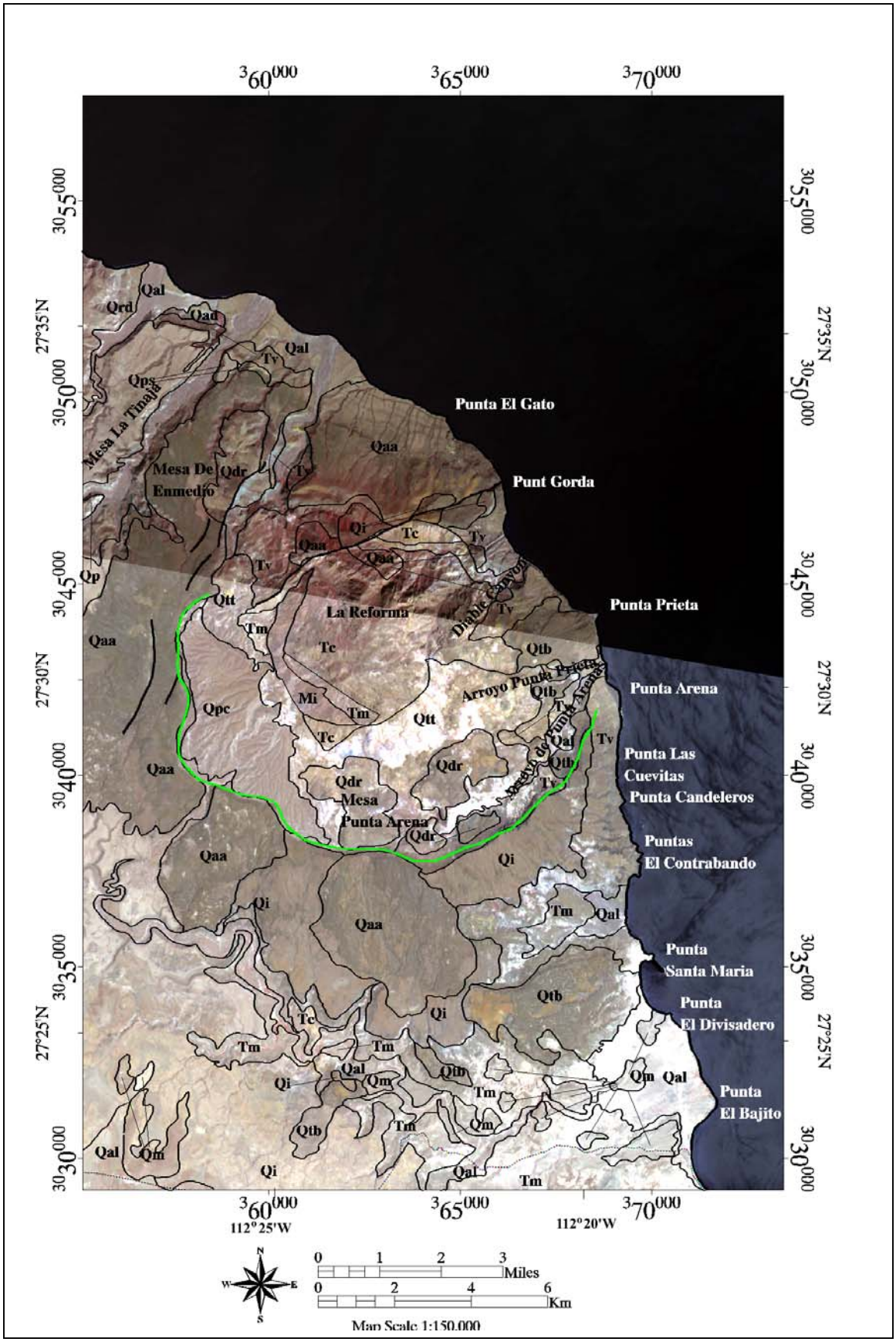
360000
365000
370000
3055000
3050000
3045000
3040000
3035000
3030000
27°35'N
27°30'N
27°25'N
112°25'W
112°20'W
Punta El Gato
Punt Gorda
Punta Prieta
Punta Arena
Punta Las Cuevitas
Punta Candeleros
Puntas El Contrabando
Punta Santa Maria
Punta El Divisadero
Punta El Bajito
Mesa La Tinaja
Mesa De Enmedio
La Reforma
Diablo Canyon
Arroyo Punta Prieta
Arroyo de Punta Arena
Mesa Punta Arena
Qal
Qrd
Qad
Tv
Qps
Qaa
Qdr
Qi
Tc
Qp
Qtt
Tm
Qpc
Mi
Qtb
Qm
0 1 2 3 Miles
0 2 4 6 Km
Map Scale 1:150,000

Figure 2. (Previous page) Geologic units and faults on top of a mosaic of two ASTER images (Red: band 3, Green: band 2, Blue: band 1). Line symbology is the same as in Figure 1. Geologic unit abbreviations are described in Table 1. Map datum and projection: NAD27 Mexico, UTM zone 12.

Figure 3. A Thematic Mapper image (Red: band 7, Green: band 4, Blue: band 1) of the La Reforma caldera, draped over a USGS 90 meter digital elevation model. Map datum and projection: NAD27 Mexico, UTM zone 12.

Figure 4. A Thematic Mapper image (Red: band 7, Green: band 4, Blue: band 1) of the Tres Vírgenes region, draped over a USGS 90 meter digital elevation model. Map datum and projection: NAD27 Mexico, UTM zone 12.

4.2 Geologic Background

4.2.1 Introduction

The TVLRVR is near the east coast of Baja California, Mexico at 27.5˚N (Fig. 5). This region lies on the western edge of the Gulf of California, which formed as a result of continental rifting and the transfer of crust from the North America plate to the Pacific plate. Responsible for forming the Comondú Volcanics to the south and west of this

region, subduction in the TVLRVR ceased approximately 12.5 - 11 Ma [*Mammerickx and Klitgord*, 1982]. The Comondú Volcanics, which are part of the Comondú Formation, as well as the Santa Lucia Volcanics, discussed later in this chapter, are thought to be the products of a caldera designated the Santa Rosalia Caldera by *Hernández* [1998], which was active 24 Ma to 13 Ma. Extension of the Gulf of California likely started some time after 12 Ma [*Gastil*, 1979].

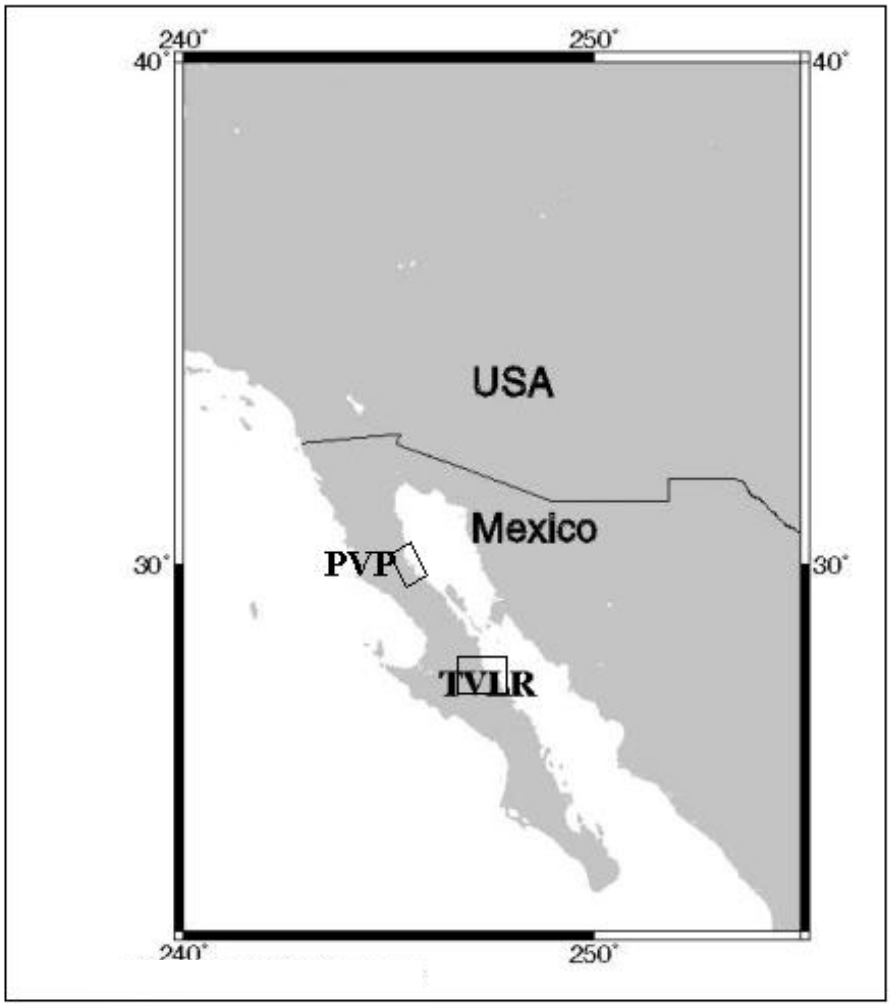

Figure 5. Map of Baja California and the Southwestern United States showing the location of the TVLRVR (labeled TVLR). The Puertecitos Volcanic Province is shown as PVP.

The TVLRVR, including three volcanic systems - La Reforma caldera to the east, El Aguajito volcanic complex to the north, and the Tres Vírgenes volcanoes to the southwest - is seismically active [*Guerrero-Guadarrama*, 1998; *Wong et al.*, 2001 and *Garduño-Monroy et al.*, 1993] and has active fumaroles [*Hernández*, 1998]. Previous geologic mapping in the region, based on *Demant* [1984], *Garduño-Monroy et al.* [1993], *Hernández* [1998], *Romero-Rojas et al.* [1997], *Schmidt* [1975], *Vargas-Ledezma and*

Garduño-Monroy [1988], and *Wong et al.* [2001], is summarized in Figures 1 and 2. The geologic units in these images are described in Table 1.

Geologic Units: A compilation of all previous mapping		
	Qal	Recent Alluvium
Tres Virgenes	Qlh	Santa Ana laharic sequence
	Qs	Satellite vent lava and domes
	Qna	Northeast vent andesite
	Qvy	Recent basaltic-andesitic lava
	Qbc	Basaltic cinders
	Qsb	El Azufre basalt
	Qdd	Dacitic El Mezquital dome
	Qlrd	Rhyodacitic dome
	Qdf	Dacitic lava
	Qad	Early andesitic to dacitic lava
	Qvb	Early basaltic lava
	Qvs	El Azufre dacite and andesite
	Qel	Dacitic deposits of El Viejo
El Aguajito	Qp	Pyroclastic flow deposits
	Qrd	Rhyolite domes
	Qrf	Rhyodacite lava
	Qps	Pyroclastic flow and marine sand deposits
La Reforma	Qtb	Basaltic to andesitic lava
	Qpc	Conglomerate
	Qdr	Dacitic and rhyolitic domes
	Qtt	Intracaldera non-welded tuffs
	Qaa	Andesitic lava
	Qi	Ignimbrite outflow sheets
Pre-TVLRVR	Qm	Quaternary marine sedimentary rocks of the Santa Rosalia Formation
	Qf	Quaternary fluvial sedimentary rocks of the Santa Rosalia Formation
	Tv	Pliocene and Pleistocene volcanic rocks (submarine and subaerial)
	Tm	Pliocene marine sedimentary rocks of the Boleo, Gloria and Infierno Formations
	Tbv	Upper Miocene mafic volcanic rocks, Basalt of La Esperanza
	Tc	Miocene Comondu Formation and the andesite of Sierra Santa Lucia
	Mi	Cretaceous batholithic rocks

Table 1. Description of the geologic units referred to in Figures 1 and 2.

The first geological map of the Santa Rosalia region, which focused on the Pliocene sedimentary rocks in the region, was presented by *Wilson* [1948]. A master's thesis describing the La Reforma region as a system of tectonic blocks was completed by *Schmidt* [1975]. *Angelier et al.* [1981] and *Colletta and Angelier* [1981] described the faulting evolution of the Santa Rosalia basin, and the marine terraces in this region were

studied by *Ortlieb* [1981]. *Sawlan* [1981a; 1995] described the late Cenozoic volcanism of the Tres Vírgenes volcanoes. *Demant* [1984] and *Demant and Ortlieb* [1981] presented volcanological, petrological and mineralogical studies of the La Reforma region. The Mexican Federal Electric Commission put forth a study on the geological and geothermal studies of the El Aguajito volcanic complex [*Vargas-Ledezma and Garduño-Monroy*, 1988]. A preliminary report of the geology of the El Aguajito caldera[17] was presented by *Garduño-Monroy et al.* [1993]. The Mexican Secretary of Commercial and Industrial Promotion (SECOFI) published a geologic map of the Santa Rosalia region. The Plinian eruptions of the La Virgen volcano were described in a paper by *Capra et al.* [1998]. A synthesis of the geology of Las Tres Vírgenes, including results from drilling, was presented by *Hernández* [1998]. The sedimentology and stratigraphy of the sedimentary sequences within the Santa Rosalia basin, particularly the Upper Miocene Boleo Formation, were presented by *Ochoa-Landin et al.* [2000]. Local seismic events were studied by *Wong et al.* [2001] in an attempt to determine the attenuation quality factor.

Cretaceous granitic rocks form the basement of the Santa Rosalia Basin and the TVLRVR, as evidenced by several outcrops within the volcanic centers [*Sawlan*, 1981b and *Schmidt*, 1975]. These volcanic centers are in the middle of a zone of extensional deformation [*Angelier et al.*, 1981; *Colletta and Angelier*, 1981]. As a result of tensional stress since the late Miocene, NW-SE faults were generated and the Santa Rosalia basin was formed [*Angelier et al.*, 1981; *Colletta and Angelier*, 1981; *Hernández*, 1998]. This

[17] The El Aguajito volcanic complex is also referred to as Sierra Santa Ana and the Santa Ana Caldera.

began the deposition of marine sediments [*Ochoa-Landin et al.*, 2000], which underlie the volcanic rocks of the TVLRVR.

By measuring the striae on 600 fault planes to determine the 3 principal tectonic stresses in the Santa Rosalia Basin, *Colletta and Angelier* [1981] describe the faulting history of the Santa Rosalia Basin in six stages: 1. A mid-late Miocene NE-SW to EW extensional regime. 2. An Upper Miocene continued extensional regime that resulted in the deposition of the Boleo Formation. 3. A late Miocene to early Pliocene strike-slip regime in which NNW-SSE normal faults were reactivated as dextral faults. 4. A 4 to 2 Ma E-W extensional regime. 5. A recent (date undetermined) WNW-ESE extensional regime. 6. Quaternary uplift, as determined by *Ortlieb* [1981]. By examination of faults in El Azufre canyon within the TVLRVR, *Umhoefer and Teyssier* [1991] determined that in Pleistocene time, the stress regime within the TVLRVR changed from being an extensional regime to a trans-tensional system, and old normal faults were reactivated as lateral faults. A schematic of this trans-tensional system is shown in Figure 6.

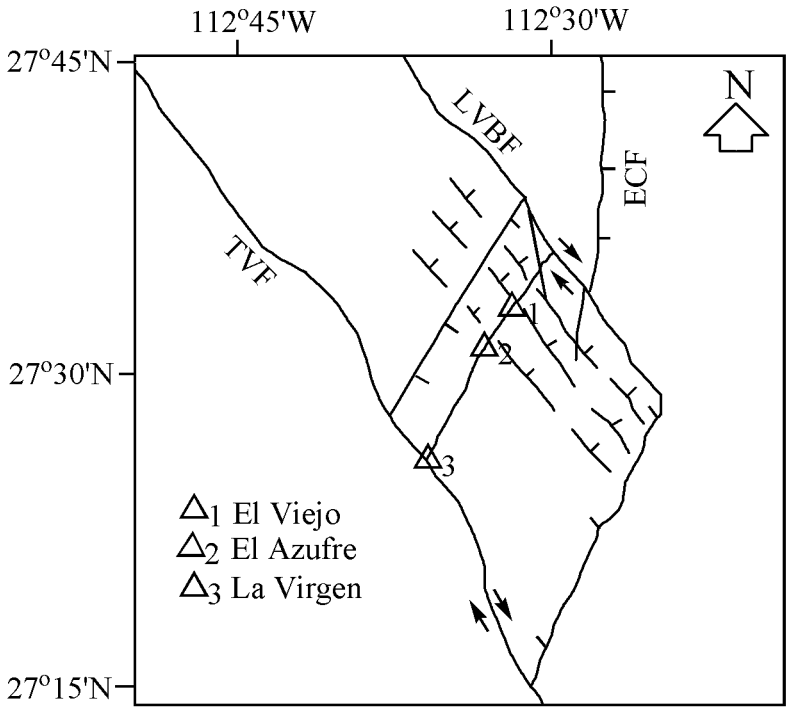

Figure 6. Schematic of the faulting regime in the TVLRVR, modified from Hernández [1998]. The faults are labeled as follows: TVF = Tres Vírgenes Fault; ECF = El Cimarron Fault; and LBVF = Las Víboras Fault.

The products of the Tres Vírgenes volcanoes have the major and trace element characteristics of typical calc-alkaline arc lavas [*Sawlan*, 1986]. Within the La Reforma caldera, there are two distinct groups of volcanic products, as described by *Demant* [1984]: a mafic group, with 56 – 60 weight percent silica and a more silicic group, with 66 – 70 weight percent silica. The rhyolitic ignimbrites within the silicic group have a peralkaline affinity [*Sawlan*, 1981b and *Demant*, 1984], while the other rhyolitic deposits have a calc-alkaline affinity [*Demant*, 1984]. The more mafic deposits within the andesitic group are calc-alkaline. The most recent mafic deposits, not defined within the two groups above, were described as having a tholeiitic affinity by *Schmidt* [1975], but *Demant* [1984] described them as being near the border of the calc-alkaline and alkaline fields of *Leterrier et al.* [1982].

4.2.2 La Reforma

La Reforma is thought to be the oldest volcanic edifice in the TVLRVR. The La Reforma volcanic complex has been dated ca. 1.09 Ma [*Schmidt*, 1975]. However, the geologic history of the complex has received differing explanations [*Demant*, 1984; *Schmidt*, 1975; *Walker et al.*, 1992]. La Reforma has typical caldera morphology, with a ring escarpment (shown in green in Figs. 1 and 2) approximately 10 km in diameter and a central block (surrounded by associated silicic domes) that stands 700 m above the caldera margins. Pyroclastic and lava outflow sheets flank the rim of the caldera and can be seen in the deep canyon walls (Qi, Figs. 1 and 2). *Demant* [1984] and *Demant and Ortlieb* [1981] interpreted the central dome of La Reforma to be a block of Miocene Comondú Formation (Tc, Fig. 2) uplifted by piston-like movement. This contrasts with the interpretations by *Schmidt* [1975], who described the feature not as a caldera, but as a system of tectonic blocks, and *Walker et al.* [1992], who described the complex as an updomed structure that has been circularly eroded.

The pre-caldera basement of La Reforma (Mi, Figs. 1 and 2) which crops out to the southwest of La Reforma's central dome [*Wilson*, 1948] was dated by K/Ar at 91.2± 2 Ma [*Schmidt*, 1975]. This unit was part of the Cretaceous batholith of northern Baja California [*Gastil et al.*, 1975]. *Schmidt* [1975] described these rocks as biotite quartz monzonite, but more recent reports identified the basement as hornblende and biotite tonalite [*Garduño-Monroy et al.*, 1993]. Overlying the basement rocks in the region of the La Reforma caldera are Miocene andesitic to dacitic lavas (Tc, Figs. 1 and 2), which

are interbedded with pyroclastic flow deposits and breccias. These were identified as the Comondú Volcanics by *Schmidt* [1975] and are part of the Comondú Formation, first described by *Heim* [1922].

Stratigraphically above these andesite and dacite Upper Miocene rocks are the Pliocene marine sedimentary rocks of the Boleo, Gloria, and Infierno Formations (mapped together as Tm, Fig. 2). These are subdivided from oldest to most recent as follows:

1. Boleo Formation (Upper Miocene): This is a conglomerate grading to gypsum facies that includes interbedded tuffaceous, clayey sandstones [*Colletta and Angelier*, 1981; *Ochoa-Landin et al.*, 2000; *Wilson*, 1948]. In order to determine the onset of marine sedimentation evidenced by the marine Boleo Formation, a single Ar/Ar isotopic age of 6.76 ± 0.90 Ma was obtained on a tephra deposit of reversed magnetic polarity within the Boleo Formation [*Holt et al.*, 2000]. *Holt et al.* [2000] used this isotopic age to calibrate a magnetostratigraphic study of the Boleo Formation and determined ages of 6.93 - 7.09 Ma and 6.14 - 6.27 Ma for the oldest and most recent members, respectively.

2. Gloria Formation (Lower to Middle Pliocene): This formation includes conglomeratic and sandy units with yellowish sandstones, clays, and tuffaceous layers [*Colletta and Angelier*, 1981; *Ochoa-Landin et al.*, 2000; *Wilson*, 1948].

3. Infierno Formation (Upper Pliocene): This formation includes conglomerates and sandstones, with some tuffaceous layers [*Colletta and Angelier*, 1981; *Ochoa-Landin et al.*, 2000 and *Wilson*, 1948].

The early volcanic deposits (Tv, Fig. 2) of the La Reforma caldera interfinger with the submarine and subaerial sedimentary rocks mentioned above. At times during deposition, the environment was submarine, as evidenced by pillow basalts, palagonitic tuff rings, and the presence of pecten-bearing layers interbedded with the volcanic deposits [*Demant*, 1984; *Demant and Ortlieb*, 1981]. The earliest of these volcanic rocks (Tv, Fig. 2) was assigned an age of 4 - 5 Ma by *Demant* [1984] by correlating the Pliocene rocks of the La Reforma region and the dated Gloria Formation in the Santa Rosalia area.

The palagonitic tuff rings and submarine lavas in Arroyo de Punta Arenas (Fig. 2) are conformably overlain by subaerial lavas, indicating the sedimentary environment was alternating between subaerial and submarine during this time. *Schmidt* [1975] identified the submarine volcanic rocks as the Reforma andesite lavas, which are overlain by the Punta Arena andesite lavas and dikes (mapped together in Fig. 2 as Tv). These Pliocene volcanic rocks, according to *Schmidt* [1975], indicate an Early Pliocene period of gas release that formed the glass shards and pumice fragments of the Boleo tuffs. These Pliocene volcanic products interbedded with the Pliocene sedimentary rocks are bimodal and include rhyolites, basic dikes, lopoliths and palagonitic tuffs [*Demant*, 1984]. The rhyolitic tuffs and domes are the earliest of these products, and the mafic products, most commonly in the form of dikes and pumice air-fall deposits [*Demant*, 1984], are the most recent. *Demant* [1984] indicated that at the end of this early volcanic sequence, the volcanic activity was subaerial. This last, subaerial volcanic unit, named the Aro Volcanics by *Schmidt* [1975], is Quaternary in age, with a K/Ar date of 1.09±0.12 Ma.

This subaerial unit is thought to be related to the disappearance of the Santa Rosalia marine gulf [*Demant and Ortlieb*, 1981] and roughly marks the age of the La Reforma caldera. Coeval with the Aro Volcanics is the Pleistocene Santa Rosalia Formation (Qm and Qf, Fig. 2), consisting of marine and fluvial fossiliferous sandstone and coarse-grained conglomerate [*Wilson*, 1948]. The uplifted terraces south of the La Reforma caldera, overlain by ignimbrites, are primarily made up of the Santa Rosalia Formation [*Ortlieb*, 1981].

The volcanic Quaternary rocks in the La Reforma complex are the caldera-forming products. *Demant* [1984] categorized these products in four stages: 1. Intumescence stage 2. Caldera forming stage 3. Post collapse rhyolitic dome stage 4. Recent basaltic eruptions. The intumescence began when the gas pressure built up in the magma chamber. The products from this stage are the more recent volcanic rocks discussed above, within the group mapped as Tv in Figures 1 and 2. This stage was followed by the caldera forming eruptions. The most widespread of these deposits are the welded tuffs (Qi, Figs. 1 and 2) extending throughout the southern and western flanks of La Reforma caldera [*Demant*, 1984]. A volume of 5 - 10 km^3 was calculated for these deposits by *Demant* [1984]. In some places, the welded tuffs are also overlain by 5 - 10 m thick andesite lavas (Qaa, Figs. 1 and 2) that are similarly cut by the caldera margin [*Demant*, 1984].

Demant [1984] describes a detailed stratigraphic section of the caldera forming deposits in a location in the upper part of the Cuesta del Infierno as follows: The youngest of

these rocks are a conglomeratic fossil-rich section, which *Demant* [1984] correlates to a Quaternary marine terrace of *Wilson* [1948], which is part of the Santa Rosalia Formation (Qm and Qf, Figs. 1 and 2). This outcrop is the highest marine terrace of the Santa Rosalia area [*Wilson*, 1948]. Overlying this conglomerate is a 10 m thick ash and pumice air-fall deposit, overlain by a 5-m-thick white air-fall ash deposit. *Demant* [1984] determined that the 5-m thick brown basaltic andesite scorias that overlie the white air-fall ash deposit demonstrate the intervention of more mafic magma in the rhyolitic system. He further inferred that the interception of the silicic magma chamber with rising, more mafic magmas may have triggered the Plinian eruption, based on the model of *Sparks et al.* [1977] for the genesis of Plinian eruptions.

The La Reforma volcanic complex clearly has a caldera morphology, indicating collapse. The stratigraphic section described above [*Demant*, 1984] is cut by the ring escarpment (shown in green in Fig. 2) and is therefore considered representative of the pre-caldera products. There has been volcanic activity since the collapse of the caldera as well. *Demant* [1984] attributed 3 domes (Qdr, Fig. 2) in the southern region of the caldera and on the northwest rim of the caldera and associated lavas to the post-collapse, pre-resurgence stage. Additionally, there are intra-caldera non-welded tuffs (Qtt in Fig. 2) surrounding the domes. *Demant* [1984] stated that the hydrostatic re-equilibrium of the collapsed mass (resurgent doming), which normally precedes the dome-forming phase [*Smith et al.*, 1970], is concealed in the La Reforma caldera by the latest uplift of the central portion of the La Reforma caldera (Tc, Fig. 2).

The youngest products in the La Reforma caldera are the recent mafic deposits (Qtb, Fig. 2). These are scoria cones and associated lavas. *Schmidt* [1975] compared normative plagioclase composition to Al_2O_3 and determined the recent scoria cones to be tholeiitic. He therefore concluded that there was an evolution from calc-alkaline to tholeiitic affinities in the La Reforma region.

Demant [1984] determined that these mafic eruptions are located along N-S fractures and thus are clearly related to the extensional tectonism of the Gulf of California. Further, *Demant* [1984] argued that the absence of such mafic eruptions within the caldera is evidence of the existence of a partially molten silicic magma in a shallow reservoir beneath the caldera. The rising mafic magma, because of its higher density, cannot cross the silicic magma body but stays in its lower part, generating current activity in the magma chamber [*Mahood*, 1981; 1980], which *Demant* [1984] determined is responsible for the uplift of the central block.

4.2.3 El Aguajito

The El Aguajito volcanic complex was determined to be a caldera based on its arcuately aligned rhyolite domes that appear to have developed over a pre-existing ring fracture [*Garduño-Monroy et al.*, 1993]. The resurgence of the central dome is indicated by the ignimbrite sheets in the region that appear to dip radially outward from the center of the volcanic edifice [*Garduño-Monroy et al.*, 1993]. By inferring that the 0.8 Ma silicic domes conceal the ring fracture of the caldera, *Garduño-Monroy et al.* [1993] determined the caldera to be 10 km in diameter.

Garduño-Monroy et al. [1993] noted that El Aguajito's eruptive products overlie those of the La Reforma caldera. In particular, the ignimbrite sheets of Mesa La Tinaja (Qps, Figs. 1 and 2), with a K/Ar date of 0.5 Ma [*Garduño-Monroy et al.*, 1993] were determined to belong to El Aguajito and overlie the ignimbrites (Qi, Figs. 1 and 2) of La Reforma. *Demant* [1984] had mapped Mesa La Tinaja as an ignimbrite sheet belonging to La Reforma. Similarly to La Reforma, the central region of El Aguajito was mapped as the Comondú Formation by most previous authors (Tc, Figs. 1 and 2)[18]. The observation and interpretation of *Garduño-Monroy et al.* [1993] and *Sawlan* [1981b] implies that the main volcanic centers in the TVLRVR have erupted in a counterclockwise fashion from La Reforma to Volcán La Virgen over the last few million years.

4.2.4 Tres Vírgenes

As volcanic activity moved from the volcanic complexes of La Reforma and El Aguajito to the Tres Vírgenes volcanic centers, the stress regime changed to a trans-tensional system, and old normal faults were reactivated as lateral faults [*Hernández*, 1998; *Umhoefer and Teyssier*, 1991]. The Tres Vírgenes volcanic centers are located in one such zone of weakness, along an unnamed fault perpendicular to the Las Viboras Fault and the Tres Vírgenes Fault (Fig. 6). The three volcanoes of Tres Vírgenes are aligned in a NE-SW direction and get progressively younger to the southwest. This NE-SW

[18] The one exception to the mapping of the central regions of La Reforma and El Aguajito as Comondú Formation in published reports is by *Hernández* [1998]. *Hernández* [1998] mapped the central region of La Reforma as Pliocene andesite and the central region of El Aguajito as Quaternary dacite. However, he referred to La Reforma and El Aguajito as volcanic complexes, rather than calderas. Thus, their central regions were not interpreted as resurgent domes.

alignment of vents in the region was attributed by *Umhoefer and Teyssier* [1991] to a N-S extensional zone resulting from a right-stepping offset between the Viboras[19] and "Highway 1"[20] faults (Figs. 1 and 6). *Umhoefer and Teyssier* [1991] also noted that older faults such as the Cimarron Fault (Fig. 6) may play a role in the location of the extensional zone (Figs. 1 and 2); preliminary investigations show the Cimarron fault[21] zone is characterized by normal faults that have been overprinted by dextral strike-slip motion.

From NE to SW the volcanic centers of Tres Vírgenes are named El Viejo, El Azufre[22], and La Virgen. El Viejo volcano was described by *Sawlan* [1981b] as a thick accumulation of dacite apparently erupted from El Azufre, rather than a separate edifice. However, it is most often shown as a separate volcano, with a dacitic dome on its northeast flank, which is thought to have originated from a satellite vent [*Hernández*, 1998]. El Viejo and El Azufre are composed primarily of dacitic lava domes and lavas and are the two oldest edifices of the Tres Vírgenes volcanoes [*Capra et al.*, 1998; *Demant*, 1984; *Sawlan*, 1981b; *Garduño-Monroy et al.*, 1993]. These two structures are relatively small compared to La Virgen (Fig. 4).

Deposits of four general volcanic episodes are recognized in the vicinity of the Tres Vírgenes volcanoes. From oldest to youngest these are: 1) Andesite of the Sierra Santa

[19] The Viboras fault is also referred to as the El Azufre fault [*Hernández*, 1998].
[20] The "Highway 1" fault is more commonly referred to as the Tres Vírgenes Fault (TVF in Figure 6).
[21] The Cimarron fault is mapped as extending through the Tres Vírgenes volcanoes by *Garduño-Monroy et al.* [1993] but only through the El Aguajito volcanic complex by *Hernández* [1998] and *Wong et al.* [2001]. Hernández designates a fracture through the Tres Vírgenes volcanoes, where *Garduño-Monroy et al.* [1993] mapped the extension of the Cimarron fault.
[22] El Azufre volcano is also referred to as La Soufre, the equivalent French name, by *Sawlan* [1981b].

Lucia of early Miocene age. 2) The sheet-like Basalt of Esperanza, which has been assigned an age of mid-to-late Miocene [*Sawlan*, 1981b] by correlation to similar basalts near San Ignacio, dated by *Gastil* [1979] at 11.1 ± 0.8 Ma; 3) Rhyolitic ignimbrite and mafic deposits from the La Reforma and El Aguajito volcanic centers; 4) Holocene and Pleistocene volcanic rocks erupted from the Tres Vírgenes volcanoes [*Sawlan*, 1981a].

There are few isotopic dates available on the volcanic deposits from Tres Vírgenes volcanics. *Hernández* [1998] noted that two reports to the Mexican Federal Electric Commission [*Hernández et al.* 1989; 1991] show a north to south migration of volcanism, with K/Ar dates of 0.44 Ma (El Viejo volcanic products) and 0.28 Ma (El Azufre volcanic products). A visiting missionary, Rev. Fernando Consag, is thought to have witnessed an eruption from Volcán La Virgen in 1746 [*Ives*, 1962]. This information is drawn from Rev. Consag's map of Baja California, which designates La Virgen as the "fiery volcano, discovered in 1746." Rev. Fernando Consag's diary recorded during the time of his discovery of La Virgen has not been found. A ^{14}C analysis of carbonized wood within a middle unit yielded a date of 6515± 75 y.b.p. [*Capra et al.*, 1998], which signifies that the upper unit must be younger and eruptions have taken place at La Virgen less than 6,515 years ago.

The La Virgen volcano is a 2000-m high Quaternary composite volcano made of low viscosity basalt lavas, pyroclastic deposits, and thick dacitic domes [*Hausback and Sawlan*, 1995a; *Sawlan*, 1981b]. La Virgen was erupted in two [*Capra et al.*, 1998; *Sawlan*, 1981b; 1982] or three [*Sawlan*, 1995] phases. These phases were described by

Sawlan [1981b] as basalt to dacite sequences. *Capra et al.* [1998] described the eruptions in six stages, but these can be correlated to the phases of *Sawlan* [1981b; 1995]. The first phase, which makes up the bulk of the stratovolcano and is primarily composed of intermediate rocks, began, according to *Capra et al.* [1998], with the construction of the central andesitic edifice by the extrusion of a scoria cone and associated domes and lavas (Qad, Fig. 1). It is inferred that the vent for these initial eruptions is now buried under the rhyodacitic dome to the southwest of the summit, labeled Qlrd in Figure 1. However, *Sawlan* [1981b] placed this vent just north of the summit. The first five stages defined by *Capra et al.* [1998] make up this first stage.

According to *Sawlan* [1981b], phase one began with basaltic emissions (Qvb in Fig. 1). These initial basaltic eruptions were followed by the andesitic eruptions [*Capra et al.*, 1998]. This basaltic to andesitic progression was then followed by the dacitic lavas to the north and south of the summit (Qdf, Fig. 1). After these dacitic lavas, the Plinian activity, from a vent on the southwest flank of La Virgen, occurred approximately 6500 yr ago [*Capra et al.*, 1998]. Development of a Plinian eruption column up to 18 km in height likely dispersed the ash to the SW with an areal extent of ~500 km^2, and a minimum volume of 1.14 km^3 [*Capra et al.*, 1998]. *Capra et al.* [1998] determined that following the Plinian stage, a rhyodacitic lava flow (Qlrd, Fig. 1) erupted on the southwest flank[23] of the volcano as well as a dacitic dome (Qdd, Fig. 1) to the south, referred to as the El Mezquital dome. Afterward, there was explosive hydromagmatic

[23] The region to the southwest of the La Virgen summit, mapped as Qlrd in Figure 1 was mapped as dacite by *Sawlan* [1981b].

activity from a new vent, which created fall-and-surge and a scoria flow deposit on the southern flank of La Virgen[24].

According to *Sawlan* [1981b] the activity of the first phase was concentrated within the northern La Virgen vent. The basalts erupted from this first stage of activity are exposed northwest and northeast of La Virgen (Qvb, Fig. 1). Andesites and dacites of the first stage comprise much of the northwest flank, but are also located around all sides of the volcano (Qad, Fig. 1) [*Sawlan*, 1981b]. Additionally, the dacite coulees on the south side of La Virgen are products of the first stage (Qbf, Fig. 1) [*Sawlan*, 1981b].

Sawlan [1995] reasoned that the progression to more silicic compositions, the mineralogic and trace element affinities, and the occurrence of quenched andesite magmatic inclusions, indicate the reservoir of this first stage differentiated from andesite to dacite and episodically mixed with andesite. By observation of reverse and oscillatory zoning of plagioclase crystals, variable composition of the plagioclase phenocrysts within the same sample, two types of disequilibrium texture in the plagioclase phenocrysts, compositionally banded pumice fragments with different mineral associations, and the presence of juvenile material with different weight percent silica contents within the same unit, *Capra et al.* [1998] determined that magma mixing processes led to the Plinian eruptions at La Virgen.

[24] The fall-and-surge deposits were described by *Capra et al.* [1998] and are located south of the El Mezquital dome. In most maps of the region, this area is mapped as recent alluvium. Therefore it is designated as Qal in Figure 1; however, this alluvium contains re-worked fall-and-surge and flow deposits [*Capra et al.*, 1998].

The most recent volcanic events at La Virgen were less explosive [*Capra et al.*, 1996; 1998]. The second phase began with basaltic emissions of El Azufre (Qsb, Figs. 1 and 2), which overlie the dacite lavas from the first phase of volcanic activity at La Virgen. This indicates that the volcanic activity at La Virgen and El Azufre occurred concurrently [*Sawlan*, 1981b]. Most recently, the second phase included mafic lavas (Qvy, Fig. 1) [*Sawlan*, 1982]. This second phase of volcanism erupted from the same vent as the earlier hydromagmatic activity [*Capra et al.*, 1996]. *Sawlan* [1995] revised this last phase to include a small volume of basalt at the northern base of La Virgen, but assigned the andesite deposited south of the summit as the beginning of a stage three sequence. *Sawlan* [1995] suggested that the phase three andesite could be the beginning of a renewed cycle of andesite to rhyolite lavas, or an isolated batch of andesite. These recent lavas north and south of the summit are grouped together by *Demant* [1984] and *Sawlan* [1981b]. *Capra et al.* [1998] designated the northern lavas as dacite and the southern lavas as andesites. These recent lavas were mapped together in Figure 1 as Qvy.

The unit mapped in Figure 1 as Qna, the most recent emission [*Sawlan*, 1981b], is designated as an andesite flow erupted from a separate satellite vent; however, it is grouped together with older dacitic lavas by *Demant* [1984] and *Capra et al.* [1998]. According to *Capra et al.* [1998], the most recent deposits in the region belong to a epiclastic laharic sequence, consisting of pumice and scoria fragments, to the northwest of Tres Vírgenes, reported to originate from the flanks of El Azufre. This sequence was determined to be due to the intense degradation and strong geothermal activity that affected the El Viejo and El Azufre volcanoes.

Within the La Virgen tephra, located SW of Volcan La Virgen, there are pumice blocks up to 40 cm in diameter, and in the Mezquital dacite dome, located 5.5 km south of the summit of La Virgen, there are pumice blocks as large as 40 cm in diameter and fragments up to 60 cm in diameter [*Hausback and Sawlan*, 1995b]. The estimated minimum volume of this tephra unit calculated by *Hausback and Sawlan* [1995b] is 4 km^3. The wide distribution of large pumice blocks within the La Virgen tephra to the southwest and southeast of the summit is attributed to either the vent once being near the summit of the volcano or the tephra having been vented from multiple vents that have subsequently been filled and buried by domes and lavas [*Hausback and Sawlan*, 1995b].

Using gravity, magnetic, and temperature profiles, *Estrada and Lopez* [1998] show evidence of the existence of magmatic bodies below the La Virgen volcano. These magmatic bodies provide the heat source for the hydrothermal plant in the Tres Vírgenes region. Although the youngest magmatic bodies, and therefore the hottest temperatures, are located to the SW within the Tres Vírgenes region, the recent faulting in the northern section near El Viejo permits the heat to come closer to the surface and is, therefore, most easily tapped in that location, where the geothermal wells are located.

Additional evidence for hot magma bodies below Tres Vírgenes was found by *Wong et al.* [2001] in their study of the attenuation of coda waves. *Wong et al.* [2001] estimated the coda-wave attenuation quality factor, Q_c, for the Tres Vírgenes volcanic region using 26 local earthquakes, ranging from a magnitude 1 to 3. Seven portable digital seismic

stations deployed in October of 1993 recorded these events. For their study, Q_c was determined using the scattering theory, using the frequency range of 6 - 24 Hz. There was a low frequency dependence of Q_c [average $Q_c(f) = (50 \pm 3)\ f^{(0.65 \pm 0.20)}$] that was determined for six of the seven stations within the Tres Vírgenes region[25]. *Wong et al.* [2001] believed this observed low frequency dependence of Q_c could be explained by the presence of a deep thermal anomaly. A low resistivity (3 to 15 Ohm-m) layer beneath the Tres Vírgenes Volcanoes between 250 and 1500 m depth was detected by *Pimentel* [1998], and is believed to be associated with hot rock zones produced by magmatic intrusions. Additionally, using the seismic array of the Pequeña Abertura (ARPA) that was installed in the Tres Vírgenes volcanic area in November and December of 1999, *Rodriguez et al.* [2001] computed the S-wave velocity structure shown in Table 2 using the spatial autocorrelation technique (SPAC). Compared to a typical P-wave velocity for crustal rocks of 6 km/s and a typical crustal S-wave velocity of 3.5 km/s, these crustal velocities appear low and could indicate partial melting below Tres Vírgenes. However, due to the very shallow depths for which P-wave velocity was calculated in this study, it is difficult to compare them to average velocities.

Km	Vp (km/s)	Vs (km/s)
0.038	0.6	0.39
0.204	1.6	1.12
0.697	4.5	2.19
1.000	5.2	3.10

Table 2. P- and S-wave velocity structure below Tres-Vírgenes according to Rodriguez et al. [2001].

[25] The seventh station, located closest to the steam production well, produced anomalously low Q_c values and therefore was not included in the average [*Wong et al.*, 2001].

4.3 Methods

4.3.1 Field Work

Two field excursions were conducted in the La Reforma region in May - June of 2000 and March of 2001. The field work done in May - June of 2000 was concentrated in Arroyo Punta Arena, Arroyo Punta Prieta, Diablo Canyon, and the southwest corner of the La Reforma caldera. Fieldwork in March of 2001 focused on the southwest corner of the La Reforma caldera and the Las Minitas region. The primary objectives of the field work were to evaluate the proposed existence of Miocene Comondú Formation within the central dome of La Reforma and collect field spectra (discussed in Chapter 2) and field samples (discussed in Chapter 3) for validation of the MASTER data.

Within Arroyo Punta Arena, outcrops of the Pliocene and Pleistocene volcanic rocks were observed, as well as the interbedded Pliocene sedimentary rocks, many of which contained layers with abundant fossils. Pillow lavas at the base of an andesite lava (within unit Tv, in Fig. 2) were also noted. This provides further evidence the region was submarine during much of the early evolution of La Reforma. Within the Arroyo Punta Prieta, *Schmidt* [1975] mapped a large unit he described as a Pliocene diorite porphyry stock. This unit was seen in fieldwork in the north side of arroyo Punta Prieta. It appeared to be primarily composed of dikes that intrude a unit of mudstone. This unit is mapped within Tv (Fig. 2) and is assumed to be part of the complex of bimodal volcanic deposits and intrusions that preceded the ignimbrite emissions of La Reforma.

On the north side of the mouth of Diablo canyon, along the cliff facing the Gulf of California, a flow-laminated rhyolite obsidian lava was observed. Stratigraphically below this unit, an ashy pumice unit, cut by dikes was also observed. These units belong to the alternating submarine and subaerial bimodal emissions of the early La Reforma volcanic complex (Tv in Fig. 2).

Within Arroyo El Grande to the southwest of the La Reforma caldera rim, very thick pyroclastic flow and fall layers were observed. These were stratified white, yellow and gray units with abundant angular lithic fragments up to 60 cm in diameter. These strata make up the unit mapped as Qi in Figures 1 and 2. These strata were overlain uncomformably by a 10 - 100 m lava flow, mapped as Qaa in Figure 2. Within Arroyo El Grande, at the rim of the caldera, a sample was collected of the lava flow directly underlying the La Reforma ignimbrite emission (the uppermost unit of the rocks mapped collectively as Tv in Fig. 2).

Within the region mapped as Tm (Fig. 2), marine sandstone and shale layers were observed. The field work in 2000 and 2001 to the NE of this region into the central dome of La Reforma suggests that the strata that make up the resurgent dome of the La Reforma caldera are composed of welded ash-flow tuffs and lavas [*Hausback et al.*, 2000], not the tuff breccias and debris flow deposits that would be characteristic of the Comondú Formation [*Heim*, 1922]. The Comondú Formation does contain volcanic units of ash and lavas, referred to as the Comondú Volcanics; however, the central dome

cannot be Miocene Comondú Formation, because this unit, as observed in the field, is stratigraphically above the younger Pliocene sedimentary rocks (Tm, Fig. 2). The strata of welded ash-flow tuffs and lavas in the central dome of La Reforma most likely originated from intracaldera pyroclastic flows erupted during the caldera's inception. The central dome, however, is primarily composed of thin units, not the very large-scale ash flow tuffs characteristic of the final caldera forming eruptions. Therefore, it is likely that these deposits, mapped as Qwa in Figure 7, were erupted before the eruption directly preceding collapse, but their age relation to the large pyroclastic layers (Qi) surrounding the caldera was not established in the field. The relationship to the intracaldera tuffs (Qtt in Figs. 1 and 2) was also not established in the field. Because the welded ash flow tuffs and lavas of Qwa lie directly above the Pliocene sedimentary rocks, however, Qtt is assumed to be a younger post-caldera unit.

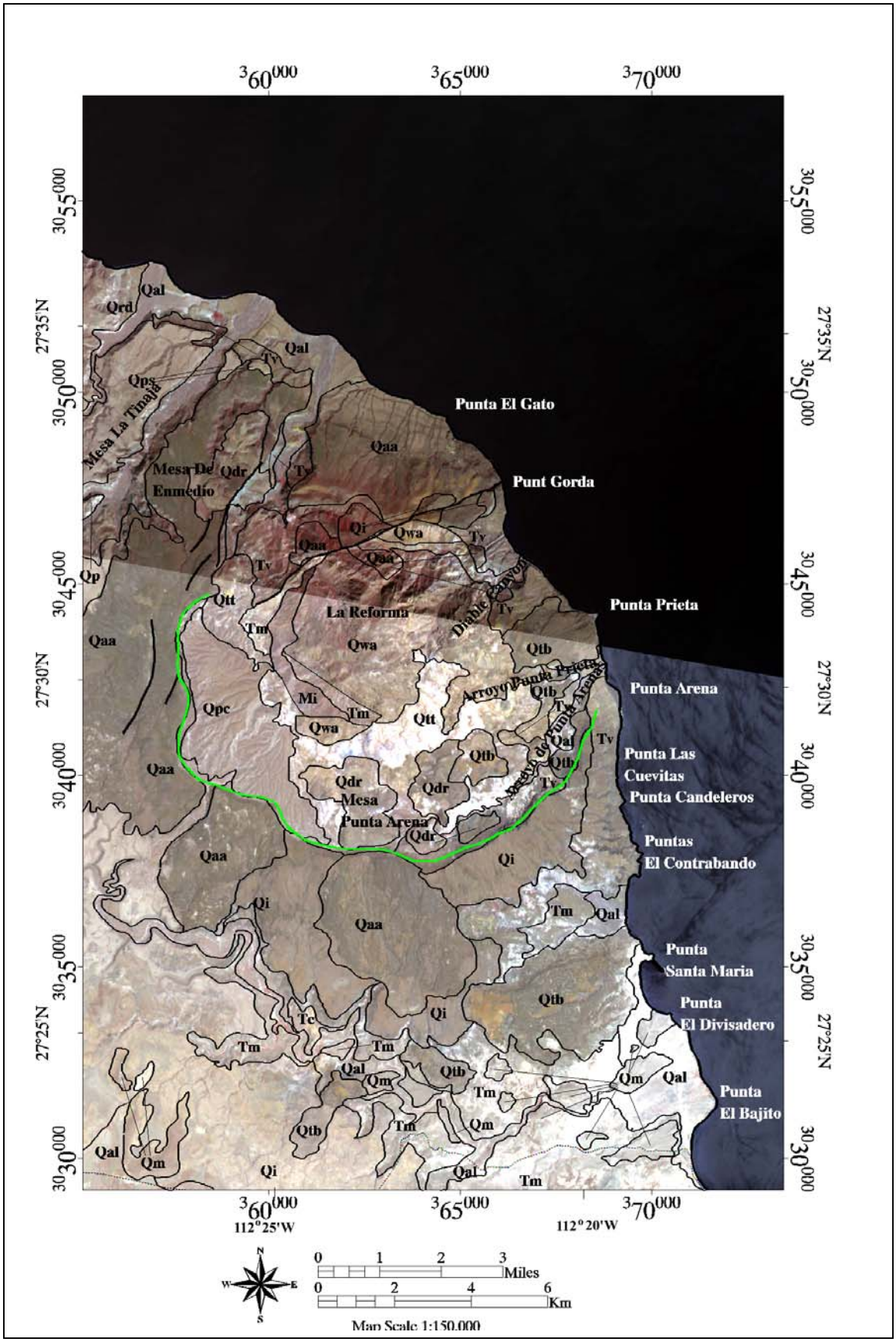
360000
365000
370000
3055000
3050000
3045000
3040000
3035000
3030000
27°35'N
27°30'N
27°25'N
112°25'W
112°20'W
Punta El Gato
Punt Gorda
Punta Prieta
Punta Arena
Punta Las Cuevitas
Punta Candeleros
Puntas El Contrabando
Punta Santa Maria
Punta El Divisadero
Punta El Bajito
Mesa La Tinaja
Mesa De Enmedio
La Reforma
Diablo Canyon
Arroyo Punta Prieta
Arroyo de Punta Arena
Qal
Qrd
Qps
Tv
Qdr
Qaa
Qi
Qwa
Qat
Qp
Qtt
Tm
Qtb
Mi
Qpc
Qm
Tc
0 1 2 3 Miles
0 2 4 6 Km
Map Scale 1:150,000

Figure 7. (Previous page) Revised geologic units and faults on top of a mosaic of two ASTER images (Red: band 3, Green: band 2, Blue: band 1). Line symbology is the same as in Figure 1. Geologic unit abbreviations are described in Table 3. Map datum and projection: NAD27 Mexico, UTM zone 12.

Fieldwork also verified the existence of Cretaceous basement rock, which crops out to the southwest of the central dome (Mi, Fig. 2). This exposure indicates extreme post-collapse uplift of La Reforma's central dome. The Pliocene sedimentary rocks are directly above this basement layer. This implies the Comondú Formation either was not present in this region, had eroded away prior to the deposition of the Pliocene sedimentary rocks, or was tectonically displaced.

Field work in the Las Minitas region primarily consisted of collecting field spectra; however, outcrops of green altered tuff, hydrothermally altered ignimbrite, and red altered tuff interbedded with altered siltstones and sandstones and cut by large dike swarms were observed. This region was mapped as Boleo Formation by *Schmidt* [1975] (Tm, in Fig. 2). One sample of the altered ignimbrite was collected for analysis and was determined to have a weight percent silica value of 70.82%.

4.3.2 MASTER Analysis

The following two sections discuss the analysis and results of the MODIS-ASTER (MASTER) data. Analysis of the VNIR-SWIR MASTER data (channels 1 - 25) yields a classification map (Plate 1). Analysis of the TIR MASTER data (channels 41 - 50) yields a weight percent silica map (Plate 2).

4.3.3 Results of Classification

As discussed in Chapter 2, the 28 images of Visible and Near Infrared to Short-wave Infrared (VNIR-SWIR) MASTER data in the TVLRVR were atmospherically corrected and classified. The VNIR-SWIR MASTER data were atmospherically corrected to a reasonable accuracy with the Empirical Line Calibration (ELC) mode in ENVI. Classifying the atmospherically corrected MASTER data, resized to exclude the bands highly affected by water absorption, was done successfully by choosing endmembers with the highest Pixel Purity Indices (PPI^{TM}) values. Endmembers from a select number of field spectra and one image-derived region were added to the list of endmembers to expand the classification. This yielded a classification map that roughly delineated surfaces that vary in their secondary minerals, produced by weathering and alteration, namely ferric oxides, hydrates, hydroxyls, and carbonates. Attempts to identify these minerals using ENVI's Spectral Analyst^{TM} were only moderately successful. The resulting classification map was overlain with the unit contacts shown in Figures 1 and 2 (Plate 1).

By comparing the delineations of previously mapped units with the classification map, and keeping in mind the likely identity of the various endmembers, a few things can be noted. The recent lavas of the Tres Vírgenes volcanoes, the older Miocene lavas, and many of the central domes of La Reforma and El Aguajito are all mapped as the endmember "Basalt." In Chapter 2 the similarity of this field spectrum to hematite, a common oxidation mineral of iron-bearing, mafic volcanic rocks, was noted. The

classification clearly does not illuminate the difference between the different lavas in the region, but does distinguish these regions from more silicic material, pyroclastic deposits, sedimentary rocks, and alluvium. It is significant that the central domes of both La Reforma and El Aguajito are primarily classified as this endmember. Because they were previously assigned to Miocene Comondú Formation, one would expect them to match the classification of the Miocene Comondú Formation in the southeastern portion Plate 1, which is classified as "n-d-2." Endmember "n-d-2" was determined in Chapter 2 to represent weathered detritus. This would be a reasonable classification for the Comondú Formation, which is described as largely tuff breccias and debris flow deposits. Although there is variation within the units of the Comondú Formation [*Heim*, 1922], the classification of the central domes as endmember "Basalt" further verifies that these central domes are not made up of the Comondú Formation, but rather are stratified domes of welded ash-flow tuffs and lavas.

The abundance of pixels classified as "Basalt" in the central dome of La Reforma also indicates this unit is different from the main ignimbrite emissions mapped as Qi, which are primarily classified as "n-d-2." This verifies the central dome has a different composition than the pyroclastic layers surrounding the caldera, but it does not establish their age relationship.

As noted in Chapter 2, endmember "n-d-10" is found near the summits of the recent mafic lavas around the La Reforma caldera. Endmember "n-d-10" was determined in Chapter 2 to most likely represent a surface with large amounts of oxidized iron. This

endmember is also found within regions previously mapped as more silicic material: within a small region mapped as Tc to the north of the La Reforma resurgent dome (Fig. 7) and within a region mapped as Qps, just northwest of El Azufre (Fig. 8).

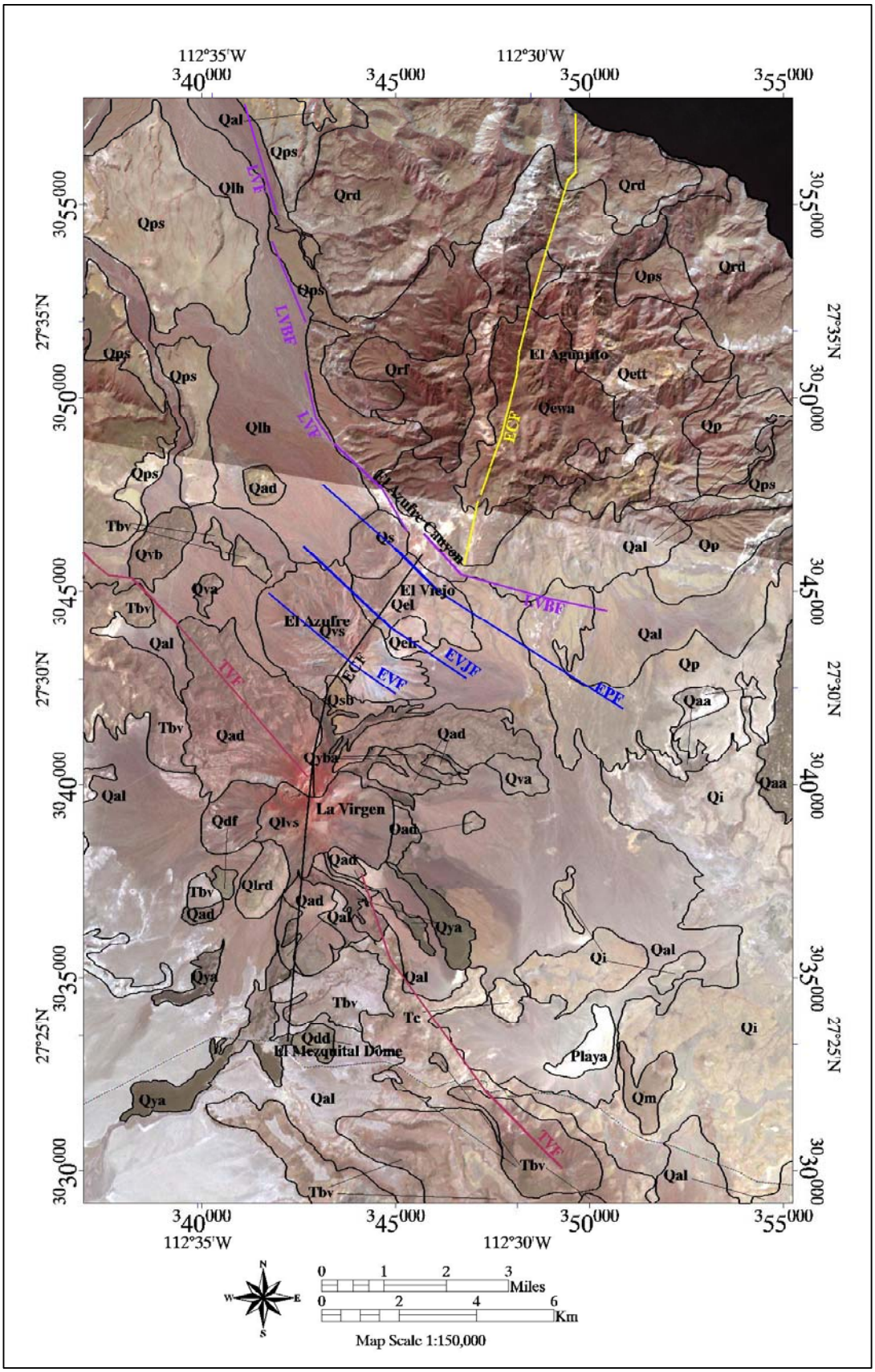
112°35'W
112°30'W
340000
345000
350000
355000
27°35'N
27°30'N
27°25'N
3055000
3050000
3045000
3040000
3035000
3030000
Qal
Qps
Qlh
Qrd
Qrf
Qett
Qewa
Qp
Qad
Tbv
Qvb
Qya
Qvs
Qel
Qelr
Qsb
Qyba
Qva
Qaa
Qi
Qdf
Qlvs
Qlrd
Qdd
Tc
Qm
Playa
El Agujito
El Viejo
El Azufre
El Mezquital Dome
La Virgen
El Azufre Canyon
LVF
LVBF
ECF
EVF
EVBF
AEPF
TVF
0 1 2 3 Miles
0 2 4 6 Km
Map Scale 1:150,000

Figure 8. (Previous page) Revised geologic units and faults on top of a mosaic of two ASTER images (Red: band 3, Green: band 2, Blue: band 1). Line symbology is the same as in Figure 1. Geologic unit abbreviations are described in Table 3. Map datum and projection: NAD27 Mexico, UTM zone 12.

Mesa La Tinaja, described by *Garduño-Monroy et al.* [1993] as an ignimbrite sheet (Qps, Figs. 1 and 2) that erupted from El Aguajito and is interfingered with sand deposits, is primarily classified as class "Faroash" (Plate 1), similar to other pyroclastic units surrounding El Aguajito. The majority of the ignimbrites attributed to eruptions from La Reforma (Qi, Figs. 1 and 2) are classified as "Farosh" as well, with their detritus primarily identified as "n-d-2." In the classification, therefore, the ignimbrites of Mesa La Tinaja cannot be distinguished from ignimbrites that belong to La Reforma caldera. However, it is expected that two ignimbrite deposits, even if erupted from separate volcanic complexes, would be very similar in their VNIR-SWIR spectral signature and weight percent silica.

In El Azufre canyon, within the heavily faulted region, which gives rise to hydrothermal vents, there are pixels classified as "n-d-3." Endmember "n-d-3" was determined in Chapter 2 to indicate the presence of mineral alunite, a common alteration mineral of hydrothermal reactions. There are also scattered pixels classified as "n-d-3" within the Las Minitas region of La Reforma, another verified region of hydrothermal activity. Within the central portion of the El Aguajito volcanic complex, however, there are no pixels classified as this endmember, indicating a lack of similar hydrothermal alteration in this volcanic complex. The only other location of this endmember is in the alluvium and Boleo Formation (Tm) in the southeast corner of Figures 1 and 2.

The unit (Qtt) within the southern moat of the La Reforma caldera (Figs. 1 and 2) is largely identified as endmember "n-d-1." In Chapter 2 it was determined that this endmember likely represents a surface with a large percentage of the mineral montmorillonite, an alteration mineral of volcanic ash. This identification helps to confirm the identity of this unit as altered ash. A large percentage of La Reforma's pyroclastic material is also identified as this endmember. Additionally, a large percentage of the pixels within the El Aguajito complex is also identified as endmember "n-d-1." This identification led to the addition of a unit similar to Qtt within the El Aguajito complex (Qett in Figs. 7 and 8).

A significant percentage of the pixels within the units identified as Tm and Qal in Figures 1 and 2, inland from Punta El Bajito, is classified as endmember "n-d-6." This endmember was determined to most likely represent a surface with a high gypsum content. Gypsum is found in large quantities within the Boleo Formation [*Wilson*, 1948]. This region, including the previously mapped alluvium, must therefore primarily contain outcrops of the Boleo Formation and has been updated accordingly in Figures 1 and 2.

Units mapped as Qaa and Qtb in Figures 1 and 2 appear nearly identical in the classification (Plate 1), the weight percent silica map (Plate 2), the ASTER image (Figs. 1 and 2), and the Thematic Mapper image (Fig. 3). These units are largely mapped as endmembers "n-d-2" and "Basalt" and appear to have a mafic composition in the weight percent silica map. Distinguishing these surfaces as two separate units was done based

on previous mapping [*Demant*, 1984]; however, nothing in the imagery suggests they differ in composition.

4.3.4 Results of Weight Percent Silica Map

As discussed in Chapter 3, the shift to longer wavelengths of the main spectral feature in the thermal infrared wavelength region (Reststrahlen band) as the mineralogy changes from felsic to mafic was utilized to map weight percent silica, using the MASTER data. Chapter 3 described an approach for determining the size of this wavelength shift using a Gaussian curve. The size of this shift is translated into weight percent SiO_2 of the surface, using a reference curve derived from laboratory data.

The results of Chapter 3 indicate that the general approach tended to underestimate the weight percent SiO_2 in the image[26]. This discrepancy was removed by fine-tuning the general approach with measurements from field samples (a site calibration) and provided good results in the calculated weight percent SiO_2 with errors of a few percent. Chapter 3 discussed the verification of this method using a small subset of the MASTER TVLRVR dataset. For this chapter, all 28 of the MASTER images within the TVLRVR were processed to weight percent silica, site calibrated, georectified, and mosaicked together. The georectification and mosaicking was done as described in Chapter 2 for the VNIR-SWIR MASTER data.

[26] In the Hiller Mountains test region, discussed by *Hook et al.* [2005], results indicate the general approach slightly overestimates the weight percent SiO_2 of low silica rocks (e.g. basalt) and underestimates the weight percent SiO_2 of high silica rocks (e.g. granite).

In order to correct for misleading high weight percent silica values for surfaces of water, high-density vegetation, and those containing a large percentage of aphyric rocks[27], the data were masked. This was done by evaluating the coefficients within the Gaussian functions:

$$f(x) = A_0 e^{\frac{-z^2}{2}} \quad \text{(3 term)}$$

$$f(x) = A_0 e^{\frac{-z^2}{2}} + A_3 \quad \text{(4 term)}$$

where:

$$z = \frac{x - A_1}{A_2} \text{ and x = wavelength } (\mu\text{m})$$

where A_0 through A_3 are the fit values for the Gaussian function *f(x)*. The 4 terms of the Gaussian function correspond to the amplitude, position along the x-axis of the minimum value, area enclosed by the function and offset, respectively. The mask was computed by assigning a minimum amplitude, A_0, of 9.6, and a maximum area of 10.7. Picture elements (pixels) that fall below the minimum amplitude and exceed the maximum area are flat spectra and therefore not good candidates for the weight percent silica method, as discussed in Chapter 3. These pixels were assigned a value of zero and appear black in Plate 2. This method works well to mask out the water within the Gulf of California and surfaces of highly aphyric rocks. However, it works less well to mask vegetation. Note that the region of high-density vegetation at the summit of La Virgen (identified in the classification as "Vegetation") is not masked. Decreasing the maximum value of area or

[27] Water, vegetation, and surfaces of aphyric rocks have fairly flat TIR spectra. These spectra typically are erroneously fit with Gaussian curves with minima toward lower wavelengths, which misidentify the pixels as containing high weight percent silica.

increasing the minimum allowed amplitude of the Gaussian degraded the value of the weight percent silica map by masking out valid surfaces.

These site calibrated, georectified, masked and mosaicked data, with each pixel assigned a weight percent silica value, are shown in Plate 2 with the unit contacts of Figures 1 and 2 overlaid. A few things are clear upon observation of this image. The overlapping regions within separate images do not always match. Some of the mismatch is due to the severe warping of the images. However, some of the mismatch is due to the inaccuracy of the temperature emissivity separation to separate emissivity entirely from temperature. The failure of this complete separation produces emissivity spectra that are still a function of temperature. In most cases, this temperature effect mimics topography, with shadows heavily influencing the spectra.

The employed temperature emissivity separation algorithm, TES, was validated over playas and ponds, regions with little or no topographical variation [*Gillespie et al.*, 1998]. A validation study has not been done on regions of high topographic relief. From observation of Plate 2 it is clear that the mismatch is largest in regions of high topographic relief (central dome of La Reforma). This is due to shadows affecting the temperature emissivity separation. Rough topography and lower solar altitudes increase the effect of shadows in the emissivity spectra. All of the images in Plate 2 were collected within 2 hours of solar noon, but with the high topographic relief in some regions, the effectiveness of the temperature emissivity algorithm is diminished due to large shadows, and the results are less reliable. This effect appears as a flattening of the

spectral signature, which changes the weight percent silica values. Pixels that are in the shadows will have an elevated weight percent silica.

In most cases, the known recent mafic deposits clearly are mapped as lower weight percent silica than the more silicic alluvium and rhyolite and dacite deposits. There is an overall trend from a bimodal distribution of silicic and mafic rocks in the La Reforma and El Aguajito volcanic complexes to a more mafic distribution of lavas in the Tres Vírgenes region.

Demant [1984] mapped 3 domes in the southern region of the La Reforma caldera. One region within the southeastern-most dome of La Reforma (Qdr) is classified as both low weight percent silica (Plate 2) and as endmember "n-d-10," an endmember associated with recent mafic deposits (Plate 1). This unit has an average weight percent silica of 58 ± 3% (standard deviation of 1.78), based on an average of 33 pixels chosen within this unit within the weight percent silica map (Plate 2). The other rhyolite domes in the southern moat of the caldera as well as one in the northwestern part of the caldera, along the ring fracture, are clearly seen in both the weight percent silica maps and the classifications (Plates 1 and 2). The dome along the northeastern ring fracture of the caldera has an average weight percent silica of 65 ± 3% (standard deviation of 1.95), based on an average of 500 pixels chosen within this unit on the weight percent silica map. The south domes appear to be more varied in their weight percent silica content, based on Plate 2, but this variation could be due to variation in the amount of weathering and vegetation on these surfaces. Based on these differences among the domes, the

eastern half of the most southeastern of the La Reforma domes is remapped here as Qtb. With this revision, there is no clear N-S trend of recent mafic vents. However, it is evident that the mafic vents have occurred outside of the central dome of La Reforma.

The recent La Virgen lavas mapped as Qvy (Figs. 1 and 2) are of two different weight percent silica contents, as *Sawlan* [1995] suggested. The southern lavas have an average weight percent silica content, 60 ± 3% (standard deviation of 2.17), based on an average of 1611 pixels chosen within the southern Qvy unit within the weight percent silica map (Plate 2), and the northern lavas have an average weight percent silica content, 56 ± 3% (standard deviation of 1.87), based on an average of 852 pixels chosen within the northern Qvy unit within the weight percent silica map (Plate 2). Therefore, the southern Qvy lavas are mapped as Qya (young andesite lavas) and the northern Qvy lavas are mapped as Qyba (young basaltic andesite lavas) in Figure 8. The unit designated by *Sawlan* [1981b] as the most recent emission from La Virgen, composed of andesitic lavas, but described as dacitic by *Capra et al.* [1998] (Qna in Fig. 1), has an average weight percent silica content of 58 ± 3% (standard deviation of 2.09), based on an average of 4200 pixels chosen within the eastern section of the Qna unit within the weight percent silica map (Plate 2). Therefore, it is believed to be an andesitic lava. However, it is difficult to determine its age relationship to the units mapped as Qad and Qvy. It does appear in Figure 4 to be overlain by the younger Qvy unit. Additionally, it is classified similarly to the Qad unit and has a similar weight percent silica value. Therefore, unit Qna in Figure 1 has been mapped as the older Qad in Figure 7.

Other revisions to the regional geological map (Figs. 1 and 2) include the re-mapping of a small outcrop previously mapped as Qvy, as Qad. This revision was based on its more similar weight percent silica value and appearance (Fig. 1 and Plate 1) to the older unit, Qad. The unit labeled Qdf in Figure 1, mapped by *Capra et al.* [1998] as early stage dacitic lavas of La Virgen, are indiscernible from Miocene mafic volcanic rocks (Basalt of La Esperanza) [*Sawlan*, 1981b] in both the weight percent silica map (Plate 2) and the classification (Plate 1). *Capra et al.* [1998] did not conduct geochemical or geochronological studies of this flow. This unit, therefore, has been remapped as the Basalt of La Esperanza in Figure 8. Additionally, a unit within the El Viejo volcano appears to have a much higher weight percent silica value than the remainder of this edifice. This unit, therefore, has been distinguished in Figure 8 as a more silicic unit (Qelr).

In addition to the revisions discussed above, some minor revisions to the outlines of previously mapped units were made to Figures 1 and 2 by overlaying the unit outlines on the classification and weight percent silica to verify the surface exposure of mapped units. The final revised map is shown in Figures 7 and 8. The geologic units in these images are described in Table 3.

Geologic Units		
	Qal	Recent Alluvium
Tres Virgenes	Qlh	Santa Ana Laharic sequence
	Qs	Satellite vent flava and domes
	Qya	Recent andesite lava
	Qyba	Recent basaltic-andesite lava
	Qbc	Basaltic Cinders
	Qsb	El Azufre basalt
	Qdd	Dacitic El Mezquital dome
	Qlrd	Rhyodacitic dome
	Qdf	Dacitic lava
	Qad	Early andesitic to dacitic lava
	Qvb	Early basaltic lava
	Qvs	El Azufre dacite and andesite
	Qel	Dacitic deposits of El Viejo
	Qelr	Silicic deposits of El Viejo (rhyodacitic?)
El Aguajito	Qp	Pyroclastic flow deposits
	Qrd	Rhyolite domes
	Qrf	Rhyodacite lava
	Qps	Pyroclastic flow and marine sand deposits
	Qett	Intracaldera non-welded tuffs
	Qewa	Welded ash flow tuffs and lavas of the central dome of El Aguajito
La Reforma	Qtb	Basaltic to andesitic lava
	Qpc	Conglomerate
	Qdr	Dacitic and rhyolitic domes
	Qtt	Intracaldera non-welded tuffs
	Qaa	Andesitic lava
	Qi	Ignimbrite outflow sheets
	Qwa	Welded ash flow tuffs and lavas of the central dome of La Reforma
Pre-TVLRVR	Qm	Quaternary marine sedimentary rocks of the Santa Rosalia Formation
	Qf	Quaternary fluvial sedimentary rocks of the Santa Rosalia Formation
	Tv	Pliocene and Pleistocene volcanic rocks (submarine and subaerial)
	Tm	Pliocene marine sedimentary rocks of the Boleo, Gloria and Infierno Formations
	Tbv	Upper Miocene mafic volcanic rocks, Basalt of La Esperanza
	Tc	Miocene Comondu Formation and the andesite of Sierra Santa Lucia
	Mi	Cretaceous batholithic rocks

Table 3. Description of the geologic units referred to in Figures 7 and 8. The units have been modified from Table 1, incorporating the new results obtained in this study.

4.4 Discussion

Using the classification, the weight percent silica map and the field observations, it is clear the central dome of La Reforma is not composed of Miocene Comondú Formation, but rather welded ash flow tuffs and lavas erupted from the La Reforma caldera. The stages of evolution of the La Reforma caldera can be revised, according to the general

model of caldera formation by *Smith and Bailey* [1968] as follows: **1. Regional tumescence** (Tv) [28] **2. Ignimbrite eruption** (Qi) **3. Caldera collapse 4. Pre-resurgence volcanism** (Qdr) **and sedimentation of megabreccia**[29] (Qpc) **5. Resurgent doming** (Qi) **6. Major ring fracture volcanism** (Qtt) **7. Fumarole and hotspring activity** (Las Minitas region[30]). The distinctly circular ring fractures of La Reforma caldera and its obvious resurgent dome make this structure best fit the "piston" type of caldera of *Lipman* [1997], with some degree of piecemeal faulting within the central dome.

The La Reforma Caldera is likely undergoing present day uplift, as evidenced by marine terraces [*Wilson*, 1948 and *Ortlieb*, 1981]. The updoming, discussed by *Demant* [1984], is not concealed. Rather, the central dome, mapped by *Demant* [1984] as an uplifted block of Miocene Comondú Formation, is the resurgent dome. The abnormal height of the central dome and the Quaternary marine terraces [*Ortlieb*, 1981] may indeed be evidence of renewed activity in the magma chamber beneath the La Reforma caldera.

The youngest products in the La Reforma caldera are the recent basalt. These are scoria cones and associated lavas, which can be easily identified in the MASTER and ASTER images due to their morphologically young features, and in the weight percent silica maps due to their mafic composition. However, these units are not distinguishable from the older unit, Qaa. Units Qtb and Qaa are also associated with endmember "n-d-10" in Plate 1. As noted from observation of the classification and the weight percent silica maps,

[28] The units in parenthesis correspond to the unit that belongs to each stage, as mapped in Figures 7 and 8.
[29] This megabreccia unit indicates a mass-wasting event associated with collapse.
[30] The Las Minitas region was mapped in detail by *Schmidt* [1975] and displays high alteration, severe faulting and ore minerals, indicative of extensive hydrothermal activity.

there is no clear N-S trend of recent mafic emissions surrounding the La Reforma caldera, contrary to the conclusion of *Demant* [1984]. However, it is evident that the mafic emissions have occurred outside of the central dome of La Reforma, and this could be evidence of an existing silicic magma chamber below the La Reforma caldera.

While field work in the El Aguajito region was not done in this study, the similarity of the central domes of the La Reforma and El Aguajito volcanic centers, in both the classification and the weight percent silica map, indicates the central region of El Aguajito likely also is not Miocene Comondú Formation, but rather is composed of welded ash-flow tuffs and lavas. If indeed El Aguajito is a caldera, its lack of an obvious collapse feature and no megabreccia unit indicate it best fits the "downsag" category of calderas [*Lipman*, 1997]. It is also possible the El Aguajito volcanic complex has never collapsed and is therefore not a caldera. It has distributed large amounts of ignimbrite sheets (Qps). Ignimbrite outflow sheets are most commonly associated with calderas. Therefore, the magmatic system of El Aguajito may be connected with that of La Reforma, and the collapse associated with the El Aguajito ignimbrite eruptions might have taken place at this older structure.

The relative ages of the volcanic edifices within TVLRVR are difficult to determine in the MASTER and ASTER images. While the volcanic complex of El Aguajito appears geomorphologically older (more eroded) in Figure 4, the El Aguajito complex was determined to be younger in age than the La Reforma caldera [*Garduño-Monroy et al.*, 1993]. Mesa La Tinaja appears similar to the ignimbrite surfaces from La

Reforma (Qi) in the Thematic Mapper image, ASTER image, classification of MASTER data, and the weight percent silica map. However, the K-Ar dates of the domes and ignimbrite sheets of El Aguajito are 0.8 and 0.5 Ma, respectively [*Garduño-Monroy et al.*, 1993]; therefore, the progression of volcanic activity from La Reforma to El Aguajito appears to be accurate. It is possible, with the lack of known dates within the more recent La Reforma volcanic products, that the La Reforma and El Aguajito volcanic eruptions have been largely coeval, and their magma chambers are connected. However, a detailed geochemical study would be necessary to make this association.

Overall, the volcanic products of the El Aguajito and La Reforma calderas appear to be bimodal. The youngest igneous rocks in the Basin and Range Province are of bimodal composition as well, consisting mostly of basalt, basaltic andesite, and rhyolite with relatively scarce intermediate-composition rocks [*Christiansen and Yeats*, 1992; *Noble*, 1988]. This bimodal assemblage of volcanic rocks formed in a continental rifting environment during Basin and Range extension [*Christiansen and Yeats*, 1992]. *Fitton et al.* [1991] proposed that the upwelling of asthenospheric mantle into the lithosphere could lead to partial melting of the subduction-modified lithospheric mantle. *John* [2001] explained that in a continental-rifting regime, the water-poor mafic magmas can ascend with very little interaction within the crust and erupt as thin lavas, shield volcanoes, and dike swarms. Water-poor rhyolitic melts are then created by partial melting of the base of the crust, which results from the underplating of the basaltic magma body. This in turn leads to eruptions of rhyolitic domes, lavas and ash-flow tuffs [*John*, 2001]. This volcanic regime appears similar to the La Reforma and El Aguajito volcanic centers.

The Tres Vírgenes volcanoes are not bimodal assemblages. Rather, the El Viejo and El Azufre volcanoes are composed primarily of dacitic lava domes and lavas, and the La Virgen volcano is a well-differentiated stratovolcano. This change in volcanism is coeval with the stress regime change to a trans-tensional system, when old normal faults were reactivated as lateral faults (*Hernández*, 1998; *Umhoefer and Teyssier* 1991].

This north-south alignment of calcalkalic volcanoes evolved within a tectonic regime of trans-tensional continental rifting. The TVLRVR is related not to an active subduction zone, as is most common for calc-alkaline volcanoes, but rather to the extensional deformation leading to the formation of the Gulf of California [*Sawlan*, 1981b; *Sawlan and Smith*, 1984, *Colletta and Angelier*, 1981]. An association has been suggested between extensional and transtensional tectonics and explosive calc-alkaline volcanism due to melting of the continental crust [*Gastil et al.*, 1975; *Sawlan*, 1991]; therefore, the calc-alkaline nature of the TVLRVR is not necessarily anomalous.

Most of the stratovolcanoes in the world occur in the subduction zones. Nonetheless, there are at least 25 stratovolcanoes described within the East African – Red Sea region [*Siebert and Simkin*, 2002], a region of extensive continental rifting. However, continental rifts such as the East African Rift Valley are characterized by rocks that are predominantly alkalic [*Barberi and Varet*, 1970], and are therefore not direct analogs for the Tres Vírgenes volcanoes.

Sawlan [1995] suggested that the phase-three andesite to the south of the La Virgen summit could be the beginning of a renewed cycle of andesite to rhyolite lavas, or an isolated batch of andesite. It seems most plausible, however, that these are part of the second phase of eruptions from La Virgen, still differentiating from basalt to more silicic emissions. These recent lavas grouped together as Qvy in Figure 1 have been re-mapped, based on the weight percent silica map (Plate 2) as Qya (young andesite lavas to the south of the summit) and Qyba (young basaltic andesite lavas to the north of the summit) in Figure 8. The unit mapped as Qna in Figure 1, which was designated by *Sawlan* [1981b] as the most recent lava flow from La Virgen, composed of andesite, but described as dacite by *Capra et al.* [1998] was established as an andesitic lava flow, based on the weight percent silica map as well (Plate 2). Qna was categorized as Qad in Figure 8. The more recent units, Qyba and Qya, are the mafic to intermediate lavas of the second phase of volcanism at La Virgen.

4.5 Summary and Conclusions

Several images were constructed in order to summarize and revise the previous geologic mapping done in the TVLRVR. These images include a classification of atmospherically corrected MASTER multi-channel VNIR-SWIR data, a weight percent silica map based on atmospherically corrected MASTER TIR data, a mosaicked ASTER image, and a Thematic Mapper image draped over a digital elevation model. These images helped to delineate previously mapped units and revise erroneously mapped regions. The resulting updated map aided in the understanding of the volcanic history of this region.

The weight percent silica technique works well overall, but the inaccuracy of the temperature emissivity separation technique in regions of high topographic relief and low solar angle prove to lessen the ability of the Gaussian fitting technique to accurately estimate the weight percent silica. This effect appears as a flattening of the spectral signature, which changes the weight percent silica values. Pixels that are in the shadows have an elevated weight percent silica. The temperature emissivity technique, and therefore the weight percent silica technique, work best on flat terrains, or with images collected at exactly solar noon.

The TVLRVR is a volcanic region that has evolved in the last few million years from producing bimodal caldera structures (the La Reforma caldera and the El Aguajito volcanic complex), within a largely extensional regime, to lavas and domes (El Viejo and El Azufre) and most recently a stratovolcano (La Virgen) within a transtensional regime.

La Reforma likely is a caldera, due to its composition and morphology, as well as the existence of both ignimbrite outflow sheets and a megabreccia unit indicating a mass-wasting event associated with collapse. The central dome is not a block of Miocene Comondú Volcanics, but is composed of welded ash-flow tuffs and lavas [*Hausback et al.*, 2000], more typical of a caldera resurgent dome. El Aguajito does not appear to fit the definition of a caldera, however. While it is possible that the rhyolitic domes surrounding the central dome could conceal a ring fracture, the lack of a megabreccia unit within the central portion of the volcanic complex and no recognizable collapse features

prohibits a definitive identification of the El Aguajito volcanic complex as a caldera. There is a possibility that the magmatic conduits of La Reforma and El Aguajito are connected and collapse took place only at the La Reforma caldera.

The Tres Vírgenes volcanoes appear to have erupted in the pull-apart basin between the Las Víboras and Tres Vírgenes fault zones. These eruptions are on average more mafic and less explosive than those that originated from the La Reforma caldera and the El Aguajito volcanic complex. But there is evidence of mixing between silicic magma bodies and hotter, more mafic rising magma in all the volcanic centers of the TVLRVR, which has led to the many Plinian eruptions in the region. In the second and most recent phase of eruptions, La Virgen appears to be following the differentiation from mafic to more silicic products.

References

Angelier, J., B. Colletta, J. Chorowicz, L. Ortlieb, and C. Rangin, Fault tectonics of the Baja California peninsula and the opening of the Sea of Cortez, *Journal of Structural Geology*, *3* (4), 347-357, 1981.

Barberi, F., and J. Varet, The Erta Ale volcanic range (Danakil Depression, Northern Afar, Ethiopia), *Bull. Volcanologique*, *34*, 848-917, 1970.

Capra, L., J.L. Macias, J.M. Espindola, and C. Siebe, Actividad pliniana del Volcan La Virgen, Complejo Volcanico de Tres Vírgenes (Baja California Sur, Mexico): mecanismos eruptivos y evolucion magmatologica, in *GEOS Union Geofisica Mexicana*, p. 221, 1996.

Capra, L., J.L. Macias, J.M. Espindola, and C. Siebe, Holocene Plinian eruption of La Virgen volcano, Baja California, Mexico, *Journal of Volcanology and Geothermal Research*, *80* (3-4), pp. 239-266, 1998.

Christiansen, R.L., and R.S. Yeats, Post-Laramide geology of the U.S. Cordilleran region, in Burchfiel, B. C., Lipman, P. W., and Zoback, M. L., The Cordilleran Orogen: conterminous U. S.: The Geology of North America, Volume G-3,

Decade of North American Geology, Geological Society of America, Boulder, p. 261-406, 1992.

Colletta, B., and J. Angelier, Faulting evolution of the Santa Rosalia Basin, Baja California, Mexico, in *Geology of Northwestern Mexico and Southern Arizona*, edited by L. Ortlieb, and J. Roldan-Quintana, pp. 265-274, Estacion Regional del Noroeste, Instituto de Geologia, U.N.A.M., Hermosillo, Sonora, Mexico, 1981.

Demant, A., The Reforma Caldera, Santa Rosalia Area, Baja California, A volcanological, petrographical and mineralogical study, in *Neotectonics and sea level variations in the Gulf of California area, a Symposium*, edited by V. Malpica-Cruz, S. Celis-Gutiérrez, J. Guerrero-Garcia, and L. Ortlieb, pp. 77-96, Univ. Nal. Auton, México, Inst. Geologia, México, D. F., 1984.

Demant, A., and L. Ortlieb, Plio-Pleistocene Volcano-Tectonic Evolution of La Reforma Caldera, Baja California, Mexico, *Tectonophysics*, *71* (1-4), 194-194, 1981.

Estrada, G.G., and M.G. Lopez, Synthesis of gravity, magnetic, and thermal studies at Las Tres Vírgenes Geothermal Zone, B. C. S., Mexico, *Geotermia, Revista Mexicana de Geoenergia*, *14* (1), 15-32, 1998.

Fitton, J.G., D. James, and W.P. Leeman, Basic Magmatism Associated with Late Cenozoic Extension in the Western United-States - Compositional Variations in Space and Time, *Journal of Geophysical Research-Solid Earth and Planets*, *96* (B8), 13693-13711, 1991.

Garduño-Monroy, V.H., H. Vargas-Ledezma, and J.O. Campos-Enriquez, Preliminary geologic studies of Sierra El Aguajito (Baja California, Mexico): a resurgent-type caldera, *Journal of Volcanology and Geothermal Research*, *59*, 47-58, 1993.

Gastil, G.R., D. Krmmenacher, and J. Minch, The record of Cenozoic volcanism around the Gulf of California, *Geological Society of America Bulletin*, *90* (839-857), 1979.

Gastil, G.R., R.P. Phillips, and E.C. Allison, Reconnaissance geology of coastal Sonora between Puerto Lobos and Bahia Kino, *Geological Society of America Memoir*, *140*, 170, 1975.

Gillespie, A.R., S. Rokugawa, T. Matsunaga, S.J. Cothern, S.J. Hook, and A.B. Kahle, A temperature and emissivity separation algorithm for advanced spaceborne thermal emission and reflection radiometer (ASTER) images, *IEEE Transactions on Geoscience and Remote Sensing*, *36* (4), 1113-1126, 1998.

Guerrero-Guadarrama, J.L., Actividad Sísmica del Campo Geotérmico de Las Tres Vírgenes, *Geotermia*, *14*,, 87-100, 1998.

Hausback, Brian P, J.M. Stock, J.E. Dmochowski, C.D. Farrar, S.J. Fowler, K. Sutter, P. Verke, and C. Winant, To be or not to be a caldera - La Reforma caldera, Baja California Sur, Mexico, in *Geological Society of America*, pp. A502, 2000.

Hausback, B.P., and M.G. Sawlan, Eruption of La Virgen tephra, Volcan Las Tres Vírgenes, Baja California Sur, Mexico, in *Third International Meeting on the Geology of the Baja California Peninsula, Abstract Volume*, pp. A502, La Paz, Baja California Sur, Mexico, 1995a.

Hausback, B.P., and M.G. Sawlan, Eruption of La Virgen Tephra, Volcan Las Tres Vírgenes, Baja California Sur, Mexico, in *III International Meeting on Geology of the Baja California Penisula*, pp. 82-83, La Paz, B. C. S., Mexico, 1995b.

Heim, A., The Tertiary of southern Lower California, *Geology*, *59*, 529-547, 1922.

Hernández, A.L., Geological Synthesis of Las Tres Vírgenes Geothermal Area, B. C. S., Mexico, *Geotermia, Revista Mexicana de Geoenergía*, *14* (1), 3-14, 1998.

Hernández, A.L., C. Robin, J.M. Cantagrel, and P. Vincent, Estudio geoquímico, mineralógico y edades radiométricos de la zona Tres Vírgenes, B.C.S. Implicaciones geotérmicas, pp. 50, Comisión Federal de Electricidad, Gerencia de Proyectos Geotermoeléctricos, 1989.

Hernández, A.L., C.Z. Unzueta, and L.R. Hernández, Estudio geológico regional de la zona geotérmica de Las Tres Vírgenes, pp. 38, Comisión Federal de Electricidad, Gerencia de Proyectos Geotermoeléctricos, 1991.

Holt, J.W., E.W. Holt, and J.M. Stock, An age constraint on Gulf of California rifting from the Santa Rosalia Basin, Baja California Sur, Mexico, *Geological Society of America Bulletin*, *112* (4), 540-549, 2000.

Hook, S.J., J.E. Dmochowski, K.A. Howard, L.C. Rowan, K.E. Karlstrom, and J.M. Stock, Mapping variations in weight percent silica measured from multispectral thermal infrared imagery—Examples from the Hiller Mountains, Nevada, USA and Tres Vírgenes-La Reforma, Baja California, Baja California Sur, Mexico, *Remote Sensing of Environment*, *95*, 273-289, 2005.

Ives, R.L., Dating of the 1746 eruption of Tres Vírgenes Volcano, Baja California del Sur, Mexico, *Geological Society of America Bulletin*, *73*, 647-648, 1962.

John, D.A., Miocene and early Pliocene epithermal gold-silver deposits in the Northern Great Basin, Western United States: Characteristics, distribution, and relationship to magmatism, *Economic Geology and the Bulletin of the Society of Economic Geologists*, *96* (8), 1827-1853, 2001.

Leterrier, J., R.C. Maury, P. Thonon, D. Girard, and M. Marchal, Clinopyroxene Composition as a Method of Identification of the Magmatic Affinities of Paleovolcanic Series, *Earth and Planetary Science Letters*, *59* (1), 139-154, 1982.

Lipman, P.W., Subsidence of ash-flow calderas: relation to caldera size and magma-chamber geometry, *Bulletin of Volcanology*, *59* (3), 198-218, 1997.

Mahood, G.A., Geological Evolution of a Pleistocene Rhyolitic Center - Sierra-La-Primavera, Jalisco, Mexico, *Journal of Volcanology and Geothermal Research*, *8* (2-4), 199-230, 1980.

Mahood, G.A., Chemical Evolution of a Pleistocene Rhyolitic Center - Sierra-La-Primavera, Jalisco, Mexico, *Contributions to Mineralogy and Petrology*, *77* (2), 129-149, 1981.

Mammerickx, J., and K.D. Klitgord, Northern East Pacific Rise - Evolution from 25 My Bp to the Present, *Journal of Geophysical Research*, *87* (NB8), 6751-6759, 1982.

Noble, D.C., Cenozoic volcanic rocks of the northwestern Great Basin: An overview, *Geological Society of Nevada Special Publication* (7), p. 31-42, 1988.

Ochoa-Landin, L., J. Ruiz, T. Calmus, E. Perez-Segura, and F. Escandon, Sedimentology and Stratigraphy of the Upper Miocene Boleo Formation, Santa Rosalia, Baja California, Mexico, *Revista Mexicana de Ciencias Geologicas*, *17* (2), 83-96, 2000.

Ortlieb, L., Sequences of Pleistocene marine terraces in the Santa Rosalia area, Baja California Sur, Mexico, in *Geology of Northwestern Mexico and Southern Arizona, Field Guides and Papers*, edited by L. Ortlieb, and J. Roldan, pp. 275-293, 1981.

Pimentel, E.B., Análisis Geoeléctrico de la zona geotérmica de La Tres Vírgenes, B.C.S., México., *Geotermia, Revista Mexicana de Geoenergía*, *14* (1), 33-41, 1998.

Rodriguez, M., F. Chavez-Garcia, and R. Ivan, Estructura somera de la velocidad de ondas S en el complejo volcanico de Las Tres Vírgenes, B. C. S., in *GEOS Union Geofisica Mexicana, A. C., 21* (3), p. 305, 2001.

Romero-Rojas, S.A., D.A. Maraver-Romero, A.A. Avalos-Zermeno, and E. Aparicio-Cordero, Carta Geologico-Minera Santa Rosalia G12-1, in *Consejo de Recursos Minerales*, Secretaria de Comercio y Fomento Industrial, 1997.

Sawlan, M.G., Episodes of volcanism in the Tres Vírgenes area, near Santa Rosalia, central Baja California Peninsula, Mexico, *Geological Society of America Abstracts with Programs*, *13* (2), 104, 1981a.

Sawlan, M.G., Late Cenozoic Volcanism in the Tres Vírgenes Area, in *GSA Cordilleran Section*, edited by L. Ortlieb, and J. Roldan-Quintana, pp. 309-319, U.N.A.M. Institue Geol., Estacion Regional del Noroeste, Hermosillo, Mexico, 1981b.

Sawlan, M.G., Geochemical Evolution of the Quaternary La Virgen Volcano older series lavas, Baja California, Mexico, *Geological Society of America Abstracts with Programs*, *14*, 231, 1982.

Sawlan, M.G., Petrogenesis of Late Cenozoic Volcanic Rocks from Baja California Sur, Mexico, Ph.D. thesis, University of California, Santa Cruz, Santa Cruz, 1986.

Sawlan, M.G., Magmatic evolution of the Gulf of California rift, in *The Gulf and Peninsular Province of the Californias: American Association of Petroleum Geologists Memoir 47*, edited by J.P. Dauphin, and B.R. Simoneit, pp. 301-369, 1991.

Sawlan, M.G., Death of a magma chamber: Evacuation of a layered Dacite/Andesite reservoir, Volcan La Tres Vírgenes, Baja California, Mexico, *Geological Society of America Abstracts with Programs*, *27* (b), 359, 1995.

Sawlan, M.G., and J.G. Smith, Late Cenozoic volcanic suites in Northern Baja California Sur, Mexico: Their relation to subduction and rifting along the Baja California Peninsula, *Geological Society of America, Abstracts with Programs*, *16* (6), 645, 1984.

Schmidt, E.K., Plate tectonics, volcanic petrology, and ore formation in the Santa Rosalia Area, Baja California, Mexico, Master of Science thesis, The University of Arizona, pp. 194, 1975.

Siebert, L., and T. Simkin, Volcanoes of the World: an Illustrated Catalog of Holocene Volcanoes and their Eruptions, in *Global Volcanism Program Digital Information Series*, Smithsonia Institution, 2002.

Smith, R.L., and R.A. Bailey, Resurgent cauldrons, *Geological Society of America Memoir*, *116*, 613-662, 1968.

Smith, R.L., R.A. Bailey, and C.S. Ross, Geologic map of the Jemez Mountains, New Mexico, U. S. Geological Survey Miscellaneous Investigations Series Maps I-0571, 1970.

Sparks, R.S.J., H. Sigurdsson, and L. Wilson, Magma Mixing: a mechanism for triggering acid explosive eruptions, *Nature*, *267* (315-318), 1977.

Umhoefer, P.J., and C. Teyssier, A preliminary structural geology study of the El Azufre Canyon area, north of Tres Vírgenes Volcano, Northern Baja California Sur, in *Primera Reunion Internacional Sobre Geologia de La Peninsula de Baja*

California, Universidad Autonoma de Baja Califonia Sur, La Paz, Baja California Sur, Mexico, 1991.

Vargas-Ledezma, H., and V.H. Garduño-Monroy, Estudio Geologico-Geotermico de La Caldera El Aguajito, B.C.S., pp. 41, Comision Federal de Electricidad, 1988.

Walker, G.P., Z. Jurado, S. Rowland, and A. Carrillo, La Reforma cryptodome: an alternative mechanism to caldera subsidence and resurgent doming, in *29th International Geological Congress Meeting*, pp. 481, Kyoto, Japan, 1992.

Wilson, I.F., Buried topography, initial structiures and sedimentation in Santa Rosalia, Baja California, Mexico, *American Association Petroleum Geologists Bulletin*, *32*, 1762-1807, 1948.

Wong, V., C.J. Rebollar, and L. Munguía, Attenuation of coda waves at the Tres Vírgenes Volcanic Area, Baja California Sur, Mexico, *Bulletin of the Seismological Society of America*, *91* (4), 683-693, 2001.

Chapter 5: Isla San Luis and the Surrounding Bathymetry

Abstract

Isla San Luis (ISL) lies in the northern Gulf of California, only 5 km from the Baja California coast. It is a Holocene, calc-alkaline volcano with an eruptive history of mildly effusive to powerfully explosive hydro-volcanic events. MASTER data were used to help map the extent of the volcanic deposits on the island. The weight percent silica maps created from the Thermal Infrared (TIR) MASTER data show the more recent deposits as high weight percent silica and the older volcanic products as lower weight percent silica. The classifications produced from the Visible and Near Infrared to Short-wave Infrared (VNIR-SWIR) MASTER data delineate some of the important geologic units on the island. Careful analysis of the bathymetric data and consideration of the island's alignment with the Ballenas transform fault zone to the south and volcanic seamounts nearby, suggest the tectonic origin of ISL could be along a "leaky" transform fault, within the transtensional regime of the Gulf of California. Isotopic dates on mollusk shells from beach deposits interbedded with the volcanic layers on ISL yield ages from 4725 to 2888 ybp. The latest eruptions are younger but undated. The last eruption was a phreatomagmatic blast at the flank of the northern rhyolite dome. Recent volcanism and mild active fumarolic activity suggest that the ISL volcano remains potentially active.

5.1 Introduction

This chapter combines bathymetric data collected during October of 2001 and February 2003 with analysis of MASTER data collected in April of 1999 to better understand the mapped units of ISL and the surrounding seafloor. Geologic fieldwork conducted by collaborators in May of 2000 and October of 2001, including isotopic dating, gas and temperature measurements, is also discussed. This chapter will first introduce the geologic background of ISL. Fieldwork done in 2000 and 2001 will then be described. This will conclude with the results from the bathymetric data and MASTER analysis.

5.2 Geologic Background

The peninsula of Baja California, Mexico, has undergone tremendous transformation in the last 25 million years. In this time it has transitioned from a region of arc volcanism, related to the subduction of the Guadalupe microplate to a transtensional region on the western edge of the transform plate boundary between the Pacific and North American plates [*Gastil*, 1979; *Sawlan*, 1991]. Between 25 Ma and 12 Ma, the triple junction among the Pacific, Guadalupe, and North American plates propagated southward down the margin of western Baja California, shutting off the arc-related volcanism in the peninsula [*Mammerickx and Klitgord*, 1982]. In northern Baja California, it appears that arc-related volcanism ceased at 17-15 Ma [*Martín et al.*, 2000]. Farther south it continued until approximately 12 Ma [*Sawlan and Smith*, 1984b], when the Guadalupe-Pacific rise ceased to spread [*Mammerickx and Klitgord*, 1982] and subduction presumably stopped. During the time of subduction, Baja California was still part of mainland Mexico. It was not until approximately 6 Ma that the extension became

localized to the region now known as the Gulf of California [*Oskin et al.*, 2001]. The complete transfer of Baja California to the Pacific plate is known to have occurred prior to 3.5 Ma, as evidenced by the formation of magnetically lineated oceanic crust at the Alarcon Rise in the southern portion of the Gulf of California [*Lonsdale*, 1989]. As early as 30 Ma, the broad area of the Gulf Extensional Province north through Arizona and New Mexico has undergone extension [Henry and Aranda-Gomez, 1992].

The North American-Pacific plate boundary is now a series of rift basins and transform faults [e.g., *Zanchi*, 1994; *Stock and Hodges*; 1990, *Persaud et al.*; 2003, *Lewis and Stock*, 1998]. Around 3.3 Ma, the plate boundary made a westward jump from the Tiburon basin to the Upper Delphin basin, and after 2 Ma the southern Tiburon basin jumped to the Lower Delphin basin [*Lonsdale*, 1989; *Stock,* 2000]. Sometime after 2 Ma, spreading jumped from the southern Tiburon basin to the lower Delphin basin [*Lonsdale*, 1989; *Stock*, 2000].

The oblique rifting that is now occurring in the Gulf of California began 6 Ma [*Oskin et al.*, 2001]; however, evidence of seafloor spreading is only found in the Alarcon basin and southward [*Klitgord and Mammerickx*, 1982]. In the northern Gulf of California, recent studies indicate there is active distributed deformation, characterized by segmented basins, and both intrusive and extrusive magmatism [*Persaud et al.*, 2003]. *Persaud et al.* [2003] suggest that seafloor spreading is not present in the northern Gulf of California due to the lack of strain-partitioned and focused deformation. The broad shear zone

beneath the thick sediment cover from the Colorado river delta causes this distributed strain pattern [*Persaud et al.*, 2003].

The Puertecitos Volcanic Province (PVP) is located on the western edge of this broad shear zone, in the Gulf Extensional Province (Fig. 1). The PVP holds many keys to understanding the tectonic history of Baja California, due to the nature of its volcanic products. In the northern PVP there are exposures of pre-17 to 15 Ma volcanic deposits related to the subduction of the Farallon-Guadalupe plate below North America [*Nagy et al.*, 1999]. There are syn-rift volcanic products (deposited 6.4 - 5.8 Ma and 3.2 - 2.7 Ma) that discordantly overlie these arc-related pyroclastic and epiclastic products [*Martin-Barajas et al.*, 1995]. Also within this province are numerous volcanic tuffs deposited during rifting, as well as related normal and strike-slip faults.

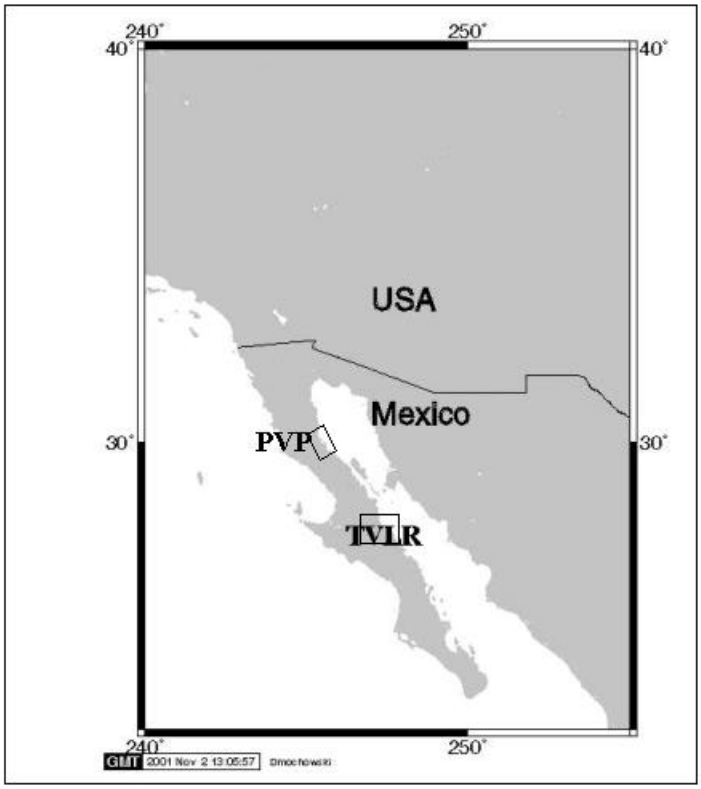

Figure 1. Map of Baja California, northwestern Mexico and the southwestern United States, showing the location of the Puertecitos Volcanic Province (PVP) and the Tres Vírgenes-La Reforma Volcanic Region (TVLR).

ISL is located 5 km from the Baja California coastline, west of the Southern Upper Delphin Basin (Fig. 2). It is 3.5 by 2.5 km^2 in size and is part of an island chain referred to as the San Luis island group. This group is part of the Puertecitos Volcanic Province and includes from north to south, El Muerto, Isla Coloradito, El Cholludo, Isla La Poma (Isla El Pomez), and Isla San Luis (Fig. 2). Geologically, ISL is only similar in origin to Isla La Poma. The other islands are of older origin [*Rossetter*, 1973]. Volcanism is highly differentiated and the compositional variation has been regular, from early basaltic andesite to the recent rhyolitic domes [*Paz-Moreno and Demant*, 1999]. Early

reconnaissance of ISL was described by *Gastil et al.*, 1975 and *Rossetter and Gastil*, 1971. *Rossetter* [1973] described the geology of the San Luis and San Lorenzo island groups, including ISL. But the only detailed petrographic study of ISL is given by *Paz-Moreno and Demant* [1999].

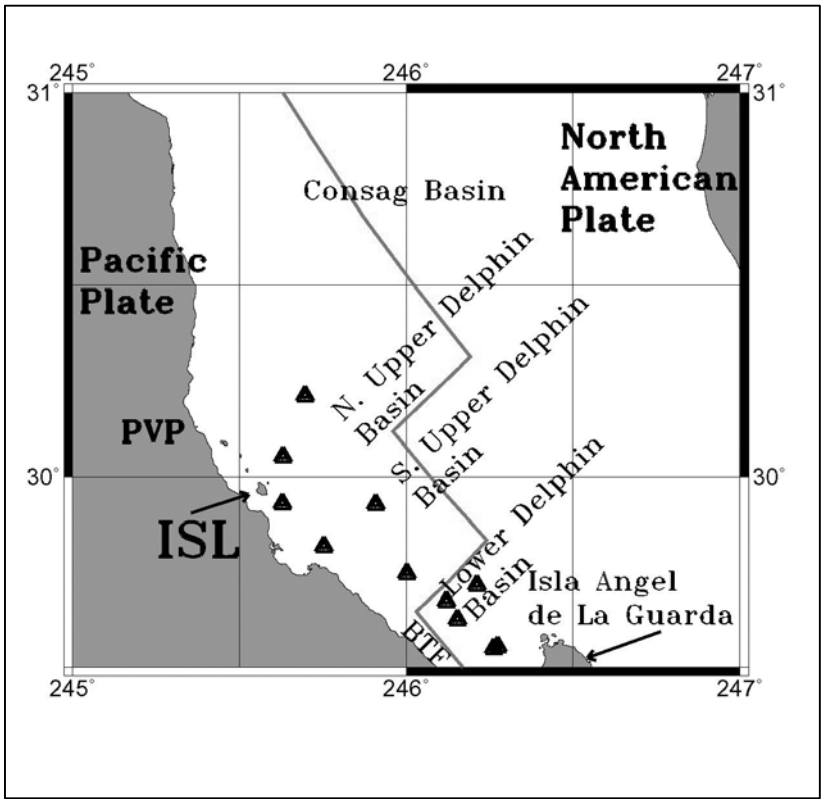

Figure 2. Map showing the location of Isla San Luis and its neighboring islands, submarine volcanic knolls (shown as triangles), and ocean basins. The gray line in the Gulf of California represents the North American-Pacific plate boundary. ISL=Isla San Luis; PVP=Puertecitos Volcanic Province.

Paz-Moreno and Demant [1999] described the evolution of ISL in four stages. The oldest rocks are part of a palagonitic unit that indicates a surtseyan episode of volcanic activity. This palagonite unit consists of thin-bedded ash and lapilli size tuffs with cauliflower bombs as large as 20 cm in diameter [*Paz-Moreno and Demant*, 1999]. The

only nonfragmented juvenile lithic fragments associated with this unit, the cauliflower bombs, have 53 to 59 wt. % silica [*Paz-Moreno and Demant*, 1999]. This unit is visible in the lower sea cliffs surrounding the island and within an arroyo in the southwestern portion of the island.

The first stage of eruptions was followed by subaerial dacitic lava eruptions. This unit can be seen in the walls of the breached explosion crater, Plaza de Toros, and in the western portion of the island. It is believed that these dacitic lavas flowed from a vent at the center of the island. This vent has been subsequently buried by the central rhyolite dome. The eruption of the dacitic lavas was followed by the more explosive eruptions of the dacitic tuff rings at Plaza de Toros. Both andesitic and dacitic juvenile lithic fragments are found in the tuffaceous units that make up the walls of Plaza de Toros [*Paz-Moreno and Demant*, 1999].

The fourth stage in the evolution of Isla San Luis was the emplacement of the rhyolite domes in the central and northern parts of the island. The emplacement of these domes was preceded by the extrusion of ash and pumice that now cover a large portion of the island and contain rhyolite bombs, some that are larger than one meter in diameter. The rhyolite domes are composed of obsidian and highly vesicular pumiceous rhyolite [*Paz-Moreno and Demant*, 1999]. *Paz-Moreno and Demant* [1999] determined that the northern rhyolite dome was slightly older than the central dome due to the presence of deposits from the central dome overlying the northern dome. These units have been

updated by the MASTER image analysis and unpublished mapping by Brian Hausback, Joann Stock, Chris Farrar, and Arturo Martin (Fig. 3). The units are described in Table 1.

Unit Name	Description
Qal	Alluvium and beach deposits
Qs	Coarse aeolian deposits
Qpm	Phreatomagmatic deposits
Qcd	Central rhyolite dome lavas
Qdt	Phreatic ejecta and surge deposits
Qct	Rhyolite fall and surge tephra from Central Dome
Qnd	Northern rhyolite dome lavas
Qnt	Pyroclastic flow deposits from North Dome
Qypt	Deposits from Plaza de Toros dacitic tuff ring
Qopt	Older pyroclastic deposits of Plaza de Toros
Qdl	Dacite lavas
Qot	Pyroclastic deposits from early eruptions, intermediate composition
Qpg	Palagonite

Table 1. Table of the geologic units shown in Figure 3. These units are according to unpublished mapping done by Brian Hausback, Joann Stock, Chris Farrar, and Arturo Martin.

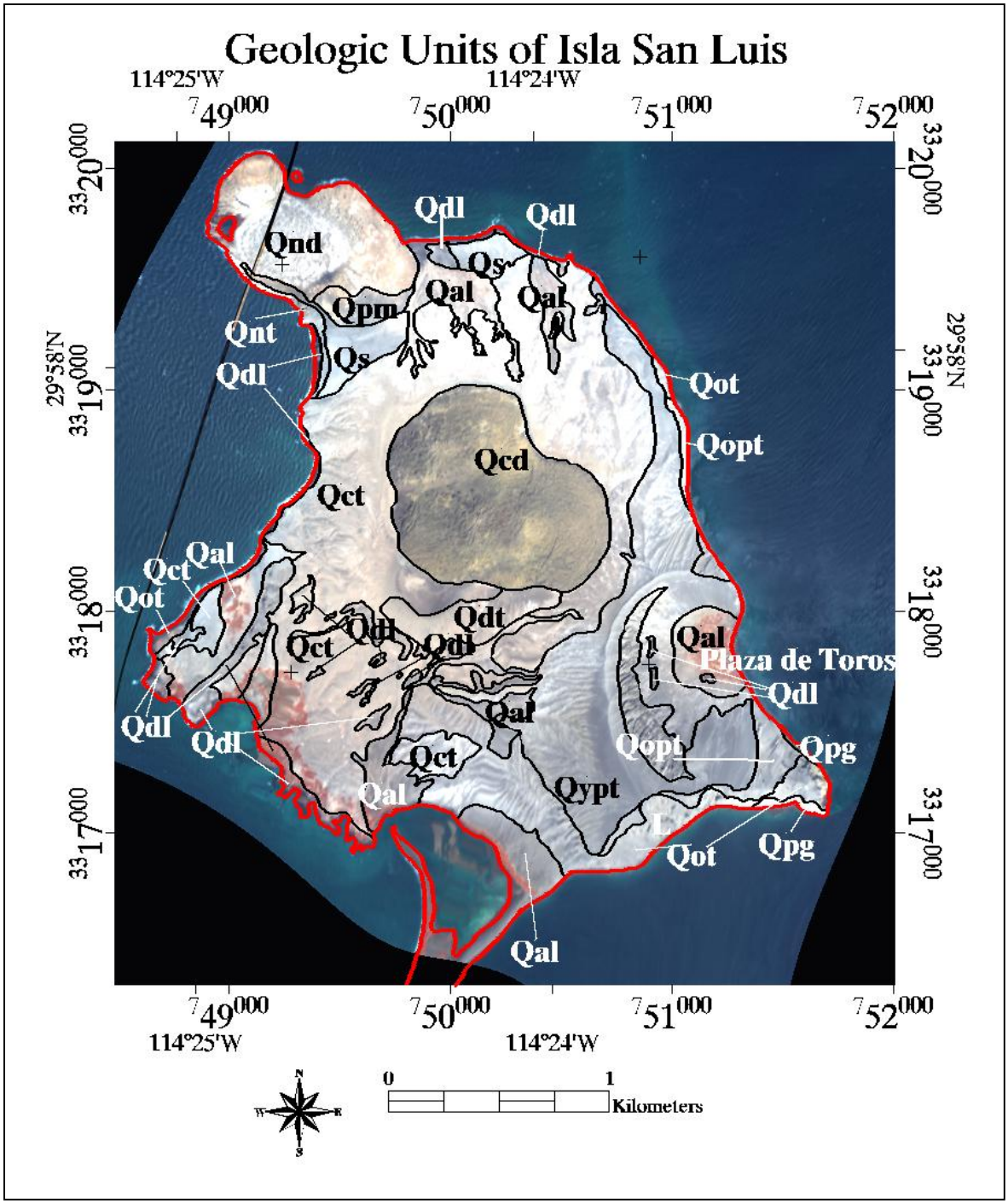

Figure 3. Geologic units according to MASTER image analysis and unpublished geologic mapping (conducted by Brian Hausback, Joann Stock, Chris Farrar, and Arturo Martin) overlain on the georectified, RGB MASTER image of Isla San Luis (Red=MASTER band 7, Green=MASTER band 4, Green=MASTER band 1). The unit abbreviations are described in Table 1. Map datum and projection: NAD27 Mexico, UTM zone 11R. This image is part of MASTER image 9900302L, acquired on April 29, 1999.

Paz-Moreno and Demant [1999] analyzed 29 samples from Isla San Luis, including basalts, basaltic andesites, andesites, dacites, and rhyolites. *Paz-Moreno and Demant* [1999] plotted the $Na_2O + K_20$ wt. % vs. SiO_2 wt. % values of these samples on a TAS diagram [*Le Bas et al.*, 1986]; K_20 wt. % vs. SiO_2 wt. % values of these samples according to *Peccerillo and Taylor* [1976] and *Le Maitre* [1989]; and the Na_2O, K_20, Fe_20_3, FeO, MgO and MnO values on an AFM diagram. With this analysis, *Paz-Moreno and Demant* [1999] determined that these samples were sub-alkaline, transitional between calc-alkaline and tholeiitic, and follow a clear basaltic andesite to rhyolite trend. The absence of Fe-Ti oxides in the more mafic, older units and the low-K_20 contents of the more silicic, younger units show a tholeiitic affinity. But, the high Rb, Ba, Th, and negative anomalies of Ta, Nb, and Ti reveal a calc-alkaline affinity of the source magma. *Paz-Moreno and Demant* [1999] determined that the evolution from mafic to more silicic eruptions indicated that the source magma was a closed system, but that the increasing Th/Ta and Th/La ratios as the magma evolved and the high rhyolite to basalt ratio suggest that there was some assimilation of crustal material at a shallow depth. Similar to the explanation for transitional geochemical affinities of the basalts dredged in the Guaymas basin [*Saunders et al.*, 1982], *Paz-Moreno and Demant* [1999] suggest the magma chamber might have been contaminated by the Cretaceous Baja California batholith. Thus, a component of calc-alkaline geochemistry could have been inherited from the vanished Cretaceous subduction component.

5.3 Field Geology

Three field excursions were made to Isla San Luis (May 2000, October 2001, and January 2003). The objective of these trips was to do field reconnaissance and collect soil temperatures, gas measurements, and bathymetric data.

Unpublished geologic mapping and stratigraphy (Brian Hausback, pers. comm.) support an eruptive evolution beginning with shallow marine deposition of palagonitic basaltic-andesite tuff. This is overlain by a locally thick sequence of andesite and dacite proximal fall and surge lapilli tuff deposits with minor glassy dacite lavas. Overlying the intermediate sequence are rhyolitic fall and pyroclastic flow deposits associated with the northern and central rhyolite domes (Fig. 3).

Gas was collected and measured in situ during our field work by Chris Farrar near the rhyolitic domes of ISL and on gas bubbles detected in the water north of ISL ("G," Fig. 4). These measurements show that there are fumarolic gas emissions from both the northern rhyolite dome and offshore marine vents. Sulfurous gas was detected at the base of the northern rhyolite dome, but the offshore vents mostly emit methane [*Farrar*, pers. comm.]. Helium isotopic analyses indicate a petroleum source for the methane [*Farrar*, pers. comm.].

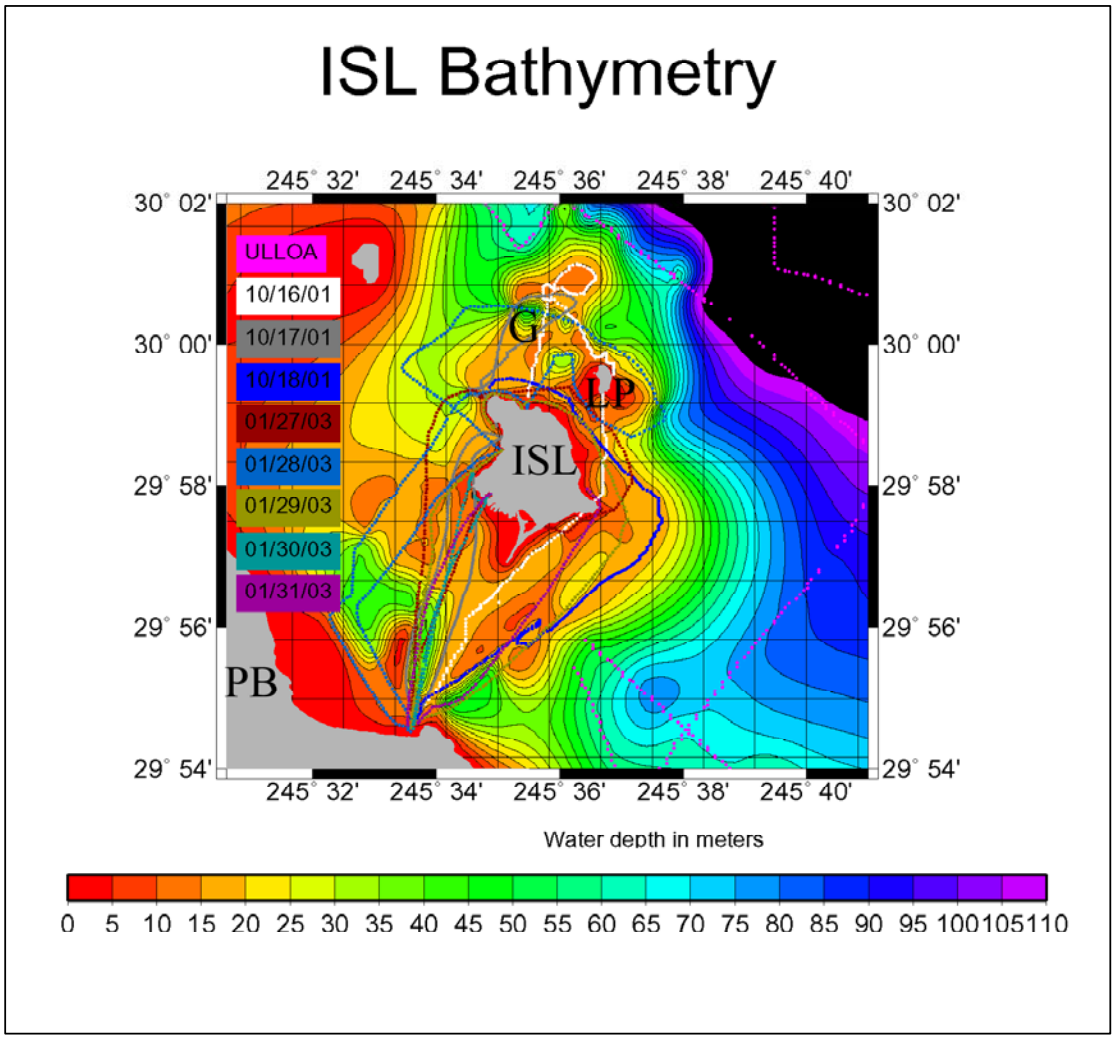

Figure 4. Bathymetry around Isla San Luis. Each dot on the map represents a depth measurement. Colors of the measurement locations are according to the dates of acquisition shown on the left. The ULLOA locations refer to the depth measurements acquired on Francisco de Ulloa cruise 9905-79 in 1999. ISL=Isla San Luis; LP= Isla la Poma; PB= Punta Bufeo; G=Location of detected methane gas bubbles.

Additionally, Chris Farrar deployed temperature loggers approximately 85 to 90 cm below the surface at three locations on ISL and one control location on the mainland (at Punta Bufeo). These temperature loggers recorded for over one year (from October of 2001 to January of 2003). The results show significantly higher temperatures on ISL than those recorded at Punta Bufeo [*Farrar*, pers. comm.]. The temperature logger

located at the base of the northern dome of ISL, near the location of the most recent volcanic activity, recorded a temperature that was, on average, 6 °C above the temperatures recorded at Punta Bufeo. The other two temperature loggers on ISL had temperatures intermediate between those measured at Punta Bufeo and the higher temperatures recorded at the northern rhyolite dome.

The morphology of ISL indicates that it has erupted very recently. The island has steep-sided tephra sea cliffs to the southeast that are eroding quickly (recent landslides) yet still have an elevation of over 100 meters (Fig. 5). A K-Ar date of 11.7 Ma was obtained on the intermediate lavas exposed along the western shore [*Rossetter*, 1973]. However, analyses on samples collected during our May 2000 fieldwork show that volcanism on ISL began at least 4,725 years before present and continued until perhaps 1,200 years ago [*Hausback et al.*, 2003]. *Hausback et al.* [2003] analyzed seven marine mollusk shells by ^{14}C acceleration methods to date beach deposits at three stratigraphic levels interbedded with the volcanic layers on ISL. The shells were embedded in beach deposits directly below the youngest of the pyroclastic deposits on the island. These young pyroclastic deposits are coarse, rhyolitic, breadcrust bomb-containing tephras associated with the early eruptive stages of the central rhyolitic domes. These marine mollusks, situated approximately 21 m above sea level, yield a maximum age of 2,888 to 3,289 ybp. Additionally, we dated three mollusks from sand deposits below the intermediate lavas exposed along the NW beach cliffs. These yield a maximum age of 3,036 to 3,289 ybp for the intermediate lavas. One mollusk embedded in the oldest palagonitic pyroclastic deposits exposed near sea level was dated at 4469 - 4725 ybp. Using these dates, it can

be determined that ISL has been uplifted at approximately 0.7 cm/yr[31] for the last ~3000 years.

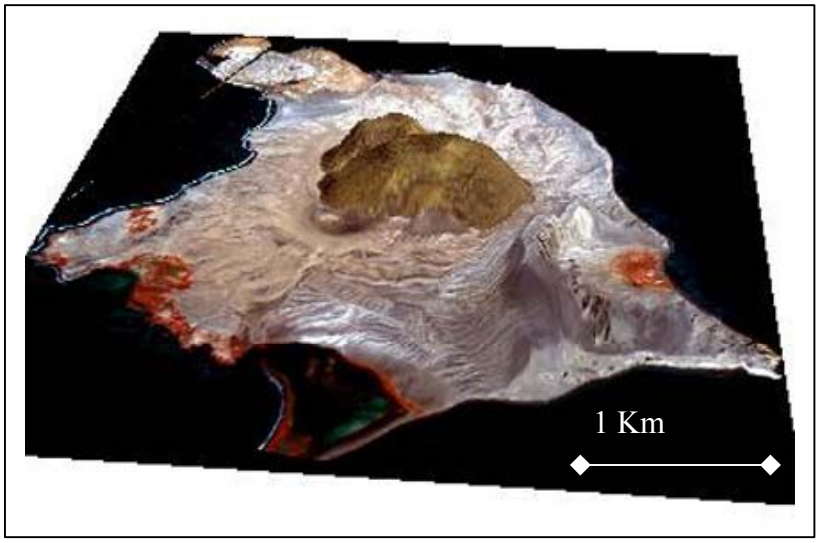

Figure 5. The MASTER image (Master bands 7= Red; 4=Green; 1=Blue) of Isla San Luis draped over a digital elevation model constructed with aerial photographs by Shaun Healy and Chloe Winant. This image is part of MASTER image 9900302L, acquired on April 29, 1999.

Hausback et al. [2003] used obsidian hydration analysis to date the youngest coarse, rhyolitic breadcrust-bomb-containing tephras associated with the early eruptive stages of the growth of the central rhyolite domes. Hydration rinds of 3.6 and 3.7 microns were measured for two separate bombs (averages of 5 measurements each). The hydration rate for obsidian in this region has not been established; however, a typical hydration rate of 2.98 microns/1,000 years yields an age of 1225 years for this tephra [*Hausback et al.*, 2003].

[31] This is a minimum estimate. Global deglaciation following the last glacial maximum involved a series of millennial-scale climate changes that resulted in global sea level rise [*Fairbanks*, 1989].

5.4 Bathymetric Map

Because no detailed bathymetry existed for the region around Isla San Luis, it was measured as part of this study (Fig. 4). On motorboat trips between the island and the peninsula, we measured depth every 30 seconds, using a Garmin Fish Finder 100 Blue, dual frequency (50 MHz/200 MHz) echo sounder. The speed of the boat varied. On average, the measurements are spaced every 70 meters, with the distance between measurements varying from less than one meter to over 100 meters. Locations were obtained simultaneously with depth from a hand-held GPS unit (Garmin GPS III+). The depths to the north, east, and southeast are also constrained by bathymetric data collected on a previous scientific cruise in the region [the Francisco de Ulloa 9905-79 operated by the Centro de Investigacion Cientifica y Educacion Superior de Ensenada (CICESE), Ensenada, Mexico]. The coastline was digitized from the 1:50,000 Punta Bufeo topographic map, available through Instituto Nacional de Estadistica Geografia y Informatica de Mexico. Our measured depths were corrected for the ocean tides using the Mar 0.5 software available through CICESE (http://oceanografia.cicese.mx/predmar/marques.html). The depth measurements were plotted using Generic Mapping Tools (GMT) with nearest neighbor resampling (*nearneighbor*) on a 5 second by 5-second grid, and the minimum curvature technique (*surface*) was used for smoothing.

The coverage is not extensive, but a few things can be noted. There are local maxima in the bathymetry in the region of detected gas bubbles ("G," Fig. 4). There were also gas

bubbles seen in deeper water (~30 m depth). We see no evidence for a SW-NE active fault through the island and adjacent seafloor in disagreement with current maps [*Paz-Moreno and Demant*, 1999], but there is a trough inland of the island that could indicate a fault in that region. ISL and its neighbor, Isla la Poma volcanic island, lie along a NW projection of volcanic knolls imaged in seismic data to the south [*Persaud et al.*, 2003] (Fig. 2). This NW trend of seamounts and volcanic islands could indicate a "leaky" transform fault extension of the Ballenas transform fault zone.

5.5 MASTER analysis

The following two sections discuss the analysis and results of the MODIS-ASTER (MASTER) data. Analysis of the VNIR-SWIR MASTER data (channels 1 - 25) yields a classification map (Fig. 6). Analysis of the TIR MASTER data (channels 41 - 50) yields a weight percent silica map (Fig. 7). This image analysis was done on the full-resolution (5 meter pixel size) MASTER data.

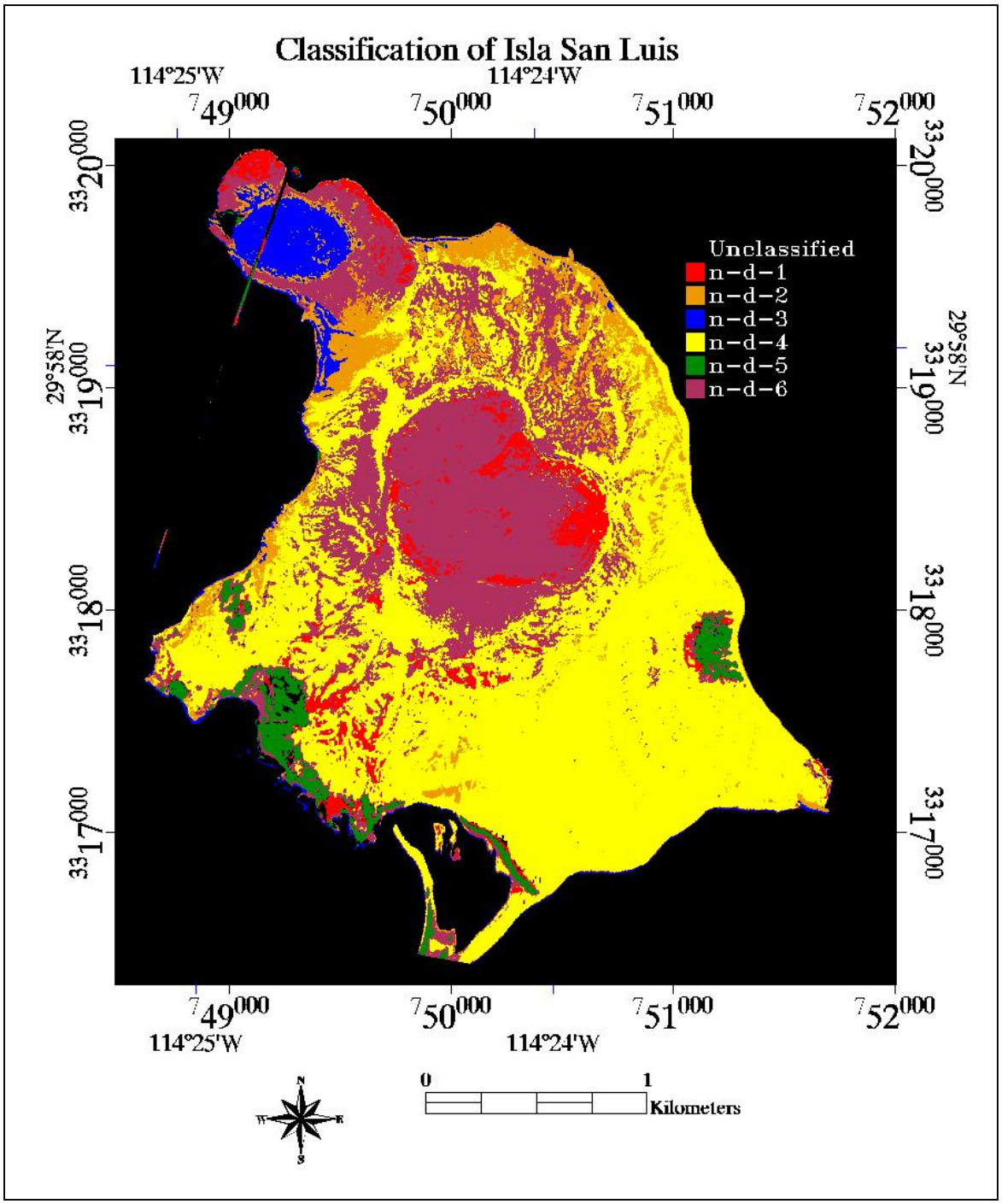

Figure 6. Classification map of Isla San Luis. The endmembers' colors are located in the upper right-hand corner. Unclassified pixels are black. Map datum and projection: NAD27 Mexico, UTM zone 11R. This image is part of MASTER image 9900302L, acquired on April 29, 1999.

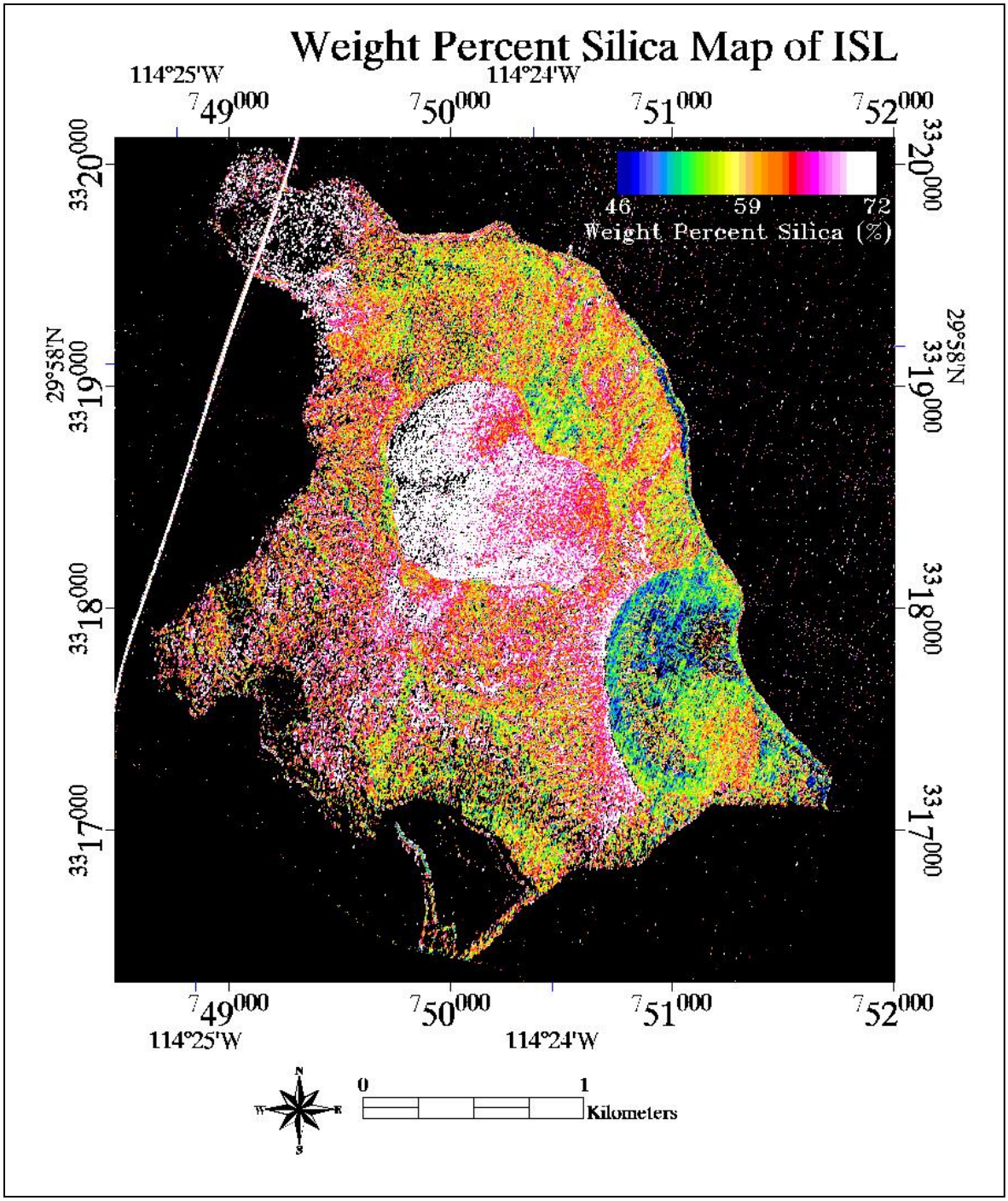

Figure 7. Weight percent silica map of Isla San Luis. Weight percent silica values are according to the blue to white color ramp shown in the upper right-hand corner of the image. Map datum and projection: NAD27 Mexico, UTM zone 11R. This image is part of MASTER image 9900302L, acquired on April 29, 1999.

5.5.1 Classification

Following the same methods of the analysis discussed in Chapter 2 for the 28 images of VNIR-SWIR MASTER data in the Tres Vírgenes-La Reforma Volcanic Region (TVLRVR), the MASTER image of ISL was atmospherically corrected and classified. The MASTER image for ISL, however, had no field spectra available for verification or for use in an empirical line calibration. (We did not have a safe way to transport the field spectrometer to the island.) Field spectra were available for regions inland, within the Puertecitos Volcanic Province, but these regions were not suitable for an empirical line calibration (no homogeneous dark and light regions within one image).

The VNIR-SWIR MASTER data for ISL were atmospherically corrected to a reasonable accuracy with the ACORN ENVI plug-in, as described in Chapter 2. A visibility of 100 km and a precipitable water vapor of 1.8 mm were used. The MASTER VNIR-SWIR data were also classified with the empirical line calibration coefficients determined from the TVLRVR. The results of these two atmospheric corrections varied primarily in their intensity values for the 18 bands least affected by water vapor (bands 1 - 10, 12 - 14, and 20 - 24); the spectral signatures of the pixels were very similar, regardless of which method was used to correct the data. Since the relative accuracy of these two corrections could not be determined without field spectra, the ACORN result was used for further processing to demonstrate the results of atmospheric correction without field spectra.

Classifying the atmospherically corrected MASTER data, resized to exclude the bands highly affected by water absorption (bands 11, 15 - 19, and 25), was done by choosing endmembers with the highest Pixel Purity Index (PPI^{TM}) values. This yielded a classification map that roughly delineated surfaces that vary in their secondary minerals, produced by weathering and alteration, namely ferric oxides, hydrates, hydroxyls, and carbonates. Attempts to identify these minerals using ENVI's Spectral Analyst^{TM} are described below. The resulting classification map is shown in Figure 6.

The atmospherically corrected MASTER data for ISL were not as suitable for mineral identification as those for the TVLRVR, discussed in Chapter 4, due to the lack of field spectra. There is not a wide range of easily identifiable secondary minerals present. Additionally, the Spectral Analyst^{TM} is only moderately helpful in determining the lithology of the surfaces represented by each endmember. In most cases, the identifications are not so absolute that a particular mineral can be assumed to constitute a large portion of the represented surface without auxiliary knowledge of the surface represented by the endmember. However, a few careful observations were made by analysis of the continuum-removed library spectra, convolved to the MASTER channels and the continuum-removed endmember spectra (Chapter 2, this thesis). Surfaces with iron oxides have small features in the continuum-removed MASTER bands 2, 3 and 8. Surfaces with a large amount of vegetation have large features in the continuum-removed MASTER band 5. Surfaces containing Al-OH minerals typically have small features in the continuum-removed MASTER bands 21 and 22. Surfaces containing Mg-OH minerals typically have small features in the continuum-removed MASTER band 23.

Surfaces containing carbonate minerals typically have small features in the continuum-removed MASTER band 22. Hydrate minerals usually show a small feature in continuum-removed MASTER band 23.

Endmembers for the atmospherically corrected VNIR-SWIR data from ISL were analyzed with the Spectral Analyst™, and the top five matches to the USGS spectral library are shown in Appendix B. The scores of the matches are according to the scheme described in Chapter 2: The output from the Spectral Analyst™ is a number from zero to 2, with two being a perfect match with both the SAM and SFF™ spectral matching algorithms, with each contributing one point. Due to the poorly constrained nature of the atmospherically corrected data, however, these identifications were not relied upon too heavily for identification of the endmembers. ISL is a small island with fairly well understood geologic units that can easily be related to the endmembers. What follows is a brief description of each endmember shown in Figure 6.

"n-d-1": Pixels identified as this endmember are most common in small regions on the edges of the central and northern rhyolite domes. The small feature in bands 2 and 3 for this endmember (Fig. 8) is similar to the features of iron oxide minerals discussed in Chapter 2. Endmember "n-d-1," therefore, most likely represents iron oxide on the surface of the domes. However, iron oxide is more commonly an alteration product of mafic rocks. The most likely origin of the iron oxide is from the seafowl excrement (guano) known to exist in these regions.

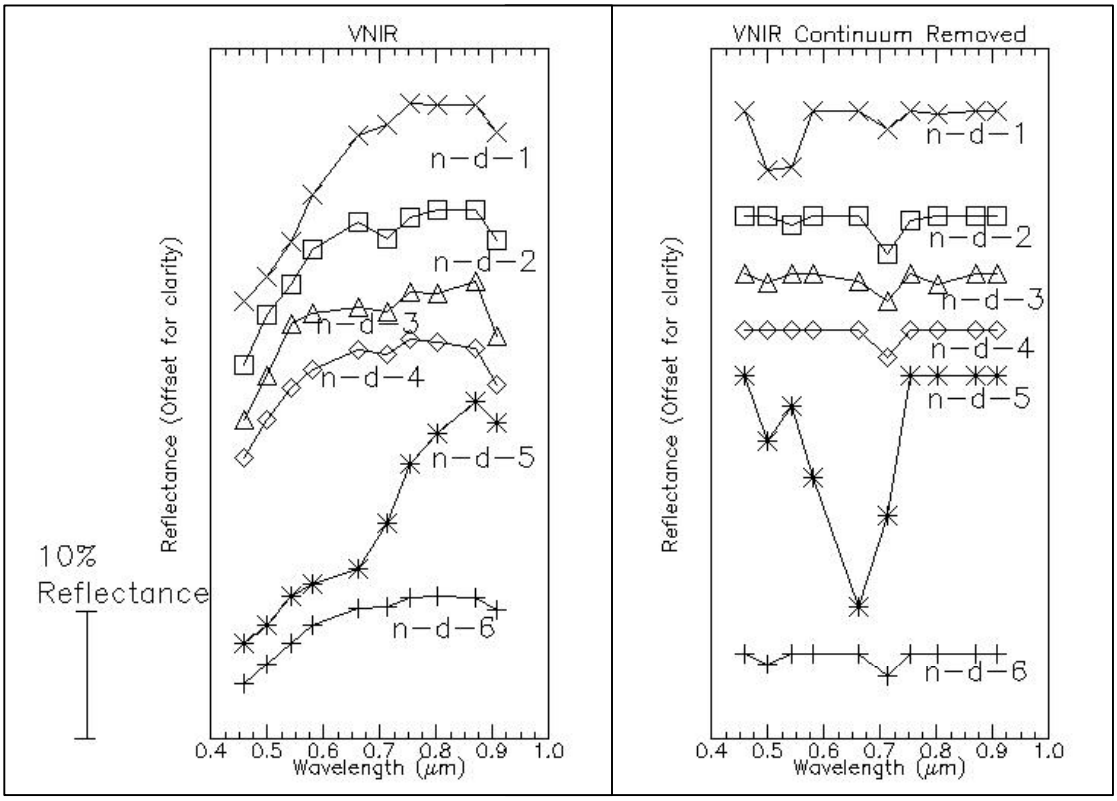

Figure 8. Shown on the left are the reflectance spectra of the endmembers for the VNIR wavelength bands (bands 1-10). Shown on the right are the spectra with their continua removed. The spectra are offset for clarity, and the bar in the lower left hand corner represents the scale on the y-axis.

"n-d-2": Pixels identified as this endmember are most common in sandy surfaces and a known region of phreatomagmatic deposits just south of the northern dome. The SWIR spectrum of this endmember (Fig. 9) does not show absorption features that can be clearly related to any specific minerals in the USGS spectral library. It is likely that the large absorption feature seen in the continuum-removed SWIR spectrum (Fig. 9) for endmember "n-d-2" is due to a hydroxyl-bearing mineral, but identifying this mineral is not possible.

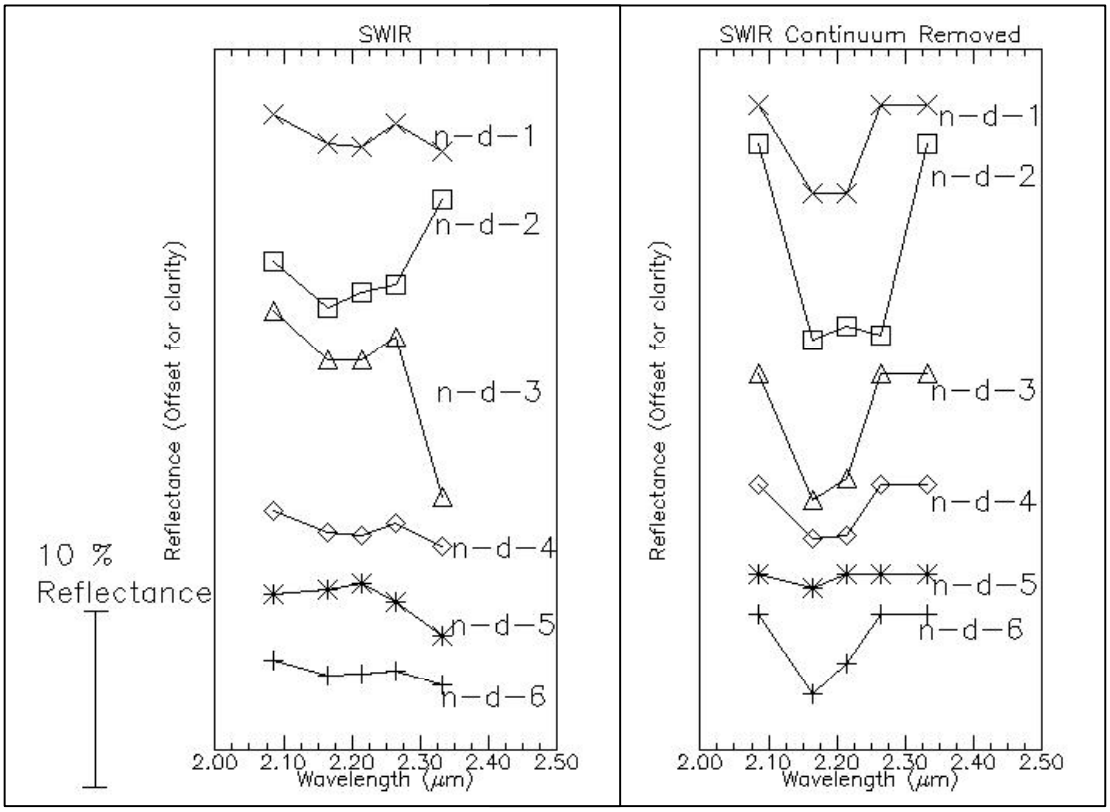

Figure 9. Shown on the left are the reflectance spectra of the endmembers for the SWIR wavelength bands (bands 20-24). Shown on the right are the spectra with their continua removed. The spectra are offset for clarity, and the bar in the lower left hand corner represents the scale on the y-axis.

"n-d-3": Pixels identified as this endmember are most common in the central portion of the northern rhyolite dome. From fieldwork done in this region, it is known that this rhyolite dome is covered by a large amount of seafowl excrement composed primarily of calcium phosphate (monetite). In some cases the deposits are up to 20 cm thick. No VNIR or SWIR spectra of monetite are available for comparison.

"n-d-4": Pixels identified as this endmember cover a large portion of the island, primarily the regions known to be composed of volcanic tephra with breadcrust obsidian bombs. Endmember "n-d-4" represents this surface of rhyolitic tephra. From observations in the field, we know that much of this surface is also covered in guano.

Based on the match to the spectral library (Appendix B), it is possible that the SWIR spectrum is partially controlled by the presence of the mineral alunite[32] or another hydroxyl-bearing alteration mineral or a portion of monetite. A sample of alunite within the USGS spectral library yields the 7th most likely match to endmember "n-d-4," with a score of 1.902.

"n-d-5": Pixels identified as this endmember are found in regions with a high density of vegetation. The location of vegetation on ISL is known from the field and a previous report [*Paz-Moreno and Demant*, 1999]. It is also obvious from Figure 8 that endmember "n-d-5" represents vegetation, with its strong absorption feature at band 5 in the continuum-removed VNIR spectral.

"n-d-6": Pixels identified as this endmember make up the bulk of the central rhyolite dome and portions of the northern rhyolite dome. These rhyolite domes are composed of coarsely vesicular rhyolite and obsidian. Mordenite and montmorillonite are typical hydrous alteration products of rhyolite glass [*Deer et al.*, 1967] and their spectral signature could be expected in the SWIR spectra of this endmember. However, there is no indication of the presence of these minerals in the SWIR spectra. This is probably due to the recent formation of the central dome and its lack of surface alteration. The small feature in the continuum-removed spectra of all endmembers at band 6 does not reveal any specific geochemistry but may indicate an incomplete atmospheric correction by ACORN.

[32] Alunite, as discussed in Chapter 2, forms from the action of sulfuric acids (often from hydrothermal solutions) upon potassium rich feldspars [*Klein and Hurlbut*, 1985].

5.5.2 Weight Percent Silica Map

As discussed in Chapter 3, the shift to longer wavelengths of the main spectral feature in the thermal infrared wavelength region (Reststrahlen band) as the mineralogy changes from felsic to mafic was utilized to map weight percent silica, using the MASTER data. Chapter 3 describes an approach for determining the size of this wavelength shift using a Gaussian curve. The size of this shift is translated into weight percent SiO_2 of the surface using a reference curve, derived from laboratory data.

The results indicate that the general approach tended to underestimate the weight percent SiO_2 in the image[33]. This discrepancy was removed by fine-tuning the general approach with measurements from samples taken in the field and measured with a lab spectrometer (a site calibration) and provided good results in the calculated weight percent SiO_2, with an average error of ± 3%. Chapter 3 discussed the verification of this method using a small subset of the MASTER TVLRVR dataset. Chapter 4 discussed the results for the entire TVLRVR. For this chapter, a portion of MASTER image 9900302L, which includes Isla San Luis, was processed to weight percent silica, georectified, and site calibrated. The georectification was done as described in Chapter 2 for the VNIR-SWIR MASTER data.

The atmospheric correction for the TIR data was verified, as described in Chapter 3, by examining the temperature measurements for pixels in the seawater. By averaging over

[33] In the Hiller Mountains test region, discussed by *Hook et al.* [2005], results indicate the general approach slightly overestimates the weight percent SiO_2 of low silica rocks (e.g. basalt) and underestimates the weight percent SiO_2 of high silica rocks (e.g. granite).

28,000 pixels surrounding the island in image 9900302L, the range in temperatures for bands 42 - 49 (the bands used for the weight percent silica map) were within one degree (Table 2). The resulting weight percent silica map, therefore, was produced from emissivity values that were atmospherically well corrected.

	Temperature (°C)			
Band	Min	Max	Mean	Standard Deviation
42	15.06	18.09	16.62012	0.38896643
43	15.76	17.71	16.76448	0.24682832
44	15.51	17.79	16.65273	0.27209282
45	15.49	17.76	16.5955	0.28010618
46	15.45	17.71	16.61902	0.28985568
47	15.69	17.72	16.67956	0.25878568
48	15.2	17.86	16.54141	0.32908467
49	13.69	19.45	16.60902	0.70801115

Table 2. Table of water temperatures retrieved from the TIR MASTER data near Isla San Luis. These were retrieved from image 9900302L taken on April 29, 1999.

In order to correct for misleading high weight percent silica values for surfaces of water, high-density vegetation, and surfaces containing a large percentage of aphyric rocks[34], the data were masked, as discussed in Chapter 4. The site calibrated, georectified, masked weight percent silica map of ISL is shown in Figure 7. In this image it is clear that the central and northern (within portions not heavily covered by guano) rhyolite domes are mapped as the highest weight percent silica and the more mafic tuffaceous deposits from Plaza de Toros are mapped as a lower weight percent silica. An average of 48 pixels within the central dome yielded a weight percent silica of 66 ± 3 % (one standard deviation of 3.72). The dacitic lavas that crop out in the walls of Plaza de Toros

[34] Water, vegetation, and surfaces of aphyric rocks have fairly flat TIR spectra. These spectra typically are erroneously fit with Gaussian curves with minima toward lower wavelengths, which misidentify the pixels as containing high weight percent silica.

have a weight percent silica of 60 ± 3% (one standard deviation of 2.48) based on 16 pixels located in this unit. The vast majority of the rocks, from the basaltic andesites to the rhyolites, are largely aphyric [*Paz-Moreno and Demant*, 1999], however. This aphyric nature of the rocks on the surface of ISL could prohibit accurate assignment of weight percent silica values to each pixel using the TIR data, as discussed in Chapter 3. However, the measurements from the image, discussed above, are roughly in agreement with the analyses on these field samples, reported by *Paz-Moreno and Demant* [1999], with the older volcanic products assigned lower weight percent silica values and the younger rhyolite domes appearing to have higher weight percent silica values.

Within the unit mapped as Qypt in Figure 3, which makes up most of the surface of Plaza de Toros, there is an obvious disagreement between weight percent silica values on either side of the crater rim, with the rim flank having a higher weight percent silica. This disagreement could be caused by a difference in composition of the freshly exposed tuff in the cliff wall and the eroded material on the western flank of the crater. It is possible that more mafic minerals in the tuffaceous unit have been weathered out of the detritus on the western flank, thus leaving a more siliceous surface.

Most likely the discrepancy in unit Qypt is due to the shortcomings of the temperature emissivity separation algorithm (TES), discussed in Chapter 4. The weight percent silica technique works well overall, but the inaccuracy of the temperature emissivity separation method in regions of high topographic relief and low solar angle prove to lessen the ability of the Gaussian fitting technique to accurately estimate the weight percent silica.

Gillespie et al. [1998] validated this separation technique only in flat regions (playas and ponds), but ISL is a region with high topographic relief. In particular, the interior crater wall at Plaza de Toros is exceptionally steep so the method may work more poorly here than on the gentler western flank of the crater.

The effect of the incomplete temperature emissivity separation appears as flattening of the spectral signature, thus changing the weight percent silica values. Pixels that are in the shadows have elevated weight percent silica values. The temperature emissivity technique, and therefore the weight percent silica technique, works best on flat terrains, or with images collected at very near solar noon. The MASTER image of ISL was acquired at 18:11 GMT, 11:11 local time. At this time, the sun was at an altitude of 65.3º, with an azimuth of 124.4º (E of N). Thus, the pixels with strongest illumination would have been those on east and southeast facing slopes, and those in the shadows are on west facing slopes. The high topographic relief of ISL makes it possible that the weight percent silica map shown in Figure 7 is heavily affected by the incomplete separation of temperature and emissivity, rather than purely variations in geochemistry. Regions in the shade have erroneously higher weight percent silica than those in direct sunlight. The overall weight percent silica values, however, are not entirely in disagreement with the mapped units. The older, more mafic volcanic products are assigned lower weight percent silica values and the younger rhyolite domes are mapped as higher weight percent silica values.

5.6 Discussion

The weight percent silica map and the classification of the VNIR-SWIR data are only moderately helpful in delineating known geologic units on ISL. The weight percent silica map appears to be influenced by shadows, a product of the variable topographic slopes and low solar angle at the time of image acquisition. The weight percent silica technique appears to work best on flat regions or with images acquired with high solar angles (near solar noon).

There is likely some significance to NW alignment of Isla San Luis with submarine volcanic knolls identified in seismic reflection data [*Persaud et al.*, 2003] (Fig. 2). The western side of the Lower Delphin Basin, just southeast of ISL, is the most tectonically active of the basins in the northern Gulf of California [*Persaud et al.*, 2003]. The NW trend of ISL, Isla la Poma, volcanic knolls imaged just north of Isla Angel de la Guarda, and volcanic knolls to the northeast of ISL could indicate a "leaky" transform fault extension of the Ballenas transform fault zone. Similar seamounts and volcanic islands are known to exist near other leaky transform faults, including Rocas Alijos, a volcanic edifice originating from a leaky transform fault on the Pacific side of Baja California Sur [*Davis et al.*, 1995].

5.7 Conclusion

The MASTER data were used to map the extent of the volcanic deposits on Isla San Luis island. The weight percent silica map produced from TIR data and the classification produced from the VNIR-SWIR data moderately delineate the geologic units. The lack

of easily identifiable alteration minerals and the high percentage of surface area covered in seafowl excrement diminish the effectiveness of the MASTER image analysis. Also, the sharp topography of ISL and the low solar angle cause the weight percent silica map (Fig. 7) to be heavily affected by the incomplete separation of temperature emissivity using the TES algorithm. This results in erroneously higher weight percent silica values for regions that are in shadows during the time of image acquisition.

Careful analysis of the bathymetric data suggests a tectonic origin of Isla San Luis along a leaky transform fault within the transtensional regime of the Gulf of California. This interpretation is in agreement with other volcanic observations, including the presence of fumarolic gas emissions that continue today from the northern rhyolite dome. Isotopic dates on mollusk shells from beach deposits interbedded with the volcanic layers on ISL yield ages from 4725 to 2888 ybp. The latest eruptions are younger but undated. Based on these dates and their present elevations, I estimate that ISL has been uplifted at approximately a rate of ~0.7 cm/yr for the last ~3000 years. Isla San Luis, Isla la Poma, and imaged volcanic seamounts north and south of ISL are aligned along a northwesterly trend, which appears to be an extension of the nearby Ballenas transform fault zone in the Gulf of California. This evidence of recent volcanism suggests ISL remains potentially active.

References

Davis, A.S., S.H. Gunn, W.A. Bohrson, L.B. Gray, and J.R. Hein, Chemically Diverse, Sporadic Volcanism at Seamounts Offshore Southern and Baja-California, *Geological Society of America Bulletin*, *107* (5), 554-570, 1995.

Deer, W.A., R.A. Howie, and J. Zussman, *Rock-Forming Minerals*, 270 pp., Longmans Green and Co., Ltd., London, England, 1967.

Fairbanks, R.G., A 17,000-Year Glacio-Eustatic Sea-Level Record - Influence of Glacial Melting Rates on the Younger Dryas Event and Deep-Ocean Circulation, *Nature*, *342* (6250), 637-642, 1989.

Farrar, C.D., Hydrologist and Volcanologist for the USGS, Lake Tahoe, California.

Gastil, G.R., The record of Cenozoic volcanism around the Gulf of California, *Geological Society of America Bulletin*, *90* (839-857), 1979.

Gastil, G.R., R.P. Phillips, and A.E. C., Reconnaissance geology of coastal Sonora between Puerto Lobos and Bahia Kino, *Geological Society of America Memoir*, *140*, 170, 1975.

Gillespie, A.R., S. Rokugawa, T. Matsunaga, S.J. Cothern, S.J. Hook, and A.B. Kahle, A temperature and emissivity separation algorithm for advanced spaceborne thermal emission and reflection radiometer (ASTER) images, *IEEE Transactions on Geoscience and Remote Sensing*, *36* (4), 1113-1126, 1998.

Hausback, B.P., A. Cook, C.D. Farrar, A. Martin, F. Paz-Moreno, J.M. Stock, and J.E. Dmochowski, Isla San Luis volcano, Baja California, Mexico - late Holocene eruptions, in *Geological Society of America, Cordilleran Section*, Puerto Vallarta, Jalisco, Mexico, 2003.

Hook, S.J., J.E. Dmochowski, K.A. Howard, L.C. Rowan, K.E. Karlstrom, and J.M. Stock, Mapping variations in weight percent silica measured from multispectral thermal infrared imagery—Examples from the Hiller Mountains, Nevada, USA and Tres Vírgenes-La Reforma, Baja California, Baja California Sur, Mexico, *Remote Sensing of Environment*, *95*, 273-289, 2005.

Klein, C., and C. Hurlbut, *Manual of Mineralogy*, 596 pp., John Wiley & Sons, New York, 1985.

Klitgord, K.D., and J. Mammerickx, Northern East Pacific Rise - Magnetic Anomaly and Bathymetric Framework, *Journal of Geophysical Research*, *87* (NB8), 6725-&, 1982.

Le Bas, M.J., R.W. Le Maitre, A. Streckeisen, and B. Zanetti, A chemical classification of volcanic rocks based on the total alkali-silica diagram, *Journal of Petrology*, *27*, 745-750, 1986.

Le Maitre, R.W., *A classification of igneous rocks and glossary of terms: recommendations of the IUGS, subcommission on the systematic of igneous rocks*, 193 pp., Blackwell Sci. Publ., London, 1989.

Lewis, C.J., and J.M. Stock, Late Miocene to recent transtensional tectonics in the Sierra San Fermín, northeastern Baja California, Mexico, *Journal of Structural Geology*, *20* (8), 1043-1063, 1998.

Lonsdale, P., Geology and tectonic history of the Gulf of California, in *The Eastern Pacific Ocean and Hawaii*, edited by D.M. Hussong, E.L. Winterer, and R.W. Decker, pp. 499-521, Geological Society of America, Boulder, Colorado, 1989.

Mammerickx, J., and K.D. Klitgord, Northern East Pacific Rise - Evolution from 25 My Bp to the Present, *Journal of Geophysical Research*, *87* (NB8), 6751-6759, 1982.

Martín, A., J.M. Fletcher, M. López-Martínez, and R. Mendoza-Borunda, Waning Miocene subduction and arc volcanism in Baja California: the San Luis Gonzaga volcanic field, *Tectonophysics*, *318* (1-4), 27-51, 2000.

Martin-Barajas, A., J.M. Stock, P. Layer, B. Hausback, P. Renne, and M. Lopez-Martinez, Arc-Rift Transition Volcanism in the Puertecitos Volcanic Province, Northeastern Baja-California, Mexico, *Geological Society of America Bulletin*, *107* (4), 407-424, 1995.

Nagy, E.A., M. Grove, and J.M. Stock, Age and stratigraphic relationships of pre- and syn-rift volcanic deposits in the northern Puertecitos Volcanic Province, Baja California, Mexico, *Journal of Volcanology and Geothermal Research*, *93* (1-2), 1-30, 1999.

Oskin, M.E., J.M. Stock, and A. Martin-Barajas, Rapid localization of Pacific-North America plate motion in the Gulf of California, *Geology*, *29* (5), 459-462, 2001.

Paz-Moreno, F.A., and A. Demant, The Recent Isla San Luis volcanic centre: petrology of a rift-related volcanic suite in the northern Gulf of California, Mexico, *Journal of Volcanology and Geothermal Research*, *93* (1-2), 31-52, 1999.

Peccerillo, A., and S.R. Taylor, Geochemistry of Eocene Calc-Alkaline Volcanic-Rocks from Kastamonu Area, Northern Turkey, *Contributions to Mineralogy and Petrology*, *58* (1), 63-81, 1976.

Persaud, P., J.M. Stock, M.S. Steckler, A. Martín-Barajas, J.B. Diebold, A. González-Fernández, and G.S. Mountain, Active deformation and shallow structure of the Wagner, Consag, and Delfín Basins, northern Gulf of California, Mexico, *J. Geophys. Res.*, *108*, 2355, 2003.

Rossetter, R.J., Geology of the San Luis and San Lorenzo Island Groups, Gulf of California, Masters of Science thesis, California State University, San Diego, San Diego, 1973.

Rossetter, R.J., and G.R. Gastil, Isla San Luis, a rift volcano in the Gulf of California, *Geological Society of America Abstracts with Programs*, *3*, 187-188, 1971.

Saunders, A.D., D.J. Fornari, and M.A. Morrison, The composition and emplacement of basaltic magmas produced during the development of continental-margin basins: the Gulf of California, Mexico, *Journal of Geological Society*, *139*, 335-346, 1982.

Sawlan, M.G., Magmatic evolution of the Gulf of California rift, in *The Gulf and Peninsular Province of the Californias: American Association of Petroleum Geologists Memoir*, edited by J.P. Dauphin, and B.R. Simoneit, pp. 301-369, 1991.

Sawlan, M.G., and J.G. Smith, Late Cenozoic volcanic suites in northern Baja California Sur, Mexico; their relations to subduction and rifting along the Baja California peninsula, *Geological Society of America Abstracts with Programs*, *16*, 645, 1984.

Stock, J.M., and K.V. Hodges, Miocene to Recent Structural Development of an Extensional Accommodation Zone, Northeastern Baja-California, Mexico, *Journal of Structural Geology*, *12* (3), p. 315-328, 1990.

Stock, J. M., Relation of the Puertecitos Volcanic Province, Baja California, Mexico, to development of the plate boundary in the Gulf of California, in Delgado-Granados, H., Aguirre-Diaz, G., and Stock, J. M., eds., Cenozoic Tectonics and Volcanism of Mexico: Boulder, Colorado, Geological Society of America Special Paper 334, p. 143-156, 2000.

Zanchi, I., The Opening of the Gulf of California near Loreto, Baja- California, Mexico - from Basin and Range Extension to Transtensional Tectonics, *Journal of Structural Geology*, *16* (12), 1619-1639, 1994.

Chapter 6: Summary and Conclusions

6.1 Introduction

This chapter summarizes the results of this thesis, outlines suggestions for others working with MASTER data, and provides a few recommendations for future remote sensing instruments.

6.2 Summary of Conclusions

6.2.1 Data Analysis Conclusions

MASTER data can be atmospherically corrected to a reasonable accuracy with both the ACORN software and the Empirical Line Calibration mode in ENVI. If known spectra are available within one line for both a dark and light spectrum, the Empirical Line Calibration appears to be a more accurate method for the MASTER data. However, with either technique, a reliable correction is difficult to obtain for those bands in the water absorption region (MASTER bands 11, 15 - 19, and 25), even if atmospheric parameters are known.

Classifying the atmospherically corrected MASTER data, resized to exclude bands 11, 15 - 19, and 25, was done by choosing endmembers with the highest PPI^{TM} values. This yielded a classification map that roughly delineated surfaces that vary in their secondary minerals, produced by weathering and alteration, namely ferric oxides, hydrates, hydroxyls, and carbonates. Attempts to identify these minerals using ENVI's Spectral

Analyst™ were only moderately successful. It is necessary to have auxiliary information about the lithology of the underlying rock and secondary minerals within the surface represented by each endmember for precise lithologic identification.

Supervised classifications were produced for the MASTER images as well. A supervised classification has the advantage that the image does not need to be atmospherically corrected before classification. These classifications were made with classes of selected pixels within regions of known lithology. The classification of the remaining pixels was based on these classes. The results outlined surfaces that likely had similar geochemistry, but because they are based on an average of pre-selected pixels, they did not yield as much information about the surfaces as the unsupervised classification scheme.

Aside from classifications, the MASTER data were also used to test a new technique for remotely estimating the weight percent SiO_2 of silicate rocks exposed on the surface. The technique uses laboratory emissivity data from widely available spectral libraries to develop a relationship between the known shift in the Reststrahlen band to longer wavelengths and decreasing weight percent SiO_2. This relationship is then applied to the emissivity data extracted from the images. The relationship is shown to depend on how well the emissivity data encompass the Reststrahlen band. Different relationships were developed for various channel combinations as well as instruments. The channel combinations were selected to include the wavelength region that can be readily corrected for atmospheric effects typically encountered with airborne and spaceborne terrestrial thermal infrared data.

The results indicate that, using the relationship developed from the library data, the image derived weight percent SiO_2, on average, agrees with the field samples only to about 7 %. The library relationship tends to underestimate weight percent silica values. This difference can be attributed to the flattened emissivity spectra from the Tres Vírgenes -La Reforma Volcanic Region (TVLRVR), and it can be corrected based on the availability of a few field samples from the study region. With the site calibration, the image derived weight percent SiO_2, on average, agrees with the field samples to about 3%.

The weight percent silica technique works well overall, but the inaccuracy of the temperature emissivity separation technique in regions of high topographic relief lessens the ability of the Gaussian fitting technique to estimate accurately the weight percent silica. The effect of high topographic relief is to flatten the emissivity spectrum. Pixels that are in shadows, therefore, have elevated weight percent silica values. The temperature emissivity technique, and therefore the weight percent silica technique, works best on flat terrains, or with images collected at exactly solar noon.

The MASTER data were also used to map the extent of the volcanic deposits on ISL. The lack of easily identifiable alteration minerals and the high percentage of surface area covered in seafowl excrement diminish the effectiveness of the MASTER image analysis. Also, the sharp topography of Isla San Luis cause the weight percent silica map shown in Chapter 5 to be heavily affected by the incomplete separation of temperature emissivity using the TES algorithm.

6.2.2 Geologic Conclusions

The images constructed in this thesis in order to summarize and revise the previous geologic mapping done in the Tres Vírgenes-La Reforma Volcanic Region and Isla San Luis included a classification of atmospherically corrected MASTER multi-channel VNIR-SWIR data, a weight percent silica map based on atmospherically corrected MASTER TIR data, a mosaicked ASTER image, a Thematic Mapper image draped over a digital elevation model, and a bathymetric map around ISL. These images helped to delineate previously mapped units and revise erroneously mapped regions. The resulting updated maps aided in the understanding of the volcanic history of these regions.

Examination of the weight percent silica map in Chapter 4 suggests the intracaldera products of La Reforma are highly varied products of mafic to silicic eruptions. The more recent volcanic products on the flanks of the caldera are of mafic to intermediate composition. It is likely, however, that a portion of the mapped unit Qtb, Quaternary basaltic-andesite lavas, is more silicic than previously described by *Schmidt* [1975] and *Demant* [1984].

The TVLRVR is a volcanic region that has evolved in the last few million years from producing bimodal caldera structures (the La Reforma caldera and the El Aguajito volcanic complex), within a largely extensional regime, to lavas and domes (El Viejo and El Azufre) and most recently a stratovolcano (La Virgen) within a transtensional regime.

La Reforma likely is a caldera, due to its composition and morphology, as well as the existence of both ignimbrite outflow sheets and a megabreccia unit indicating a mass-wasting event associated with collapse. The central dome is not a block of Miocene Comondú volcanics, but is composed of welded ash-flow tuffs and lavas [*Hausback et al.*, 2000], more typical of a caldera resurgent dome. El Aguajito does not appear to fit the definition of a caldera, however. While it is possible that the rhyolitic domes surrounding the central dome could conceal a ring fracture, the lack of a megabreccia unit within the central portion of the volcanic complex and no recognizable collapse features prohibits a definitive identification of the El Aguajito volcanic complex as a caldera. There is a possibility that the magmatic piping of La Reforma and El Aguajito are connected and collapse took place only at the La Reforma caldera.

The Tres Vírgenes volcanoes appear to have erupted in the pull-apart basin between the Las Viboras and Tres Vírgenes fault zones. These eruptions are on average more mafic and less explosive than those that originated from the La Reforma caldera and the El Aguajito volcanic complex. But there is evidence of mixing between silicic magma bodies and hotter, more mafic rising magma in all the volcanic centers of the TVLRVR, which has led to the many Plinian eruptions in the region. In the second and most recent phase of eruptions, La Virgen appears to be following the differentiation from mafic to more silicic products.

Careful analysis of the bathymetric data suggests a tectonic origin of Isla San Luis along a leaky transform fault within the transtensional regime of the Gulf of California. This

interpretation is in agreement with other volcanic observations, including the presence of fumarolic gas emissions that continue today from the northern rhyolite dome. Isotopic dates on mollusk shells from beach deposits interbedded with the volcanic layers on ISL yield ages from 4725 to 2888 ybp. The latest eruptions are younger but undated. Based on these dates and their present elevations, I estimate that ISL has been uplifted at a rate of ~0.7 cm/yr for the last ~3000 years. Isla San Luis, Isla la Poma, and imaged volcanic seamounts north and south of ISL are aligned along a northwesterly trend, which appears to be an extension of the nearby Ballenas transform fault zone in the Gulf of California. This evidence of recent volcanism suggests ISL remains potentially active.

6.3 Recommendations for Working with MASTER

6.3.1 Recommendations for Bands 1-25

Despite much analysis of various atmospheric correction codes, the atmospheric correction for MASTER bands 1-25 was very difficult to obtain, particularly for the bands highly affected by water, bands 11, 15 - 19, and 25. In order to have a spectrum considered well-corrected, bands 11, 15 - 19, and 25 had to be excluded, which left only 18 bands for the spectral fitting algorithm. With only 18 bands, the accuracy of the spectral fitting algorithm was diminished, resulting in fits that had to be verified with auxiliary information. In this case, it was difficult to do unsupervised classifications. Future researchers using MASTER data in its current form might consider not attempting atmospheric corrections and undertaking only supervised classifications, particularly if there is no need to obtain information about secondary minerals on the surfaces. To do

this well, one would need to know the exact lithology of several rock types in the image in order to infer the lithology of other pixels with a similar spectral signature.

If atmospheric correction is still a specific goal with MASTER data, several spectrally light and dark regions should be imaged with a field spectrometer at solar noon. These light and dark regions should then be used to perform an empirical line calibration. If the goal is to mosaic several images and atmospherically correct them, as done in this study, it would be best if the reference spectra were taken from various parts of the mosaicked image and that each image in the mosaic is captured at nearly the same time of day under very similar atmospheric conditions.

6.3.2 Recommendations for Bands 41-50

The temperature emissivity separation technique and mapping of the weight percent silica work best if the image analyzed was acquired at solar noon and has little topographic variation within the image. Caution should be taken in analyzing an image with the techniques outlined in this thesis if the region has high topographic relief, or the image was not acquired very near solar noon. As done in this thesis, reasonable values for weight percent silica can be obtained with a site calibration; however, this involves using several well-known field samples. When using field samples for this purpose, the field sample should be part of a surface that is large and easily identified in the image. The laboratory spectrum or field spectra of the sample should be taken of the surface that is exposed in the image. Additionally, samples should be acquired from as wide a variety of weight percent silica values as possible.

6.4 Recommendations for Future Instruments

The obstacles involved in this research included the following: adequately warping the images in order to mosaic them seamlessly and have each pixel be well-located, difficulty in atmospherically correcting bands 11, 15 - 19, and 25, fitting the inverse Gaussian to very low weight percent silica rock spectra, and using the temperature emissivity separation technique on very flat spectra. Fortunately, the first obstacle has been removed for future researchers. The MASTER instrument now has a gyroscope attached during flight to keep the instrument steady.

To improve the ability to match spectra to secondary minerals using the VNIR bands, the band currently in a region of water absorption (band 11) could be moved to more useful wavelengths, such as between 0.85 and 0.92 microns (between bands 8 and 9), where the Fe^{3+} absorption feature is readily apparent in all iron-containing minerals. This feature is important in lithologic identification, because the most common minerals produced by the weathering of olivine, pyroxene, amphibole, and biotite (four of the primary minerals in mafic igneous rocks) are iron oxides, which include limonite, hematite, and goethite.

In the SWIR wavelength bands (MASTER bands 20 - 25), there is room for added channels to help diagnose spectral absorption features due to overtone bending and stretching vibrations in layered silicates and carbonates. A channel could be added between channels 20 and 21. Channel 25 could be moved to a slightly shorter wavelength to avoid large atmospheric absorption but to still aid in identifying minerals such as calcite and talc that have features beyond 2.3 μm, due to the absorption of CO_3

and Mg-OH, respectively. Bands 15-19 are fairly useless because they are entirely within water absorption wavelengths. These could be moved to the 2.0 –2.4 μm region in order to help differentiate minerals with CO_3, Mg-OH, Al-OH, and H_2O.

References

Schmidt, E.K., Plate tectonics, volcanic petrology, and ore formation in the Santa Rosalia Area, Baja California, Mexico, Master of Science thesis, The University of Arizona, pp. 194, 1975.

Demant, A., The Reforma Caldera, Santa Rosalia Area, Baja California, A volcanological, petrographical and mineralogical study, in *Neotectonics and sea level variations in the Gulf of California area, a Symposium*, edited by V. Malpica-Cruz, S. Celis-Gutiérrez, J. Guerrero-Garcia, and L. Ortlieb, pp. 77-96, Univ. Nal. Auton. México, Inst. Geologia, México, D. F., 1984.

Glossary

ACORN – Atmospheric Correction Now. This ENVI plug-in module is a radiative transfer model. The ACORN module relies on user input of date and time of image capture, mean elevation within image, atmospheric visibility, precipitable water vapor, and the altitude of image acquisition (in order to determine atmospheric pressure) to correct for atmospheric effects.

ASD – Analytical Spectral Devices Field Spectrometer

ASTER – Advanced Spaceborne Thermal Emission Reflection Radiometer

"Basalt" – The reference field spectra "Basalt," "Wttfgp," and "Faroash" were chosen for the classification because they had high separability (low matches in the Spectral Analyst™ to one another and the endmembers derived from the N-dimensional Visualizer™). "Basalt" was acquired from a lava flow of La Virgen. The location is shown in Figure 8 in Chapter 2.

"Faroash" – This reference spectrum is an average of spectra collected at 29.89° N, 114.41° W from as ash unit in the Puertecitos Volcanic Province in Northern Baja California.

HDF – Hierarchical Data Format

ISL – Isla San Luis

"LV-Veg" –This reference spectrum is an average of 9 pixels over known vegetation at the peak of La Virgen.

MASTER –MODIS-ASTER. This multi-channel remote sensing instrument has an instantaneous field of view of 2.5 milliradians and a total field of view of 85.92 degrees and was developed for the Advanced Spaceborne Thermal Emission Reflection Radiometer (ASTER) satellite as well as the Moderate Resolution Imaging Spectroradiometer (MODIS) projects.

MMD –Maximum and Minimum Difference. This is the difference between the maximum and minimum beta residual of a given pixel, which is used to determine the unknown minimum emissivity of the pixel using a calibration curve developed from laboratory spectra.

MNF –Minimum Noise Fraction transform. This transformation is performed to determine if the dimensionality of the data could be reduced. Ideally, an MNF produces a spectral subset of the data without the noise. An MNF transform is produced by two principal component analysis rotations and a noise-whitening step. The first rotation uses the principal components of the noise covariance matrix. The second rotation uses the

principal components derived from the original image after it has been noise whitened by the first rotation and rescaled by the noise standard deviation.

MODTRAN – This is a radiative transfer code that models atmospheric gas absorption and scattering. Using the look-up tables generated by MODTRAN, the calibrated radiances are converted to apparent surface reflectance. As with similar radiative transfer codes, the calibrated data are atmospherically corrected using both the calibrated radiance at sensor data and the atmospheric parameters in order to derive and model the scattering and absorption processes of the atmosphere. The radiative transfer code then calculates the transmittance of the various paths and the different components of the sky irradiance and path radiance.

NCEP – National Center for Environmental Prediction

PPI – Pixel Purity Index. This feature in ENVI finds the most extreme, or outlying, pixels when viewed in multidimensions. These pixels are referred to as "pure," since they should represent pixels with of the most homogeneous surface in the image. The PPI™ is a measure of the relative degree of local convexity, in any dimension. The convexity is computed by using repeated projections of n-dimensional scatterplots onto a lower dimensional subspace and marking the extreme pixels in each projection. The digital number (DN) of each pixel in the PPI™ image corresponds to the number of times that pixel was recorded as extreme. (Higher PPI™ indicates a higher purity)

PVP – Puertecitos Volcanic Province

SAM – Spectral Angle Mapper. This technique, when used on calibrated reflectance data, is relatively insensitive to illumination and albedo effects because it uses an n-dimensional angle to match pixels to reference spectra. The algorithm treats the pixels as n-dimensional vectors, with the dimensionality equal to the number of bands, and determines the spectral similarity between two spectra by calculating the angle in radians between the spectra. A value of zero radians defines a perfect fit.

SFF – Spectral Feature Fitting™. This is an absorption-feature-based methodology, where the unknown spectrum is scaled to match each library spectrum after continuum removal from both spectra.

SSE – Single Spectrum Enhancement. This is similar to an empirical line calibration, as it forces the image spectra to fit the known field spectra. and can only be computed for images that contain field spectra.

SWIR – Short Wave Infrared

TIR – Thermal Infrared

TVLRVR – Tres Vírgenes-La Reforma Volcanic Region

VNIR – Visible and Near Infrared

"Wttfgp" – This reference spectrum was collected from a tuff unit within the Las Minitas region (site latitude and longitude: 27.51° N, -118.42° W).

Appendix A: Homogeneous Regions for Use in the Single Spectrum Enhancement

Using reflectance data output from ACORN for the TVLRVR, the Single Spectrum Enhancement (SSE) was used to force the image spectra to fit the known field spectra. This method works well to atmospherically correct the spectra similar to the target spectrum; however, in some cases the SSE over-corrects or under-corrects other pixels within the image. Without known spectra for these regions, it is difficult to correct for these errors.

This single spectrum enhancement was first done on image 9900303H, which contains field spectra for a region of basalt, "Basalt." An acceptable atmospheric correction for this image was obtained. Although 6 other images also contain field spectra, in most cases the exact location within the image of the collection site was difficult to determine, and the sites themselves were not significantly larger than one pixel. Additionally, the other images do not contain both spectrally dark regions, with relatively low reflectance values, and spectrally light regions, with relatively high reflectance values. The 21 other images within the study area contained no field spectra. In order to calculate a SSE on the 27 other images in the TVLRVR, a technique was developed to find matching dark and light spectra on adjacent images. In this way, one can continue from one atmospherically corrected image to the next, using known spectra from the previously corrected image. This technique involves first locating areas of high homogeneity, where each pixel is spectrally similar to its adjacent pixels. A code was written to calculate the standard deviation between adjacent pixels and the mean for each pixel and its

neighboring pixels within an image. This is computed pixel by pixel for each band and can be done for a 3+n by 3+n pixel region, where n=1, 2, 3, etc. A spectrally homogeneous region is defined by minimizing the sum of the standard deviations of the region of pixels for all bands. Spectrally light regions were defined as those with a relatively large quotient of mean to standard deviation. Spectrally dark regions were defined as those with relatively small products of mean multiplied by the standard deviation.

Adjacent images were analyzed, and overlapping dark and light regions were chosen for each overlapping pair of images. The means of these regions were calculated and used as the spectra in the single spectrum enhancement. This approach did not atmospherically correct adjacent images well. The failure of this method to match adjacent images is likely due to the variability within the matching regions. In order to keep all 28 of the MASTER images within the region as similar as possible for processing, either all or none of the images needed to be spectrally enhanced by the field spectra. Therefore, this method was not used for further processing.

Appendix B Top Five Matches to the USGS Spectral Libraries

Table B.1 Endmembers from the Tres Vírgenes-La Reforma Region

Endmember	Match to the VNIR Region	Score	Match to the SWIR Region	Score
n-d #1	Montmorillonite SCa-2	1.883	Pinnoite NMNH123943	1.886
	Ammonioalunite NMNH145596	1.879	Sillimanite HS186	1.876
	Alunite GDS84 (K)	1.875	Beryl GDS9	1.863
	Ammonio-Smectite GDS86 (Sy)	1.870	Gypsum SU2202	1.862
	Montmorillonite CM20	1.865	Dumortierite HS190	1.860
n-d #2	Microcline HS151 Feldspar	1.844	Beryl GDS9	1.876
	Spessartine WS481	1.843	Pinnoite NMNH123943	1.861
	Polyhalite NMNH92669-4	1.841	Alunite GDS83 (Na)	1.861
	Microcline HS103 Feldspar	1.839	Sillimanite HS186	1.860
	Hydrogrossular NMNH120555	1.830	Chalcopyrite S26-36	1.842
n-d #3	Microcline HS151 Feldspar	1.851	Alunite GDS83 (Na)	1.888
	Microcline HS103 Feldspar	1.845	Alunite GDS83 (K)	1.776
	Carnallite HS430	1.841	Mesolite+Hydroxyapophyll	1.765
	Hectorite SHCa-1	1.840	Alunite GDS82 (Natroalunite)	1.762
	Montmorillonite CM27	1.838	Pyrophyllite SU1421	1.759
n-d #4	Gypsum HS333 (Selenite)	1.851	Kaolin/Smectite KLF508	1.929
	Actinolite HS315	1.819	Mizzonite HS351 Scapolite	1.922
	Illite IL105	1.810	Kaolin/Smectite KLF506	1.922
	Diopside NMNHR18685	1.804	Rectorite ISR202	1.917
	Olivine HS285 Fo80	1.801	Rectorite RAr-1	1.908
n-d #5	Augite, Pyroxene HS119	1.784	Diaspore HS416	1.993
	Acmite NMNH133746	1.783	Meionite WS700	1.985
	Jadeite HS343	1.767	Marialite NMNH126018-2	1.985
	Glauconite HS313	1.741	Grossular WS483 Garnet	1.978
	Illite IL101	1.660	Celsian HS200	1.977
n-d #6	Magnetite HS78	1.874	Gypsum SU2202	1.921
	Chert ANP90-6D	1.872	Dumortierite HS190	1.904
	Galena S105-2	1.863	Gypsum HS333 (Selenite)	1.839
	Diopside NMNHR18685	1.859	Pectolite NMNH94865	1.797
	Galena S102-1B	1.853	Colemanite GDS143	1.790
n-d #7	Galena S102-1B	1.833	Hematite HS45	1.926
	Galena S102-17	1.820	Olivine GDS70 Fo89	1.898
	Galena S105-2	1.814	Augite NMNH120049	1.877
	Topaz Glen_Cove_#8	1.812	Anorthite HS201 Plagioclase	1.866
	Galena S26-40	1.809	Augite WS592 Pyroxene	1.857

n-d #8	Andradite WS487 Garnet	1.911	Chlorite SMR-13 Mg	1.980
	Montmorillonite SAz-1	1.895	Dolomite HS102	1.976
	Goethite WS219 (Limonite)	1.891	Prochlorite SMR-14	1.975
	Endellite GDS16	1.889	Nontronite GDS41	1.971
	Montmorillonite+Illite CM42	1.889	Zoisite HS347	1.970
n-d #9	Juniper_Bush IH91-4B	1.613	Dry_Long_Grass AV87-2	1.950
	Fir_Tree IH91-2	1.454	Cassiterite HS279	1.890
	Rabbitbrush ANP92-27	1.432	Tumbleweed ANP92-2C	1.880
	Russian_Olive DW92-4	1.429	Olivine KI3189 Fo60	1.867
	Blue_Spruce DW92-5	1.419	Goethite HS36	1.866
n-d #10	Hematite FE2602	1.814	Oligoclase HS143 Plagioclase	1.973
	Siderite HS271	1.749	Oligoclase HS143 Plagioclase	1.971
	Spessartine NMNH14143	1.714	Adularia GDS57 (Orthoclase)	1.970
	Andalusite NMNHR17898	1.696	Grossular WS485 Garnet	1.970
	Sphene, Titanite HS189	1.671	Albite HS324 Plagioclase	1.970
n-d #11	Dickite NMNH46967	1.957	Labradorite HS105 Plagioclase	1.986
	Natrolite NMNH83380 Zeolite	1.915	Olivine GDS71 Fo91	1.982
	Sepiolite SepNev-1	1.889	Olivine GDS71 Fo91	1.978
	Muscovite GDS120	1.875	Andradite WS488 Garnet	1.973
	Topaz Harris_Park_#9	1.873	Cobaltite HS264	1.973
n-d #12	Kaolinite/Smectite H89-FR-2	1.821	Manganite HS138	1.827
	Clinozoisite HS299	1.814	Pectolite NMNH94865	1.695
	Rhodochrosite HS67	1.796	Almandine HS114 Garnet	1.679
	Andradite GDS12 Garnet	1.790	Orthoclase NMNH113188	1.629
	Sepiolite SepSp-1	1.785	Augite WS592 Pyroxene	1.597
Basalt	Staurolite HS188	1.853	Augite NMNH120049	1.963
	Andalusite NMNHR17898	1.851	Grossular WS484 Garnet	1.949
	Zircon WS522	1.835	Diopside NMNHR18685	1.946
	Barite HS79	1.831	Almandine WS477 Garnet	1.942
	Spessartine WS481 Garnet	1.823	Mizzonite HS351 Scapolite	1.941
Faroash	Montmorillonite SCa-2	1.969	Spessartine WS480 Garnet	1.960
	Cookeite CAr-1	1.965	Almandine WS478 Garnet	1.956
	Muscovite GDS108	1.963	Almandine WS477 Garnet	1.953
	Saponite SapCa-1	1.961	Sphene, Titanite HS189	1.951
	Pyrite S26-8	1.960	Almandine WS476 Garnet	1.949

Wttfgp	Grossular WS485 Garnet	1.916	Alunite GDS82 (Natroalunite)	1.802
	Carnallite NMNH98011	1.907	Pyrophyllite SU1421	1.748
	Hectorite SHCa-1	1.901	Alunite AL706	1.733
	Kaolinite CM9	1.901	Rivadavite NMNH170164	1.732
	Hectorite SHCa-1	1.900	Mesolite+Hydroxyapophyll	1.712
LV-Veg	Rubber Rabbitbrush	1.502	Dry_Long_Grass AV87-2	1.941
	Juniper_Bush IH91-4B	1.492	Olivine KI3189 Fo60	1.932
	Sage_Brush IH91-1B	1.484	Tumbleweed ANP92-2C	1.920
	Cheatgrass ANP92-11A	1.443	Goethite HS36	1.905
	Kerogen BK-Cornell	1.408	Galena S26-39	1.880

Table B.2 Endmembers from Isla San Luis

Compared to the USGS Spectral Libraries, using bands 1-10 (0.4589-0.91 microns) Mineral Name/Plant Name; Mineral Type/Plant Type; Formula	Score
n-d-1	
Staurolite; Nesosilicate; $Fe^{2+}{}_2Al_9O_6(SiO_4)_4(O,OH)_2$	1.865
Zircon; Nesosilicate; $ZrSiO_4$	1.826
Barite; Sulfate; $BaSO_4$	1.819
Sauconite; Phyllosilicate; $Na_{0.33}Zn_3(Si,Al)_4O_{10}(OH)_2 \bullet 4H_2O$	1.811
Almandine; Nesosilicate; $Fe^{+2}{}_3Al_2(SiO_4)_3$	1.799
n-d-2	
Magnesio-Hornblende (Amphibole group); Inosilicate; $Ca_2(Mg,Fe^{+2})_4Al(Si_7Al)O_{22}(OH,F)_2$	1.871
Microcline (Feldspar group); Tectosilicate; $KAlSi_3O_8$	1.869
Tremolite (Amphibole group); Inosilicate; $Ca_2Mg_5Si_8O_{22}(OH)_2$	1.861
Illite; Phyllosilicate; $(K,H_3O)(Al,Mg,Fe)_2(Si,Al)_4O_{10}[(OH)_2,H_2O]$	1.858
Oligoclase (Plagioclase)(Feldspar group); Tectosilicate; $(Na,Ca)Al(Al,Si)Si_2O_8$	1.853
n-d-3	
Tremolite (Amphibole group); Inosilicate; $Ca_2Mg_5Si_8O_{22}(OH)_2$	1.87
Magnesio-Hornblende (Amphibole group); Inosilicate; $Ca_2(Mg,Fe^{+2})_4Al(Si_7Al)O_{22}(OH,F)_2$	1.865
Palygorskite (Attapulgite); Phyllosilicate; $(Mg,Al)_2Si_4O_{10}(OH) \bullet 4H_2O$	1.863
Microcline (Feldspar group); Tectosilicate; $KAlSi_3O_8$	1.861
Bytownite (Plagioclase)(Feldspar group); Tectosilicate; $(Na,Ca)Al(Al,Si)Si_2O_8$	1.861
n-d-4	
Tremolite (Amphibole group); Inosilicate; $Ca_2Mg_5Si_8O_{22}(OH)_2$	1.903
Microcline (Feldspar group); Tectosilicate; $KAlSi_3O_8$	1.895
Oligoclase (Plagioclase)(Feldspar group); Tectosilicate; $(Na,Ca)Al(Al,Si)Si_2O_8$	1.885
Magnesio-Hornblende (Amphibole group); Inosilicate; $Ca_2(Mg,Fe^{+2})_4Al(Si_7Al)O_{22}(OH,F)_2$	1.875
Pectolite; Inosilicate; $NaCa_2Si_3O_8(OH)$	1.872
n-d-5	
Saltbrush; Shrub	1.306
Juniper; Shrub	1.235
Blue Spruce; Tree	1.196
Pinon Pine; Tree	1.152
Aspen; Tree	1.094
n-d-6	
Phyllosilicate;$(Na,Ca)_{0.33}(Al,Mg)_2Si_4O_{10}(OH)_2 \bullet nH_2O$ +	1.873
Kaolinite/Smectite; Phyllosilicate; $Al_2Si_2O_5(OH)_4$ + $(Na,Ca)_{0.33}(Al,Mg)_2Si_4O_{10} \bullet nH_2O$	1.864
$(Na,Ca)_{0.33}(Al,Mg)_2Si_4O_{10}(OH)_2 \bullet nH_2O$ + $(K,H_3O)(Al,Mg,Fe)_2(Si,Al)_4O_{10}[(OH)_2,H_2O]$	1.863
Sphalerite; Sulfide; ZnS	1.858
Montmorillonite; Phyllosilicate; $(Na,Ca)_{0.33}(Al,Mg)_2Si_4O_{10}(OH)_2 \bullet nH_2O$	1.857

Compared to the USGS Spectral Libraries, using bands 20-24 (2.0-2.233250 microns) Mineral Name/Plant Name; Mineral Type/Plant Type; Formula	Score
n-d-1	
Beryl; Cyclosilicate; $Be_3Al_2Si_6O_{18}$	1.912
Alunite (Na_{63})(Alunite group); Sulfate; $(Na,K)Al_3(SO_4)_2(OH)_6$ (Na_{63})	1.894
Thenardite; Sulfate; Na_2SO_4	1.893
Mesolite + Hydroxyapophyllite; Tectosilicate; $Na_2Ca_2Al_6Si_9O_{30}•8H_2O$ + $KCa_4Si_8O_{20}(OH,F)•8H_2O$	1.889
Chalcopyrite (Chalcopyrite group); Sulfide; $CuFeS_2$	1.877
n-d-2	
Hematite; Oxide; alpha-Fe_2O_3	1.775
Galena; sulfide; PbS	1.754
Almandine (Garnet group); Nesosilicate; $Fe^{+2}{}_3Al_2(SiO_4)_3$	1.747
Psilomelane (Romanechite); Hydroxide (Mineral mixture); $BaMn^{+2}Mn^{+4}{}_8O_{16}(OH)_4$	1.712
Acmite (Aegirine)(Pyroxene group); Inosilicate; $NaFeSi_2O_6$	1.698
n-d-3	
Alunite (Na_{63})(Alunite group); Sulfate; $(Na,K)Al_3(SO_4)_2(OH)_6$ (Na_{63})	1.855
Anthophyllite (Amphibole group); Inosilicate; $(Mg,Fe^{+2})_7Si_8O_{22}(OH)_2$	1.827
Pyrophyllite; Phyllosilicate; $Al_2Si_4O_{10}(OH)_2$	1.814
Cronstedtite (Kaolinite-Serpentine group); Phyllosilicate; $Fe_2{}^{+2}Fe^{+3}(Si,Fe^{+3})O_5(OH)_4$	1.796
Mesolite + Hydroxyapophyllite; Tectosilicate; $Na_2Ca_2Al_6Si_9O_{30}•8H_2O$ + $KCa_4Si_8O_{20}(OH,F)•8H_2O$	1.796
n-d-4	
Thenardite; Sulfate; Na_2SO_4	1.939
Beryl; Cyclosilicate; $Be_3Al_2Si_6O_{18}$	1.938
Mesolite + Hydroxyapophyllite; Tectosilicate; $Na_2Ca_2Al_6Si_9O_{30}•8H_2O$ + $KCa_4Si_8O_{20}(OH,F)•8H_2O$	1.916
Beryl; Cyclosilicate; $Be_3Al_2Si_6O_{18}$	1.915
Chalcopyrite (Chalcopyrite group); Sulfide; $CuFeS_2$	1.912
n-d-5	
Cheatgrass; Grass	1.945
Sage Brush; Shrub	1.926
Tumbleweed; Shrub	1.923
Dry Long Grass; Grass	1.913
Rabbitbrush; Shrub	1.89
n-d-6	
Thenardite; Sulfate; Na_2SO_4	1.959
Beryl; Cyclosilicate; $Be_3Al_2Si_6O_{18}$	1.937
Cronstedtite (Kaolinite-Serpentine group); Phyllosilicate; $Fe_2{}^{+2}Fe^{+3}(Si,Fe^{+3})O_5(OH)_4$	1.937
Mesolite + Hydroxyapophyllite; Tectosilicate; $Na_2Ca_2Al_6Si_9O_{30}•8H_2O$ + $KCa_4Si_8O_{20}(OH,F)•8H_2O$	1.899
Alunite (Na_{63})(Alunite group); Sulfate; $(Na,K)Al_3(SO_4)_2(OH)_6$ (Na_{63})	1.889